applied sciences

Special Issue Reprint

# Fault Diagnosis for Electrical Machines, Power Electronics, and Drives

Edited by
Jose M. Guerrero, Araitz Iturregi Aio and Sergio Toscani

mdpi.com/journal/applsci

MDPI

# Fault Diagnosis for Electrical Machines, Power Electronics, and Drives

# Fault Diagnosis for Electrical Machines, Power Electronics, and Drives

Guest Editors

**Jose M. Guerrero**
**Araitz Iturregi Aio**
**Sergio Toscani**

MDPI

Basel • Beijing • Wuhan • Barcelona • Belgrade • Novi Sad • Cluj • Manchester

*Guest Editors*

Jose M. Guerrero
Department of Electrical Engineering
Universidad del País Vasco/Euskal Herriko Unibertsitatea
Bilbao
Spain

Araitz Iturregi Aio
Department of Electrical Engineering
Universidad del País Vasco/Euskal Herriko Unibertsitatea
Bilbao
Spain

Sergio Toscani
Dipartimento di Elettronica, Informazione e Bioingegneria (DEIB)
Politecnico di Milano
Milano
Italy

*Editorial Office*
MDPI AG
Grosspeteranlage 5
4052 Basel, Switzerland

This is a reprint of the Special Issue, published open access by the journal *Applied Sciences* (ISSN 2076-3417), freely accessible at: https://www.mdpi.com/journal/applsci/special_issues/JJ7309YABX.

For citation purposes, cite each article independently as indicated on the article page online and as indicated below:

Lastname, A.A.; Lastname, B.B. Article Title. *Journal Name* **Year**, *Volume Number*, Page Range.

**ISBN 978-3-7258-8001-0 (Hbk)**
**ISBN 978-3-7258-8002-7 (PDF)**
**https://doi.org/10.3390/books978-3-7258-8002-7**

© 2026 by the authors. Articles in this reprint are Open Access and distributed under the Creative Commons Attribution (CC BY) license. The reprint as a whole is distributed by MDPI under the terms and conditions of the Creative Commons Attribution-NonCommercial-NoDerivs (CC BY-NC-ND) license (https://creativecommons.org/licenses/by-nc-nd/4.0/).

# Contents

**About the Editors** . . . . . **vii**

**Preface** . . . . . **ix**

**MohammadSaleh Hedayati, Ailin Barzegar and Afshin Rahimi**
Fault Diagnosis and Prognosis of Satellites and Unmanned Aerial Vehicles: A Review
Reprinted from: *Appl. Sci.* **2024**, *14*, 9487, https://doi.org/10.3390/app14209487 . . . . . **1**

**Ignacio Martin-Diaz, Tomas Garcia-Calva, Óscar Duque-Perez and Daniel Morinigo-Sotelo**
Imbalanced Diagnosis Scheme for Incipient Rotor Faults in Inverter-Fed Induction Motors
Reprinted from: *Appl. Sci.* **2024**, *14*, 7237, https://doi.org/10.3390/app14167237 . . . . . **43**

**Jose L. Contreras-Hernandez, Dora L. Almanza-Ojeda, Rogelio Castro-Sanchez and Mario A. Ibarra-Manzano**
Quaternion Signal Analysis for Detection of Broken Rotor Fault Degrees in Induction Motors
Reprinted from: *Appl. Sci.* **2025**, *15*, 1787, https://doi.org/10.3390/app15041787 . . . . . **58**

**Inyeol Yun, Hyunwoo Kim, Ju Lee and Sung-Gu Lee**
Inter-Turn Fault Diagnosis of Induction Motors Based on Current Vector Pattern Analysis in Stationary Coordinate Frame
Reprinted from: *Appl. Sci.* **2025**, *15*, 8414, https://doi.org/10.3390/app15158414 . . . . . **71**

**Jungho Ahn, Ju Lee and Hyunwoo Kim**
Impedance-Based Inter-Turn Fault Diagnosis in Integrated Induction Motor and Drive Systems Using Space Voltage Vectors
Reprinted from: *Appl. Sci.* **2025**, *15*, 6065, https://doi.org/10.3390/app15116065 . . . . . **86**

**Jérémy Creux, Najla Haje Obeid, Thierry Boileau and Farid Meibody-Tabar**
Online High Frequency Impedance Identification Method of Inverter-Fed Electrical Machines for Stator Health Monitoring
Reprinted from: *Appl. Sci.* **2024**, *14*, 10911, https://doi.org/10.3390/app142310911 . . . . . **101**

**Caixia Gao, Zhen Jiang, Xiaozhuo Xu and Jikai Si**
Demagnetization Fault Location of Direct-Drive Permanent Magnet Synchronous Motor Based on Search Coil Data-Driven
Reprinted from: *Appl. Sci.* **2026**, *16*, 870, https://doi.org/10.3390/app16020870 . . . . . **126**

**Rubén Pascual, Eduardo Rivero, José M. Guerrero, Kumar Mahtani and Carlos A. Platero**
Influence of Temperature on Brushless Synchronous Machine Field Winding Interturn Fault Severity Estimation
Reprinted from: *Appl. Sci.* **2024**, *14*, 8061, https://doi.org/10.3390/app14178061 . . . . . **146**

**Sanja Antić, Marko Rosić, Branko Koprivica, Alenka Milovanović and Milentije Luković**
Detection, Isolation, and Identification of Multiplicative Faults in a DC Motor and Amplifier Using Parameter Estimation Techniques
Reprinted from: *Appl. Sci.* **2025**, *15*, 8322, https://doi.org/10.3390/app15158322 . . . . . **161**

# About the Editors

**Jose M. Guerrero**

Jose M. Guerrero is a Research Associate Professor at the Department of Electrical Engineering, University of the Basque Country (UPV/EHU). He received a B.Sc. in energy resources, fuels and explosive engineering, an M.Sc. in electrical engineering, and a Ph.D. degree in Electrical Engineering from Universidad Politécnica of Madrid, Spain, in 2018, 2019, and 2022 respectively. His main field of interest relates to the diagnosis and protection of electrical systems that involve power electronics, such as electric drives, DC links, energy storage systems or DC microgrids. He has authored and co-authored more than 100 scientific contributions and more than 25 patents in the field. His expertise mainly resides in ground fault diagnosis and frequency response analysis applied to drives and electrical machines for condition monitoring. As researcher, he has taken part in multiple interdisciplinary collaborative projects. The combined funding of these projects exceeds 1,750,000 € for the organizations in which he has participated. Furthermore, he is member of the technical committee for research project evaluation at the Agency for Scientific and University Quality of Andalusia, and of the local committee of the Developments in Power System Protection Conference.

**Araitz Iturregi Aio**

Araitz Iturregi Aio is an Associate Professor at the Department of Electrical Engineering, University of the Basque Country (UPV/EHU), where she also received her M.Sc. and PhD in 2006 and 2013, respectively. She began her professional career at SEW Eurodrive, specializing in frequency inverters and decentralized drive systems. In 2007, she joined the Department of Electrical Engineering at the Bilbao School of Engineering (UPV/EHU), a role she still holds today. Her main research interests include current interruption techniques, the simulation of electric arc behaviors in current interruption switches, and the design of power systems protection. Her primary interests also encompass HIL simulation techniques for design and validate protection algorithms in power systems. She has completed pre- and post-doctoral research stays at the Technische Universität Ilmenau in Germany. Additionally, she also collaborates with the Leibniz Institute for Plasma Science and Technology (INP Greifswald), Ostschweizer Fachhochschule, TU Delft or companies such as Iberdrola, ZIV or Tecnalia in several joint national and international research projects.

**Sergio Toscani**

Sergio Toscani is an Associate Professor with the Dipartimento di Elettronica, Informazione e Bioingegneria, Politecnico di Milano. In 2007, he received an M.Sc. degree (summa cum laude) in Electrical Engineering from Politecnico di Milano, where he also obtained his Ph.D. degree (summa cum laude) in 2011. His research activity primarily focuses on the characterization of electrical devices and measurements in power systems. His main research interests include the development and characterization of voltage and current transducers, advanced digital signal processing techniques for power system measurements, diagnostic methods for electrical devices, and the monitoring of photovoltaic systems. He serves as Technical Program Co-Chair of the IEEE Workshop on Applied Measurements for Power Systems and he is member of the Technical Committee TC39—Measurements in Power Systems of the IEEE Instrumentation and Measurement Society. He has been Guest Editor for several Special Sections published in leading journals in the field of electrical measurements and is member of the Editorial Board of the MDPI journal *Applied Sciences*.

# Preface

The reprint "Fault Diagnosis for Electrical Machines, Power Electronics, and Drives" brings together a collection of review and research articles addressing one of the most significant challenges in modern electrical engineering.

This reprint aims to contribute to the current literature by presenting advanced fault diagnosis and protection methods for electrical drives incorporating power electronics. The increasing use of power electronic converters, while enabling higher efficiency, better performance, and greater flexibility, also intensifies stress on electrical machines, produced by modulation strategies and high-frequency switching. This increases the likelihood of electrical, mechanical and magnetic faults. Additionally, conventional protection systems often struggle to properly and timeously detect faults under non-sinusoidal and variable-frequency operating conditions for which they were not originally designed.

Despite their negative impact on system lifetime, power electronic converters also provide new opportunities, as they can actively take part in advanced fault diagnosis and protection techniques. The coexistence of these challenges and opportunities constitutes the main motivation behind this reprint.

On behalf of the editorial team and the contributing authors, we would like to recommend this reprint to researchers working on fault detection and protection of electrical machines supplied by power electronics, as well as to practicing engineers interested in implementing advanced diagnostic techniques in industrial environments.

This reprint includes an extensive review of general fault diagnosis methods for aerospace and satellite applications, together with research contributions addressing specific and relevant failures such as inter-turn short-circuits, broken rotor bars in induction machines, demagnetization in permanent magnet synchronous machines, and multiple fault identification in DC motors. Through these advanced diagnostic techniques, this reprint provides readers with relevant insights for the development and implementation of fault diagnosis strategies in electrical machines, power electronics, and drives.

**Jose M. Guerrero, Araitz Iturregi Aio, and Sergio Toscani**
*Guest Editors*

applied sciences

MDPI

*Review*

# Fault Diagnosis and Prognosis of Satellites and Unmanned Aerial Vehicles: A Review

**MohammadSaleh Hedayati †, Ailin Barzegar † and Afshin Rahimi *,†**

Department of Mechanical, Automotive and Materials Engineering, University of Windsor, 401 Sunset Ave, Windsor, ON N9B 3P4, Canada; hedayat2@uwindsor.ca (M.H.); barzegaa@uwindsor.ca (A.B.)

* Correspondence: arahimi@uwindsor.ca

† These authors contributed equally to this work.

**Abstract:** This paper comprehensively analyzes advanced Fault Diagnosis and Prognosis (FDP) techniques employed in aerial and space agents such as satellites, spacecraft, and Unmanned Aerial Vehicles (UAVs). The critical engineering functions of fault diagnostics and prognosis, particularly the emerging field of fault prognosis, emphasize the necessity for further advancement. Integrating these methodologies enriches the system's capacity to diagnose faults in their early stages. Additionally, it enables the prediction of fault propagation and facilitates proactive maintenance to mitigate the risk of severe failure. This paper aims to introduce diverse FDP methods, followed by a discussion on their application and evolution within single and multisatellite/UAV systems. Throughout this review, eighty-five relevant works are analyzed and discussed and their evaluation metrics are expanded upon as well. Within the works analyzed in this review, it was found that data-driven methods constitute 54% and 7% of the methodologies utilized in single- and multiagent FDP, respectively, which underscores the rise of these methods in the field of single-agent FDP and their unexplored potential in multiagent condition monitoring. Finally, this review is brought to a close with a suggested classification scheme of the utilized methodologies in the field, a quantitative analysis of their contributions to the field, and remarks and mentions of the potential gaps in the area.

**Keywords:** fault detection; fault isolation; fault identification; fault prognosis; single/multisatellite/UAV

## 1. Introduction

The reliability of satellite and Unmanned Aerial Vehicle (UAV) missions has received significant attention in recent years owing to the cost and time needed to launch satellites [1]. The possible severe consequences in the case of satellite and UAV failures also contribute to this cause in addition to the manufacturing and operational costs. According to [2], 32% of on-orbit spacecraft failures are attributed to the attitude and orbit control system (AOCS) and 27% to the power subsystem. Consequently, addressing the AOCS and power subsystem health monitoring could significantly boost onboard spacecraft mission reliability. Moreover, 51% of the malfunctions are due to Reaction Wheel (RW), momentum wheels, Control Moment Gyro (CMG), thrusters, and gyroscopes, and 18% are due to unknown reasons, warranting the need to explore health monitoring in the mentioned system components. Regarding the time of failure after launch, 41% of the recorded failures in [2] occurred in the first year of operation, making Fault Diagnosis and Prognosis (FDP) strategies imperative to extending on-orbit spacecraft and satellites' lifetimes. On the other hand, for UAVs, malfunctions could be caused by intentional or unintentional factors. Among the various operation-endangering abnormalities, the following are the most prevalent: cyber-attacks, such as signal jamming, spoofing, measurement sensor, keylogging viruses, control system attacks, and exogenous physical factors, such as sudden aerodynamic disturbances, and damaged actuators [3]. The satellite and UAV actuator and

sensor failures could also be attributed to intrinsic hardware wear-and-tear and degradation. To increase the mission reliability of these agents, all kinds of significant faults should be fixed or circumvented regardless of their source. There are two main approaches for increasing the mission reliability of satellites and UAVs [4]: hardware redundancy and analytical redundancy. Hardware redundancy involves incorporating redundant components for switching to a healthy component once the primary unit malfunctions. However, this poses a major issue. With the rise in the number of launched satellites and the decrease in their sizes, embedding redundant components becomes impractical [5]. The limited space available in UAVs also does not allow for hardware redundancy. In addition, switching from a faulty to a healthy component could disturb the operational continuity of missions [6]. Due to hardware redundancy's evident shortcomings, there is a need for advanced analytical redundancy methods. Analytical redundancy methods comprise vastly different means to monitor the health status of agents, namely, data-driven, model-based, and expert manpower-based methods. Compared with the methods reliant on expert personnel to go through the operational data of the agents, autonomous methods are distinctly superior, especially since they are more cost-effective and time-efficient while being less prone to errors. Hence, the advantages of autonomous analytical redundancy methods have inspired researchers to explore this area further. Among the host of analytical redundancy methods, data-driven and model-based methods are the most prevalent in the literature owing to their advantages. To address the health monitoring requirements of agents more precisely, analytical redundancy methods are divided into fault diagnosis and fault prognosis fields. The former accounts for informing the system of a fault in it, whereas the latter is responsible for estimating the system's Remaining Useful Life (RUL) given the diagnosed faults. From a mission reliability perspective, the insights derived from the FDP modules are used as input to the fault-tolerant control module. To increase the readability and understandability of this work among the myriad of works on general system reliability applications, we employ and explain the terminology in our work decided upon by the International Federation of Automatic Control (IFAC) Technical Committee SAFEPROCESS and outlined in [7]. Here, we briefly go over the most prevalent definitions presented in [7]: "Fault Detection" is defined as the determination of an existing system fault with an emphasis on the time of detection. Following this stage, "Fault Isolation" is described as the stage responsible for determining the location, kind, and time of detection. The subsequent step is labeled "Fault Identification", which involves determining the size details of the isolated fault and the time-variant behavior that it exhibits. Alternatively, "Fault Diagnosis" is defined as a step that follows "Fault Detection", contains "Fault Isolation and Identification" in itself, and entails measuring the size, kind, location of the fault, and the time of its detection. Finally, "Monitoring" means continuous online or real-time physical system condition evaluation through storing operational information and discerning and annunciating the emerging anomalies in its operation.

In the current study, we review the different FDP methods for satellites and UAVs that work individually or as members of a multisatellite/UAV network using analytical redundancy methods. The inclusion of both satellites and UAVs is due to the similarities in how health-monitoring approaches have been implemented for these agents. Investigating the methods employed in one agent could help provide valuable takeaways for utilizing them in the other agent. As a result of the prominence of data-driven and model-based methods in this area, this study has been divided into sections covering each category while also reviewing other methods that are fusions of the two mentioned categories (i.e., hybrid methods) or completely different methodologies.

The diagnostic and prognostic methods used for increasing the mission reliability of satellites, spacecraft, and UAVs in this work can be applied to more than one class of each of these agents. Many of the techniques addressed in this work are applicable to various actuators, sensors, and subsystems onboard satellites and UAVs. Satellites are usually categorized based on their mass, which can lie in ranges of 1 g to upwards of 1000 kg [8]. Some of the most prominent satellite classes include nanosatellites and small-, medium-,

and large-sized satellites. However, the methods analyzed in this review are presented with the mindset of applying them to more than their original classes. Conversely, when a method is applicable to only one or a few scenarios, it is declared. Furthermore, different classes of UAVs are also considered. The main categories of UAVs include the two groups of Vertical Takeoff and Landing (VTOL) and Conventional Takeoff and Landing (CTOL) UAVs. Some examples of VTOLs covered in this work are Hex-rotor, quadrotor, and tilt-rotor UAVs and fixed-wing UAVs for the CTOL class. The same analysis logic described for the FDP of different satellite classes also holds for different UAV classes.

It is notable to mention that in this review, relevant quantitative validation results of the discussed studies are presented when possible. However, the test results of different studies are usually acquired under different circumstances unless compared directly. Therefore, deep analysis solely based on the quantitative results might prove erroneous, but they are provided for reference in this review and expanded upon when possible.

The rest of the article is structured as follows. Section 2 provides initial details, encompassing the problem's definitions and setting the groundwork for subsequent discussions. Section 3 goes over the review methodology that was adopted in this review and important considerations and assumptions for the readers of this review. Sections 4 and 5 explore and review FDP approaches, respectively. Finally, Section 6 summarizes this paper, presents a classification of the prominent methodologies in the field of satellite and UAV FDP, and proposes potential future research directions based on the identified gaps in the field.

## 2. Preliminaries and Definitions

Faults are an inevitable part of dynamic systems and must be accounted for and dealt with, particularly for applications where reliability is paramount. Faults are defined as unpredicted alterations of the system behavior occurring naturally or intentionally, prohibiting the system's subcomponents from continuing nominal operation. These faults could leave a detrimental effect on the whole system and take some time to cause failure, or in some cases, they could cause instantaneous system failures. Consequently, searching for means of diagnosing and prognosing faults is warranted to deal with faults with lasting effects as part of a health monitoring strategy. General satellite, spacecraft, and UAV fault types could be broken down into four categories: abrupt, transient, intermittent, and incipient. Abrupt malfunctions are classified as spontaneously caused by hardware failure and will not be alleviated until fully repaired. In other words, they are characterized by system changes that are faster than the system's nominal dynamics. Transient malfunctions comprise deviations from the nominal operating conditions that may disappear without external intervention. Recurring transient faults are called intermittent faults. The likelihood of intermittent faults occurring is proportional to the system complexity [9]. Finally, incipient faults are defined as malfunctions caused by the deterioration of a system over time [10]. These four fault types are illustrated in Figure 1. Faults could also be modeled as additive and multiplicative faults depending on their effects on a system's dynamics. Multiplicative faults affect a system's inputs and outputs in a multiplicative way and stem from systematic parameter variations [11].

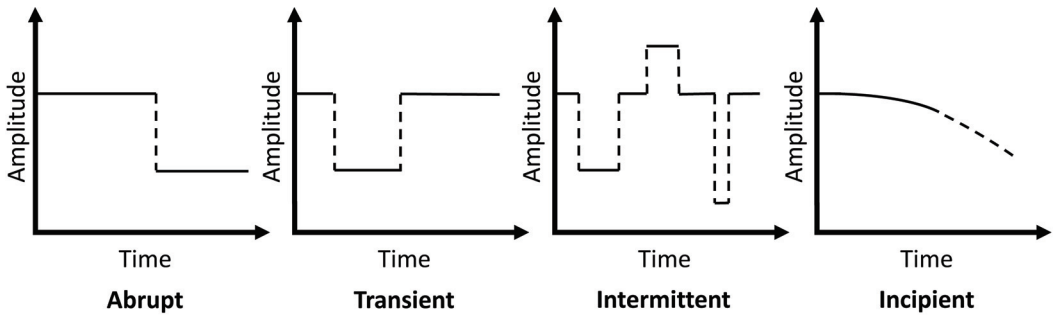


**Figure 1.** Behavior of different fault types over time.

The fault diagnosis process in nonlinear systems, including satellites and UAVs, involves multiple layers. The common classification used to delineate these stages of fault diagnosis includes detection, isolation, identification, estimation, and reconstruction. The term "malfunction detection" or "fault detection" refers to the capability of an analytically redundant methodology to recognize the presence of a fault. We have achieved the detection stage once our diagnostic schemes accurately identify when a fault originated. Isolation, conversely, involves determining the fault's location within the system. Therefore, a system's detection and isolation processes have temporal and spatial aspects, respectively. Detection always precedes or co-occurs with isolation but never follows it. Fault identification, estimation, and reconstruction are often used interchangeably to convey a similar concept. This stage of diagnosis aims to determine the characteristics of the malfunction. A malfunction's characteristics could include its severity, shape, depth, etc. Two main approaches for performing fault identification on a system are qualitative and quantitative. The two methods are subsets of identification techniques; however, their implementations tend to be vastly different and depend on the application. For instance, qualitative techniques necessitate a predefined set of malfunction types for classifying future occurrences as one of them or, conversely, for clustering them based on emerging malfunction types. In contrast, quantitative techniques rely on quantifying system performance degradation to achieve identification. The next step towards health monitoring is to predict the future course of faults and their effect on the RUL of a system. Prognosis becomes especially beneficial when a system is dealing with incipient faults, as its RUL could be evaluated using prognostics and lengthened by operators by taking appropriate remedying measures accordingly [12]. The results of the FDP schemes are then incorporated into fault-tolerance and recovery strategies to compensate for the malfunctions of single and multiagent systems. The visual representation of the mentioned process is depicted in Figure 2. Nevertheless, the intricate details of fault-tolerant methods and the literature related to them fall beyond the scope of this paper.

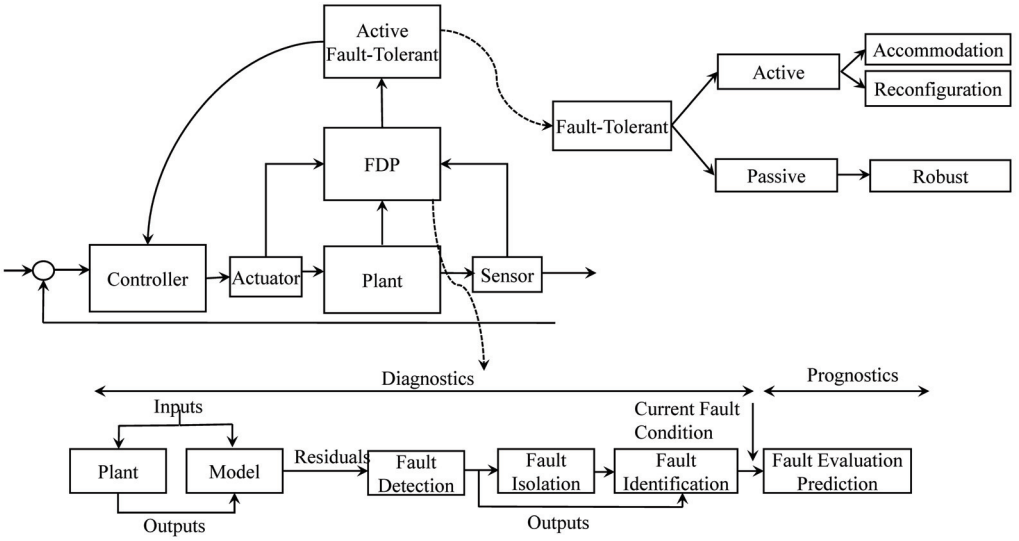


**Figure 2.** FDP and fault-tolerant control schemes.

FDP methodologies mostly monitor the health state of satellites, spacecraft, and UAVs through model-based and data-driven methods. Model-based techniques rely on high-fidelity models of systems and estimators to evaluate fault-sensitive states, analyze them, and compare the results with the model of the system operating nominally. Model-based methods comprise deterministic and stochastic strategies. Stochastic estimation schemes account for the added process and measurement noise while estimating states. Among stochastic schemes, Kalman Filter (KF) are utilized for linear models with added Gaussian noise, and Unscented Kalman Filter (UKF) and Extended Kalman Filter (EKF) for

nonlinear models with added Gaussian noise. When several faults are involved, interacting multiple model (IMM) methods could be used which employ several interacting filters to classify different fault modes [13]. Meanwhile, the Particle Filter (PF) class is reliable for estimation in nonlinear models with non-Gaussian noise. All in all, the main drawback of using model-based methods is their requirement for precise models that are not always available and are difficult to derive for every application. Essentially, the family of KFs can estimate the internal states of a linear or nonlinear dynamic system in the presence of known parameters and noisy processes and measurements. They could also be used to estimate the parameters instead of states, considering only states, and the process and measurement noises are known. Keep in mind that in this text, states refer to the dynamical representation of systems that tend to exhibit rapid changes. In contrast, parameters are virtually time-invariant elements closely tied to the system's characteristics. System state estimation is used to study the deviations of the system's dynamical behavior from nominal conditions. However, the system's parameters, as opposed to states, could also indicate a system's health, especially when it is undergoing degradation. There are also approaches for simultaneously estimating the states and parameters of a system, namely, dual and joint estimation. On the other hand, parameter estimation is usually, but not necessarily, associated with time delays, restricting their usage to offline health monitoring and not accommodating online monitoring requirements [14]. Model-based methods usually utilize residual-based algorithms to diagnose faults in control systems. To clarify the practicality of residual-based algorithms in fault diagnosis, an example of their use in a general discrete linear system along with a linear KF was outlined in [15]. Accordingly, the linearized system model in state-space form is represented by

$$\begin{cases} X_k = A_{k-1}X_{k-1} + \Gamma_{k-1}w_{k-1} \\ Z_k = C_kX_k + v_k + f_{k,\varphi}\gamma \end{cases} \tag{1}$$

where $X_k \in \mathbb{R}^n$ denotes the system state, $Z_k \in \mathbb{R}^m$ denotes the measurement output, $A_{k-1} \in \mathbb{R}^{n\times n}$ is a constant matrix, $\Gamma_{k-1} \in \mathbb{R}^{n\times r}$ denotes the noise matrix, $w_k \in \mathbb{R}^r$ denotes the process zero-mean Gaussian white noise sequence, and $v_k \in \mathbb{R}^m$ denotes the measurement zero-mean Gaussian white noise sequence. The process and measurement noises are independent. In addition, the control input is assumed to be zero. $\gamma$ denotes a random vector representing the fault size, while $f_{k,\phi}$ is set to be one when the system is faulty and zero when the system is nominal.

Subsequently, we aim to update the a priori state estimate with a gain of weighted time duration and the new measurement in each iteration of running the following iterative equation:

$$\begin{cases} \hat{X}_k^- = A_{k-1}\hat{X}_{k-1}^+ \\ P_{k/k-1} = A_{k-1}P_{k-1}A_{k-1}^T + \Gamma_{k-1}Q_{k-1}\Gamma_{k-1}^T \\ L_k = P_{k/k-1}C_k^T\left[C_kP_{k/k-1}C_k^T + R_k\right]^{-1} \\ \hat{X}_k^+ = [I - L_kC_k]A_{k-1}\hat{X}_{k-1}^+ + L_kZ_k \\ P_k = [I - L_kC_k]P_{k/k-1} \end{cases} \tag{2}$$

where $\hat{X}_k^+$ denotes the estimated state using the measurement update vector of $Z_k$, $\hat{X}_k^-$ denotes the predicted state using the last iteration's estimated state only. $P_{k/k-1}$ and $P_k$ denote the error covariance time and measurement updates, respectively. Finally, the state residual is defined as the difference between the estimated and the predicted states and is evaluated as follows:

$$\beta_k = \hat{X}_k^- - \hat{X}_k^+ \tag{3}$$

The calculated residual is then continuously compared with a threshold. The residual can also be created using differences between nominal and estimated measurement outputs instead of predicted and estimated outputs. Figure 3 represents the process of generating output residuals and delivering them to the fault diagnosis block.

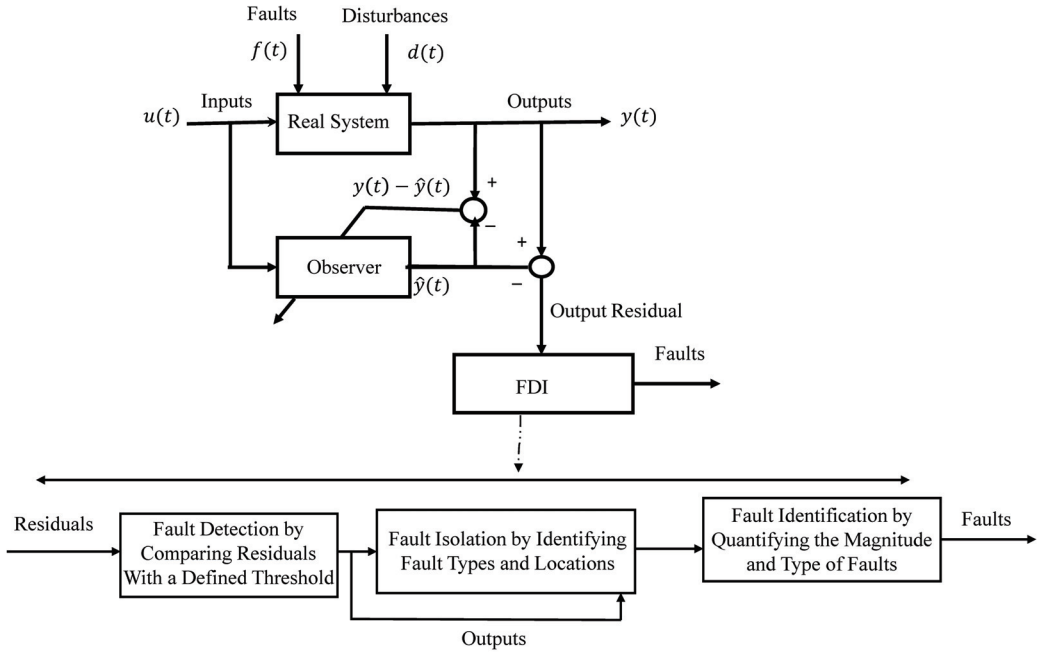


**Figure 3.** Fault diagnosis strategy.

When a threshold is surpassed, a fault is identified, and depending on the context, it may be isolated and described based on where and the extent to which the threshold has been surpassed. Residual-based algorithms have the flexibility to employ different residual definitions, but they fundamentally share the same concept as exemplified in [15]. However, using constant thresholds could yield unsatisfactory results or cause divergence, especially when they are poorly defined and when the nonmeasurable parameters of the system undergo abrupt changes [16]. To avoid this problem, adaptive thresholding methods have been utilized in the literature. Data-driven methods are another popular approach for health monitoring in nonlinear systems. Data-driven techniques encompass a broad spectrum of Machine Learning (ML) and Artificial Intelligence (AI) algorithms that can learn and extract patterns from datasets. The major advantages of using these techniques are analyzing complex nonlinear systems through learning the patterns in their output and accommodating applications where either labeled or unlabeled datasets are available, eliminating manual work. Data-driven methods develop an understanding of the studied linear or nonlinear dynamic systems and essentially model them as black boxes capable of analyzing real systems' performance. However, this imposes two major challenges: (i) large amounts of data are needed for data-driven methods to become reliable, and (ii) they lack interpretability compared with other methods. For instance, a broad range of neural networks are utilized in literature for learning the features of nonlinear systems; however, generally, we do not have meaningful and effective access to the inner workings of neurons and how they reach a specific output. Meanwhile, model-based method outputs are easily justifiable since high-fidelity models are accessible and can be examined. Nevertheless, the advantages of data-driven methods outweigh their disadvantages, and although they must be extensively addressed, data-driven techniques remain one of the most viable approaches for health monitoring. Furthermore, data-driven approaches for health monitoring of satellites and UAVs mainly focus on examining time series datasets, as is warranted by the nature of these agents' operations. An underlying assumption in data-driven approaches is that operational time series datasets exhibit similar characteristics, which is needed to justify their use in such applications [17]. Since time series datasets constitute a substantial portion of the available training data for satellites, spacecraft, and UAVs, neural networks, particularly Recurrent Neural Network (RNN), have emerged as attractive approaches for conducting FDP on such datasets. Another option for FDP in satellites and UAVs is signal processing and frequency analysis.

They consist of the two categories of parametric and nonparametric methods. Parametric techniques operate under the assumption that the analyzed signals conform to a specific mathematical model, such as autoregression and state-space models [18]. Parametric methods are most effective when the assumed model matches closely with the signal. On the other hand, nonparametric methods are those where the analyzed signals are not associated with a known model or their attributes are not well-known. For instance, the Fourier transform, fast Fourier transform (FFT), and wavelet transform. Nonparametric methods are more robust to deviations and more flexible in application. However, these methods suffer from spectrum leakage and the picket fence effect, causing inaccuracies in frequency estimation. The drawbacks of nonparametric methods have been addressed in the literature; however, some barriers still exist in utilizing them [18]. Signal processing methods can also be combined with data-driven methods. In the literature, they provide time–frequency spectrums from the system and train Convolutional Neural Network (CNN) models with them, leveraging the advantages of data-driven methods. One of the drawbacks of signal processing methods that discourage their use in the health monitoring of satellites and UAVs is their predisposition toward making false alarms [19].

A visual representation of the discussed monitoring modes and methodologies is provided in Figure 4.

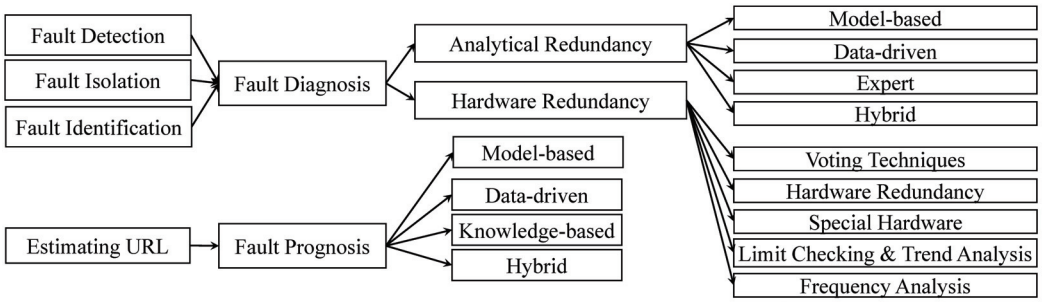


**Figure 4.** Fault Diagnosis and Prognosis approaches.

On the other hand, if a fault is to be addressed through a network of satellites or UAVs, we must be aware of the communication between these agents in all fault diagnosis methods. By evaluating the communication topology, we can determine the required quantity of observers/filters and the designed architectures to diagnose faults across the entire network. A communication graph/topology consists of nodes interconnected by edges. Directed edges create connections between groups of nodes in a single specified direction. Conversely, undirected graphs do not restrict the direction of information flow. The fault diagnosis observers for a network of agents can have three main architectures based on an analysis provided in [20]:

1. A centralized architecture involves a single master observer or filter that gathers information and manages inputs throughout the entire network. This approach results in a significant communication load because the master filter/observer must provide state information to all agents in the team for state and fault estimation.
2. A distributed architecture utilizes a hierarchical system of filters/observers. Each spacecraft operates a local filter that offers estimates to the master filter. This design effectively distributes the computational load among the local agents, simplifying the process.
3. A decentralized architecture operates without a hierarchy, eliminating the need for central supervision. Within this structure, each spacecraft processes its measurement data simultaneously with other spacecraft in the network, enabling efficient state and fault estimation without a centralized control mechanism. Clear schematic diagrams of all three fault diagnosis architectures are presented in Figure 5.

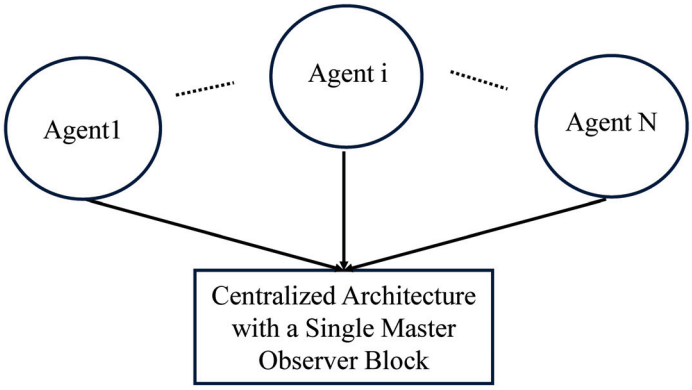


(**a**)

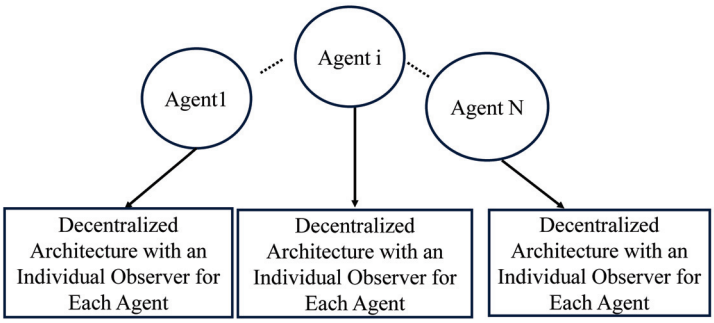


(**b**)

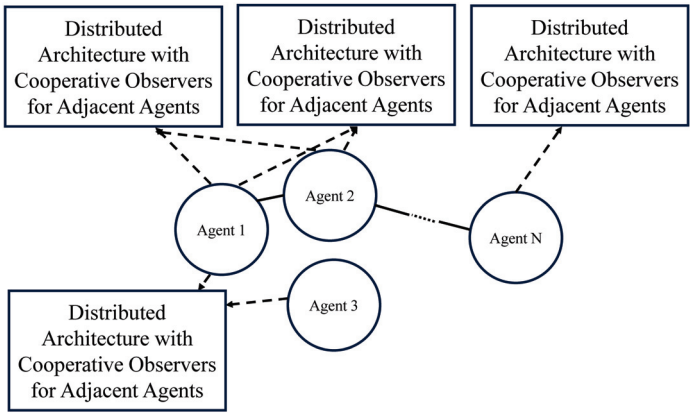


(**c**)

**Figure 5.** Fault diagnosis architectures: (**a**) centralized; (**b**) decentralized; (**c**) distributed.

The communication between agents can be either continuous or event-triggered. The event-triggered communication method allows communication when necessary to reduce the overall communication load. This flexibility ensures efficient utilization of resources and minimizes unnecessary data transmission.

In Sections 4 and 5, we review the existing publications concerning the FDP in both single satellite/UAV systems and networks comprising satellites and UAVs.

## 3. Review Methodology

In this review paper, a systematic search and screening procedure (depicted by Figure 6) for relevant works in the field was carried out. First, an initial database of all the work that is reliable and relevant to the authors' knowledge pertaining to satellite, spacecraft, and UAV condition monitoring published by relatively reputable sources was curated. In this step, the main keywords and features of the gathered works were extracted. Then, a subsequent search procedure for relevant works was carried out with the most prominent scholarly search engines by using the main keywords. Even so, there is always the possibility of human oversight in this type of search process. Therefore, after conducting a comprehensive exploration using academic search engines, we studied the works cited by the already identified works and added the relevant citations to our database or pool of accumulated studies. The same process was repeated until all the relevant citations in every work in our database were examined.

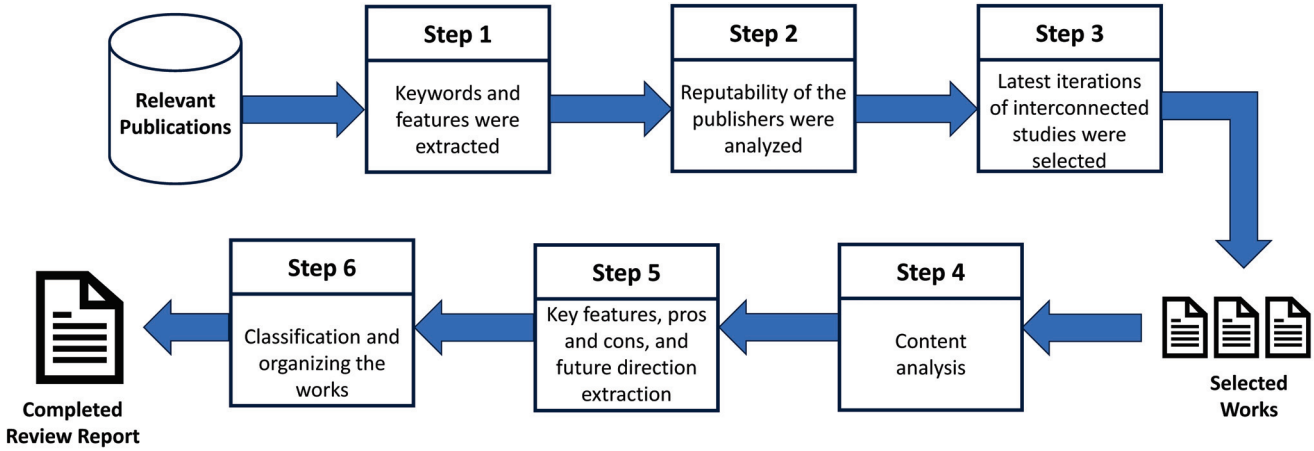


**Figure 6.** The review's systematic search, screening, and analysis approach.

Furthermore, having a reputable publisher was an important screening criterion while gathering our database of studies. By reputable sources, we do not necessarily mean a journal that has a high impact factor or a high-ranking conference. Especially in the field of satellite FDP, with the limited work that has been published in this field, it might prove fallacious to consider a study publisher's ranking as the definitive deciding factor. Therefore, there were more nuanced approaches involved in judging a source's credibility. The challenge in this step arose from the lesser known sources. The papers published by the distinguished sources in the field were automatically entered into the next screening step, which is step #3 in Figure 6. The credibility of the other sources was gauged through an examination of the works published by them. If the publications of a source displayed glaring issues and mishaps, that source and its corresponding studies in our pool were disqualified. If the source exhibited patterns of bulk research papers with minimal contribution to their field, which was assessed by inspecting their content, year-of-publication, and number of citations, they were disqualified. The other factor that caused disqualifications was works that built upon prior methodologies but with insignificant and superficial additions and innovations.

Through the reviewing process, for the sake of brevity, the works that were determined to be continuations of each other were discarded, except for the latest variation of the

research conducted in them, while conserving the main takeaways of each series of papers. This does not imply that the studies that shaped the current state of the literature of the field were not suitable but that they were so developed throughout different researchers' work that repeating them did not add much value to this review. Furthermore, in this review, emphasis was placed on promising works with high potential for improvement or real-life implementation. Therefore, as long as an article was scientifically sound, sophisticated, and with promising potential, they were included in the review regardless of its publication date. However, since the latest iterations of ongoing research movements were included in this review, many of the works are quite recent. The reviewing procedure is illustrated in Figure 6 for more clarity. By this step in the reviewing process, a pool of promising works had been compiled. The initial works contained about 130 works, of which 85 were selected for analysis in this review through the screening process. After this stage, a comprehensive content analysis was carried out, and the results are provided in Sections 4 and 5.

Different criteria tables were also curated through the reviewing process with a summary table outlining the focus of each in Table 1, under Tables 2–8, that outlined the pros and cons of different categories of work, as well as the finer details of their research. This was performed to provide the reader with a comprehensive overview of the important strong suits and weaknesses of the works and their assumptions for ease in reimplementing and reproducing them in the future. At times, some details we thought would be useful for reproducing or enhancing the existing works were left out in their respective manuscripts or not greatly and definitively expanded on. In such cases, we left those specifications blank in our tables. The layout of the criteria tables also proved to be greatly helpful in determining whether a scientific work is relevant to our review's scope.

There is a need to further elaborate on the advantages and disadvantages provided in Tables 2–4. An advantage or pro was defined as a feature that served to solve a persisting problem in the area or gave the proposed strategy an edge over its competitors to be applied in real life. Conversely, a disadvantage or con was defined as an inherent shortcoming that deterred their implementation in real-life applications. The most commonly identified advantage across the works was their capability to be applied to more than only fault detection, isolation, identification, estimation, prognosis, etc. In contrast, the most prominent disadvantage was observed to be the computational burden of the proposed strategies. Generally, the more fault diagnosis modes a strategy can support, the better they are at being suited for more real-life problems. However, higher generalizability often comes with higher computational intensity, making them less suitable for solving other problems requiring less consideration. Therefore, many of the strengths and limitations listed in Tables 2–4 are due to their respective works' problem statements or focus. Even so, there are other types of strengths and limitations that are specific to each study's methodology, such as their assumptions, which should not be neglected if one decides to adopt them in real life. The summary and strengths and limitations tables also aim to provide a bite-sized summary of each work that facilitates the study of this review by readers.

The defining criteria and key characteristics have been compiled in Tables 5–8. Table 5 contains the works on single-agent fault diagnosis with the criteria being focused on diagnosis mode, the specific approach, the strategies' application, the fault types considered, and the measurement parameters that are used for monitoring. The diagnosis mode is imperative since it is one of the deciding factors as to whether a strategy is applicable to a problem or not. The strategies' application was included as a criterion to highlight the areas where they have been employed and which applications they have not been utilized in yet. This serves to reduce the risk of oversight on the researchers' part in failing to consider all the possible solutions for a specific application. The fault type details are also extremely useful since different types might need dissimilar monitoring methods or some are more prevalent in certain applications which helps in identifying which works are beneficial in addressing a condition monitoring problem. The studied measurement outputs are also compiled to highlight what information is needed from a system for the readers to be able to incorporate the methodologies in this review into

their desired systems. Table 6 includes the works on single-agent fault prognosis with its focus being on the same criteria. Moving on, Table 7 consists of diagnosis studies on multiagent systems with their main criteria being the type of diagnosis, approach, application, and fault type. In the field of multiagent fault diagnosis, there is more focus placed on the relationship between satellites and UAVs. Therefore, detailed information about the measurements that are used for monitoring is not substantial and not provided in Table 7. Table 8 presents the secondary criteria that are useful for identifying the contributions of the studied works in multiagent fault diagnosis. These criteria include their architecture, communication topology and types, agent dynamic modeling, and control approaches. The architecture plays a crucial role in reducing computational complexity and system burden, as explained in Figure 5 and Section 2. In a centralized architecture, a single master observer receives information from all agents to diagnose and estimate agents' faults. While this approach involves high computational complexity, it is highly accurate. In contrast, the decentralized architecture reduces computational complexity by allowing each agent to run its own observer. However, since there is no exchange of relative information between agents, this architecture sacrifices some precision. Finally, the distributed architecture offers a trade-off between computational complexity and accuracy by assigning observers to groups of neighboring agents. Regarding communication, agents can transmit information either unidirectionally (directed) or bidirectionally (undirected). In practice, the communication within a graph can be a combination of both. Additionally, communication can either be continuous over time or event-based, where information is transmitted only when necessary. This event-based approach helps reduce the overall communication load. Moving on, we have the homogeneous and heterogeneous agent dynamic modeling and control logic criteria. The agent dynamics focus on whether the agents in the system have identical (homogeneous) or different (heterogeneous) dynamic behaviors. The control approaches in multiagent systems are divided into four main categories: consensus, formation, coverage, and flocking, depending on the mission goals. Literature shows that formation and consensus are more commonly used than other methods. It is also important to consider that, in real-world applications, the dynamics of agents in multiagent systems may vary due to operational conditions or environmental factors. This variability should be considered when working on control strategies and fault diagnosis in multiagent systems to ensure a more realistic and robust approach. An overview of all of the descriptive tables is provided in Table 1. These tables serve to guide the reader to know the defining features of the studies included in this review. For example, suppose the reader refers to this review to find a prospective methodology to compare their own with. In that case, these criteria are crucial in determining which methodologies are eligible for comparison. Or if the reader aims to find the gaps within the applications and strategies employed in the said studies, the tables serve to highlight the works that are promising in that regard.

Finally, classification and organization of the utilized methodologies and studies in the literature were achieved through the content analysis, and the results are provided in Section 6.1. The identified gaps and shortcomings of the existing works are also compiled in Section 6.2 for readers' consideration.

For the works in which the final quantitative results are explicitly provided, they are included in this review as well. In some works, detailed context is needed to understand the quantitative results. For these works, the final quantitative results are not included in this review to minimize the risk of misconstruing the results by the reader and inflating the text; however, their main takeaways are provided in Sections 4 and 5. Some works proposed solutions to solving persisting issues in the field and quantitative results do not highlight their contributions. Even so, among the works that do have explicit and easily understandable final quantitative results, direct comparison of these results might prove erroneous. For example, comparing the results of fault classifiers proposed by different works is not easily and intuitively possible. Different classifiers are usually trained on different datasets with different assumptions in the absence of a significant and

rigorous dataset in the field. Furthermore, the faults inserted into the training and testing datasets might not be identical either. A classifier with a high efficiency and accuracy rate that is trained and tested on a specific dataset might have a much lower efficiency and accuracy rate if applied to a dataset used by another classifier. In such cases, if explicit comparisons are provided by the authors of the studies, they are provided in this review, and if not, they are not included to conserve the scientific integrity of this review, since comparisons prove fallacious when they are conducted between different methodologies with different assumptions and different main features, as described by Tables 5–8. In this way, Tables 5–8 also help the reader identify which methodologies are eligible for comparison with their own prospective strategies. Consequently, to avoid the risk of presenting wrong comparisons to readers, we refrained from providing a detailed quantitative results comparison between all the works.

**Table 1.** Reference tables provided in this review for summary, extra, and detailed information about the outlined studies.

| Table Ref. | Description |
|---|---|
| Table 2 | strengths and limitations of diagnosis studies on single-agent systems |
| Table 3 | strengths and limitations of diagnosis studies on multiagent systems |
| Table 4 | strengths and limitations of prognosis studies on single-agent systems |
| Table 5 | Criteria and key features of diagnosis studies on single-agent systems |
| Table 6 | Criteria and key features of prognosis studies on single-agent systems |
| Table 7 | Main criteria and key features of diagnosis studies on multiagent systems |
| Table 8 | Secondary important criteria of diagnosis studies on multiagent systems |

**Table 2.** Papers on single-agent fault diagnostics and their strengths and limitations.

| Refs. | Strengths (+)/Limitations (−) |
|---|---|
| **1. Generalizability and Data Efficiency** | |
| [10,16,21–23] | (+) Generalizable frameworks applicable to various motors and systems<br>(+) Reduced requirements for historical data and training samples<br>(+) Capable of diagnosing multiple faults and unexpected/untrained faults<br>(–) Limitations in accuracy under conditions of scarce training data |
| **2. Fault Detection and Sensitivity** | |
| [13,15,24–26] | (+) Enhanced sensitivity to fault amplitudes and shapes<br>(+) Improved accuracy and interpretability through advanced techniques<br>(–) Higher computational requirements in complex scenarios |
| **3. Computational Complexity and Model Robustness** | |
| [27–31] | (+) Robustness to noise and disturbances with efficient algorithms<br>(+) Enhanced interpretability and efficiency through various models<br>(–) Increased computational burden due to model complexity<br>(–) Potential for false positives and negatives in certain methodologies |
| **4. Fault Diagnosis Methods and Techniques** | |
| [32–36] | (+) Application of diverse techniques (e.g., ML, NN) improves diagnosis accuracy<br>(+) Flexibility in diagnosing both actuator and sensor faults<br>(–) Assumptions regarding system behavior may lead to inaccuracies |
| **5. Limitations and Challenges** | |
| [31,37–40] | (+) Addressing key challenges like fault detection and model interpretability<br>(–) Various limitations including the need for specific data types and assumptions that may not hold in real-world applications |
| **6. Specific Applications and Innovations** | |
| [36,41–44] | (+) Innovative applications in digital twins and communication resources<br>(+) Enhanced methodologies for fault diagnosis in specific systems<br>(–) Complexity in adapting these methods across different scenarios |

**Table 3.** Papers on multiagent fault diagnostics and their strengths and limitations.

| Refs. | Strengths (+)/Limitations (−) |
|---|---|
| **Fault Detection and Isolation Techniques** | |
| [45] | (+) Considers simultaneous faults<br>(–) Limited by over-actuated systems for isolating multiple faults |
| [46] | (+) Instant fault detection via local observers<br>(+) Reliable detection regardless of fault magnitude |
| [47] | (+) Hybrid approach isolates low-severity faults |
| [48] | (+) Structural perturbation minimizes observer errors |
| [49] | (+) Identifies multiple faults in linear systems with correlated signatures |
| [50] | (+) Operates with inaccurate information |
| [51] | (+) Distributed FDI using local measurements |
| [52] | (+) Decentralized control strategy satisfies communication constraints |
| [53] | (+) Decentralized strategy for communication limitations |
| [54] | (+) Switching method contains errors in specific parts |
| **Comm. Strategies** | |
| [55] | (+) Decentralized control meets deep space communication needs<br>(–) Healthy satellites must allocate more resources |
| [56] | (+) Expanded framework for fault diagnosis in broader contexts |
| [57] | (+) Nonlinear system capability in adverse conditions |
| [58] | (+) Uses primary satellite data to diagnose faults without extra sensors |
| [59] | (+) Develops decentralized UIO for actuator faults |
| [60] | (+) Heterogeneous clusters reduce computational load |
| [61] | (+) Similar advantages as previous entry |
| [62] | (+) Robust against disturbances in varying conditions |
| **Resource Management and Performance** | |
| [63] | (+) Reduces operational costs while enhancing reliability |
| [64] | (+) MIMO structure analysis for optimality |
| [65] | (+) CKF achieves superior estimation performance<br>(–) Increases communication cost |
| [66] | (+) Quaternion representation simplifies complex systems<br>(–) Computational load managed by rule-based systems |
| [67] | (+) Robustness through H-infinity method |
| [68] | (+) Multiple-leader structure considers communication data noise |

**Table 4.** Papers on prognostics and their strengths and limitations.

| Ref. | Approach | Strengths (+) / Limitations (−) |
|---|---|---|
| [5,12] | **D-D** | (+) Could operate even with limited historical data<br>(+) Employs regressors for prognosis, which adds to the interpretability and quantitativeness of the predictions |
| [69] | **D-D** | (+) Eliminates the need for component-level measurements<br>(+) Significantly diminishes the need for historical operational data |
| [70] | **M-B** | (+) The methodology is robust to Gaussian and non-Gaussian noises<br>(+) Does not require historical data due to being a M-B strategy<br>(–) Implementation complexity and computational burden incurred by using CAUKF and PFs |
| [71] | **M-B** | (+) Accounts for non-Gaussian noise<br>(+) More accurate than classic PFs<br>(+) Investigates the bearing lubrication faults in more detail using the lubrication temperature<br>(–) Only accounts for lubrication faults as a result of temperature gradients |
| [72] | **M-B** | (+) Real-time prognosis analysis of the UAV<br>(+) Multiactuator RUL prediction<br>(–) Nonlinear but stationary degradation models are employed for brushless Direct Current (DC) motors<br>(–) Only addresses the hovering state of the UAV |

**Table 5.** An overview of papers on single-agent fault diagnosis.

| Ref. | Monitor Type | Approach | Application | Fault Type | Measurement Parameters |
|---|---|---|---|---|---|
| **Data-Driven Approaches** | | | | | |
| [3,15,73] | FD, FId | **D-D** Various Neural Networks (CNN, LSTM) | UAV Sensors | Operational, Bias, Drift, Stuck Faults | Sensor Data (IMU, Gyroscope, GPS) |
| **Model-Based Approaches** | | | | | |
| [6,10,16,45,74] | FD, FId | **M-B (Det.)** Observer-Based Methods | Satellite, UAV, and Other Systems | Multiplicative, Additive | Attitude Rates, Angular Velocities, Position Data |
| **Hybrid Approaches** | | | | | |
| [14,21,24,36,37] | FD, FIs, FId | Combination of Various Algorithms (e.g., SVM, Ensemble Learning) | Multiple Applications Including UAVs and Power Systems | Anomalies, Failures | Multiple Sensor Outputs Including Voltage, Current, and Attitude Data |
| **Fault Types** | | | | | |
| **1. Operational and Physical Attacks** | | | | | |
| [3,15,73] | FD, FId | **Various Data-Driven Methods** | UAV Sensors | Operational Faults, Physical Attacks | Sensor Data |
| **2. Sensor and Actuator Faults** | | | | | |
| [27,38] | FD, FIs, FId | **Model-Based and Hybrid** | Various UAV Systems | Stuck, Bias, and Intermittent Faults | Sensor and Actuator Data |
| **3. Systematic Anomalies and Failures** | | | | | |
| [29,33] | FD | **Data-Driven Approaches** | Telemetry Data | Anomalies | Telemetry Sensor Outputs |
| **4. Comprehensive Fault Detection and Isolation** | | | | | |
| [23,41,75] | FD, FId | **Model-Based and Data-Driven** | Satellite and UAV Systems | Various Fault Types | Multiple Measurement Parameters |

**Table 6.** An overview of papers on single-agent fault prognosis.

| Ref. | Approach | Application | Fault Type | Measurement Parameters |
|---|---|---|---|---|
| [5] | **D-D** LSTM | Single RW | Multiplicative | Motor current, RW rates |
| [12] | **D-D** ARIMA, LSTM | Single RW | Multiplicative | RW rates |
| [69] | **D-D** Chebyshev NN | Pyramid CMG | Multiplicative | Satellite rates |
| [70] | **M-B (Stoch.)** CAUKF and PF | Single RW | Multiplicative | Motor current, RW rates |
| [71] | **M-B (Stoch.)** PF | Single RW | Lubrication loss over time | Lubrication temperature, Lubrication degradation model, Lubricant's injected amount |
| [72] | **M-B (Stoch.)** TSKF, Entropy weight method, Laguerre function-based model predictive control | Quadrotor UAV Actuators | Degradation | — |

**Table 7.** An overview of papers on multiagent fault diagnosis and their main features.

| Ref. | Monitor Type | Approach | Application | Fault Type |
|---|---|---|---|---|
| [45] | FD, FIs, Recon. | **M-B** Observer-based Sliding mode | RW | loss-of-effectiveness |
| [46] | FD | **D-D** DNN | RW | Bus voltage, Motor current fault, Viscous friction |
| [63] | FD, FIs | **D-D** NNs | PPT actuators | Change in the Amount of Produced Thrust |
| [66] | FD | **M-B** CDM and fuzzy rule-based reasoning | RW, Battery | Intermittent bus voltage, RW current, Viscous Friction |
| [52,55] | FA | **M-B** KF | Actuator | loss-of-effectiveness |
| [47] | FD, FIs | **M-B** Hybrid and consists of both low-level (agent/team level) and high-level | Actuator | loss-of-effectiveness |
| [48] | FD, FIs | **M-B** Hybrid consists of a bank of residual generators and a DES-based fault diagnose | Actuator, Sensor | loss-of-effectiveness |
| [53] | FA | **M-B** Conventional Recovery Method | Actuator | loss-of-effectiveness |
| [54] | FE, FA | **M-B** KF | Actuator | loss-of-effectiveness |
| [76] | FD, FE | **M-B** KF | Actuator | Fault signal |
| [56] | FA | **M-B** KF | Actuator | loss-of-effectiveness |
| [57] | FD, FIs | **M-B** Hybrid consists of a bank of residual generators and a DES-based fault diagnoser | Actuator | loss-of-effectiveness |
| [65] | FE | **M-B** CKF | Actuator | loss-of-effectiveness |
| [64] | FD, FIs | **M-B** KF | Actuator | Change in the Amount of Produced Thrust |
| [77] | FD, FIs | **M-B** EKF | Actuator | loss-of-effectiveness |
| [78] | FE | **M-B** Observer-based $H\infty$ | Actuator | intermittent fault |
| [58] | FD, FIs | **M-B** Decision-making algorithm based on relative dynamic | Gyroscopes | Bias faults, Scale factor faults |
| [67] | FD, FIs, FE | **M-B** Observer-based | Actuator | Additive Abrupt Fault, Slow-varying Fault |
| [59] | FE | **M-B** Observer-Based UIO | Actuator | loss-of-effectiveness |
| [60] | FE | **M-B** Observer-based UIO | Actuator | loss-of-effectiveness |
| [61] | FD, FE | **M-B** Observer-Based UIO | Actuator | loss-of-effectiveness |
| [62] | FD, FE | **M-B** Observer-based UIO | Actuator | loss-of-effectiveness |
| [51] | FD, FIs | **M-B** Observer-Based UIO | Actuator | Cyber-attack/additive fault |
| [49] | FD, FIs | **M-B** KF | Actuator | loss-of-effectiveness |
| [50] | FE | **M-B** KF | Actuator | loss-of-effectiveness |
| [68] | FD, FIs | **M-B** KF | Actuator | loss-of-effectiveness |
| [79] | FD, FIs | **M-B and Knowledge-based** Fuzzy reasoning | RW | loss-of-effectiveness |

**Table 8.** Overview of fault diagnosis techniques in multiagent systems.

| Ref. | Architecture | Comm. Topology | Homogeneous/ Heterogeneous | Control Logic |
|---|---|---|---|---|
| [46] | Decentralized | Directed | Homogeneous | Formation |
| [63] | Leader–Follower | Undirected | Homogeneous | Formation |
| [66] | Leader–Follower | Directed | Homogeneous | Formation |
| [52] | Decentralized | Undirected | Homogeneous | Formation |
| [55] | Distributed | Undirected | Homogeneous | Formation |
| [47] | Centralized | Undirected | Homogeneous | Formation |

**Table 8.** *Cont.*

| Ref. | Architecture | Comm. Topology | Homogeneous/ Heterogeneous | Control Logic |
|---|---|---|---|---|
| [48] | Distributed | Undirected | Homogeneous | Formation |
| [53] | Distributed | Undirected | Homogeneous | Formation |
| [54] | Distributed | Directed | Homogeneous | Formation |
| [76] | Distributed | Undirected | Homogeneous | Formation |
| [56] | Distributed | Directed | Homogeneous | Formation |
| [57] | Centralized, Decentralized | Continuous | Homogeneous | Formation |
| [65] | Distributed | Directed | Homogeneous | Formation |
| [64] | Decentralized-MIMO | Undirected | Homogeneous | Formation |
| [77] | Centralized, Decentralized, and Distributed | Undirected | Homogeneous | Formation |
| [78] | Distributed | Undirected | Homogeneous | Formation |
| [58] | Decentralized | Directed | Homogeneous | Formation |
| [67] | Distributed | Directed | Homogeneous | Formation |
| [59] | Leader–Follower | Directed | Homogeneous | Formation |
| [60] | Distributed | Directed | Heterogeneous | Consensus |
| [61] | Distributed | Directed | Heterogeneous | Formation |
| [51] | Distributed | Undirected | Homogeneous | Formation |
| [49] | Distributed | Undirected | Homogeneous | Formation |
| [50] | Distributed | Undirected | Homogeneous | Formation |
| [68] | Distributed /Leader–Follower | Directed | Homogeneous | Formation |
| [79] | Leader–Follower | Undirected | Homogeneous | Formation |

## 4. Diagnostics

The domain of diagnostics plays a crucial role in the health assessment of satellites, spacecraft, and UAVs. Detecting, localizing, and identifying faults are essential to rescuing a malfunctioning agent's mission. Furthermore, successful prognosis relies on the awareness of a system's fault and the availability of relevant information. As a result, fault diagnosis for these agents has garnered significant interest, spurring extensive research in this field. Due to the increasing attention that the field of fault diagnosis has received in monitoring a broad range of agents, scientists have expanded its implementation to include satellite, spacecraft, and UAV fault diagnosis. The predominant strategies employed in the current body of literature for performing fault diagnosis within Aerospace applications, with a specific focus on satellites and UAVs, encompass data-driven and model-based techniques. While there have been occasional references to their fusion and alternative methods in published works, these approaches have not been subjected to the same rigorous scrutiny in the literature as the previously mentioned strategies. This section comprehensively lists and reviews the applications of data-driven, model-driven, hybrid, and other methods on diagnostics of a single and a group of satellites, spacecraft, and UAVs in the current literature. To provide a detailed and yet concise overview of each paper's strong suits and shortcomings, Table 2 presents the advantages and disadvantages of each study on single-agent fault diagnostics. Table 3 offers a similar analysis for a team of aerial and space agents. In order to provide a broad yet comprehensive overview of the innovations featured in the studies reviewed in this research, each study has been scrutinized and an extensive list of their characteristics is presented in Tables 5 and 7 for single-agent and multiagent fault diagnosis, respectively. Table 5 is structured in a way to highlight the exact architectures, health monitoring modes, considered fault types and variables, and applications of each study on single-agent systems. Consequently, facilitating the process of deriving insights from each paper. In addition, Table 5 serves as a comparative standpoint over the methodologies utilized in this field. Furthermore, Table 7 offers an overview of the attributes in research related to fault diagnosis in multisatellite/UAV systems.

### *4.1. Data-Driven Methods*

Data-driven methods have become one of the most prevalent methods for diagnostics in satellites and UAVs, especially in recent years. The literature on diagnostics has utilized these methods to a great extent to capitalize on their capability of assessing the health status of systems without having rigid mathematical models. Deep learning approaches as well as other supervised, and unsupervised approaches constitute most of the body of

work in this area. Their ability to accommodate applications where autonomous diagnosis is required or when manually defined features are not available has made data-driven techniques a popular method to perform diagnostics. This section reviews how the existing literature has employed data-driven techniques for fault diagnostics.

Talebi et al. [27] proposed a robust data-driven methodology for fault diagnosis of actuators and sensors onboard a broad range of nonlinear systems. Their methodology incorporates two recurrent neural network-based observers for Fault Detection, Isolation, and Identification (FDII) and operates based on the studied nonlinear system's state-space model. More specifically, FDII is achieved simultaneously as the diagnosis scheme gets alerted. This is performed by indicating where the fault has formed using fault-sensitive thresholds and obtaining its intensity. The proposed methodology is also strengthened against unmodeled dynamics, unknown faults, noises, and uncertainties. The methodology was tested using a case study on magnetorquer actuators and magnetometer sensors onboard the Attitude Control System (ACS) subsystem of Low Earth Orbit (LEO) satellites, and the test results verified the methodology's capability to be used in real-life situations. While actuator fault diagnosis is of paramount significance to increase the reliability of control systems, sensor FDII is also influential in affecting an agent's lifetime. Sensor faults could emerge due to external disturbances, aging, and power fluctuations [6]. The work of Talebi et al. addressed the reliability requirements for actuators and sensors.

Rahimi et al. [80] advanced the idea of utilizing data-driven approaches for Fault Detection and Isolation (FDI) using an ensemble of Adaboost decision tree, Adaboost Random Forest (RF), MultiLayer Perceptron (MLP), and K-Nearest Neighbors (KNN) ML algorithms applied to a four-wheel configuration of RWs. Principal Component Analysis (PCA) was also incorporated into the scheme to perform dimension reduction. Their method in [80] underperformed the required expectations for an FDI system with the highest classifier precision of 58.78%. Rahimi et al. claimed that implementing more complicated datasets for running the algorithms and utilizing optimization methods for hyperparameter evaluation could lead to more accurate results. Expanding the scheme to address different malfunction intensities, symmetrical RW arrangements, and computation overload would be the next step in this scheme's progression.

Varvani Farahani et al. [21] discussed data-driven fault isolation for locating multiple concurrently existing malfunctions in a four-CMG pyramid assembly. The proposed data-driven scheme consists of a feature extraction method, a feature reduction method, and a classification algorithm, which, through testing, are chosen to be Correlation Analysis, PCA, and an optimized Support Vector Machine (SVM), respectively. A sensitivity analysis was carried out to demonstrate the proposed method's robustness against added noise signals, unavailable sensors, and skipped measurements. The results of the sensitivity analysis displayed suitable error margins for practical implementations. The simulations exhibit 100% and 99% accuracies for healthy and single-malfunctioning-CMG assemblies, respectively, and 97.8%, 91.4%, and 77% accuracies which correspond to two, three, and four in-phase malfunctions coexisting in a system. The problem of diagnosing simultaneous faults is best countered using data-driven methods. As Jiang and Khorasani have demonstrated in [45], where concurrent faults can occur, e.g., RW assemblies, the model-based methods may struggle with diagnosing all of the faults depending on the system and if more than two are present.

Rahimi et al. [32] explored detecting and isolating in-phase malfunctions using automated data-driven methods applied on three-orthogonal, standard four-wheel, and pyramid RW configurations. Their proposed approach preprocesses the time series input data by automatically extracting features from the temporal, spectral, and statistical domains and then passing it through a feature reduction stage. Subsequently, several classification methods were considered: Gradient Boosting, RF, Decision Tree, and MLP. It was shown that Gradient Boosting and RF performed the best among the methods. However, both operated poorly under complex fault scenarios. The FDI methodology fared relatively better for the three-orthogonal case than the standard four-wheel, and pyramid arrange-

ments, especially due to the symmetry in the pyramid assembly. Expanding upon the presented scheme by improving the accuracy of FDI for more complicated malfunction scenarios would be the next step in developing a more robust FDI scheme. Moreover, Rahimi et al. mentioned that for RW configurations that have each RW manipulating torques in more than one axis (e.g., pyramid and standard four-wheel), fault complexities (including inception and duration) could have a detrimental effect on the FDI scheme's accuracy.

Vaz Carneiro et al. [81] formulated a data-driven approach to fault detection in RW assemblies employing supervised and unsupervised learning techniques, including Gaussian Mixture Model (GMM), SVM, Artificial Neural Networks, and Long Short-Term Memory (LSTM) Neural Networks. The learners receive a combination of RW attitude, temperature, control torques, and power consumption to detect the occurrence of faults. However, temperature proved to be the most sensitive variable to faults. The models are trained with the simulated datasets provided by the Basilisk simulation framework [82], a novel approach to training data-driven models for satellite fault diagnosis applications. Producing and using large amounts of synthetic data could be conducive to achieving adeptly trained models due to not having a limitation on the amount of data produced and knowing the exact details of the occurring faults beforehand as opposed to using historical data for training models [81]. Conversely, to avoid overfitting, amply-sized synthetic and historical datasets could also be created using generative models. The datasets acquired using generative AI could become a promising approach to alleviate the problems associated with the training phase of data-driven methods.

Suo et al. [83] developed a feature selection algorithm based on the fuzzy Bayesian risk theory along with a heuristic forward greedy algorithm for fault diagnosis of power systems of in-orbit satellites. The proposed algorithm works with an SVM for classifying faulty or nominal states. While the proposed feature selection method is observed to obtain more accurate results than other prevalent methods, it is computationally intensive, and overcoming this shortcoming could be a favorable approach to progressing this research.

Cui et al. [17] provided a solution to overcome the problem of faulty dataset scarcity for training data-driven satellite fault detection models. The solution incorporates redistributing the healthy and faulty datasets by oversampling the faulty samples using Dynamic Time Warping (DTW). Their proposed fault detection scheme is then completed by employing the fast DTW method for assessing correlations between samples and a KNN model for detecting malfunctions. Cui et al. tested the methodology, and DTW oversampling significantly increased the fault detection accuracy. The proposed method by Cui et al. could also help mitigate the training difficulties of data-driven methods for applications where several distinct fault types could be present in a system. Data augmentation is a technique that has been widely employed in the field of ML to make classification models more robust to diverse test cases. Data augmentation is especially common in the field of computer vision. To demonstrate how data augmentation works, an example is provided in Figure 7. Let us assume that we want to train a data-driven model to be able to discern dog images among other classes. If our dataset only consists of images like the original image in Figure 7, our dataset would be scarce and the data-driven model would be prone to overfitting. For example, the data-driven model through the training process might come to the conclusion that dogs are only dogs if the ear-shaped features are towards the top of the image or the paw-shaped features are toward the bottom of the image. To us humans, this conclusion appears clearly erroneous; however, this must be clarified to data-driven models by curating a comprehensive dataset or using a more robust architecture. In this case, a myriad of image modifications are imposed on the original dataset to make the dataset more diverse as shown in Figure 7. This process is referred to as data augmentation, and it is applicable to more than just images. For example, in the work of Cui et al. [17], DTW oversampling was used that in some way operates as a deterministic way of finding an in-between time series between two original time series data points to make the training dataset more diverse. Therefore, data augmentation is also

a viable way of enhancing data-driven methods' performance aside from feeding them synthetically generated datasets.

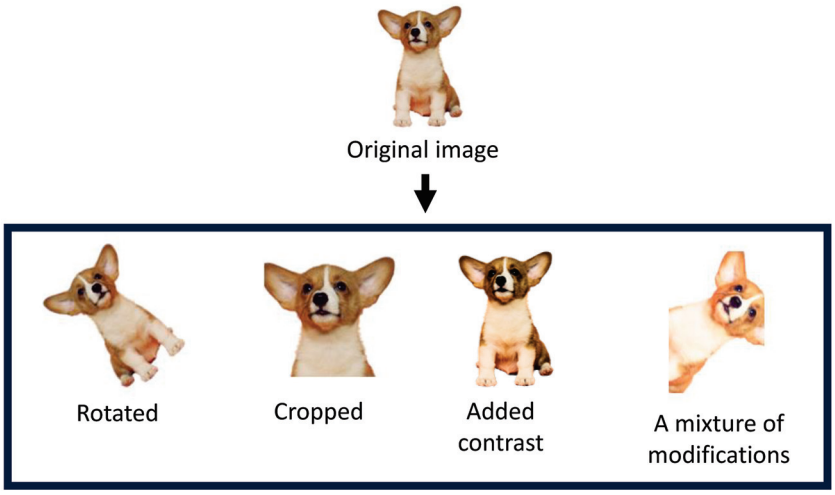


**Figure 7.** Data augmentation for a sample image of a dog (the original image is available https://unsplash.com/photos/short-coated-brown-and-white-puppy-eoqnr8ikwFE here) (accessed on 10 July 2024).

Hedayati et al. [84] proposed a data-generative AI model based on the Wasserstein Generative Adversarial Network (WGAN) architecture to balance scarce satellite RW datasets for use in training data-driven models. The utilized WGAN model comprises 1D convolutional layers within its generator and critic (discriminator). First, to train the WGAN model, multiple datasets for each fault type are curated. Each dataset contains very few data points as compared with the nominal RW dataset to reflect a real-life scenario. Then, identical instances of their proposed WGAN model are trained on each RW faulty class dataset. In this way, the overall training dataset becomes balanced. The final datasets augmented by the proposed framework of Hedayati et al. were tested quantitatively using an LSTM architecture and qualitatively as well. The LSTM model was trained separately on the WGAN-augmented, naturally balanced, imbalanced, artificially duplicated (inflated), and DTW-oversampled datasets and obtained accuracy rates of 84.17%, 93.25%, 48.35%, 97.51%, 89.32% as tested on a natural test dataset. The reason for WGAN-augmented dataset's underperformance as compared with other augmentation methods was attributed to WGAN adding too much diversity to faulty datasets and some resultant classes resembling each other. However, qualitatively it was observed that the WGAN added immense diversity and variability to the base dataset while retaining its most defining patterns whereas the other data augmentation methods added little to no diversity to the base dataset.

Pan et al. [85] used a novel data-driven method to detect faults in satellite power systems. Their presented method consists of forming correlations between time series datasets of several sensor measurements employing association rules between sensor datasets and incorporating them into a Kernel Principal Component Analysis (KPCA) model for detection. Association rule learning is especially effective since the sensor relationships change when an anomaly occurs. The novelty of the study of Pan et al. warrants the need for it to be examined further, but scant work has been carried out on this approach and application.

Ganesan et al. [28] presented a method employing a One Dimensional (1D)-CNN to address the fault detection problem in the power systems of satellites. The input data are preprocessed using the Stockwell transform before being fed into the CNN. When tested using the Advanced Diagnostics and Prognostics Testbed [86], the univariate detection methodology achieved an accuracy of 96.7%. Furthermore, Ganesan et al. claimed that

the methodology could be extended to multivariate detecting, locating, and classifying malfunctions in the power systems.

Muthusamy and Kumar [10] presented a data-driven methodology for FDI in CMGs. Their methodology relies on the following elements for fault diagnosis: a predictive data-driven model reducing the dependency of the method on *a priori* operational data by 93.75%, a Chebyshev neural network for detecting malfunctions in CMGs, and an optimization-based scheme using a Genetic algorithm for locating faults. The input data are limited to attitude rate measurements to accommodate satellite measurement limitations, but more comprehensive input data could be incorporated into the method. Simulated results showed a 93.25% accuracy rate in isolating different types of faults. Muthusamy and Kumar's proposed method is suitable for applications where sensor redundancy poses problems or when historical flight records are unavailable.

Nozari et al. [24] proposed a mixed-learning approach to FDI of a tetrahedral RW assembly and performed a comparative study of the mixed and individual models. Nozari et al. incorporated the RF, SVM, partial least square, and Naïve Bayes (NB) algorithms into their mixed-learning strategy. The proposed model consists of training several local classifiers whose outputs are used to train a meta-level classifier. The proposed mixed strategy mostly outperformed its constituent learners under noisy, noiseless, and mixed circumstances. Additionally, training using mixed noisy and noiseless datasets yielded more accurate results. However, one of the main shortcomings of mixed-learning strategies is that some mediocre learners within the scheme could negatively affect the overall mixed-learning strategy's performance [32].

The research conducted by Abdelghafar et al. [29] presented a data-driven predictive method employing an Extreme Learning Machine (ELM) for detecting faults by analyzing satellite telemetry data. The proposed methodology of Abdelghafar et al. first predicts the nominal operating data of the satellite. Then, it applies a static confidence interval to obtain a range containing the values corresponding to a normal operating state. ELMs are especially useful for time-sensitive applications such as satellite system fault diagnosis due to their learning speed and generalizability. They also require less expert manpower utilization [87]. The gray wolf optimization algorithm is also utilized to enhance the biases and input weights of the learner. Testing using the NASA shuttle valve benchmark dataset [88] achieved 98.5% to 99.6% accuracy in detecting deviations from nominal operating states, outperforming both unoptimized ELM and SVM.

A fault detection method for satellite telemetry data is presented by Xie et al. [33]. The detection method employs a graph neural network that considers the correlations between extracted features. Based on the cyclical operation schedule of satellites, malfunction thresholds are dynamically evaluated for detecting instances where the thresholds are exceeded. The proposed method demonstrated an accuracy of 98.30% for fault detection during testing on a satellite power system telemetry information dataset. Contrary to most ML methods, graph neural networks do not require the assumption of independent features as within graph-like data, nodes are interconnected, and there are dependencies between the nodes [89].

Luo et al. [34] developed a ResNeXt-based slice residual attention network for the health monitoring of a CMG onboard spacecraft. The proposed data-driven method utilizes random slicing and an attention mechanism stage. As part of the data preprocessing phase of the proposed method, the short-time Fourier transform (STFT) is employed to generate spectrogram images to boost the diagnosis capability. The model identifies the CMG's fault states but falls short in accurately measuring each sub-component's fault severity. Luo et al. expressed the prospects of converting the approach of distinct fault classification into a regression model for more rigorous fault diagnosis or using reinforcement learning to address more fault types.

The research carried out by Zhao et al. [35] presented a CNN-based spacecraft and mobile robot CMG fault diagnosis scheme that comprises two attention-enhanced convolutional blocks. The input data are preprocessed into time–frequency spectrums using

the STFT to enhance the fault diagnostic scheme. The scheme successfully classifies the overall CMG fault states; however, it fails to quantify each subcomponent's state of failure accurately. A demonstration of time–frequency transformation and the final images that get fed into the data-driven models is provided in Figure 8.

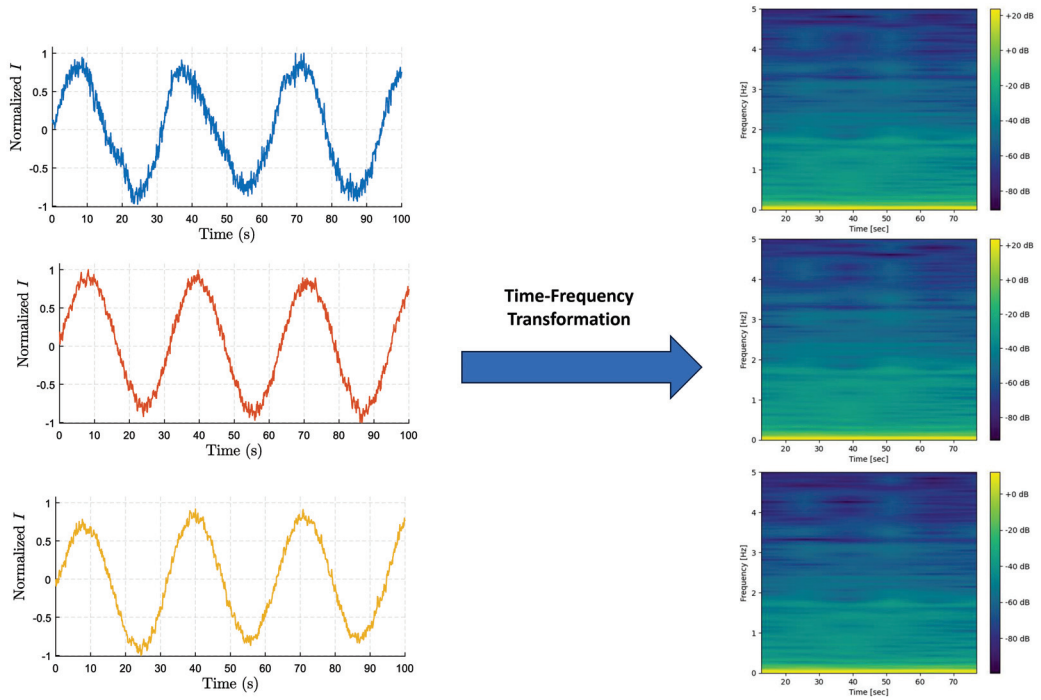


**Figure 8.** An example of generating spectrograms from RW time series signals for use in image-based data-driven models.

Liu et al. [90] developed two data-driven models to identify fault scenarios in a CMG onboard spacecraft. Both models employ the K-means algorithm to carry out diagnostics. However, one of the models utilizes the PCA for feature extraction, whereas the other uses the t-distribution random neighborhood embedding method based on the t-distributed Stochastic Neighbor Embedding (t-SNE) technique. Simulation results indicate the latter model provides significantly better performance. Liu et al. also indicated three ways of approaching the fault diagnosis of CMGs, namely, from the perspective of the system, assembly, and component. Their investigation into CMGs was conducted from a component-centric standpoint, considering both the physical and digital variables associated with CMGs for diagnostic purposes.

Jado and Moncayo [25] proposed a data-driven framework utilizing an multiple-model adaptive estimation (MMAE) comprised of multiple autoencoders to perform fault diagnosis on spacecraft. Each autoencoder is trained on an operational mode of the spacecraft and a Bayesian probability framework is used to gauge the probabilities of each model correctly representing the real system. The proposed methodology was numerically and experimentally tested and demonstrated to be able to timely diagnose faults resembling the training dataset. However, there lies an issue with this approach. The issue is that due to each autoencoder being trained on a singular operational mode, the in-between modes and relatively unknown failures could cause uncertainties in the model performance even though it is capable of detection, isolation, and identification to some extent. Their model could be bolstered by training more autoencoders to account for new failure modes.

Xiao and Yin [37] introduced a data-driven approach for FDI in satellite thrusters. They transformed the input data from the thrusters into image representations and established distinct fault categories based on these images. Subsequently, a CNN was employed for binary image classification. Their testing results revealed accuracy rates ranging from 98.30% to 98.71%, varying according to the thrusters' axis directions.

Sadhu et al. [3] developed a data-driven approach to detect and identify malfunctions in UAVs using sensor data from the Inertial Measurement Unit (IMU). Their proposed model combines a convolutional and bidirectional LSTM autoencoder for fault detection and a fault identification system based on CNN and LSTM. The identification component is activated only upon detecting a malfunction. During testing with empirical data, the detection module achieved an accuracy rate exceeding 90%, while the identifier module reached 85%. Sadhu et al. suggested that future work should involve applying their techniques to diverse UAV fleets and evaluating their method's performance in such scenarios.

An LSTM-based multivariate regressor using residual filtering is proposed by Wang et al. [73] for fault detection and recovery of UAVs. The proposed data-driven model automatically derives spatial and temporal correlations as features and utilizes a filter to cancel out the effect of random noise. Fault detection is accomplished by applying thresholds to the estimated parameters, and recovery is achieved by using the model's regressive nature to reconstruct the detected faulty data. The model's accuracy rate in detecting faults was determined by tests to be 99% and 93% for the gyroscope sensor's bias and drift faults, respectively, which outperforms the least-squares SVM and the LSTM model without residual filtering. Wang et al. also indicated that the possible future steps in developing this model are considering different fault magnitudes and flight modes' interference and addressing the online monitoring requirements by applying the model to an embedded monitoring unit.

Du et al. [26] proposed a data-driven approach to the mechanical fault diagnosis of damaged and cracked UAV rotors. The proposed methodology employs a 1D CNN to estimate faults using rotors' surface vibration acceleration signal as input during hovering and rising. Du et al. found that the preprocessing of input data significantly affects the model's performance in identifying small faults. Consequently, they used interval sampling instead of sequential sampling to reconstruct the vibration signals to obtain better results in diagnosing minor faults. The developed model's accuracy during the hovering and rising phases reached about 100% and 98%, respectively, while using the proposed sampling method and outdid the results yielded by sequential sampling. The model's accuracy rate was also indifferent to various loading conditions.

Taimoor et al. [91] proposed an adaptive radial basis functions (ARBF) approach based on the Lyapunov function theory and sliding-mode concept-based methodology to tune the weight parameters of neural network-based observers. The Neural Network (NN) observers are then utilized for fault estimation of sensors onboard quadrotor UAVs. The ARBF method's performance is compared with conventional radial basis functions (CRBF), adaptive multilayer perceptron (AMLP), conventional multilayer perceptron (CMLP), and Extended State Observer (ESO) methods and was shown to be more accurate and efficient than them.

Park et al. [22] developed a fault detection scheme based on unsupervised learning for diagnosing cyber-attacks and physical damages in the control systems of UAVs. This approach was incentivized by the shortcomings of supervised learning-based methods in requiring labeled data and failing to detect unexpected faults. The proposed model consists of a stacked autoencoder and uses thresholds for detecting faults. The input data features comprise UAV coordinates, attitude, IMU and sensors' data, and control inputs to the actuators. The next steps in this research could be adding to the features or incorporating sequential flight features, sequential autoencoders, or RNNs for enhanced detection performance. The presented model performed better in detecting Global Positioning System (GPS) spoofing attacks, denial-of-service (DoS) attacks, and rudder failure than in detecting elevator, aileron, and engine failures.

Li et al. [23] developed a novel Siamese hybrid neural network (SHNN) scheme based on Few-Shot Learning (FSL) for fault diagnosis of fixed-wing UAVs. FSL is an ML approach specializing in learning from a limited dataset for mainly supervised learning-based applications and exhibits high generalizability [92]. The FSL strategies' advantages have been leveraged to compensate for the lack of sufficient faulty state data for training

the data-driven models, considering that the available faulty data for fixed-wing UAVs are scarce. Li et al. carried out comprehensive experimental testing to validate the proposed scheme under the following conditions: different training data sizes, different flights, and unknown faults. The tests also demonstrate that the SHNN framework performs better than SVM and 1D CNN models for fewer training sample sizes. The future scope of this research includes utilizing attention mechanisms and alleviating the computational burden of the algorithm.

The work by Huang et al. [31] proposes an ensemble data-driven model for actuator fault diagnosis of UAVs, specifically the ailerons. The proposed ensemble method uses a weighted combination of three different hybrid models. The difference between ensemble and hybrid methods in this context is that ensemble methods take the final diagnosis output of different models and make a weighted decision based on each individual model's output and are more akin to a parallelized structure between the individual models. Whereas a hybrid data-driven model combines different architectures within one holistic model and their combination only outputs one diagnosis. Weighted ensemble architectures could be used to alleviate the dominance within lopsided models and increase the generalizability of the model. On the other hand, in a hybrid model, each segment is usually responsible for one duty, e.g., feature extraction. Huang et al. used an overarching ensemble model of three hybrid models as follows: (1) A CNN-bidirectional LSTM (CNN-BiLSTM), (2) A CNN-bidirectional Gated Recurrent Unit (CNN-BiGRU), and (3) A CNN-bidirectional Gated Recurrent Unit-LSTM (CNN-BiGRU-LSTM). The CNN model that is shared across the three models is responsible for feature extraction whereas the subsequent structures are responsible for further processing and diagnostics. A combination of random search with grid search is used for pinpointing the optimal weights of the ensemble method. Through testing and comparing the model to different state-of-the-art models for this application, the proposed ensemble method mostly outperformed the other models at the cost of increased computational intensity.

Li et al. [75] proposed a transformer and local interpretable model-agnostic explanations (LIME) combination to perform fault diagnosis on a fixed-wing UAV's elevator. The LIME strategy was used to increase the interpretability of the transformer model by locally approximating the output of the proposed transformer and examining the effect of different features in the final diagnosis. The LIME algorithm also gives insights about how to simplify the transformer further by specifying the features that do not contribute extensively to the diagnosis and could be dropped. Furthermore, Li et al. implemented a loss function to mitigate the problem of faulty categories' imbalance. The proposed methodology displayed high accuracy in diagnosing faults and efficient convergences owing to the utilized loss function.

Huang and Ferguson [93] conducted work on satellite RW fault detection by proposing a simple One-Class Linear Regression (OC-LR) algorithm. The proposed OC-LR framework works by only training on nominal RW operational datasets which is curated using a simple polynomial representation of RW motor current's relationship with its angular velocity and acceleration. This simplified approach to monitoring the RW health state enables the algorithm to perform without the need for a rigorous mathematical model. Then, three detection metrics are used as follows: if a faulty data point falls within one, two, and three standard deviations of the training dataset's mean, there is a 68%, 95%, and 99.7% chance that it would be detected as a faulty data point, respectively. Through simulated and real-life tests, it was found that depending on how obvious the emerged fault is, any of the three detection metrics could surpass the other two, with their accuracy rates ranging from 76.7% to 99.1%. Huang and Ferguson's proposed algorithm is relatively simple, readily applicable, and not demanding, especially when dynamic models and faulty operational datasets are not available. However, this approach carries a relatively higher risk of false positives and negatives that could be catastrophic in a space system. Moreover, solely performing anomaly detection while only outputting the anomaly's degree of deviation from the nominal operation may not be enough for a fault-tolerant subsystem to save the

whole satellite system, especially considering that different faults with different dynamics that require dissimilar remedying measures might exhibit the same levels of deviation. One of the possible avenues for enhancing this methodology is to implement a voting strategy between the different detection metrics.

Mousavi and Khorasani [46] introduced a Dynamic Neural Network (DNN)-based system for FDI in RWs of satellite formation flying (SFF) missions with a decentralized architecture. DNNs are trained with extended backpropagation using input/output data from the attitude control subsystem to model the nonlinear dynamics of each spacecraft. A fine-tuned set of DNN parameters is used to minimize estimation errors and to meet performance criteria. The methodology effectively detects low-severity actuator faults by employing local and neighboring spacecraft-based fault detectors. In the study, multilayer DNNs are trained based on relative attitude measurements and used to represent SFF dynamics.

Using DNNs, Valdes and Khorasani [63] developed an effective FDI system for Pulsed Plasma Thruster (PPT) used in ACS for SFF missions. The proposed approach involves three FDI strategies: a basic FDI scheme, an advanced FDI scheme, and an integrated FDI scheme. Basic schemes accurately detect and isolate faults in PPT actuators but have low precision and high error rates. The advanced scheme analyzes relative attitude data from formation flying, resulting in excellent detection but lacking isolation capability. With the integrated scheme, accuracy, precision, and minimal misclassification rates can be achieved, as well as insights into thrust production levels during faults can be obtained. Compared with traditional attitude control actuators, fault diagnosis for PPTs has been less explored because of challenges with force measurement and mathematical modeling.

### *4.2. Model-Based Methods*

Model-based methodologies have been a staple of fault diagnostic strategies, specifically ACS diagnostics, for many years. Their capacity to carry out precise and timely FDII using high-fidelity models has made them reliable techniques for time-sensitive missions. On top of that, the interpretability present in the outputs provided by model-based methods is conducive to making appropriate judgments and taking remedying fault-tolerant measures. This section discusses their applicability in a broad spectrum of satellite and UAV diagnostic case studies.

Jiang and Khorasani [45] utilized a second-order nonlinear sliding mode observer for FDII in a tetrahedron RW assembly. Jiang and Khorasani indicated that due to the over-actuatedness of the RW assembly and redundant RWs, no more than two in-phase faults could be fully diagnosed, and postprocessing is needed to perform isolation and identification. However, even with two concurrently occurring faults, isolating their locations proved challenging since several permutations of faulty RWs could have the same effect on the generated residuals. Jiang and Khorasani worked around this problem by taking measures to make distinctions between the different possibilities.

Chen and Liu [41] utilized a two-stage EKF to estimate satellite actuator and sensor faults. The focal point of their study is estimating both multiplicative and additive faults while modeling actuator faults as multiplicative and additive and sensor faults as additive. Chen and Liu represented multiplicative faults as control effectiveness parameters and additive faults as added amplitudes. Their proposed model was also tested using the telemetry data of an on-orbit satellite, and the faults were successfully estimated.

Another work addressing the problem of diagnosing multiplicative faults is the study by Shahriari-kahkeshi et al. [11], which presents an adaptive model-based methodology applicable to Lipschitz nonlinear systems. The proposed methodology performs fault detection and identification simultaneously. It involves an adaptive state observer leveraging a robust adaptive law effective against unknown faults, measurement, and modeling uncertainties. The scheme was tested on a single-link flexible joint robot arm and displayed rapid convergence and better accuracy rates than a similar existing fault estimation scheme.

To accommodate the adaptivity requirements in satellite ACS diagnosis applications, Rahimi et al. [19] used Adaptive Unscented Kalman Filter (AUKF) techniques for fault detection of RWs. They expanded upon them by combining them with the Particle Swarm Optimization (PSO) method. The PSO method is used to circumvent the complicated procedure of setting up the AUKF for parameter estimation and making it more precise and efficient. The model-based methodology is based on a high-fidelity RW model developed by Bialke [94]. It is indicated by Rahimi et al. that for more rigorous results, a more sophisticated implementation of the PSO and AI manipulation is required.

Furthermore, Rahimi et al. addressed the fault diagnosis of RW assemblies in [95] by introducing a model-based hierarchical approach for FDII of RWs onboard satellites. Their three-step proposed methodology consists of (1) an AUKF for detection, (2) multiple UKFs along with Bayes' probability theorem and probability distributions for isolation, and (3) dual-state and parameter estimation using UKFs for identification. The methodology's accuracy rate in detecting, isolating, and identifying faults was determined by simulations to be 89.5% on average.

During their research on enhancing AUKFs for single RW usages, Rahimi et al. [16] also presented the Covariance-based Adaptive Unscented Kalman Filter (CAUKF), a variant of the AUKF with the aim of refining parameter estimation. The model-based method incorporates adaptive covariance matrices of states and parameters to be robust to sudden fluctuations in nonmeasurable parameters of the system. The proposed CAUKF generally takes more time to diagnose faults compared with the AUKF while displaying 4%, 14%, 42%, and 90% less mean square errors for residuals of the RW model parameters under abrupt, transient, intermittent, and incipient malfunction scenarios, respectively.

Moreover, Rahimi et al. [14] built upon their work in [16] by proposing the binary Binary Grid Covariance Adaptive Unscented Kalman Filter (GAUKF) methodology and a two-step hierarchical method for FDII of CMGs. The first step employs the adaptive thresholding approach, and the second step encapsulates fault isolation and identification by introducing an adaptive covariance-based binary grid search procedure. The GAUKF method was developed to address the high computational cost of the CAUKF and its suboptimal operation when the control system is closed-loop. GAUKF's fault isolation and identification performance surpasses both CAUKF and UKF methodologies in terms of precision. Additionally, the average execution time for the GAUKF is shorter than that of CAUKF and UKF when utilized in a closed-loop control system. However, the symmetry of the pyramid configuration poses problems in isolating the faults in RWs across from each other. Also, another drawback is the inaccurate estimation of one of the four wheels' fault parameters due to the system's lower dynamical sensitivity to the fourth RW's output [14,95].

Later on, Rahimi [96] proposed the Simplified Binary Grid Covariance Adaptive Unscented Kalman Filter (SGAUKF) methodology and further developed the isolation and identification modules presented in [14,16]. The SGAUKF method updates only the even or odd rows or columns of the posterior estimate covariance matrix's diagonal elements, cutting the order of computations to its square root. The method also features either an increase or no change, as the name binary implies. The Monte Carlo simulation results show that SGAUKF adds to the GAUKF isolation accuracy by 1% while speeding up the process by about 27%, making it an even more viable approach to online monitoring. The SGAUKF also suffers from the issue of imprecise identification performance for the fourth flywheel, which could be addressed in future research.

Nasrolahi and Abdollahi [6] designed a nonlinear observer for fault detection of attitude and rate sensors onboard satellites and presented a fault recovery strategy. Fault detection is achieved using the satellite's measured angular velocities and attitude parameters. However, attitude parameters are described using Modified Rodriguez Parameters (MRP), which enables the fault detection of different attitude sensor types with different configurations using the same observer.

Carvalho et al. [74] presented a fault detection filter that incorporates both $H_\infty$ and $H_2$ simultaneously for Markovian Jump Linear System (MJLS). Carvalho et al.'s proposed approach aims to make the filter robust to disturbances, noises, and applied inputs and sensitive to malfunction signals. The filter is then applied to a CMG to demonstrate its performance. A brief description of MJLSs is included below. A discretized dynamical Markovian jump linear system's state-space model is defined as follows [97]:

$$X_{k+1} = A_{\theta(k)} X_k + B_{\theta(k)} u_k \tag{4}$$

where $X_k \in \mathbb{R}^d$ denotes the system's state at discrete time step $k$, the initial state $X_0$ follows a distribution of $D$, $u_k \in \mathbb{R}^r$ denotes the control command at time step $k$, $\theta(k)$ takes a value corresponding to a finite set of $N = 1, \ldots, n$ for each time step $k$, where $\theta(k)$ forms a discretized Markov process from $N$. The probability of transition between two states for $\theta(k)$ is defined as

$$p_{ij} = P(\theta(k+1) = j \mid \theta(k) = i) \tag{5}$$

where for each $i$ the sum of all $p_{ij}$ amounts to one. The initial distribution of $\theta(k)$ is also represented as follows:

$$\omega = [\omega_1 \ldots \omega_n]^T \tag{6}$$

where the sum of all $\omega_i$ is one. From Equation (5), Markov processes are described by the quality of their transition probability from one state to another solely depending on the current state of the system, irrespective of how it arrived at its current state. For demonstration, Figure 9 depicts a Markov chain of a fault-prone system with a transition probability matrix of $P = \begin{bmatrix} p_{11} & p_{12} \\ p_{21} & p_{22} \end{bmatrix}$.

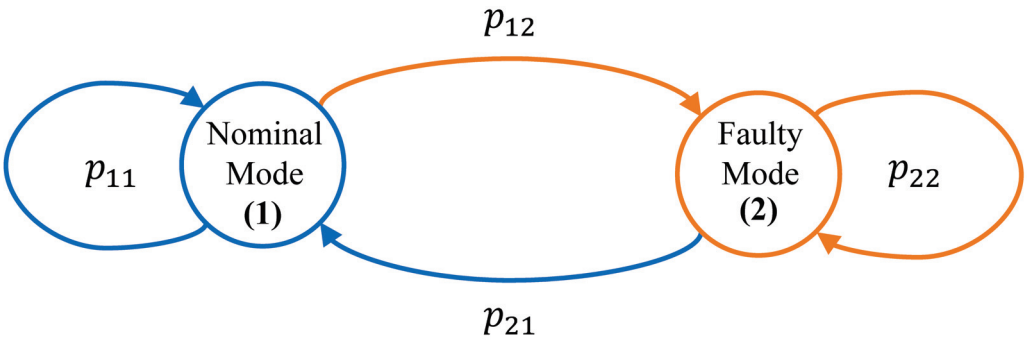


**Figure 9.** A schematic inspired by [98] of how a dynamic system abiding by a simple Markov process transitions between nominal and faulty modes.

Iglesis et al. [13] utilized the idea of jump Markov processes by presenting a Jump Markov Regularized Particle Filter (JMRPF) for nonlinear Inertial Navigation Sensor (INS) fault identification used in longitudinal control of a fixed-wing UAV. The jump Markov approach was introduced into a regularized PF to address the transitions of the system between faulty and nominal modes based on the Markov property. The proposed scheme of Iglesis et al. does not require predefined fault models to operate. Instead, estimation is carried out for additive abrupt and incipient faults with unexpected dynamics and amplitudes. A Kalman correction strategy is also incorporated into the proposed scheme, which distributes the particle states in the more probable state-space areas to enhance the state and malfunction estimation further. Under numerical simulations, JMRPF showed 77% less root-mean-square error in estimation than a regularized PF while exhibiting shorter convergence times and more robustness to faults with larger amplitudes.

Wang et al. [99] developed a model-based method for actuator FDII of a Hex-rotor UAV. Faults are classified as total actuator failures and gain faults attributed to the actuator lift factor's deviations from the nominal condition. The diagnosis model includes a set of EKF-based fault observers whose output is employed to achieve fault reconstruction. The

proposed methodology of Wang et al. surpasses the accuracy of sliding mode observers in attitude angle tracking.

Maqsood et al. [42] developed an enhanced high gain observer for FDII of angular rate sensors in quadrotor UAVs to further address UAV sensor health monitoring. The proposed model is tested under incipient, oscillatory, and intermittent fault conditions, and its results are compared with the integral chain differentiator and basic high-gain observer techniques. The accuracy rate of the proposed approach significantly surpasses that of traditional techniques while being less computationally intensive and providing fast diagnostics.

Gai et al. [43] proposed a novel dynamic Event-Triggered Mechanism (ETM) for fault detection in UAV actuators to achieve minimal communication resource usage and remove correlations between generated residuals and dynamic event-triggered transmission errors while circumventing the Zeno phenomenon. Zeno phenomenon refers to the existence of an infinite number of events in a finite time interval, making ETMs prone to errors. The dynamic ETM approach employed by Gai et al. is based on the $H_i/H_\infty$ optimization problem, which is solved using the Riccati recursion method. Their fault detection scheme also utilized a new residual evaluation and thresholding method. The simulation results indicate that the proposed dynamic ETM detection scheme outperforms the static variant in terms of accuracy, requiring at least 13% less event transmission information. Gai et al. also expressed that the next steps in this research would be to evaluate the effect of the dynamic ETM on quantitative fault inspection and examine the effect of closed-loop control systems on faults' noticeability.

Gao et al. [36] used a stochastic-model-based method for FDII of actuators onboard tilt-rotor UAVs. Their employed methodology consists of several EKF observers, each assigned to a single corresponding actuator. Moreover, it utilizes the MMAE method to use each observer's residuals and the state error covariance matrix for obtaining the fault conditional probabilities, which are then employed to achieve fault diagnosis. The proposed methodology of Gao et al. also enhances the efficiency of the MMAE method. It does not require additional sensors to monitor actuator deflections and change the flight controller.

Guzmán-Rabasa et al. [38] designed an $H_\infty$ observer for FDI of actuators onboard a quadrotor UAV where the rotational dynamics are modeled as a reduced quasi-linear parameter-varying system. The numerical test results demonstrate that the proposed approach performs on the same accuracy level as similar methods. However, it is claimed to be more efficient because it only accounts for the system's rotational dynamics. On the other hand, it falls short in carrying out fault diagnosis while considering translational dynamics. The next progressions for this research could include validating the proposed approach with an experimental setup, developing a mixed $H/H_\infty$ scheme for fault diagnosis or using it with a fault-tolerant controller.

To also address surface icing, Rotondo et al. [39] presented a model-based methodology for UAV icing and actuator fault diagnosis. Their approach is structured around combining the concepts of internal and Unknown Input Observers (UIO) and exploiting their fusion to develop a linear parameter-varying observer to circumvent the issues surrounding model uncertainties and unknown inputs. Rotondo et al. also suggested the following additions to enhance the proposed methodology: Alleviating the methodology's conservativeness, improving its performance, and generalizing it for more comprehensive operating conditions.

An innovative hierarchical approach for fault diagnosis in satellite components or subsystems is presented in [66]. This method emphasizes dividing the complex system into smaller pieces for structured diagnostic reasoning based on rules specific to each element. These modules are interconnected through a Component Dependency Model (CDM) using Bayesian networks. A leader–follower SFF is used to demonstrate the method's functionality and prove its potential to enhance satellite health monitoring. The approach will be extended to dynamic Bayesian network-based CDMs and systematically generated, providing promising directions for enhancing fault diagnosis capabilities.

In [52,55], Azizi and Khorasani explored strategies for managing actuator malfunctions in a decentralized manner for SFF. This is facilitated through a cooperative framework comprising three layers. Initially, established recovery methodologies are employed at the bottom-layer fault recovery based on assessments of fault severity. Nevertheless, inaccurate fault assessments can result in violations of mission error protocols. The higher layer supervising identifies faults and initiates the formation layer of fault recovery. This high-level supervision endeavors to adjust for the satellite partially restored at the lower level. In another paper, Tousi and Khorasani [47] developed a hybrid method that combined FDI stages such as [52,55] for a team of cooperating UAVs. Their hybrid methodology incorporates both bottom-layer and top-layer FDI modules. Simulation results involving a team of five UAVs are provided, demonstrating the effectiveness of this approach. In [48], Tousi et al. expanded the work in [47] and used Discrete-Event Systems (DES) at the top level to diagnose faults, while traditional diagnostic methods are used at the lower level. A broader spectrum of faults can be detected and isolated using this method than has been reported in the literature.

In another study [53], Azizi and Khorasani explored a novel distributed KF approach designed to estimate actuator faults for SFF. When addressing a complicated hierarchical system, they converted the representation of the system from an Overlapping Block-Diagonal State Space (OBDSS) to their innovative Constrained-State Block-Diagonal State Space (CSBDSS). The proposed approach can simplify the implementation of KFs in a distributed manner. During Kalman filtering iterations, the constrained-state condition must be met, equivalent to solving local constrained optimization cost functions. Various systems, including power systems and sensor networks, can be addressed with this technique.

A hierarchical fault estimation and accommodation approach is proposed in [54]. To minimize the adverse effects of unmodeled dynamics, uncertainty, and disturbances within the SFF, Azizi, and Khorasani seek to encourage cooperative interactions across levels and modules. Additionally, they highlighted a crucial finding: centralized estimation schemes exhibit notable drawbacks when faced with unmodeled dynamics, uncertainties, and disturbances. As a result, the cooperative estimation procedure proposed in [54] proves to be a highly applicable method for overcoming the mentioned challenges.

An advanced approach to cooperative actuator fault estimation in deep space is presented in [76] that integrates hybrid and switching techniques. Every operational mode represents a distinct cooperative estimation strategy and communication pattern between the localized filters responsible for detecting and estimating the SFF's status. With the help of this approach, fault estimation accuracy is likely to be enhanced in a cooperative and dynamically changing space environment.

A cooperative fault accommodation challenge within SFF is explored in [56]. It used absolute rather than relative measurements, like other studies by Khorasani's team [45,52,55,57], making the approach applicable to a wide range of SFFs operating in planetary orbits. In this study, collaboration between controllers maximizes the efficiency of supporting a faulty satellite. Therefore, the scope of this study is expanded to include a broader spectrum of SFF based on the cooperative fault accommodation framework.

In another study [65], Azizi and Khorasani introduced an innovative, collaborative framework designed to estimate the states of SFF. This framework employed the concept of sub-observers, each dedicated to estimating specific states based on provided input, output, and state information. To maintain estimation errors at a manageable level, they proposed a directed graph representing the interdependencies among subobservers. By carefully selecting the optimal path within these subobservers, a higher-level supervisor gains the ability to thoughtfully choose and configure a set of sub-observers, ensuring accurate estimation of all system states. In cases where unreliable information is introduced due to significant disturbances, noise, or actuator faults, specific subobservers may lose their efficacy. In such scenarios, the supervisor dynamically adjusts the subobserver set by selecting a new path within the subobserver's digraph. This adaptive approach effectively manages and restricts the impact of these uncertainties, ensuring they only influence local

estimates of states and faults. Consequently, the spread of uncertainties throughout the estimation process is minimized, preventing extensive performance degradation across the entire SFF [65].

In [64], a particular structure is described by Meskin and Khorasani. The SFF is considered to be a Multiple-Input, Multiple-Output (MIMO) system in this study. By employing this structural approach, the overall formation is optimally managed, and a viable stability analysis can be conducted. One problem, however, is that the MIMO structure is not resilient to local faults. As a result, it is imperative to develop FDI filters capable of detecting such localized faults. FDI filters operating in a local or decentralized capacity were devised and presented to mitigate this vulnerability.

Ghasemi and Khorasani proposed an innovative FDI strategy for the ACS in SFF [77]. This method can use three different setups: decentralized, centralized, and semi-decentralized (distributed). As a result of these three configurations, a fault diagnostic system can be created for multisatellite systems. Compared with the other two FDI architectures, the centralized FDI architecture is more effective in missions incorporating angular velocity sensors. However, it also generates more false alarms. On the other hand, FDI decentralized architectures announce fault occurrences more frequently and produce fewer false alarms. The centralized Fault Detection (FD) architecture performs better in FDI, resulting in fewer false alarms in missions when formation flight integrates attitude-measuring sensors than the other two systems. Furthermore, the decentralized FD architecture communicates fault occurrences less frequently while producing fewer false alarms compared with the distributed FD architecture.

An $H_\infty$-based robust distributed observer to synchronize the orientations of several satellites is investigated in [78]. A powerful distributed $H_\infty$ is established at each satellite to detect intermittent faults. To calculate the gains for observers, they designed two sets of Linear Matrix Inequality (LMI) criteria. Numerous satellite numerical simulations show that the resilient $H_\infty$ observer effectively estimates time-varying and intermittent faults when the satellite's communication layout is an undirected graph. Additionally, the designed observer is shown to be effective when several satellites have problems at once.

In [58], Shakouri and Assadian introduced a novel approach involving intersatellite measurements, considering relative positional data and orbital parameters. Their focus was on FDI within spacecraft rate gyroscopes. This innovative technique identifies a consistent motion characteristic, specifically restricting dynamic states during relative motion. Consequently, the primary satellite's angular velocity vector aligns with a quadratic surface. This ascertained motion characteristic aids in diagnosing faults within the gyroscope system and providing a rough estimation of the relevant scale factor or bias for the rate gyroscopes associated with the primary satellite. The proposed approach eliminates the need for additional subsystems within the SFF framework.

An exploration concerns a comprehensive approach for FDI within a specific class of nonlinear SFF systems [67]. The methodology considers model uncertainties, input variations, and environmental disturbances throughout the diagnostic process. To address fault detection, a nonlinear observer is carefully engineered to minimize uncertainty within the robust $H_\infty$ framework. The observer gain matrices are computed using an LMI formulation. Robust UIO are developed to pinpoint the faulty actuator and facilitate fault isolation. This isolation is executed through a strategic implementation of generalized observer techniques. The novel observer architecture can concurrently estimate faults and states while effectively mitigating the impact of unknown input disturbances, model uncertainties, and external disturbances. This is achieved by employing Lipschitz formulations and the Linear Parameter Varying (LPV) method across all proposed observers, resulting in less conservative LMI conditions. It is essential to mention that this approach allows each satellite to diagnose its faults and those of its adjacent satellites.

Gao and Wang [59] introduced an approach to estimate faults and ensure fault tolerance in the control system for nonlinear SFF systems, explicitly addressing actuator faults. A decentralized UIO is designed to estimate the actuator fault factors. The estimated fault

values obtained are then utilized to design a distributed fault-tolerant controller for SFF. Subsequently, an algorithm for fault-tolerant formation control is developed, using Adaptive Terminal Sliding Mode Control (ATSMC) techniques to improve the synchronization of each follower spacecraft with the leader spacecraft, even when faced with actuator faults.

In another research, Barzegar and Rahimi [60] undertook to design a robust UIO specifically crafted to estimate faults within clusters of small satellites. Operating within clusters, these satellites present heterogeneous dynamics characterized by significant diversity owing to environmental conditions and inherent nonlinearities. The study extends its focus beyond fault estimation, investigating that the designed observer and controller logic not only estimate faults accurately but also arrange synchronized behavior among satellites within each cluster. This synchronization shows as a state of consensus, steering the satellites towards a collective achievement of predefined objectives and trajectories designed for their mission. In a separate study, Barzegar and Rahimi [61] investigated the problem of fault diagnosis within clusters of small satellites. These satellites operate during diverse environmental conditions, presenting a difficult challenge in mitigating both disturbances and faults while maintaining the desired formation state among the satellites. The study aimed to alleviate the adverse effects of disturbances through an elaborate fault diagnosis approach, ultimately ensuring a consistent and reliable formation state among the small satellites, even in dynamically changing environments. To fortify the observer's resilience against external disturbances as outlined in Barzegar and Rahimi's work [60,61], they employed the $H_\infty$ approach. In a separate study conducted by the same authors, a dissipativity-based UIO is implemented for the Lipschitz nonlinear multisatellite systems. This strategy is designed to mitigate the impact of disturbances across two scenarios: one where matching conditions are met and another where they are not [62].

Negash et al. [51] aimed to detect cyber-threats during UAV Formation Flight (UFF). Negash et al. have adopted a decentralized approach using UIO for FDI, which is particularly suited to the distinctive attributes of UFF and their associated control algorithms, which may involve unknown parameters. This approach facilitates the identification of system faults and extends its utility to detecting cyber intrusions and precisely locating compromised UAVs. The primary objective of this study is to introduce an algorithm capable of identifying compromised UAVs without compromising the overall performance of the formation. Numerical simulations conducted by the authors provide evidence that diagnosing cyber intrusions within a hexagonal UAV formation is highly effective [51].

Meskin et al. [49] proposed a unique solution to the problem of implementing UAVs in environments subject to significant disturbances. The FDI method was developed to integrate a continuous-time residual generator with a fault diagnosis system using a DES. Specifically, their hybrid FDI algorithm is applied to detect and isolate actuator faults in a quad-rotor network to demonstrate its efficacy.

Meskin and Khorasani [50] explored investigating, designing, and examining FDI filters for actuator systems within a network of aerial and space unmanned vehicles. The study emphasizes the actuator fault patterns within the team of agents, characterizing it as an excessively actuated system. An insolubility measure is introduced to evaluate fault patterns and design a novel set of structured residuals. This set is engineered to perform detection selectively and accurately, as well as isolate multiple faults that have been identified, particularly those with dependent fault patterns, such as excessively actuated systems. Based on these concepts, their algorithm is implemented to tackle the actuator FDI challenge in unmanned vehicle networks operating under different architectures, including centralized, distributed, and decentralized. Additionally, in [50], a comparative analysis was conducted, evaluating each architecture's advantages and limitations.

Zaeri Amirani et al. [68] focused on managing formations that change with time, especially when leaders move and followers lack information about their actions. The study also investigated altering the number of leaders and followers in the formation. Arrays of KFs were developed to handle noise reduction and integrate data using the state vector. A $\chi^2$-test was utilized for FDI in this study. The coefficients in the formation control

logic were set in advance, considering changes in the model, eliminating the need for real-time adjustments. The formation control law utilized integral state feedback based on the relative position integral of the agents, allowing followers to track leaders without their input.

### 4.3. Hybrid Methods

Hybrid methods are characterized by their ability to integrate data-driven and model-based methods. Using hybrid methodologies, the idea is to cover both main approaches' shortcomings using each approach's specializations. The term "Hybrid" implies the fusion of data-driven and model-driven methods; however, it does not restrict how the two approaches are combined. In other words, the word hybrid mostly serves as an umbrella term. This is also because hybrid methods in satellite, spacecraft, and UAV health monitoring have not been thoroughly explored in the literature, leaving hybrid methods a promising solution to further boost the existing FDII methods. This section reviews the few existing hybrid methodologies applicable to fault diagnosis applications.

Abbasi Nozari et al. [100] presented an enhanced FDI methodology for two RWs of a four-RW assembly, including both model-based and data-driven approaches used in residual generation and evaluation, respectively. The residual generation is conducted using the nonlinear geometric approach, and evaluation is carried out using a blended learning strategy with two separate hierarchically activated detection and isolation modules. The strategy incorporates robustness against external disturbances and model parametric uncertainties through the residual generation and evaluation modules. Consequently, the advantages of both the model-based and data-driven techniques are leveraged for the extra robustness of the strategy. The learning algorithm used in Abbasi Nozari et al.'s methodology employs a two-step classification approach by training several classifiers and using their test outputs to train the second-level learner. They adjusted their strategy to perform diagnostics using parallel and series formations. However, the series formation mostly surpassed the parallel formation. The simulations verify the hierarchical residual evaluation module's capability to provide satisfactory predictions using different validation datasets under real-life circumstances.

An NN-based observer is presented by Li et al. in [40] to minimize the impact of external interference on malfunction isolation and identification of single gimbal CMGs onboard spacecraft in periodic orbits. In addition, Li et al. employed multiple local fault adaptive estimators for fault isolation and basic identification for spacecraft with extra actuators. Then, their results are used to fuse gimbal and attitude data via neural networks. Finally, these NNs are used to isolate and identify malfunctions in the system.

Chen et al. [30] proposed a hybrid method for fault detection, isolation, and recovery of satellite IMU sensor faults. The proposed scheme works in two steps that get activated in succession: (1) a preliminary diagnosis and (2) a more precise diagnosis. The first step uses an adaptive unscented KF and the QUaternion ESTmiator (QUEST) algorithm in conjunction with each other to be able to examine different sensors and make the fault isolation problem deterministic. The second step consists of two Radial Basis Function (RBF) neural networks and an adaptive complementary filter. During normal operation, the two RBF neural networks get trained on the quaternion outputs of the AUKF and QUEST, and their training is halted when the first step is begun. After stopping their training, they predict the system quaternion outputs and contribute to achieving a higher level of accuracy in fault diagnosis and recovery of IMU faults. Furthermore, Chen et al. incorporated hypothesis testing, Parity equation, and Chi-Square approaches into their residual generators to address the problem of the residual thresholding being sensitive to factors beyond only faults and false alarms. Their proposed scheme was tested using an air-bearing table and demonstrated to have consistently better accuracies than the AUKF and QUEST algorithms used individually.

Another implementation of hybrid methods is conducted by Zhang et al. in [15] by devising a hybrid fault detection methodology for sensor health monitoring of the integrated

navigation system of UAVs. Their proposed methodology uses a KF to estimate the residual sequences of sensor data. Then, a fuzzy logic system is employed to detect and determine the fault type where the membership functions are updated using a neural network.

Baura and Khorasani proposed a structured hierarchical framework for FDI within SFF [79]. In this framework, different diagnostic techniques are incorporated in a hierarchical structure, facilitating the integration of model- and knowledge-based diagnostic techniques. As part of our investigation, they used fuzzy reasoning to isolate faults in a leader–follower formation control system, focusing on ACS faults. The method is also considerably more efficient than traditional diagnostic approaches, which rely on individual satellite telemetry data trend analysis.

### *4.4. Other Methods*

This section covers methodologies that do not fall into either the data-driven or model-driven spectrum. The literature addressing methods other than the focal points of this paper could provide us with useful insight, especially on combining extra methods with the existing model-based and data-driven solutions, for example, the methods incorporating time–frequency spectrums into CNN models.

Shangguan et al. [44] suggested a digital twinning approach to the fault diagnosis of satellites based on the Modelica language [101] for accommodating precise and online monitoring requirements. The model obtains valuable information for online monitoring by fusing the real satellite's telemetry data and simulation data. The proposed method was tested for the power system diagnosis of a satellite and provided accuracies of 83.33% to 93.33%, depending on the preset fault detection threshold.

Zhang et al. [18] proposed a time-domain frequency estimation methodology utilizing the subspace identification method. The presented frequency spectrum analysis approach is used with a gap-metric-oriented indicator and thresholding to achieve structural fault detection and identification in the rotor blades of UAVs. Test results expressed that the proposed methodology surpasses the signal reconstruction accuracy of the FFT and an interpolating FFT method for longer data lengths. It is also observed that blade faults are detected within one second of receiving damage. Future research could include devising more rapid recursive estimation methods and incorporating the malfunction detection scheme into a fault-tolerant control system.

## 5. Prognostics

Earlier, we covered the various ways the literature has achieved fault prognosis in satellites, spacecraft, and UAVs. The next step to advancing the health monitoring of the studied agents is to forecast the effect of the diagnosed malfunctions and obtain their RULs, namely, conducting fault prognosis. Performing prognostics for satellite and spacecraft applications is captivating, especially since their launch and operation are costly. Therefore, fault prognosis is a favorable approach to lengthening the lifetime or optimizing the use of satellites by knowing their RUL and time-to-failure. For UAVs, prognostics is not as pressing an issue since their flight time is usually limited and they can undergo maintenance between flights. Nonetheless, predicting their RUL and prolonging it is favorable. In addition, embedded analytical redundancy techniques for performing prognostics could incur high computational burdens, impeding the UAVs' main functionalities. As a result, UAVs have not received extensive attention in the field of prognostics from researchers. This section reviews the work that has currently been conducted on these agents' fault prognoses. Tables 2–4 list the strengths and limitations of each work on fault prognostics of single-agent systems. Table 6 outlines the main features of the fault prognosis works in a manner similar to Table 5. The reviewed literature indicates that, to the best of the authors' knowledge, very few published works exist on the actuator and sensor fault prognosis of a team of satellites or UAVs.

### 5.1. Data-Driven Methods

With the ability of data-driven methods to obtain predictive information on systems' time series operational data with access to prior historical data, performing fault prognosis on the studied agents becomes feasible. However, given the unrealized potential of data-driven methods in prognosis and unexplored areas of satellite and UAV prognostics, not many works are available in the literature about these agents' fault prognoses using data-driven methods. The following outlines the studies at hand regarding this area.

Islam and Rahimi [12] presented the first part in a double-module RW prognosis scheme using a data-driven approach. The first module is responsible for estimating the future values of the accessible system states. An AutoRegressive Integrated Moving Average (ARIMA) model and an LSTM network are tested for time series prediction, and the latter is shown to fare better in the first module on the input datasets. Later, Islam and Rahimi [5] expanded upon this scheme by augmenting it with the second module. The second module uses the first module's estimated states to predict the RW's inaccessible parameters. Another LSTM network is employed to evaluate the nonmeasurable system parameters and their future values that could give us insight into the health state of the RW. Relating these parameters to the RW's RUL is left for future research by the authors.

Muthusamy and Kumar discussed fault prognosis in CMGs in [69] using a predictive data-driven method that solely involves attitude rate sensor responses to circumvent the problem of unavailable measurement data for component-level variables. Component-level information includes temperature, vibrational and rotational measurements, and lubricant specifications. Muthusamy and Kumar's method consists of a Chebyshev neural network to simulate healthy system dynamics, along with a general path model, historical failures, and real-time measurements to estimate the remaining operating life of the system. According to performance results, the proposed method provides 96.25% accuracy, assuming 70% of the real-time satellite data are unavailable.

### 5.2. Model-Based Methods

Model-based strategies enable researchers to perform prognostics on a relatively straightforward but basic level when high-fidelity models are available compared with data-driven techniques. This is because data-driven techniques can accept numerous features that could affect the RUL of the studied agents, thus yielding more precise and descriptive estimations of agents' RUL. Incorporating the said features into models and accounting for coupling between different parameters could prove challenging and sometimes infeasible. Despite the established usage of model-driven techniques, their implementation in the fault prognosis area is scarce in the current literature. Some of the works in this area are reviewed in the following.

Rahimi et al. [70] suggested a model-based approach to the fault prognosis of RWs that is robust to Gaussian and non-Gaussian noises. After malfunction detection, the prognosis methodology activates by obtaining the fault-sensitive and nonmeasurable system parameters using the CAUKF scheme presented in [16] and outlined in Section 4.2. A PF is then used along with a health-decay model to estimate the damage model parameters and, through propagation in time, yields the RUL of the RW. The simulation test results demonstrate that implementing this approach would be conducive to acquiring accurate RW RUL estimations.

Alidadi and Rahimi [71] designed a stochastic model-based methodology for RUL estimation of RWs onboard satellites that accounts for the bearing lubrication faults. The proposed methodology consists of three key steps: First, lubricant temperature state estimation using an adjusted PF; second, model parameter estimation via a two-step PF accepting the lubricant's injected volume, estimated temperature, and degradation model as inputs, and third, RW RUL estimation under two lubrication malfunction cases. Alidadi and Rahimi also presented a PF resampling method for enhancing the accuracy and efficiency of the filters. The adaptive resampling method used in conjunction with the PFs demonstrated more accurate results for higher measurement noises as compared

with the adjusted PF. The proposed methodology's performance in estimating the RWs' RUL exhibited errors between 0.1 and 4%. Future research could involve developing hybrid model-based and data-driven methods for more confident results or enhancing the proposed methodology by monitoring more RW parameters.

In the relatively unexplored field of UAV actuator fault prognosis, Shen et al. [72] proposed a prognostic and predictive maintenance strategy to increase the mission lifetime of quadrotor UAV actuators. Shen et al. first use a Two-Stage Kalman Filter (TSKF) to estimate the UAV state and actuator degradations in real time. To more easily analyze the degradation of multiple actuators, a comprehensive degradation variable was defined using the entropy weight method that assigns weights to actuators based on their degradation processes. Then, a health index is defined employing the Mahalanobis distance and three health stages are described based on the deviation of the UAV's health index from a nominal health index. Stage 1 encompasses the health conditions that are more degraded than the nominal state but do not influence the UAV performance heavily. Stage 2 is representative of health conditions that have lessened the UAV performance due to degradation and the inferred RUL may not realize the mission's requirements. Finally, the third stage describes the health states that are not able to meet mission stipulations. Then the results of these steps are used to autonomously extend the mission lifetime of the system. The proposed method of Shen et al. is applicable to hovering UAVs, and future research could address extending their method to other flight states.

## 6. Conclusions and Future Work

In this literature review, we have explored FDP within space and aerial vehicles, primarily focusing on satellites and Unmanned Aerial Vehicles. The insights from this study pave the way for future recommendations and research directions in this critical field of study. Tables 5–7 delineate a comprehensive overview of each study indicating the approaches and applications that have already been addressed in the literature.

### *6.1. Literature Analysis*

According to the review strategy outlined in Section 1, the main details of the analyzed works are compiled in Tables 5–8. Each work's significance, advantages and disadvantages, and key features have been discussed in detail in the closing tables. However, in this section, we are going to carry out an analysis of the state of the literature in this field.

One of the key characteristics of each work in the literature was the methodology that was employed in them. Through compiling all these works, we arrived at a methodology/framework classification that explains the relationships between the employed strategies. This classification is illustrated by Figure 10.

In Figure 10, the three main classes that are presented include data-driven, model-based, and other methods. In the existing literature of this field, great emphasis was placed on data-driven and model-based methods with limited attention extended to other miscellaneous methods. Therefore, the same outlook is kept in this review to represent the current state of the existing works while shedding light on other methods, as well as pronounce their potential. The two main subcategories of data-driven methods are ML algorithms and deep learning, which are comprehensively discussed in Sections 4.1 and 5.1, as well as the commonly used dimensionality reduction techniques. Statistical models such as ARIMA are a simpler set of data-driven methods that share some aspects with ML techniques. Moving on to model-based methods, deterministic and stochastic dynamic system observers or state and parameter estimators are prevalent in this field. Deterministic methods are usually used when robustness to noise is not a strict requirement. Some works within this category also employed rule-based systems such as fuzzy logic-based works, and other probabilistic analysis methods which resemble the stochastic state and parameter estimators. The intersection of data-driven and model-based methods are referred to as hybrid methods and they have been covered in Section 4.3. The research into hybrid methods is not as prolific as its parent categories. These methods mostly include

NN observer-based strategies or hierarchical structures of data-driven and model-based frameworks that get activated hierarchically and work in conjunction with each other. Moreover, the vibration analysis-based methods as well as human-operated condition monitoring were classified as other methods since they were not integral to the research trends of this field but influential nonetheless. The attention that data-driven and model-based methods have been met in recent years is also a testament to the effects of the Fourth Industrial Revolution (4IR) or Industry 4.0 that has popularized the use of AI-based methodologies, big data analytics, and Internet of Things (IoT) (in autonomous FDP techniques and interconnected sensors and other components).

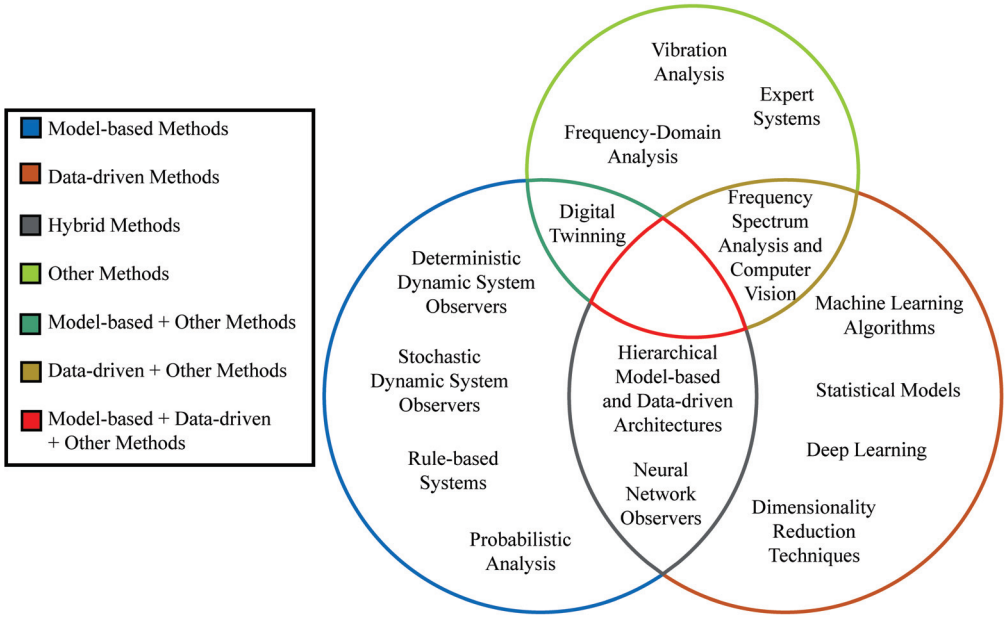


**Figure 10.** Compilation and classification of the methodologies utilized in the literature on satellite/UAV Fault Diagnosis and Prognosis.

The intersection of other methods and data-driven methods results in strategies that combine spectrograms with computer vision capabilities enabled by data-driven methods. In the same vein, digital twinning frameworks were identified as part of the intersection between other methods and model-based methods. Strictly speaking, digital twinning could be classified as a solely model-based methodology; however, these techniques usually require more insight into the other unrelated subsystems of the studied system than the unit FDP is carried out on. For example, many of the model-based methods in this field only require the models of the power subsystems to monitor their condition, whereas a digital twinning approach might need more context into the interactions of all the other subsystems with the power subsystem. For this reason, digital twinning approaches have been recognized to be a combination of model-based and other methods. To the authors' knowledge, the combination of all three categories of data-driven, model-based, and other methods does not exist in the literature. This combination on the surface appears to be too complicated and does not have any obvious advantages. Possible implementations within the red area in Figure 10 could include digital twin models with embedded AI capabilities, and finite element method-based models that account for satellites' and UAVs' surface vibrations that use data-driven models for FDP. These methodologies have not been explored in the literature; therefore, their respective area is left empty in Figure 10.

Furthermore, to obtain more insight into how often these methods are used in the current literature, pie charts of the number of works designed around each of the prominent method categories are demonstrated by Figures 11 and 12 for single-agent and multiagent literature, respectively.

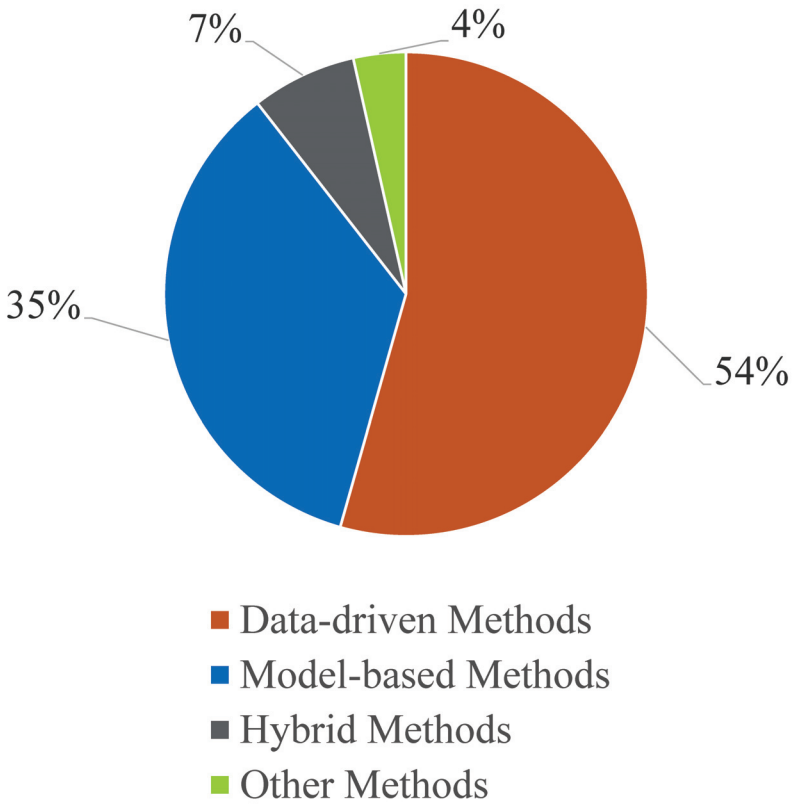


**Figure 11.** Breakdown of the methodologies used in the single-agent FDP literature.

It is noticeable from Figure 11 that data-driven methods are being heavily employed in the area of single satellite and UAV FDP. Consequently, with these methods now composing a significant portion of the literature (54%), it is imperative to address some of the underlying issues that inhibit their real-life implementations such as real-time monitoring shortcomings, faulty dataset dependencies, and poor integration with other subsystems such as the fault-tolerant module. Model-based methods also constitute an extensive share of the research on single-agent FDP especially because of their added robustness to noise. Hybrid methods are shown to be on the rise, with only 7% of the works focused on them, underscoring the need to develop them further. Finally, other methods are rarely used on their own in this field only appearing in 4% of the works, but it is beneficial to be familiarized with their potential combinations with other method categories.

On the other hand, the same pie chart depicted by Figure 12 for multiagent FDP shows a complete detachment from hybrid and other methods which could be due to the works on multiagent systems being fewer in numbers. It can also be seen that model-based methods are significantly more popular in this area appearing in 93% of the works. This signifies the potential for data-driven methods to become increasingly involved with multiagent FDP.

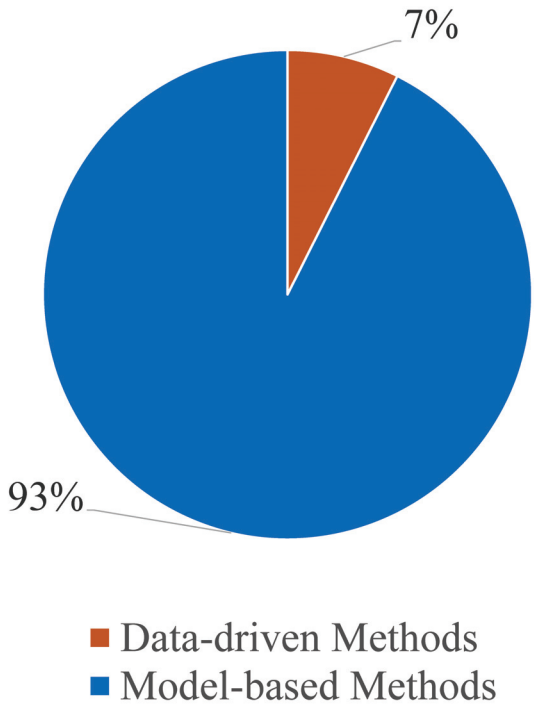


**Figure 12.** Breakdown of the methodologies used in the multiagent FDP literature.

### 6.2. Future Directions

To provide promising avenues to further the works presented in this review, below, we outline the potential areas for future exploration and improvements based on the gaps that have been identified:

Data-Driven FDP: Due to the scarcity of available historical operational datasets, generating artificial datasets that resemble real-life scenarios using AI-based methods is a promising approach for more rigorous exploration. Artificial datasets can address the limitations of mathematical models and provide a more comprehensive basis for FDP.

Increasing user trust in data-driven methods: Due to the low interpretability of many data-driven methods, user trust in these methods could suffer in spite of their effectiveness given how sensitive satellites, spacecraft, and UAVs could be. Methods such as LIME, which is utilized in [75], could alleviate this issue, although with an added trade-off with computational burden.

Dynamical Variables: Many works in the literature have considered different dynamical variables to achieve reliable fault diagnosis in single-agent systems according to their intended use. Experimenting with all possible dynamical variables in a system to train data-driven methods could yield intriguing results. Incorporating new features into data-driven methods allows for flexibility, albeit with additional computational demands.

Hybrid Methods: Leveraging a hybrid approach combining model-based and data-driven methods could help overcome the shortcomings of each individual method, leading to superior analytical techniques in the field of FDP.

Prognostics: While diagnostics for single-agent systems have been explored, there is room for further research in prognostics, particularly for satellites and UAVs. Comprehensive research on fault prognosis for multisatellite/UAV systems is currently lacking and warrants further exploration.

Markovian Jump Systems: The integration of Markovian Jump Systems (MJS) and multiple models into fault diagnosis methods such as [13,74,102] for both single and multiagent systems presents an attractive opportunity, as they can handle abrupt system changes efficiently.

Association Rule Learning: As demonstrated by Pan et al. [85], association rule learning could serve as a not widely explored but viable means of analyzing the relationships

between a bank of sensors or actuators. This approach could benefit the mission reliability of an agent even more if hardware redundancy is also available.

Graph Neural Networks: These networks differ from most traditional ML methods in the sense that they do not require feature independence [89]. Therefore, they have the capability to analyze a broader range of variables within the space and aerial agents which could render examining certain fault-sensitive parameters possible. These networks have also been utilized in the pertinent literature [33].

Multiagent Systems: There is a significant gap in research concerning fault diagnosis methods for multisatellite/UAV systems that prioritize consensus, coverage, or multiagent system control logic. Addressing this gap is a valuable direction for future research. Two of the few examples in this field include [60,62].

Heterogeneous Dynamics: Existing research mainly focuses on multiagent systems with homogeneous dynamics, while real-world systems exhibit heterogeneous dynamics influenced by environmental factors and mission objectives. Investigating FDP strategies that consider dynamic variability is essential for future research on fault diagnosis in multiagent systems. Examples of such work include [60–62].

Event-Triggered Communication: Exploring event-triggered communication can optimize information flow and reduce network workload, aligning research with practical applications and enhancing system efficiency. A summary is provided in Table 8.

Fractional-Order Systems: Future research should address fault diagnosis for fractional-order or reduced-order multisatellite systems. Balancing model accuracy and computational load is crucial when simplifying system complexity.

The recommendations and insights derived from this study will guide and inform future research endeavors in the critical field of Fault Diagnosis and Prognosis for satellites, spacecraft, and UAVs, ensuring the reliability and fault-tolerance of these systems.

**Author Contributions:** Conceptualization, methodology, software, validation, data curation, formal analysis, resources, and writing—original draft preparation, M.H.; conceptualization, methodology, software, validation, data curation, formal analysis, resources, and writing—original draft preparation, A.B.; funding acquisition, project administration, software, resources, formal analysis, supervision, visualization, and writing—review and editing, A.R. All authors have read and agreed to the published version of the manuscript.

**Funding:** This study was supported by Natural Sciences and Engineering Research Council of Canada (NSERC) through RGPIN-2020-05513, Canada. The APC was funded by RGPIN-2020-05513.

**Institutional Review Board Statement:** Not applicable as this study did not involve humans or animals.

**Informed Consent Statement:** Not applicable as this study did not involve humans or animals.

**Data Availability Statement:** No new data were created or analyzed in this study.

**Acknowledgments:** This study was supported by Natural Sciences and Engineering Research Council of Canada (NSERC) through RGPIN-2020-05513, and the University of Windsor, Canada.

**Conflicts of Interest:** The authors declare that they have no known competing financial interests or personal relationships that could have appeared to influence the work reported in this paper.

## References

1. Barzegar, A.; Rahimi, A. Fault Diagnosis and Prognosis For Satellite Formation Flying: A Survey. *IEEE Access* **2022**, *10*, 26426–26442. [CrossRef]
2. Tafazoli, M. A study of on-orbit spacecraft failures. *Acta Astronaut.* **2009**, *64*, 195–205. [CrossRef]
3. Sadhu, V.; Zonouz, S.; Pompili, D. On-board Deep-learning-based Unmanned Aerial Vehicle Fault Cause Detection and Identification. In Proceedings of the 2020 IEEE International Conference on Robotics and Automation (ICRA), Paris, France, 31 May–31 August 2020; pp. 5255–5261. [CrossRef]
4. Pourtakdoust, S.; Fakhari Mehrjardi, M.; Hajkarim, M.; Nasihati Gourabi, F. Advanced fault detection and diagnosis in spacecraft attitude control systems: Current state and challenges. *Proc. Inst. Mech. Eng. Part J. Aerosp. Eng.* **2023**, *237*, 2679–2699. [CrossRef]

5. Sirajul Islam, M.; Rahimi, A. Fault Prognosis of Satellite Reaction Wheels Using a Two-Step LSTM Network. In Proceedings of the 2021 IEEE International Conference on Prognostics and Health Management (ICPHM), Detroit (Romulus), MI, USA, 6–8 June 2021; pp. 1–7. [CrossRef]
6. Nasrolahi, S.; Abdollahi, F. Sensor fault detection and recovery in satellite attitude control. *Acta Astronaut.* **2018**, *145*, 275–283. [CrossRef]
7. Isermann, R.; Ballé, P. Trends in the application of model-based fault detection and diagnosis of technical processes. *Control Eng. Pract.* **1997**, *5*, 709–719. [CrossRef]
8. Barnhart, D.J.; Vladimirova, T.; Baker, A.M.; Sweeting, M.N. A low-cost femtosatellite to enable distributed space missions. *Acta Astronaut.* **2009**, *64*, 1123–1143. [CrossRef]
9. Abbaspour, A.; Mokhtari, S.; Sargolzaei, A.; Yen, K. A Survey on Active Fault-Tolerant Control Systems. *Electronics* **2020**, *9*, 1513. [CrossRef]
10. Muthusamy, V.; Kumar, K. A novel data-driven method for fault detection and isolation of control moment gyroscopes onboard satellites. *Acta Astronaut.* **2021**, *180*, 604–621. [CrossRef]
11. Shahriari-kahkeshi, M.; Sheikholeslam, F.; Askari, J. Adaptive fault detection and estimation scheme for a class of uncertain nonlinear systems. *Nonlinear Dyn.* **2015**, *79*, 2623–2637. [CrossRef]
12. Sirajul Islam, M.; Rahimi, A. Use of A Data-Driven Approach for Time Series Prediction in Fault Prognosis of Satellite Reaction Wheel. In Proceedings of the 2020 IEEE International Conference on Systems, Man, and Cybernetics (SMC), Toronto, ON, Canada, 11–14 October 2020; pp. 3624–3628. [CrossRef]
13. Iglesis, E.; Horri, N.; Dahia, K.; Brusey, J.; Piet-Lahanier, H. Nonlinear Estimation of Sensor Faults With Unknown Dynamics for a Fixed Wing Unmanned Aerial Vehicle. In Proceedings of the 2021 International Conference on Unmanned Aircraft Systems (ICUAS), Athens, Greece, 15–18 June 2021; pp. 404–412. [CrossRef]
14. Rahimi, A.; Dev Kumar, K.; Alighanbari, H. Fault detection and isolation of control moment gyros for satellite attitude control subsystem. *Mech. Syst. Signal Process.* **2020**, *135*, 106419. [CrossRef]
15. Zhang, Q.; Wang, X.; Xiao, X.; Pei, C. Design of a fault detection and diagnose system for intelligent unmanned aerial vehicle navigation system. *Proc. Inst. Mech. Eng. Part J. Mech. Eng. Sci.* **2019**, *233*, 2170–2176. [CrossRef]
16. Rahimi, A.; Kumar, K.; Alighanbari, H. Fault estimation of satellite reaction wheels using covariance based adaptive unscented Kalman filter. *Acta Astronaut.* **2017**, *134*, 159–169. [CrossRef]
17. Cui, L.; Zhang, Q.; Shi, Y.; Yang, L.; Wang, Y.; Wang, J.; Bai, C. A Method For Satellite Time Series Anomaly Detection Based on Fast-Dtw and Improved-Knn. *Chin. J. Aeronaut.* **2023**, *36*, 149–159. [CrossRef]
18. Zhang, X.; Luo, H.; Li, K.; Kaynak, O. Time-Domain Frequency Estimation with Application To Fault Diagnosis Of The Unmanned Aerial Vehicles' Blade Damage. *IEEE Trans. Ind. Electron.* **2022**, *69*, 5257–5266. [CrossRef]
19. Rahimi, A.; Kumar, K.; Alighanbari, H. Enhanced Adaptive Unscented Kalman Filter For Reaction Wheels. *IEEE Trans. Aerosp. Electron. Syst.* **2015**, *51*, 1568–1575. [CrossRef]
20. Kang, B.H.; Hadaegh, F.Y.; Scharf, D.P.; Ke, N.P. Decentralized and self-centered estimation architecture for formation flying of spacecraft. In Proceedings of the 16th International Symposium on Space Flight Dynamics, Pasadena, CA, USA, 3–7 December 2001.
21. Varvani Farahani, H.; Rahimi, A. Data-Driven Fault Diagnosis For Satellite Control Moment Gyro Assembly with Multiple In-Phase Faults. *Electronics* **2021**, *10*, 1537. [CrossRef]
22. Park, K.; Park, E.; Kim, H. Unsupervised Fault Detection on Unmanned Aerial Vehicles: Encoding and Thresholding Approach. *Sensors* **2021**, *21*, 2208. [CrossRef]
23. Li, C.; Li, S.; Zhang, A.; Yang, L.; Zio, E.; Pecht, M.; Gryllias, K. A Siamese Hybrid Neural Network Framework For Few-Shot Fault Diagnosis Of Fixed-Wing Unmanned Aerial Vehicles. *J. Comput. Des. Eng.* **2022**, *9*, 1511–1524. [CrossRef]
24. Nozari, H.; Castaldi, P.; Banadaki, H.; Simani, S. Novel Non-Model-Based Fault Detection and Isolation Of Satellite Reaction Wheels Based on A Mixed-Learning Fusion Framework. *Ifac Pap. Online* **2019**, *52*, 194–199. [CrossRef]
25. Jado, R.; Moncayo, H. Deep-Learning Based Multiple-Model Bayesian Architecture for Spacecraft Fault Estimation. In Proceedings of the AIAA SCITECH 2024 Forum, Orlando, FL, USA, 8–12 January 2024. [CrossRef]
26. Du, C.; Zhang, X.; Zhong, R.; Li, F.; Yu, F.; Rong, Y.; Gong, Y. Unmanned Aerial Vehicle Rotor Fault Diagnosis Based on Interval Sampling Reconstruction of Vibration Signals and A One-Dimensional Convolutional Neural Network Deep Learning Method. *Meas. Sci. Technol.* **2022**, *33*, 065003. [CrossRef]
27. Talebi, H.; Khorasani, K.; Tafazoli, S. A Recurrent Neural-Network-Based Sensor and Actuator Fault Detection and Isolation For Nonlinear Systems with Application To The Satellite's Attitude Control Subsystem. *IEEE Trans. Neural Netw.* **2009**, *20*, 45–60. [CrossRef]
28. Ganesan, M.; Lavanya, R.; Nirmala Devi, M. Fault Detection in Satellite Power System Using Convolutional Neural Network. *Telecommun. Syst.* **2020**, *76*, 505–511. [CrossRef]
29. Abdelghafar, S.; Darwish, A.; Hassanien, A.; Yahia, M.; Zaghrout, A. Anomaly Detection Of Satellite Telemetry Based on Optimized Extreme Learning Machine. *J. Space Saf. Eng.* **2019**, *6*, 291–298. [CrossRef]
30. Chen, X.; Bettens, A.; Xie, Z.; Wang, Z.; Wu, X. Kalman Filter and Neural Network Fusion for Fault Detection and Recovery in Satellite Attitude Estimation. *Acta Astronaut.* **2024**, *217*, 48–61. [CrossRef]

31. Huang, Q.; Liang, B.; Dai, X.; Su, S.; Zhang, E. Unmanned Aerial Vehicle Fault Diagnosis Based on Ensemble Deep Learning Model. *Meas. Sci. Technol.* **2024**, *35*, 046205. [CrossRef]
32. Rahimi, A.; Folami, M. Reaction Wheels Fault Isolation Onboard 3-Axis Controlled Satel-Lite Using Enhanced Random Forest with Multidomain Features. *Int. J. Progn. Health Manag.* **2021**, *12*. [CrossRef]
33. Xie, L.; Pi, D.; Zhang, X.; Chen, J.; Luo, Y.; Yu, W. Graph Neural Network Approach For Anomaly Detection. *Measurement* **2021**, *180*, 109546. [CrossRef]
34. Luo, T.; Liu, M.; Zhao, H.; Duan, G.; Cao, X. Data-Driven Fault Monitoring For Spacecraft Control Moment Gyro with Slice Residual Attention Network. *J. Frankl. Inst.* **2022**, *359*, 9313–9333. [CrossRef]
35. Zhao, H.; Liu, M.; Sun, Y.; Chen, Z.; Duan, G.; Cao, X. Fault Diagnosis Of Control Moment Gyroscope Based on A New Cnn Scheme Using Attention-Enhanced Convolutional Block. *Sci. China Technol. Sci.* **2022**, *65*, 2605–2616. [CrossRef]
36. Gao, J.; Zhang, Q.; Chen, J. Ekf-Based Actuator Fault Detection and Diagnosis Method for Tilt-Rotor Unmanned Aerial Vehicles. *Math. Probl. Eng.* **2020**, *2020*, 1–12. [CrossRef]
37. Xiao, B.; Yin, S. A Deep Learning Based Data-Driven Thruster Fault Diagnosis Approach For Satellite Attitude Control System. *IEEE Trans. Ind. Electron.* **2021**, *68*, 10162–10170. [CrossRef]
38. Guzmán-Rabasa, J.; López-Estrada, F.; González-Contreras, B.; Valencia-Palomo, G.; Chadli, M.; Pérez-Patricio, M. Actuator Fault Detection and Isolation on A Quadrotor Unmanned Aerial Vehicle Modeled As A Linear Parameter-Varying System. *Meas. Control* **2019**, *52*, 1228–1239. [CrossRef]
39. Rotondo, D.; Cristofaro, A.; Johansen, T.; Nejjari, F.; Puig, V. Robust Fault and Icing Diagnosis in Unmanned Aerial Vehicles Using Lpv Interval Observers. *Int. J. Robust Nonlinear Control* **2018**, *29*, 5456–5480. [CrossRef]
40. Li, Y.; Hu, Q.; Shao, X. Neural Network-Based Fault Diagnosis for Spacecraft with Single-Gimbal Control Moment Gyros. *Chin. J. Aeronaut.* **2022**, *35*, 261–273. [CrossRef]
41. Chen, X.; Liu, M. A Two-Stage Extended Kalman Filter Method for Fault Estimation of Satellite Attitude Control Systems. *J. Frankl. Inst.* **2017**, *354*, 872–886. [CrossRef]
42. Maqsood, H.; Taimoor, M.; Ullah, Z.; Ali, N.; Sohail, M. Novel Sensor Fault Detection and Isolation for An Unmanned Aerial Vehicle. In Proceedings of the 2021 International Bhurban Conference on Applied Sciences and Technologies (IBCAST), Islamabad, Pakistan, 12–16 January 2021; pp. 486–493. [CrossRef]
43. Gai, W.; Li, S.; Zhang, J.; Zheng, Y.; Zhong, M. Dynamic Event-Triggered $H_i/H_\infty$ Optimization Approach To Fault Detection for Unmanned Aerial Vehicles. *IEEE Trans. Instrum. Meas.* **2022**, *71*, 1–11. [CrossRef]
44. Shangguan, D.; Chen, L.; Ding, J. A Digital Twin-Based Approach for The Fault Diagnosis and Health Monitoring of A Complex Satellite System. *Symmetry* **2020**, *12*, 1307. [CrossRef]
45. Tao, J.; Khorasani, K. A Fault Detection, Isolation and Reconstruction Strategy for A Satellite's Attitude Control Subsystem with Redundant Reaction Wheels. In Proceedings of the 2007 IEEE International Conference on Systems, Man and Cybernetics, Montreal, QC, Canada, 7–10 October 2007; pp. 3146–3152. [CrossRef]
46. Mousavi, S.; Khorasani, K. Fault Detection of Reaction Wheels in Attitude Control Subsystem of Formation Flying Satellites. *Int. J. Intell. Unmanned Syst.* **2014**, *2*, 2–26. [CrossRef]
47. Tousi, M.; Khorasani, K. A Hybrid Fault Detection and Isolation Strategy for a Team of Cooperating Unmanned Vehicles. *Int. J. Control* **2014**, *88*, 90–103. [CrossRef]
48. Tousi, M.M.; Aghdam, A.G.; Khorasani, K. A Hybrid Fault Diagnosis for A Team of Unmanned Aerial Vehicles. In Proceedings of the 2009 IEEE International Conference on System of Systems Engineering (SoSE), Albuquerque, NM, USA, 30 May–3 June 2009; pp. 1–6.
49. Meskin, N.; Khorasani, K.; Rabbath, C. A Hybrid Fault Detection and Isolation Strategy for a Network of Unmanned Vehicles in Presence of Large Environmental Disturbances. *IEEE Trans. Control. Syst. Technol.* **2010**, *18*, 1422–1429. [CrossRef]
50. Meskin, N.; Khorasani, K. Actuator Fault Detection and Isolation for a Network of Unmanned Vehicles. *IEEE Trans. Autom. Control* **2009**, *54*, 835–840. [CrossRef]
51. Negash, L.; Kim, S.H.; Choi, H.L. Distributed Unknown-Input-Observers for Cyber Attack Detection and Isolation in Formation Flying UAVs. *arXiv* **2017**, arXiv:1701.06325. [CrossRef]
52. Azizi, S.; Khorasani, K. A Decentralized Cooperative Actuator Fault Accommodation of Formation Flying Satellites in Deep Space. In Proceedings of the 2009 3rd Annual IEEE Systems Conference, Vancouver, BC, Canada, 23–26 March 2009; pp. 230–235. [CrossRef]
53. Azizi, S.; Khorasani, K. A Distributed Kalman Filter for Actuator Fault Estimation of Deep Space Formation Flying Satellites. In Proceedings of the 2009 3rd Annual IEEE Systems Conference, Vancouver, BC, Canada, 23–26 March 2009; pp. 354–359. [CrossRef]
54. Azizi, S.; Khorasani, K. A Hierarchical Architecture for Cooperative Actuator Fault Estimation and Accommodation of Formation Flying Satellites in Deep Space. *IEEE Trans. Aerosp. Electron. Syst.* **2012**, *48*, 1428–1450. [CrossRef]
55. Azizi, S.; Khorasani, K. A Hierarchical Architecture for Cooperative Fault Accommodation of Formation Flying Satellites in Deep Space. In Proceedings of the 2009 American Control Conference, St. Louis, MO, USA, 10–12 July 2009; pp. 4178–4183. [CrossRef]
56. Azizi, S.; Khorasani, K. Cooperative Actuator Fault Accommodation of Formation Flying Vehicles with Absolute Measurements. In Proceedings of the 49th IEEE Conference on Decision and Control (CDC), Atlanta, GA, USA, 15–17 December 2010; pp. 6299–6304. [CrossRef]

57. Azizi, S.; Khorasani, K. Cooperative Actuator Fault Accommodation in Formation Flight of Unmanned Vehicles Using Relative Measurements. *Int. J. Control* **2011**, *84*, 876–894. [CrossRef]
58. Shakouri, A.; Assadian, N. Fault Detection and Isolation of Satellite Gyroscopes Using Relative Positions in Formation Flying. *Aerosp. Sci. Technol.* **2018**, *78*, 403–417. [CrossRef]
59. Gao, Z.; Wang, S. Fault Estimation and Fault Tolerance Control for Spacecraft Formation Systems with Actuator Fault and Saturation. *Optim. Control. Appl. Methods* **2021**, *42*, 1591–1611. [CrossRef]
60. Barzegar, A.; Rahimi, A. Distributed Simultaneous Fault Estimation and Cluster Consensus Control of Small Satellites. *IEEE Trans. Aerosp. Electron. Syst.* **2023**, *59*, 7654–7665. [CrossRef]
61. Barzegar, A.; Rahimi, A. A Distributed Fault Detection and Estimation for Formation of Clusters of Small Satellites. In Proceedings of the 2023 IEEE International Conference on Prognostics and Health Management (ICPHM), Montreal, QC, Canada, 9–11 June 2023; pp. 1–11. [CrossRef]
62. Barzegar, A.; Rahimi, A. A dissipativity-based robust fault diagnosis approach for clusters of small satellites. *Acta Astronaut.* **2024**, *214*, 182–195. [CrossRef]
63. Valdes, A.; Khorasani, K. A Pulsed Plasma Thruster Fault Detection and Isolation Strategy for Formation Flying of Satellites. *Appl. Soft Comput.* **2010**, *10*, 746–758. [CrossRef]
64. Meskin, N.; Khorasani, K. Fault Detection and Isolation of Actuator Faults in Spacecraft Formation Flight. In Proceedings of the Proceedings of the 45th IEEE Conference on Decision and Control, San Diego, CA, USA, 13–15 December 2006; pp. 1159–1164. [CrossRef]
65. Azizi, S.; Khorasani, K. Cooperative State and Fault Estimation of Formation Flight of Satellites in Deep Space Subject To Unreliable Information. *IFAC Pap. Online* **2019**, *52*, 206–213. [CrossRef]
66. Barua, A.; Khorasani, K. Hierarchical Fault Diagnosis and Health Monitoring in Multi-Platform Space Systems. In Proceedings of the 2009 IEEE Aerospace conference, Big Sky, MT, USA, 7–14 March 2009; pp. 1–13. [CrossRef]
67. Nemati, F.; Safavi Hamami, S.; Zemouche, A. A Nonlinear Observer-Based Approach To Fault Detection, Isolation and Estimation for Satellite Formation Flight Application. *Automatica* **2019**, *107*, 474–482. [CrossRef]
68. Zaeri Amirani, M.; Bigdeli, N.; Haeri, M. Distributed Fault Detection and Isolation in Time-Varying Formation Tracking Uav Multi-Agent Systems. *Asian J. Control* **2022**, *25*, 604–622. [CrossRef]
69. Muthusamy, V.; Kumar, K. Failure Prognosis and Remaining Useful Life Prediction of Control Moment Gyroscopes Onboard Satellites. *Adv. Space Res.* **2022**, *69*, 718–726. [CrossRef]
70. Rahimi, A.; Kumar, K.; Alighanbari, H. Failure Prognosis for Satellite Reaction Wheels Using Kalman Filter and Particle Filter. *J. Guid. Control. Dyn.* **2020**, *43*, 585–588. [CrossRef]
71. Alidadi, M.; Rahimi, A. Fault Diagnosis of Lubrication Decay in Reaction Wheels Using Temperature Estimation and Forecasting Via Enhanced Adaptive Particle Filter. *Sensors* **2023**, *23*, 1474. [CrossRef]
72. Shen, F.; Li, W.; Jiang, D.; Mao, H. Autonomous Predictive Maintenance of Quadrotor Uav with Multi-Actuator Degradation. *Aeronaut. J.* **2024**, 1–25. [CrossRef]
73. Wang, B.; Liu, D.; Peng, Y.; Peng, X. Multivariate Regression-Based Fault Detection and Recovery Of Uav Flight Data. *IEEE Trans. Instrum. Meas.* **2020**, *69*, 3527–3537. [CrossRef]
74. Carvalho, L.; Toriumi, F.; Angélico, B.; Costa, O. Model-Based Fault Detection Filter for Markovian Jump Linear Systems Applied To A Control Moment Gyroscope. *Eur. J. Control* **2021**, *59*, 99–108. [CrossRef]
75. Li, Y.; Jia, Z.; Liu, Z.; Shao, H.; Zhao, W.; Liu, Z.; Wang, B. Interpretable Intelligent Fault Diagnosis Strategy for Fixed-Wing Uav Elevator Fault Diagnosis Based on Improved Cross Entropy Loss. *Meas. Sci. Technol.* **2024**, *35*, 076110. [CrossRef]
76. Azizi, S.; Khorasani, K. A hybrid and switching framework for cooperative actuator fault estimation of formation flying satellites in deep space. In Proceedings of the 2009 7th Asian Control Conference, Hong Kong, China, 27–29 March 2009; pp. 1126–1131.
77. Ghasemi, S.; Khorasani, K. Fault Detection and Isolation of the Attitude Control Subsystem of Spacecraft Formation Flying Using Extended Kalman Filters. *Int. J. Control* **2015**, *88*, 2154–2179. [CrossRef]
78. Han, W.; Wang, Z.; Shen, Y. Robust $H_\infty$ Fault Diagnosis Observer Design for Multiple Satellites Attitude Synchronization with Disturbance. In Proceedings of the 2016 35th Chinese Control Conference (CCC), Chengdu, China, 27–29 July 2016; pp. 6575–6580. [CrossRef]
79. Barua, A.; Khorasani, K. Intelligent Model-Based Hierarchical Fault Diagnosis for Satellite Formations. In Proceedings of the 2007 IEEE International Conference on Systems, Man and Cybernetics, Montreal, QC, Canada, 7–10 October 2007; pp. 3191–3196. [CrossRef]
80. Rahimi, A.; Saadat, A. Fault Isolation Of Reaction Wheels Onboard Three-Axis Controlled In-Orbit Satellite Using Ensemble Machine Learning. *Aerosp. Syst.* **2020**, *3*, 119–126. [CrossRef]
81. Vaz Carneiro, J.; Schaub, H.; Lahijanian, M.; Lang, K.; Borozdin, K. Machine Learning For Reaction Wheel Fault Detection Using Simulated Telemetry Data. In Proceedings of the AIAA SCITECH 2022 Forum, San Diego, CA, USA & Virtual, 3–7 January 2022. [CrossRef]
82. Kenneally, P.; Piggott, S.; Schaub, H. Basilisk: A Flexible, Scalable and Modular Astrodynamics Simulation Framework. *J. Aerosp. Inf. Syst.* **2020**, *17*, 496–507. [CrossRef]
83. Suo, M.; Zhu, B.; An, R.; Sun, H.; Xu, S.; Yu, Z. Data-Driven Fault Diagnosis Of Satellite Power System Using Fuzzy Bayes Risk and Svm. *Aerosp. Sci. Technol.* **2019**, *84*, 1092–1105. [CrossRef]

84. Hedayati, M.; Barzegar, A.; Rahimi, A. Mitigating Data Scarcity for Satellite Reaction Wheel Fault Diagnosis with Wasserstein Generative Adversarial Networks. In Proceedings of the 2024 IEEE International Conference on Prognostics and Health Management (ICPHM), Washington, DC, USA, 11–13 October 2024; pp. 367–376. [CrossRef]
85. Pan, D.; Liu, D.; Zhou, J.; Zhang, G. Anomaly Detection For Satellite Power Subsystem with Associated Rules Based on Kernel Principal Component Analysis. *Microelectron. Reliab.* **2015**, *55*, 2082–2086. [CrossRef]
86. Ossenfort, J. Advanced Diagnostic and Prognostic Testbed (ADAPT) Testability Analysis Report. In *Technical Report*; Ames Research Center: Moffett Field, CA, USA, 2008.
87. Huang, G.; Wang, D.; Lan, Y. Extreme Learning Machines: A Survey. *Int. J. Mach. Learn. Cybern.* **2011**, *2*, 107–122. [CrossRef]
88. Ferrell, B.; Santuro, S. NASA Shuttle Valve Data. 2005. Available online: http://www.cs.fit.edu/~pkc/nasa/data/ (accessed on 10 October 2023).
89. Wu, Z.; Pan, S.; Chen, F.; Long, G.; Zhang, C.; Yu, P. A Comprehensive Survey on Graph Neural Networks. *IEEE Trans. Neural Netw. Learn. Syst.* **2021**, *32*, 4–24. [CrossRef]
90. Liu, W.; Yuan, L.; Wang, S.; Liu, C. Research on Fault Diagnosis Method Of Control Moment Gyroscope Based on K-Means Algorithm. In Proceedings of the 2020 39th Chinese Control Conference (CCC), Shenyang, China, 27–29 July 2020; pp. 4119–4123. [CrossRef]
91. Taimoor, M.; Lu, X.; Maqsood, H.; Sheng, C. Adaptive Rapid Neural Observer-Based Sensors Fault Diagnosis and Reconstruction Of Quadrotor Unmanned Aerial Vehicle. *Aircr. Eng. Aerosp. Technol.* **2021**, *93*, 847–861. [CrossRef]
92. Wang, Y.; Yao, Q.; Kwok, J.; Ni, L. Generalizing From A Few Examples. *Acm Comput. Surv.* **2020**, *53*, 1–34. [CrossRef]
93. Huang, Y.; Ferguson, P. Automated One-Sided Learning Fault Detection System for Reaction Wheel Bearing Friction Anomalies. *J. Aerosp. Inf. Syst.* **2024**, *21*, 380–391. [CrossRef]
94. Bialke, B. High Fidelity Mathematical Modeling of Reaction Wheel Performance. In Proceedings of the Annual AAS Rocky Mountain Guidance and Control Conference, Breckenridge, CO, USA, 4–8 Janurary 1998; pp. 483–496.
95. Rahimi, A.; Kumar, K.; Alighanbari, H. Fault Isolation of Reaction Wheels for Satellite Attitude Control. *IEEE Trans. Aerosp. Electron. Syst.* **2020**, *56*, 610–629. [CrossRef]
96. Rahimi, A. Fault Isolation and Identification of A Four-Single-Gimbal Control Moment Gyro On-Board a 3-Axis Stabilized Satellite. *Int. J. Progn. Health Manag.* **2021**, *12*. [CrossRef]
97. Jansch-Porto, J.; Hu, B.; Dullerud, G. Convergence Guarantees of Policy Optimization Methods for Markovian Jump Linear Systems. In Proceedings of the 2020 American Control Conference (ACC), Denver, CO, USA, 1–3 July 2020; pp. 2882–2887. [CrossRef]
98. Norris, J.R., Discrete-time Markov chains. In *Markov Chains*; Cambridge Series in Statistical and Probabilistic Mathematics; Cambridge University Press: Cambridge, UK, 1997; p. 1–59.
99. Wang, R.; Zhao, C.; Bai, Y.; Du, W.; Wang, J. An Actuator Fault Detection and Reconstruction Scheme for Hex-Rotor Unmanned Aerial Vehicle. *IEEE Access* **2019**, *7*, 93937–93951. [CrossRef]
100. Abbasi Nozari, H.; Sadati Rostami, S.; Castaldi, P.; Simani, S. Hybrid Robust Fault Detection and Isolation of Satellite Reaction Wheel Actuators. *J. Control Decis.* **2022**, *11*, 117–131. [CrossRef]
101. Mattsson, S.; Elmqvist, H.; Otter, M. Physical System Modeling with Modelica. *Control Eng. Pract.* **1998**, *6*, 501–510. [CrossRef]
102. Meskin, N.; Khorasani, K. Fault Detection and Isolation of Discrete-Time Markovian Jump Linear Systems with Application to a Network of Multi-Agent Systems Having Imperfect Communication Channels. *Automatica* **2009**, *45*, 2032–2040. [CrossRef]


**Disclaimer/Publisher's Note:** The statements, opinions and data contained in all publications are solely those of the individual author(s) and contributor(s) and not of MDPI and/or the editor(s). MDPI and/or the editor(s) disclaim responsibility for any injury to people or property resulting from any ideas, methods, instructions or products referred to in the content.

applied sciences

MDPI

*Article*

# Imbalanced Diagnosis Scheme for Incipient Rotor Faults in Inverter-Fed Induction Motors

**Ignacio Martin-Diaz [1], Tomas Garcia-Calva [2], Óscar Duque-Perez [1] and Daniel Morinigo-Sotelo [1,*]**

[1] Research Group ADIRE, Institute of Advanced Production Technologies, University of Valladolid, 47002 Valladolid, Spain; ignacio.martin.diaz@uva.es (I.M.-D.); oscar.duque@uva.es (Ó.D.-P.)
[2] Department of Electrical Engineering, University of Valladolid, 47002 Valladolid, Spain; tomasalberto.garcia@uva.es
* Correspondence: daniel.morinigo@uva.es

**Abstract:** Recently, fault diagnosing supervised classifiers have been widely proposed to diagnose both electric and mechanical faults in induction motors (IM). However, many of them require a large amount of data, which implies a great effort required for processing fault-related features and building the training set. Furthermore, in real-world datasets, it is required to deal with highly skewed data distributions, also known as class imbalance, which is a limiting issue and can misguide the tuning of machine learning algorithms. Resampling techniques based on a synthetic generation of minority class observations aim to address this problem. Last but not least is the fact that inverter-fed IM introduces undesired harmonics in the monitoring signal altering the diagnosis patterns. This diagnosis scheme is evaluated on experimental imbalanced data oriented to deal with the diagnosis of a rotor in situations where it is fed with an inverter. The results show how this imbalanced approach determines the actual diagnosis performance on a small amount of data. The experimental results demonstrate that balanced training sets built with class balancing techniques improve the classifier and therefore its performance for diagnosing incipient rotor faults in inverter-fed IM with studied and interpretable features recently proposed in this field of study.

**Keywords:** rotor faults; diagnosis features; induction motor; inverter; small data; imbalance correction

## 1. Introduction

Condition monitoring is a growing concern in predictive maintenance tasks to prevent unexpected machinery breakdowns and production losses. Consequently, strengthening the ability to detect and diagnose machine faults can reduce costs in modern production planning and operations. As a primary energy consumer, induction motors (IM) are a crucial element in electromechanical equipment and currently dominate in both the industrial and commercial sectors [1]. Therefore, a well-designed condition-based monitoring system can minimize maintenance costs and correctly target necessary maintenance tasks [2].

Motor current signature analysis (MCSA) has been preferred for extracting fault signatures at both transient [3] and stationary regimes [4]. This technique has several advantages over vibration analysis, such as remote sensing, low implementation cost, and online monitoring.

Furthermore, voltage source inverters are increasingly used to feed IM in variable speed applications. This, however, introduces a new set of challenges. Using inverters introduces undesired harmonics into the stator current, negatively altering the extraction of features based on spectral analysis. Consequently, many diagnosis techniques that worked for line-fed IM do not perform appropriately on inverter-fed IM. As a result, the methodologies proposed to date as well as novel ones have to take into account this challenge to avoid the loss of performance of the diagnosis systems.

Nowadays, automatic diagnosis through machine learning techniques is one of the most promising fields for this challenge. Automatic diagnosis has been conceived as a tool for improving the efficiency and reliability of a balanced or unbiased fault detection scheme. In fact, an important research community has proposed supervised classifiers to diagnose the health of the electric machine [5–7]. Basically, a classifier consists of a function (linear or nonlinear) that tries to separate the classes defined in the problem by minimizing the expected loss. In other words, it tries to identify which class corresponds to each observation with the lowest classification error. The different motor states form classes of the problem to diagnose.

Hence, it is clear that data-driven approaches oriented to an automatic diagnosis have emerged recently [8]. Authors in [9] demonstrate an interest in data-driven methods where actual field data are obtained from railway electrification networks. The data is continuously collected from the most important variables, which gives a data-driven detection approach for low-frequency oscillation events in alternating current railway catenaries. In addition, there are works where the simulation-driven machine learning training phase has also been developed by generating raw input data. This kind of approach tries to overcome limitations such as data scarcity and data imbalance [10].

Data imbalance is a crucial concern, since actual datasets are not entirely balanced [11], and it is common for actual industrial data obtained both from destructive tests of the machine and during its useful life to be imbalanced [12]. When the minority class representation is extremely low, the problem is usually denominated as an anomaly detection case [13]. Unlike the case of balanced classification, under an imbalanced scenario, the classifier directly labels new observations to the majority class because of the existing inherent bias as the imbalance proportion between classes increases. This fact is detrimental to the performance of diagnosis systems and requires much more attention. To deal with class imbalance, the data science literature has presented several techniques relating to the following approaches: embedded methods, data processing, and ensemble methods. Within data processing approaches, resampling methods have offered adequate characteristics to balance previously imbalanced training sets. Moreover, in engineering scenarios, the reduced machine information about abnormal conditions limits intelligent fault diagnosis performances since diagnosis tools with small and imbalanced data reduce the accuracy of fault identification [12,14].

This paper aims to improve the diagnosis of faults in inverter-fed induction motors, mainly focusing on rotor bar failure. It proposes using the SMOTE oversampling technique to address imbalances in datasets to enhance diagnostic performance and interpretability. The proposed method is intended to work with a small and unbalanced dataset. Additionally, the fault features will be derived from the stator current in an inverter-fed motor, which is a source of high harmonic and polluted content in this signal (as mentioned before). Hence, this study aims to create an effective diagnostic tool for the circumstances previously described. This work begins by reviewing various techniques used to generate synthetic data to balance the initial dataset, focusing on the computed feature space. The implemented techniques will be Safe-Level SMOTE, Relocating Safe-Level SMOTE, and Majority weighted minority oversampling technique (MWMOTE), which have been proposed for balancing datasets. Firstly, the ReliefF algorithm performs the feature selection. Then, the developed diagnosis methodology uses a resampling technique for balancing data. When the training set is balanced, a supervised classifier is used for the fault diagnosis of rotor asymmetries with different degrees of bar breakage. The fault signatures proposed in the bibliography are introduced in the next section. These signatures are computed from signals collected during experimentation from an induction motor fed from inverters and the line.

## 2. Background

An appropriate condition monitoring system can detect the machine's potential rotor breakage in its early stages, and its diagnosis can be automated based on fault-related

features. The monitored signal is the stator currents, which have proven effective for stationary and non-stationary operating conditions. In this paper, the fault signatures are derived from the frequency and time domains and calculated to diagnose issues during stationary operation.

### *2.1. Diagnosis Signals*

From the scientific literature, it seems to be a consensus that MCSA is a noninvasive diagnostic method [3,4,8,12,15] with several advantages: easy acquisition of signals; signal collection does not interfere with the operation of the motor; the obtained signal is reliable under noisy environments; and sensors with reasonable accuracy are not too expensive. Once an IM is manufactured, free of rotor faults, and it is fed from an ideal stator current signal, the temporal expression of this current contains exclusively the fundamental component of its power supply:

$$i_0(t) = I_m \cos(\omega_0 t + \phi_0), \tag{1}$$

where $\omega_0$ denotes the power supply angular pulsation, $I_m$ denotes the amplitude of the stator current, and $\phi_0$ is the phase. However, when a rotor breakage develops, fault-related harmonics emerge in the observed signal and can be used for diagnosis purposes. Nevertheless, when the IM supply comes from an inverter or from the mains with the presence of considerable harmonic content, the amplitude quantification of these fault patterns complicates their identification [16].

This project will utilize a single stator phase as a monitoring signal, which will be obtained from the motor when it is powered by an inverter or the grid. A data acquisition system will then digitize the signal in the time domain. Following this, the digital signal will undergo processing in both the time and frequency domains to identify fault patterns.

### *2.2. Time-Domain Fault Signatures*

Statistics computed from time domain signals have been employed as features for several fault diagnosis approaches in literature [6,7,11]. High-order statistics are sensitive to non-Gaussian distribution measurements. On the other hand, low-order statistics (e.g., first and second moments) are more robust. In Table 1, the time-domain statistical features used in this study are defined.

**Table 1.** Statistics computed from the time-domain signal.

| **Variables in Time-Domain** | | |
|---|---|---|
| **Variable** | **Notation** | **Formula** |
| 1st. Moment | $m_1$ | $\frac{1}{N}\sum x[n]$ |
| 2nd. Moment | $m_2$ | $\frac{1}{N}\sum(x[n]-\bar{x}[n])^2$ |
| 3rd. Moment | $m_3$ | $\frac{1}{N}\sum(x[n]-\bar{x}[n])^3$ |
| 4th. Moment | $m_4$ | $\frac{1}{N}\sum(x[n]-\bar{x}[n])^4$ |
| 2nd. Cumulant | $c_2$ | $m_2 - m_1^2$ |
| 3rd. Cumulant | $c_3$ | $m_3 - 3\cdot m_1 m_2 + 2\cdot m_1^3$ |
| 4th. Cumulant | $c_4$ | $m_4 + 3m_3m_1 - 3\cdot m_2^2 + 12\cdot m_2 m_1^2 - 6\cdot m_1^4$ |
| Skewness | *Skew* | $\frac{m_3}{(\sqrt{m_2})^3}$ |
| Kurtosis | *Kurt* | $\frac{m_4}{(\sqrt{m_2})^4}$ |
| Absolute mean (ABM) | $\lvert\bar{x}\rvert$ | $\frac{1}{N}\sum\bar{x}$ |
| Peak value | PV | $\frac{1}{2}(\max(x[n]) - \min(x[n]))$ |
| Squared root value | SRV | $\left(\frac{1}{N}\sum\sqrt{\lvert x\rvert}\right)^2$ |
| RMS value | RMS | $\sqrt{\frac{1}{N}\sum_{n=0}^{N-1}[x[n]-\bar{x}]^2}$ |
| Crest factor | CF | $\frac{PV}{RMS}$ |
| Shape factor | SF | $\frac{RMS}{\lvert\bar{x}\rvert}$ |

*2.3. Fault Signatures from Spectra*

Fault signatures from the stator current can also be obtained in the frequency domain. When a rotor bar breakage occurs, a current is induced, and torque and speed pulsations originate, giving place to two sidebands around the fundamental frequency and other harmonics. These fault-related frequency components are observable in the frequency spectrum [15]. This motivates the use of these sidebands' amplitude to be considered a fault severity indicator of the rotor condition. For their frequency location, Equation (2) is used.

$$f_{BRB} = (1 \pm 2s)f, \tag{2}$$

where $f$ is the supply frequency and $s$ is the rotor slip. The frequency corresponding to the minus sign is known as the left sideband harmonic (LSH); the other one is known as the right sideband harmonic (RSH). Both sidebands are separated from the integer harmonics, a distance that depends on rotor slip and, thus, on the motor load level. Nonetheless, when an IM is fed from an inverter, the stator current contains time harmonics. These harmonics modify the amplitude of the present harmonics or they generate new airgap spatial harmonics. The author in [17] proposed additional faulty signatures for diagnosing rotor cage asymmetries in inverter-fed IM. Some of them are used as candidate features for the diagnosis methodology and they are defined as follows:

$$\Gamma_5 = \frac{G7\ (LSH)}{G_5} \tag{3}$$

$$\Gamma_7 = \frac{G5\ (RSH)}{G_7} \tag{4}$$

$$\Gamma_{11} = \frac{G13\ (LSH)}{G_{11}} \tag{5}$$

$$\Gamma_{13} = \frac{G11\ (RSH)}{G_{13}} \tag{6}$$

The above expressions' numerators correspond to the amplitudes of the fault-related sidebands around the fifth, seventh, eleventh, and thirteenth harmonics. The nomenclature used is LSH for the left sideband harmonic and RSH for the right sideband harmonic. The denominators are the amplitudes of the above-mentioned integer harmonics. Figures 1 and 2 show the spectrum of one stator phase current to illustrate the presence of these harmonics. Figures 1 and 2 are the spectra for a line-fed and an inverter-fed induction motor respectively. As can be seen, the signal that comes from the inverter supply introduces different harmonics, inter-, and sub-harmonics, into the stator current spectrum, affecting more negatively the extraction of the above-defined indicators and, thus, the diagnosis compared with the line-fed IM case.

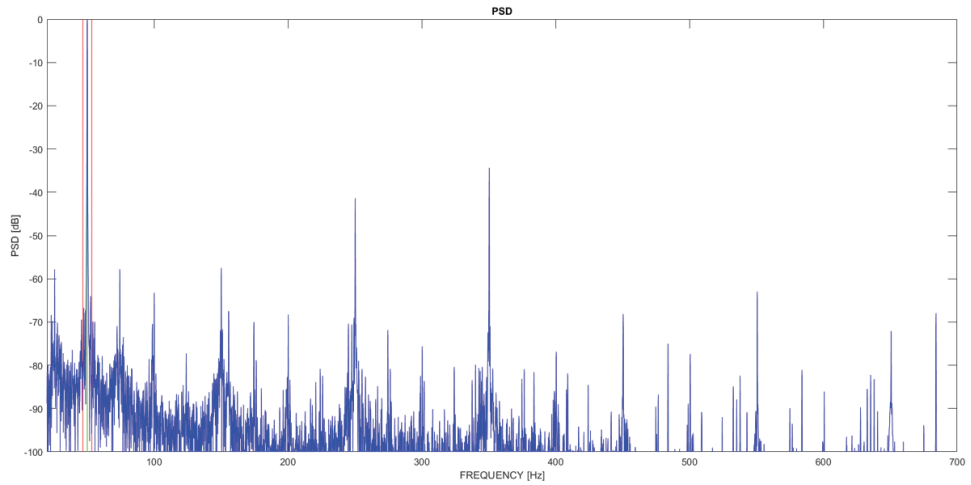


**Figure 1.** Power spectral density of a measured stator current from a line−fed induction motor.

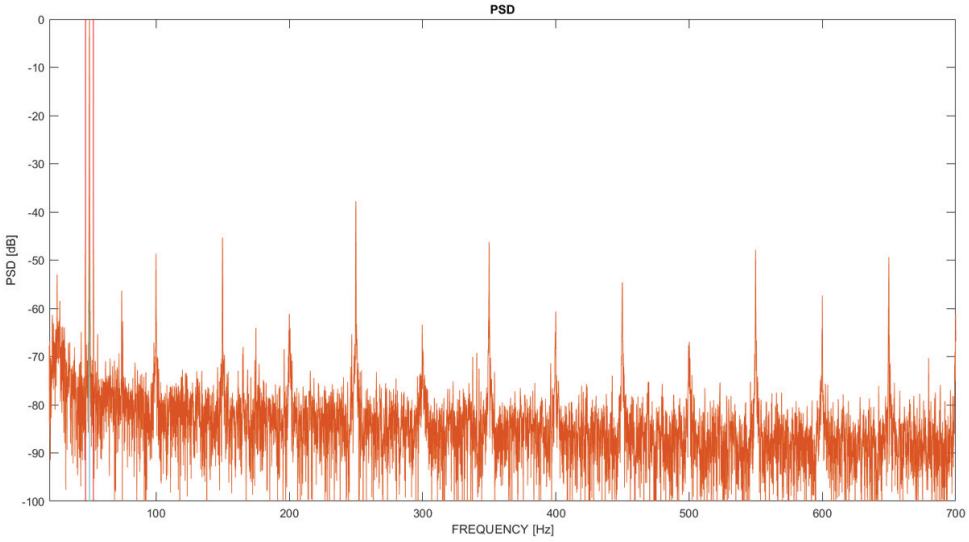


**Figure 2.** Power spectral density of a measured stator current from an inverter−fed induction motor.

*2.4. Feature Selection through ReliefF Algorithm*

The fault signatures mentioned above are obtained through a manual inspection process assisted by MATLAB© software version number R2023a. After collecting these fault signatures, a feature selection process is commonly used to eliminate noisy, irrelevant, and redundant variables from the set. This selective analysis aims to improve subsequent classification. For this purpose, the Algorithm 1 (ReliefF algorithm [18]) is applied. This technique scores the impact of changes based on how their values distinguish closely labelled observations.

ReliefF [18] is an extension of the Relief algorithm designed for binary problems. However, RefliefF can deal with more than two classes and is more robust considering that it can deal with incomplete and noisy data [19]. Given a randomly selected observation $S_o$, ReliefF searches for $k$ of its nearest neighbours in the same class. These are called the closest results $R_j$, hits or successes. This algorithm also searches for $k$ nearest neighbours of each different class. They are called nearest misses $M_j(C)$. The quality estimate $W[F]$ is updated for all features $F$ based on their values for $S_o$, $M_j(C)$ and $R_o$. The contributions of all successes and misses are averaged through the update expression. That is to say, the contribution for each class of the misses is weighted with the prior probability of that class $P(C)$ that, using the training set, is estimated. If the observations $S_o$ and $R_j$ have different values of the characteristic $F$, then the characteristic $F$ will separate two observations belonging to the same class, which is undesirable. The estimation of quality $W[F]$ is reduced. This process is repeated $m$ times. The choice of $k$ successes and failures ensures higher algorithm reliability concerning noise. The difference between the values of the variable or feature $F$ for two observations $O_1$ and $O_2$ is computed by the function $diff(F, O_1, O_2)$. For numerical variables, the function is defined as follows:

$$diff(F, O_1, O_2) = \frac{|value(F, O_1) - value(F, O_2)|}{max(F) - min(F)} \tag{7}$$

The $diff$ function calculates the distance between observations to determine the nearest neighbor's location. The total distance is calculated as the sum of the distances across all features or variables, known as the Manhattan distance.

**Algorithm 1** ReliefF [18]

**Input:** Training observations with their respective vector of features
**Output:** The vector $W$ with the quality estimation of the features

Set all feature weights to zero $W[F] = 0$
**for** $o \leftarrow 1, \ldots, m$ **do**
  Random selection of an observation $S_o$
  Locate $k$ nearest results, named as $R_j$
  **for** each class $C \neq class(S_o)$ **do**
    From class $C$ identify $k$ nearest misses named as $M_j(C)$
    **for** $F = 1$ to $f$ **do**
      $W[F] = W[F] - \sum_{j=1}^{k} \frac{diff(F,S_o,R_j)}{m \cdot k} + \sum_{C \neq class(S_o)} \frac{\left[\frac{P(C)}{1-P(class(S_o))} \sum_{j=1}^{k} diff(F,S_o,M_j(C))\right]}{m \cdot k}$
    **end for**
  **end for**
**end for**

## 3. Problem Statement for a Class-Imbalanced Scenario

The dataset of the IM obtained from the laboratory setup leads to a normal distribution as the data collection increases, as is the case for healthy motor instances. However, instances corresponding to faulty rotor states are fewer than healthy ones. Thus, a classifier cannot find the core of the distribution from the minority set of observations since it is too reduced to be identified. Therefore, minority-class observations must be over-sampled to perform successfully in a small data diagnosis scheme. This task even increases in complexity when features are computed from a polluted stator current signal due to the presence of undesired inverter harmonics [20]. The following sections describe the different approaches that have led to the already presented fault-related feature space treatment of the problem.

### *3.1. SMOTE and Following Extensions for Balancing Datasets*

Synthetic Minority Over-Sampling Technique (SMOTE), proposed by Chawla et al. in [21], is a technique that oversamples the observations belonging to a minority class creating synthetic samples. This oversampling is made iteratively through a selection approach where each observation from the minority class is iterated until the total number of classes is balanced. The synthetic generation procedure consists of applying the $k$ nearest neighbours algorithm. One of the $k$ nearest neighbours is randomly selected, and later, it is synthesized, letting the algorithm continue until every needed synthetic sample is built. In the proposed methodology, an imbalanced dataset is characterized by its imbalanced ratio ($IR$), which is the quotient between the number of healthy class observations and the number of faulty cases belonging to each rotor state. For imbalanced datasets, a new observation denoted as $x_{n+1}$ is generated from the features of the random sample $x_j$ and the original $x_i$ observation used to generate it. The generation of new features is created by multiplying a random number $r$ between 0 and 1 and the difference between feature $x_i$ and $x_j$ as indicated in (8).

$$x_{n+1} = x_i + r(x_j - x_i), \qquad 0 \leq r \leq 1 \tag{8}$$

This random multiplication is the main disadvantage of SMOTE when used for diagnosis purposes. However, the borderline-SMOTE (BLS) method acts selectively, and it was useful as inspiration for the following density-based SMOTE. The BLS method focuses on observations close to the boundary areas prone to misclassification. This method defines a danger group for minority instances in danger of misclassification, which makes it possible to take these ones as candidates to oversample.

*3.2. Safe Level-SMOTE*

The Safe-Level SMOTE algorithm is an extension of the original SMOTE method. This version considers the "safe" observations found in the minority class [22]. The observations corresponding to this "safe" group are from the set of minority class observations that $k$-NN finds by computing the Euclidean distance. Observations that fall outside of this term coined as "safe" are considered noise. For this reason, a "safe" level ratio ($slr$) needs to be defined to obtain synthesized candidates. This ratio is defined as $slr = slp/sln$. The notation is as follows: $slp$ is the "safe" level for a given observation $x_i$, and $sln$ is the level for the selected neighbour of $x_i$, which is called $x_j$. In general, only candidates with minority class observations for $x_i$ and $x_j$ are considered. The generation of new synthetic observations goes under Equation (8). But now, $r$ is calculated as

$$r \in \begin{cases} (0, (1/slr)), & \text{if } slr \geq 1 \\ ((1 - slr), 1), & \text{if } slr < 1 \end{cases} \tag{9}$$

The ratio $slr = 1$ means that $x_i$ and $x_j$ are equally important or "safe". Therefore, the aggregate observations can be randomly selected. On the one hand, if this ratio is greater than 1, the newly aggregated data will be weighted in the direction of the minority class, which brings the new aggregation closer to the $x_i$ example. On the other hand, if $slr < 1$, it is weighted in the direction of the majority class, which brings the most recent sample closer to the example $x_j$.

*3.3. Relocating Safe Level SMOTE*

A limitation of the Safe Level-SMOTE method may be that it places some synthetic observations where they may be too close to the nearby majority class, leading to classifier confusion [23]. The location of each surrounding majority class observation is not considered in the safety level SMOTE, i.e., the generation of these synthetic observations may be close to some majority class observations. To prevent this situation, a later extension was proposed in [23]. This SMOTE extension is called Relocating Safe-Level SMOTE (RSLS). RSLS is conceived as a procedure to relocate synthetic observations once they are located close to minority-class observations. This approach follows the SMOTE steps on the safe side, starting with finding the $k$-NN of each minority class observation and computing its corresponding proportions. This approach follows the SMOTE steps on the safe side, starting with finding the $k$-NN of each minority class observation and computing its corresponding proportions. Once the observation $O$ and its minority class neighbour $\hat{m}$ are determined, the "safe" level values and their safe level ratio are used to determine the possible range of observed aggregation. Once the location of the synthetic observation is randomly selected from this range, this new location is used to calculate the distance between the new synthetic observation and the observations of the surrounding majority group. These distance values are compared with the distance of these aggregate observations to their nearest point, $O$ or $\hat{m}$. Suppose the distance between the composite observation and one of the observations of the surrounding majority group is less than the distance to its nearest point. In that case, the composite observation under consideration is moved closer to this point until it is excluded from the observations of the surrounding majority group.

*3.4. Density-Based SMOTE*

This method is inspired by the borderline-SMOTE. This technique applies density-based clustering by combining it with SMOTE. The synthetic observations are generated by calculating the shortest path from each instance of the minority class to the pseudo-centroid of the cluster corresponding to the minority class.

*3.5. Majority Weighted Minority Oversampling Technique*

The method was introduced in [24] and is also known as MWMOTE. The idea behind it is to ensure that the synthetically generated minority observations fall into the correct

class cluster. To achieve this, a mechanism calculates the weight according to the distance to the nearest majority class point. Then, synthetic examples are generated from the minority class instance with weighted information using the clustering method.

Figure 3 illustrates the operation of the MWMOTE algorithm for synthetically generating data from the minority class. The figure shows two scatter plots presenting the amplitude of the LSH failure indicator as a function of motor slip (which also represents the motor load level). The green circles represent the majority class, i.e., the LSH value when the motor is healthy. The blue points represent the minority class, i.e., the LSH value when the motor experiences a broken bar. The synthetic values generated using this technique to balance the two classes are represented in red on the right side of the figure (Figure 3b).

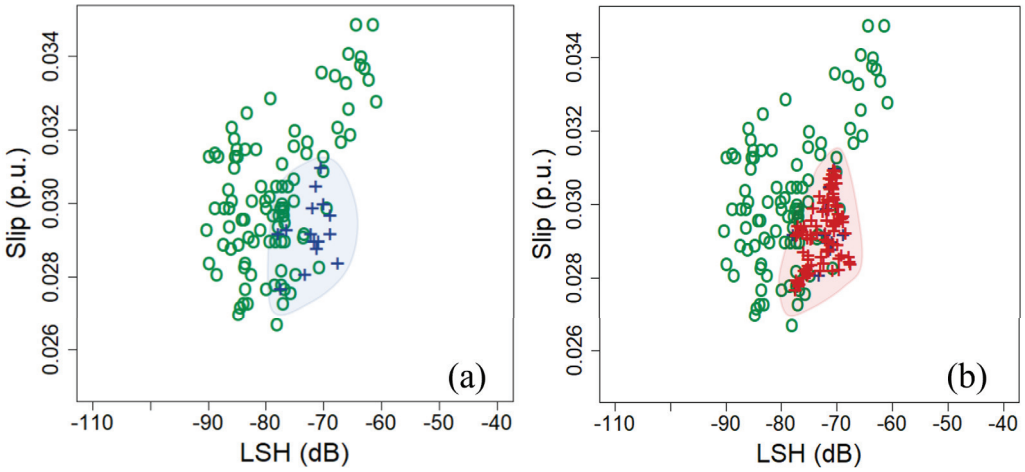


**Figure 3.** Demonstration of the operation of the MWMOTE algorithm. A dataset from an inverter−fed motor is used. The green markers represent the majority class (healthy motor), and the blue markers represent the minority class (motor with failure). (**a**) Case with imbalanced classes; (**b**) synthetically balanced case (synthetically created markers are shown in red).

## 4. Test Bench and Signal Acquisition

The test bench designed for this research is shown in Figure 4. The IM is fed from the line supply and from inverters whose specifications are defined in the Appendix A. In both cases, the voltage main frequency is 50 Hz. The motor load is a magnetic powder brake with its control unit. A Hall Effect current transducer by LEM® (Meyrin, Switzerland) is used to measure the stator current. A National Instruments® (Austin, TX, USA) NI cDAQ-9174 base platform with an NI 9215 acquisition module is used for the signal collection. The sampling frequency is 50 kHz.

The rotor fault is simulated by drilling a hole in one of the bars near the short circuit ring. Three rotor condition states are considered: (i) The rotor is healthy in the first tests. This condition is labeled as R1; (ii) After that, a 4.2 mm depth hole is drilled in one of the bars. This intermediate-severity rotor condition is labeled as R3; (iii) Finally, a more severe rotor fault is provoked by drilling the whole rotor bar. This rotor condition is known (R5). The stator current signal is collected while the motor is operating in a steady state for 10 s with a constant load torque. During these tests, the motor slip is in the range of 3–5%, according to the motor specifications mentioned in Appendix A.

Different tests, considering the type of power supply, the state of health of the rotor, and the level at which the motor is loaded, have been developed to develop an automatic steady-state diagnosis tool.

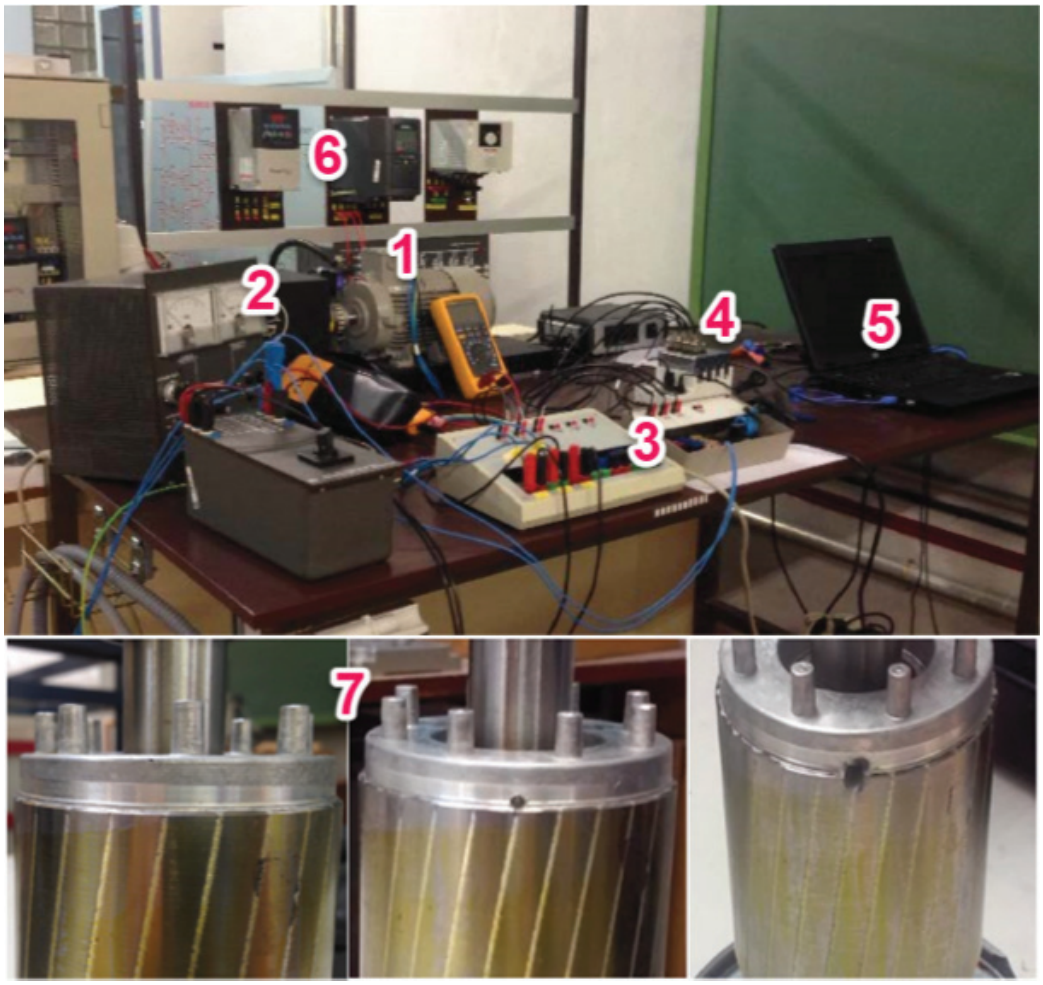


**Figure 4.** Test bench employed in this research. (1) Induction motor; (2) magnetic powder brake and load control unit (3) custom-made hall effect sensor board; (4) DAQ board; (5) laptop and software; (6) inverters; (7) simulated broken rotor bars.

## 5. Experimental Results

The diagnosis methodology begins with a feature selection stage, the training of a supervised classifier, and finally, an evaluation phase, in which the global performance of the diagnosis tool is evaluated. Table 2 shows the main characteristics of the dataset. The columns describe the voltage supply, faults severities, the imbalance ratio (IR), and the number of samples for the healthy and faulty cases, also expressed as a percentage. The last column is a label for each case.

The IR for each case is the rate between the number of healthy and faulty class instances of each rotor condition. The IRs considered in this study are those indicated in the corresponding column in Table 2. This selection of IR analyses the influence of the level of imbalance under this particular small data problem. The chosen IRs depend on the observations from the experimental trials, which are then processed to obtain the characteristic fault features or variables.

**Table 2.** Description of the experimental datasets

| Supply | Severities | Imbalance Ratio (IR) | #Samples (Healthy–Faulty) | % (Healthy–Faulty) | Case Number |
|---|---|---|---|---|---|
| Line-fed | R1–R3 | 12 | 195–15 | 92.85–07.15 | 1 |
| | R1–R3 | 7 | 105–15 | 87.50–15.50 | 2 |
| | R1–R3 | 3 | 45–15 | 75.00–25.00 | 3 |
| Line-fed | R1–R5 | 12 | 195–15 | 92.85–07.15 | 4 |
| | R1–R5 | 7 | 105–15 | 87.50–15.50 | 5 |
| | R1–R5 | 3 | 45–15 | 75.00–25.00 | 6 |
| Inverter-fed | R1–R3 | 12 | 195–15 | 92.85–07.15 | 7 |
| | R1–R3 | 7 | 105–15 | 87.50–15.50 | 8 |
| | R1–R3 | 3 | 45–15 | 75.00–25.00 | 9 |
| Inverter-fed | R1–R5 | 12 | 195–15 | 92.85–07.15 | 10 |
| | R1–R5 | 7 | 105–15 | 87.50–15.50 | 11 |
| | R1–R5 | 3 | 45–15 | 75.00–25.00 | 12 |

### *5.1. Feature Selection*

After applying the ReliefF algorithm, the feature selection results for both power supplies are shown in Figure 5. In this figure, the red dashed line is the threshold for the features selected for the classification stage. Although a threshold choice is arbitrary, this threshold is set to 0.06, representing the percentile of best-scoring features to select. The analysis of this figure provides some interesting results. The algorithm highlights more relevant features for the line supply case than the inverter-fed case. It is also noticeable what happens with the $m_3$ and $c_3$ statistics: they were the worst features in the analysis with line-fed IM data but are selected for the inverter-fed case. The loss of relevance for *Skew* in the inverter-fed IM case is also appreciable. However, as was expected, *LSH* and *RSH* are the most significant features for all power supply cases. Furthermore, the Γ features proposed in [17] do not show outstanding relevance for the diagnosis.

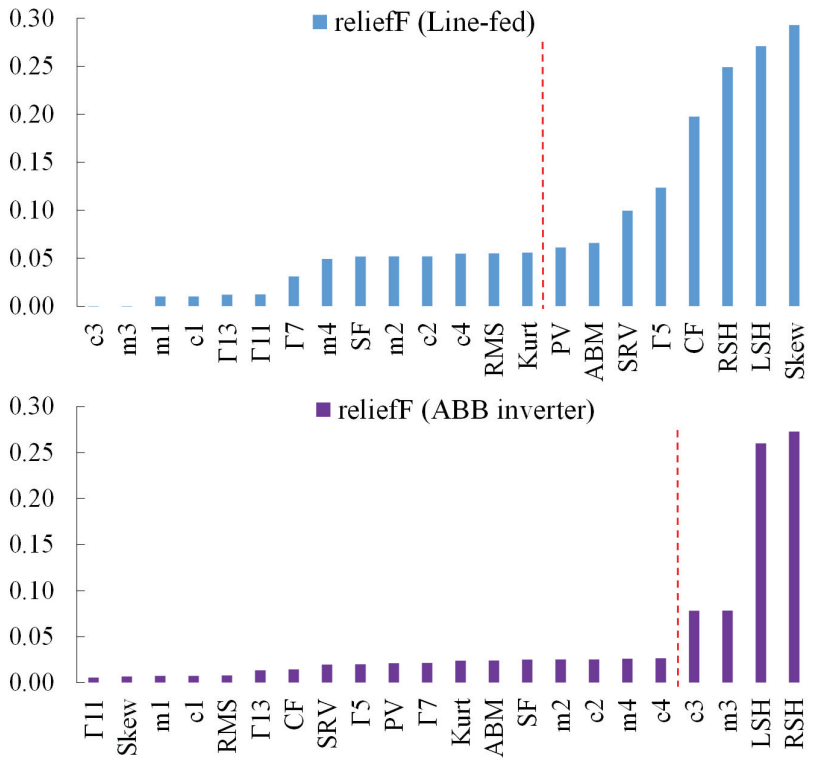


**Figure 5.** Results of the feature selection with the ReliefF algorithm: a line-fed case at the (**top**) and an inverter-fed case at the (**bottom**) of the figure.

### *5.2. Effect on the Feature Subspace*

After the feature selection stage, the IR is improved by the generation of synthetic data for the minority class using the different techniques previously described: SLSMOTE, RSLSMOTE, and MWMOTE. The balanced datasets are shown in Figures 6 and 7. The first figure is for the motor line-fed case, and the second is for the inverter-fed case. The LSH fault feature vs. the motor slip is represented in all these figures for different failure severities. The different rotor conditions are depicted as follows: healthy case (**O**); original rotor fault data (**+**); synthetic rotor fault data (**+**).

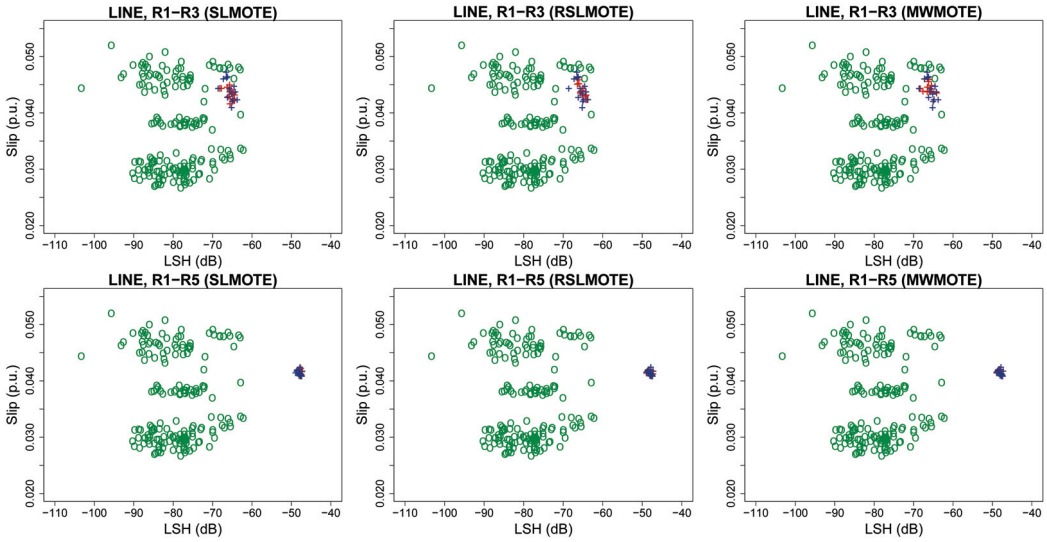


**Figure 6.** Bidimensional feature scatterplot (slip and LSH) for synthetically balanced data from line supply with the resampling techniques: Safe Level-SMOTE (SLMOTE), Relocating Safe Level SMOTE (RSLMOTE), and Majority weighted minority oversampling technique (MWMOTE). An imbalanced ratio of 12. Top figures: R3 rotor severity. Bottom figures: R5 rotor severity. The different rotor conditions are depicted as follows: healthy case (**O**); original rotor fault data (**+**); synthetic rotor fault data (**+**).

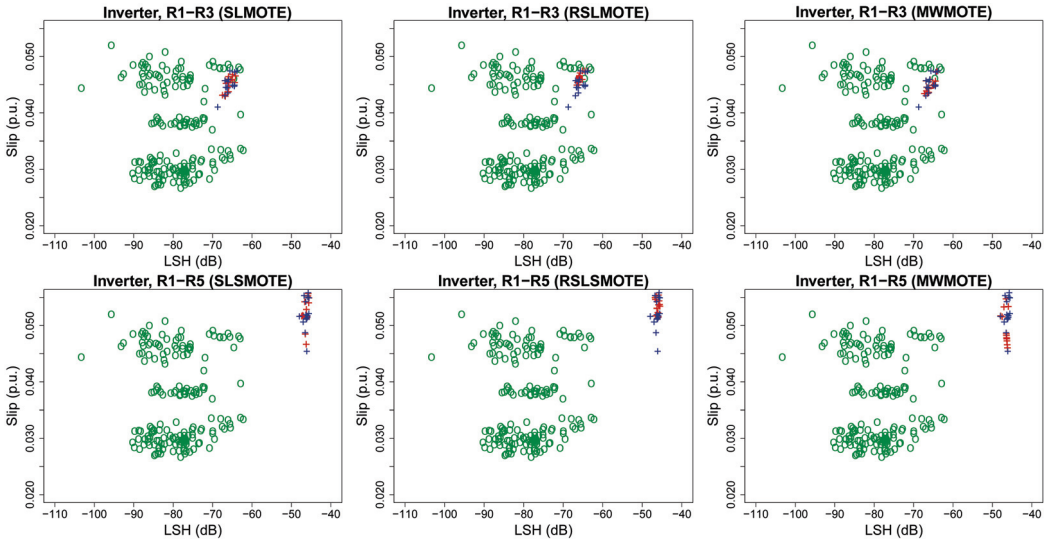


**Figure 7.** Bidimensional feature scatterplot (slip and LSH) for synthetically balanced data from inverter-based supply with the resampling techniques: Safe Level-SMOTE (SLMOTE), Relocating Safe Level SMOTE (RSLMOTE), and Majority weighted minority oversampling technique (MWMOTE). An imbalanced ratio of 12. Top figures: R3 rotor severity. Bottom figures: R5 rotor severity. The different rotor conditions are depicted as follows: healthy case (**O**); original rotor fault data (**+**); synthetic rotor fault data (**+**).

In both figures, the LSH feature is represented vs. the motor slip. In the first row, the following two-rotor conditions are represented: healthy or R1 and intermediate severity or R3. In the second row, these two conditions are plotted: healthy or R1 and fully broken bar or R5. In all cases, the healthy observations outnumber the faulty ones, producing an IR of 12.

The resampling results for each algorithm are shown with red markers for each algorithm. The synthetic data generated with the SMOTE technique for the line supply case shows dispersed decision boundaries for the two-rotor severity (R3 and R5). However, with Safe-Level SMOTE and Relocating Safe-Level SMOTE variants, this does not happen. In the inverter-fed case, the results are quite similar.

### *5.3. Classification Stage*

After balancing the datasets, three classification techniques are trained: Support Vector Machine (SVM) with Gaussian kernel as a radial basis function, Adaptive Boosting (AdaBoost), and instance-based k-nearest Neighbors (k-NN). The tuning parameters are $C = 1$ for SVM, the number of neighbours for k-NN, and SMOTE set to $k = 5$. Previously, different combinations of tuning parameters were explored during the parameter tuning procedure. The amount of oversampling is predetermined from the beginning for the imbalanced ratios indicated in Table 2.

## 6. Discussion

The twelve case studies are summarized in Table 2, while Table 3 presents the metrics used to evaluate the classification results of these cases. The performance of three classification algorithms is compared with datasets obtained after variable selection and class balancing using three oversampling algorithms. The comparison metrics were obtained through a 10-fold cross-validation process and were used for the comparative study of imbalanced classes. The metrics used for comparison are Area Under the ROC Curve (AUC) and G-mean1. AUC is derived from ROC analysis, which evaluates the performance of classifiers by plotting the True Positive Rate against the False Positive Rate while varying a score threshold. It is a scalar value representing the probability that a classifier performs better at classifying a fault instance over a healthy one, providing a single score for evaluating which algorithm is better on average. $G_{mean1}$ is used to evaluate the relative balance of classifier performance on all classes, computed as negative (Healthy) and positive (Fault):

$$G_{mean1} = \sqrt{TPR \times TNR}, \tag{10}$$

where $TPR$ and $TNR$ are True Positive Rate and True Negative Rate, respectively.

For study cases 8 and 9, the combination of MWMOTE for class balancing and the AdaBoost classifiers performs better than the rest of the oversampling algorithms and classifiers. These cases correspond to the motor fed by inverter and intermediate inverter feeding, intermediate fault severity (R3), and imbalance ratios IR = 7 and IR = 3, respectively. However, when the imbalance ratio increases, every classifier and oversampling tool performs quite similarly, i.e., no statistical significance is found in their results. The statistical significance is checked with the Holm test. This test is applied for a pairwise performance among each oversampling approach whose $p$-values are shown in Table 3. The outcome is to reject the null hypothesis when this p-value falls below a threshold. This outcome implies that the corresponding SMOTE extension is outperformed by the remaining ones. This situation is highlighted with an asterisk in the $p$-value and found that only happens for the MWMOTE approach. Studies 4–6 and 10–12 cover both power sources, the maximum fault severity (R5), and all class imbalance rates. The classification metrics obtained are good for the various combinations of oversampling techniques and classification algorithms.

**Table 3.** Classification results with feature selection and oversampling with SLSMOTE, RSLSMOTE, and MWMOTE.

| Classifier | Supply | Case Number | Severity | Imbalance Ratio (IR) | AUC (%) | *p*-Value | Gmean1 (%) |
|---|---|---|---|---|---|---|---|
| SVM | Line-fed | 1 | R3 | 12 | $97 \pm 2.55$ | 0.085 | $98 \pm 1.58$ |
| | Line-fed | 2 | R3 | 7 | $97 \pm 2.52$ | 0.251 | $97 \pm 2.63$ |
| | Line-fed | 3 | R3 | 3 | $97 \pm 1.36$ | 0.651 | $97 \pm 2.14$ |
| | Line-fed | 4 | R5 | 12 | $100 \pm 0.00$ | 0.156 | $100 \pm 0.00$ |
| | Line-fed | 5 | R5 | 7 | $100 \pm 0.00$ | 0.746 | $100 \pm 0.00$ |
| | Line-fed | 6 | R5 | 3 | $100 \pm 0.00$ | 0.365 | $100 \pm 0.00$ |
| | Inverter | 7 | R3 | 12 | $97 \pm 2.11$ | 0.711 | $97 \pm 2.77$ |
| | Inverter | 8 | R3 | 7 | $96 \pm 1.23$ | <0.01 | $97 \pm 2.98$ |
| | Inverter | 9 | R3 | 3 | $96 \pm 2.58$ | <0.01 | $97 \pm 2.73$ |
| | Inverter | 10 | R5 | 12 | $100 \pm 0.00$ | 0.411 | $100 \pm 0.00$ |
| | Inverter | 11 | R5 | 7 | $100 \pm 0.00$ | 0.709 | $100 \pm 0.00$ |
| | Inverter | 12 | R5 | 3 | $100 \pm 0.00$ | 0.177 | $100 \pm 0.00$ |
| AdaBoost | Line-fed | 1 | R3 | 12 | $97 \pm 1.23$ | 0.785 | $98 \pm 1.42$ |
| | Line-fed | 2 | R3 | 7 | $97 \pm 2.58$ | 0.150 | $97 \pm 2.40$ |
| | Line-fed | 3 | R3 | 3 | $98 \pm 1.32$ | 0.255 | $98 \pm 1.84$ |
| | Line-fed | 4 | R5 | 12 | $100 \pm 0.00$ | 0.456 | $100 \pm 0.00$ |
| | Line-fed | 5 | R5 | 7 | $100 \pm 0.00$ | 0.606 | $100 \pm 0.00$ |
| | Line-fed | 6 | R5 | 3 | $100 \pm 0.00$ | 0.865 | $100 \pm 0.00$ |
| | Inverter | 7 | R3 | 12 | $97 \pm 1.10$ | 0.545 | $97 \pm 2.66$ |
| | Inverter | 8 | R3 | 7 | $97 \pm 1.23$ | <0.01 * | $97 \pm 2.09$ |
| | Inverter | 9 | R3 | 3 | $98 \pm 2.58$ | <0.01 * | $97 \pm 2.20$ |
| | Inverter | 10 | R5 | 12 | $100 \pm 0.00$ | 0.811 | $100 \pm 0.00$ |
| | Inverter | 11 | R5 | 7 | $100 \pm 0.00$ | 0.709 | $100 \pm 0.00$ |
| | Inverter | 12 | R5 | 3 | $100 \pm 0.00$ | 0.387 | $100 \pm 0.00$ |
| k-NN | Line-fed | 1 | R3 | 12 | $97 \pm 1.02$ | 0.113 | $98 \pm 1.88$ |
| | Line-fed | 2 | R3 | 7 | $96 \pm 2.52$ | 0.852 | $97 \pm 2.81$ |
| | Line-fed | 3 | R3 | 3 | $97 \pm 2.02$ | 0.673 | $97 \pm 2.88$ |
| | Line-fed | 4 | R5 | 12 | $98 \pm 1.56$ | 0.555 | $100 \pm 0.00$ |
| | Line-fed | 5 | R5 | 7 | $100 \pm 0.00$ | 0.143 | $100 \pm 0.00$ |
| | Line-fed | 6 | R5 | 3 | $100 \pm 0.00$ | 0.861 | $100 \pm 0.00$ |
| | Inverter | 7 | R3 | 12 | $97 \pm 1.10$ | 0.219 | $97 \pm 2.97$ |
| | Inverter | 8 | R3 | 7 | $95 \pm 3.32$ | <0.01 * | $97 \pm 2.62$ |
| | Inverter | 9 | R3 | 3 | $96 \pm 3.88$ | <0.01 | $96 \pm 3.66$ |
| | Inverter | 10 | R5 | 12 | $100 \pm 0.00$ | 0.815 | $100 \pm 0.00$ |
| | Inverter | 11 | R5 | 7 | $100 \pm 0.00$ | 0.113 | $100 \pm 0.00$ |
| | Inverter | 12 | R5 | 3 | $100 \pm 0.00$ | 0.770 | $100 \pm 0.00$ |

* Outcome of the test from pairwise performance where MWMOTE outperforms the rest.

## 7. Conclusions

This article reviews and applies several resampling techniques for diagnosing rotor faults in line-fed and inverter-fed induction motors. These resampling techniques are SMOTE extensions and produce synthetic observations belonging to the minority fault class for balancing training sets and improving the synthetic data generation according to boundary area behavior.

The evaluation of the classifier performance with the metrics $AUC$ and $G_{mean1}$ metrics shows that for the highest fault severity of the broken rotor bar fault (R5), all resampling techniques considered have similar behavior, which implies that in terms of performance, any of them can obtain successful diagnostic results independent of the motor power supply and the imbalanced ratio analyzed.

Therefore, by incorporating any of these oversampling techniques into the diagnosis methodology to predict the rotor's condition, it is possible to construct a more precise and robust diagnosis of the rotor faults of inverter-powered induction motors with small and unbalanced data.

In addition, from this experimental study, the authors observed that one area of exploration is the application of these oversampling methods to more incipient rotor breakages, where the feature differences regarding the healthy class are much more reduced.

**Author Contributions:** Conceptualization, I.M.-D. and D.M.-S.; data curation, I.M.-D.; methodology, I.M.-D. and D.M.-S.; software, T.G.-C.; validation, D.M.-S. and T.G.-C.; writing—original draft, I.M.-D.; writing—reviewing and editing, D.M.-S. and Ó.D.-P. All authors have read and agreed to the published version of the manuscript.

**Funding:** This research was partially funded by the University of Valladolid.

**Institutional Review Board Statement:** Not applicable.

**Informed Consent Statement:** Not applicable.

**Data Availability Statement:** The data presented in this study are available on request.

**Acknowledgments:** The authors are grateful for the institutional support received from the University of Valladolid as well as the Department of Electrical Engineering, which has made it possible to have the necessary material and human resources, who, in one way or another, contributed to the experimental design. In addition, we would like to thank the editor and reviewers for taking the time and effort necessary to review the manuscript. We sincerely appreciate all valuable comments and suggestions, which helped us to improve the quality of the manuscript.

**Conflicts of Interest:** The authors declare no conflicts of interest.

## Abbreviations

The following abbreviations are used in this manuscript:

| | |
|---|---|
| AUC | Area Under the ROC Curve |
| BRB | Broken Rotor Bar |
| DBSMOTE | Density-Based Synthetic Minority Oversampling Technique |
| FD | Fault Data |
| HT | Holm Test |
| k-NN | k-Nearest Neighbors |
| MCSA | Motor Current Signature Analysis |
| MWMOTE | Majority weighted minority oversampling technique |
| RSLS | Relocating Safe-Level SMOTE |
| SLSMOTE | Safe-Level SMOTE |
| SMOTE | Synthetic Minority Oversampling Technique |
| SVM | Support Vector Machine |

## Appendix A. Equipment Specifications

Three-phase asynchronous squirrel cage motor (Siemens®, Munich, Germany), star connected. Nominal characteristics: power = 0.75 kW, f = 50 Hz, voltage = 400 V, current = 1.9 A, nominal speed = 1395 rpm, and the number of pole pairs is two. Three three-phase inverters from different brands were used. The first one is an ABB® (model ACS355, Zürich, Switzerland), the second one is an Allen Bradley® (model PowerFlex 40, Milwaukee, WI, USA), and the last one is a Telemecanique® (model Altivar 66, Rueil-Malmaison, France) with range power from 0.37 to 4 kW, 0.4 to 2.2 kW and 0.75 to 250 kW, respectively. The switching frequency of all inverters is 4 kHz.

## References

1. Park, Y.; Jeong, M.; Bin Lee, S.; Teska, M.; Antonino-Daviu, J.A. Influence of Blade Pass Frequency Vibrations on MCSA-Based Rotor Fault Detection of Induction Motors. *IEEE Trans. Ind. Appl.* **2017**, *53*, 2049–2058. [CrossRef]
2. Zhou, Z.J.; Hu, C.H.; Wang, W.B.; Zhang, B.C.; Xu, D.L.; Zheng, J.F. Condition-based maintenance of dynamic systems using online failure prognosis and belief rule base. *Expert Syst. Appl.* **2012**, *39*, 6140–6149. [CrossRef]
3. Pons-Llinares, J.; Antonino-Daviu, J.; Roger-Folch, J.; Morinigo-Sotelo, D.; Duque-Perez, O. Mixed eccentricity diagnosis in Inverter-Fed Induction Motors via the Adaptive Slope Transform of transient stator currents. *Mech. Syst. Signal Process.* **2014**, *48*, 423–435. [CrossRef]

4. Benbouzid, M.E.H. A review of induction motors signature analysis as a medium for faults detection. *IEEE Trans. Ind. Electron.* **2000**, *47*, 984–993. [CrossRef]
5. Cunha Palacios, R.; Da Silva, I.; Goedtel, A.; Godoy, W. A comprehensive evaluation of intelligent classifiers for fault identification in three-phase induction motors. *Electr. Power Syst. Res.* **2015**, *127*, 249–258. [CrossRef]
6. Prieto, M.D.; Cirrincione, G.; Espinosa, A.G.; Ortega, J.A.; Henao, H. Bearing fault detection by a novel condition-monitoring scheme based on statistical-time features and neural networks. *IEEE Trans. Ind. Electron.* **2013**, *60*, 3398–3407. [CrossRef]
7. Ghate, V.N.; Dudul, S.V. Cascade neural-network-based fault classifier for three-phase induction motor. *IEEE Trans. Ind. Electron.* **2011**, *58*, 1555–1563. [CrossRef]
8. Gonzalez-Jimenez, D.; del Olmo, J.; Poza, J.; Garramiola, F.; Madina, P. Data-Driven Fault Diagnosis for Electric Drives: A Review. *Sensors* **2021**, *21*, 4024. [CrossRef]
9. Gonzalez-Jimenez, D.; Del-Olmo, J.; Poza, J.; Garramiola, F.; Madina, P. Data-Driven Low-Frequency Oscillation Event Detection Strategy for Railway Electrification Networks. *Sensors* **2023**, *23*, 254. [CrossRef]
10. Gonzalez-Jimenez, D.; del Olmo, J.; Poza, J.; Garramiola, F.; Sarasola, I. Machine Learning-Based Fault Detection and Diagnosis of Faulty Power Connections of Induction Machines. *Energies* **2021**, *14*, 4886. [CrossRef]
11. Martin-Diaz, I.; Morinigo-Sotelo, D.; Duque-Perez, O.; Romero-Troncoso, R.J. Early fault detection in induction motors using AdaBoost with imbalanced small data and optimized sampling. *IEEE Trans. Ind. Appl.* **2016**, *53*, 3066–3075. [CrossRef]
12. Niu, G.; Dong, X.; Chen, Y. Motor Fault Diagnostics Based on Current Signatures: A Review. *IEEE Trans. Instrum. Meas.* **2023**, *72*, 1–19. [CrossRef]
13. Rivera, W.A. Noise Reduction A Priori Synthetic Over-Sampling for class imbalanced data sets. *Inform. Sci.* **2017**, *408*, 146–161. [CrossRef]
14. Zhang, T.; Chen, J.; Li, F.; Zhang, K.; Lv, H.; He, S.; Xu, E. Intelligent fault diagnosis of machines with small & imbalanced data: A state-of-the-art review and possible extensions. *ISA Trans.* **2022**, *119*, 152–171. [CrossRef] [PubMed]
15. Kliman, G.; Stein, J. Methods of motor current signature analysis. *Electr. Mach. Power Syst.* **1992**, *20*, 463–474. [CrossRef]
16. Martin-Diaz, I.; Morinigo-Sotelo, D.; Duque-Perez, O.; Delgado-Arredondo, P.; Camarena-Martinez, D.; Romero-Troncoso, R. Analysis of various inverters feeding induction motors with incipient rotor fault using high-resolution spectral analysis. *Electr. Power Syst. Res.* **2017**, *152*, 18–26. [CrossRef]
17. Bruzzese, C. Analysis and Application of Particular Current Signatures (Symptoms) for Cage Monitoring in Nonsinusoidally Fed Motors With High Rejection to Drive Load, Inertia, and Frequency Variations. *IEEE Trans. Ind. Electron.* **2008**, *55*, 4137–4155. [CrossRef]
18. Robnik-Sikonja, M.; Kononenko, I. Theoretical and empirical analysis of ReliefF and RReliefF. *Mach. Learn.* **2003**, *53*, 23–69. [CrossRef]
19. Kononenko, I.; Robnik-Sikonja, M.; Pompe, U. *ReliefF for Estimation and Discretization of Attributes in Classification, Regression, and ILP Problems*; IOS Press: Amsterdam, The Netherlands, 1996; Volume 35.
20. Murcia-Sepúlveda, N.; Cruz-Duarte, J.M.; Martin-Diaz, I.; Garcia-Perez, A.; Rosales-García, J.J.; Avina-Cervantes, J.G.; Correa-Cely, C.R. Fractional Calculus-Based Processing for Feature Extraction in Harmonic-Polluted Fault Monitoring Systems. *Energies* **2019**, *12*, 3736. [CrossRef]
21. Chawla, N.V.; Bowyer, K.W.; Hall, L.O.; Kegelmeyer, W.P. SMOTE: Synthetic minority over-sampling technique. *J. Artif. Intell. Res.* **2002**, *16*, 321–357. [CrossRef]
22. Bunkhumpornpat, C.; Sinapiromsaran, K.; Lursinsap, C. Safe-Level-SMOTE: Safe-Level-Synthetic Minority Over-Sampling TEchnique for Handling the Class Imbalanced Problem. In Proceedings of the Advances in Knowledge Discovery and Data Mining, Bangkok, Thailand, 27–30 April 2009; Theeramunkong, T., Kijsirikul, B., Cercone, N., Ho, T.B., Eds.; Springer: Berlin/Heidelberg, Germany, 2009; pp. 475–482.
23. Siriseriwan, W.; Sinapiromsaran, K.; Tipawanna, M.; Bunkhumpornpat, C.; Keatruangkamala, K. The effective redistribution for imbalance dataset: Relocating Safe-level SMOTE with minority outcast handling. *Chiang Mai J. Sci.* **2016**, *43*, 1288–1300.
24. Barua, S.; Islam, M.M.; Yao, X.; Murase, K. MWMOTE—Majority weighted minority oversampling technique for imbalanced data set learning. *IEEE Trans. Knowl. Data Eng.* **2014**, *26*, 405–425. [CrossRef]


**Disclaimer/Publisher's Note:** The statements, opinions and data contained in all publications are solely those of the individual author(s) and contributor(s) and not of MDPI and/or the editor(s). MDPI and/or the editor(s) disclaim responsibility for any injury to people or property resulting from any ideas, methods, instructions or products referred to in the content.

*applied sciences*

MDPI

*Article*

# Quaternion Signal Analysis for Detection of Broken Rotor Fault Degrees in Induction Motors

**Jose Luis Contreras-Hernandez *, Dora Luz Almanza-Ojeda, Rogelio Castro-Sanchez and Mario Alberto Ibarra-Manzano**

Telematics and Digital Signal Processing Research Groups (CAs), Electronics Engineering Department, DICIS, University of Guanajuato, Salamanca 36885, Mexico; dora.almanza@ugto.mx (D.L.A.-O.); castro@ugto.mx (R.C.-S.); ibarram@ugto.mx (M.A.I.-M.)
* Correspondence: jose.contreras@ugto.mx; Tel.: +52-464-647-9940

**Abstract:** Fault detection in induction motors is essential for maintaining the reliability of industrial operations. In practical applications, induction motors experience gradual wear on critical components, such as rotor bars, affecting their performance. This paper introduces a new methodology for modeling predictive wear functions related to rotor faults in induction motors, providing accurate forecasts and optimal performance through Quaternion Signal Analysis in the time domain. Our approach accurately detects wear in broken rotor bars and anticipates their degradation over time. The methodology involves coupling four vibration signals from the motor, representing them as quaternion coefficients, and calculating their rotational attributes to derive a statistical mean. We employ polynomial and Fourier regression techniques to construct a predictive wear function. We assess its accuracy through root mean square error (RMSE) analysis, which improves with increased sample size and regression complexity. Our findings indicate that polynomial regression, particularly at the second degree, achieves superior RMSE results compared to Fourier regression, even within limited sample windows. This approach offers a robust framework for early fault detection and wear prediction in induction motors, supporting enhanced maintenance strategies.

**Keywords:** bar quantification; induction motor fault; QSA; quaternions; regression

## 1. Introduction

Induction motors are important electric machines in industry processes and must be kept in optimal operation. Signal analysis techniques are essential for early fault detection in rotating machinery, helping to prevent unexpected downtime, economic losses, and potential major failures [1,2]. Common faults in induction motors include bearing defects [3], stator winding failures, air-gap eccentricity, unbalanced bars, and broken rotor bar (BRB) faults [4]. BRB faults are particularly significant in the literature due to their high risk of causing additional damage [5]. Numerous methodologies have been developed to detect or characterize BRB faults, focusing on spectral analysis, machine learning, and statistical approaches [6].

Spectral analysis methods involve extensive data processing and are primarily oriented toward fault detection and classification. Fourier and wavelet transforms are methodologies in spectral analysis valued for their ability to associate specific signal frequencies with BRB faults. In addition, studies in the literature often integrate statistical analysis into spectral techniques to enhance fault detection accuracy, as in [7], where a methodology combining the digital Taylor–Fourier transform (DTFT) with variance analysis effectively identified

rotor bar wear across states ranging from healthy to BRB. In wavelet algorithms, the authors of [8] successfully classified multiple BRB faults by extracting statistical features directly from raw signals using advanced techniques such as Matching Pursuit (MP) and Discrete Wavelet Transform (DWT). Moreover, several studies leverage machine learning methods like k-Nearest Neighbor (KNN) and support vector machines (SVMs) for BRB classification. For instance, the approach in [9] integrates Discrete Wavelet Transform (DWT) with these machine learning algorithms to achieve robust multi-class BRB classifications.

Recently, there has been a surge of interest in utilizing machine learning and deep learning techniques for fault detection in induction motors. This trend reflects these approaches' proven accuracy and efficiency in identifying and diagnosing faults, marking significant progress in predictive maintenance [6]. Specifically, for BRB fault detection using time-domain signals, studies such as [10] have explored various machine learning algorithms—including fuzzy ARTMAP networks, SVM, KNN, and Multilayer Perceptron (MLP) networks—without requiring prior domain knowledge. This adaptability underscores the capability of machine learning methods to capture complex patterns related to BRB faults. Additionally, ref. [11] presents an innovative algorithm that classifies BRB conditions by applying statistical metrics derived from motor vibration signals, such as kurtosis, skewness, and variance. These metrics are then processed through classifiers like Naive Bayes, MLP, SVM, and Optimum-Path Forest, further demonstrating the efficacy of machine learning in accurate BRB fault classification. In [12], homogeneity and kurtosis metrics were employed to classify motor conditions, from healthy states to the presence of two BRBs, using a backpropagation artificial neural network. This approach demonstrates the power of neural networks in identifying complex data patterns and accurately diagnosing motor faults. Similarly, ref. [13] leveraged stator current signals to obtain comprehensive two-dimensional insights into BRB severity across time and frequency domains, calculating entropy at various load levels to assess fault impact. Conversely, in [14], the authors proposed a degradation model for BRB faults by applying principal component analysis (PCA). Using raw torque, stator current, and speed signals, they estimated the remaining useful life of the BRBs, highlighting PCA's utility in modeling the degradation process.

The works presented above classify BRB using methods that involve a certain level of complexity and require significant computational resources. Utilizing quaternions could simplify this process, as they provide a unique mathematical framework because they are an extension of complex numbers, consisting of a real part and a three-dimensional vector of imaginary components [15]. This distinctive configuration has spurred interest across various fields, revealing quaternions' versatility and potential in advanced applications. For example, in image processing, quaternions have been shown to facilitate image enhancement and manipulation in ways that surpass conventional methods [16], offering new data representation and transformation possibilities. In robotic motion tracking, as detailed in [17], quaternions provide a sophisticated framework for accurately monitoring and controlling robot movement, delivering the precision essential for executing complex tasks. In control systems, quaternions are equally valuable, enabling the design of robust control mechanisms with high accuracy and reliability [18]. The versatility of quaternions in various domains highlights their impact on advancing technological innovation. In spectral analysis, quaternions have been effectively combined with the Fourier Transform, as demonstrated in [19], to perform comprehensive spectral analysis of three-phase currents in induction motors, achieving a bearing fault classification accuracy of approximately 94.2%. Likewise, in [20], researchers developed the Quaternion Empirical Wavelet Transform (QEWT) based on the Quaternion Fourier Transform to diagnose outer ring, inner ring, and rolling bearing faults, illustrating quaternions' capability in high-precision fault detection.

We have demonstrated the versatility of quaternions in previous works as [21,22], where we employed Quaternion Signal Analysis (QSA) to detect multiple faults and their combinations in induction motors. This methodology involves rotating quaternion signals and performing statistical analyses, calculating mean, variance, kurtosis, skewness, standard deviation, root mean square, and shape factor. Subsequently, machine learning techniques are applied to classify various fault conditions and combinations. This approach highlights the effectiveness of QSA in capturing and classifying complex fault patterns. Similarly, the QSA was used in [23] to diagnose short-circuit damage in transformer windings demonstrating that this method is not exclusive to classifying faults in induction motors. QSA has shown high accuracy in fault classification through simple mathematical operations in the time domain, even using four statistical values from three-phase currents as in [24], where four levels of inter-turn short circuit faults per phase and healthy states were classified.

On the other hand, regression methods utilize statistical processes to model relationships between variables, providing simplicity and low computational costs, especially with polynomial regressions. Furthermore, techniques like Fourier regressions can improve the effectiveness of stepped models. Studies have introduced methodologies for modeling predictive wear functions capable of quantifying BRB faults providing accurate forecasts and optimal performance as in [25]. In this, the authors present regression-based methods to evaluate BRB degradation using curve-fitting techniques such as linear, polynomial, and least squares regression with a power law. The method utilizes fault sideband parameters from the current spectrum, machine rating, and load torques of 50%, 75%, and 100% to gauge BRB severity levels from one to six, providing a structured model for fault severity assessment.

As BRB faults in induction motors develop gradually, establishing an effective model to predict future behavior with straightforward calculations becomes crucial. This approach not only helps prevent severe damage but also ensures timely maintenance, safeguarding your equipment and investment. Our method combines QSA with statistical feature analysis and polynomial and Fourier regressions to deliver reliable, practical predictive wear functions for motor maintenance. The proposed method utilizes four vibration signals with 29,999 samples measured from an induction motor operating at steady state and full load (100%): tangential mechanical vibration speed in the housing ($V_h$), axial mechanical vibration speed on the driven side ($V_a$), radial mechanical vibration speed on the non-driven side ($V_s$), and radial mechanical vibration speed on the driven side ($V_d$). The use of four signals to adapt them to the quaternions allows us to analyze different elements of the motor in various axes. This approach allows us to cover more variables, which may reflect the characteristics of the analyzed failures. However, a disadvantage of using quaternions is that they require four signals, which means that it is necessary to use at least two or more sensors. Not all databases have access to this number of sensors, which can limit the analysis. The method is evaluated across motor conditions ranging from healthy states to one, two, and three BRB faults, demonstrating its effectiveness in fault quantification and progression tracking.

This paper is structured into four sections: Section 1 introduces BRB fault detection. Section 2 describes the background of QSA and statistical methodology. Section 3 presents and discusses the results, comparing the results of polynomial and Fourier regressions. Finally, Section 4 presents conclusions and future work.

## 2. Methodology

As BRB faults in induction motors develop gradually, establishing an effective model to predict future behavior with straightforward calculations becomes crucial. This approach

not only helps prevent severe damage but also ensures timely maintenance, safeguarding your equipment and investment. By modeling quaternion-based statistical features, the proposed method characterizes BRB through predictive wear functions from a healthy motor state to three BRBs. Unlike traditional approaches that provide only discrete fault levels, this model enables a continuous fault severity assessment. The algorithm comprises two main stages: (1) the Quaternion Signal Analysis (QSA) method and (2) the fitting and evaluation procedures. Figure 1 illustrates the method's flowchart for detecting BRB severity, utilizing four vibration signals as input. Each stage of the method, as shown in Figure 1, is detailed in the following subsections.

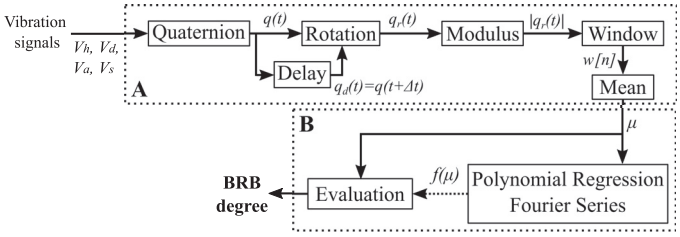


**Figure 1.** Proposed workflow diagram. (**A**) QSA method. (**B**) Fitting and evaluation procedures.

### *2.1. QSA Method*

Quaternions model the three-dimensional movements of a point in space. In a complementary way, the QSA method allows modeling the signals that generate the movements, facilitating a multidimensional analysis adapted to spatial and temporal problems. This approach detects spatial signatures using quaternion arithmetic and temporal signatures by estimating statistical displacement models. Combining both elements enables the method to achieve greater precision and robustness in fault detection than the classic techniques.

This section outlines the methodology for defining quaternion signals and calculating their rotations. Subsequently, our approach computes modulus and statistical measures based on these rotations. The quaternion $q$ is constructed as shown in (1), using the coefficients $q_0$, $q_1$, $q_2$, and $q_3$ [26].

$$q = q_0 + q_1 i + q_2 j + q_3 k \tag{1}$$

The quaternion signal $q(t)$ shown in section A of Figure 1 is constructed from the vibration signals $V_h(t)$, $V_d(t)$, $V_a(t)$, and $V_s(t)$, as formulated in (2). Signals $V_h(t)$, $V_d(t)$, and $V_a(t)$ were chosen to assess vibrations along the $x$-, $y$-, and $z$-axes of the induction motor, while $V_s(t)$ provides insight into rear motor vibrations. By selecting signals from different motor sections, our methodology enables a more comprehensive analysis, as Quaternion Signal Analysis (QSA) integrates the distinct characteristics of each signal. The vibration signals are represented discreetly with a total of 29,999 samples.

$$q(t) = V_h(t) + V_d(t)i + V_a(t)j + V_s(t)k \tag{2}$$

Then, the shifted quaternion signal $q_d(t)$ is obtained by the displacement of $\Delta t$ samples in $q(t)$. Equation (3) presents the equality [22].

$$q_d(t) = q(t + \Delta t) \tag{3}$$

The coefficients $V_{hd}$, $V_{dd}$, $V_{ad}$, and $V_{sd}$ form the quaternion $q_d(t)$ shown in Figure 1 with 29,998 samples, as defined in (4). These coefficients are the vibration coefficients $V_h$, $V_d$, $V_a$, and $V_s$ in $t + \Delta t$.

$$q_d(t) = V_{hd}(t) + V_{dd}(t)i + V_{ad}(t)j + V_{sd}(t)k \tag{4}$$

A quaternion model can represent the transition from a current quaternion sample, $q$, to a delayed quaternion sample, $q_d$. This means that we can identify the quaternion model that enables $q$ to achieve the values of $q_d$ through quaternion rotation operations, as illustrated in Figure 2.

Rotation quaternions represent three-dimensional rotations and they are related to the axis and angle. Based on Euler's rotation theorem, any rotation can be defined using unit vectors $\hat{x}, \hat{y}$, and $\hat{z}$ and angle $\theta$. The axis-angle components can be converted into components of a rotation quaternion $q_r$ by Equations (5)–(8).

$$q_{r0} = \cos\left(\frac{\theta}{2}\right) \tag{5}$$

$$q_{r1} = \hat{x}\sin\left(\frac{\theta}{2}\right) \tag{6}$$

$$q_{r2} = \hat{y}\sin\left(\frac{\theta}{2}\right) \tag{7}$$

$$q_{r3} = \hat{z}\sin\left(\frac{\theta}{2}\right) \tag{8}$$

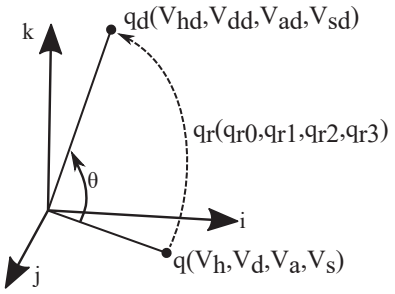


**Figure 2.** Rotation of $q(t)$ to obtain $q_d(t)$.

The above-mentioned process generates a rotated quaternion for each sample and its corresponding delayed value. This operation is applied to all samples of the signals to characterize the rotational behavior of the signal over time.

Taking into account the above described, $q$ and $q_d$ are algebraically related by (9) [21], where $q_r^{-1}$ is the inverse of rotation quaternion.

$$q_d = q_r \otimes q \otimes q_r^{-1} \tag{9}$$

The operator $\otimes$ refers to the Hamilton product which is described as in (10).

$$\begin{aligned} q_r \otimes q = {} & (q_{r0}V_h - q_{r1}V_d - q_{r2}V_a - q_{r3}V_s) \\ & +(q_{r0}V_d + q_1 V_h + q_{r2}V_s - q_{r3}V_a)i \\ & +(q_{r0}V_a - q_1 V_s + q_{r2}V_h - q_{r3}V_d)j \\ & +(q_{r0}V_s + q_1 V_a - q_{r2}V_d + q_{r3}V_h)k. \end{aligned} \tag{10}$$

By the properties of quaternions, the relation of $q_r$, $q_d$, and $q$ can be written as (11) [23].

$$q_d(t) = q_r(t) \cdot q(t) \tag{11}$$

This means that if we know the values of $q$ and $q_d$, we can obtain $q_r$ through the product of general rotation matrix and $q$ presented in (12) [21] using the coefficients values

shown in (2) and (4). This value contains the two-sample quaternion model, which helps us obtain statistical values of multiple models to quantify BRBs later.

$$q_r = \begin{bmatrix} 1-2V_{ad}^2-2V_{sd}^2 & 2(V_{dd}V_{ad}+V_{hd}V_{sd}) & 2(V_{dd}V_{sd}-V_{hd}V_{ad}) \\ 2(V_{dd}V_{ad}-V_{hd}V_{sd}) & 1-2V_{dd}^2-2V_{sd}^2 & 2(V_{ad}V_{sd}+V_{hd}V_{dd}) \\ 2(V_{dd}V_{sd}+V_{hd}V_{ad}) & 2(V_{ad}V_{sd}-V_{hd}V_{dd}) & 1-2V_{dd}^2-2V_{ad}^2 \end{bmatrix} \begin{bmatrix} V_d \\ V_a \\ V_s \end{bmatrix} \tag{12}$$

Next, we compute and organize the rotational models for the signal based on the pure quaternion $q_r(t)$ as defined in (13) [23]. Here, $q_{r0}$ is set to zero, reflecting that the rotation is confined to the three-dimensional space of the imaginary components.

$$q_r(t) = q_{r1}(t)i + q_{r2}(t)j + q_{r3}(t)k \tag{13}$$

We have vibration signals containing 29,999 samples, and the quaternion $q_r$ is calculated for each sample with the next one, resulting in 29,998 pure quaternions. After this, we calculate the modulus of each quaternion using Equation (14), which generates a constant value for each one.

$$|q_r| = \sqrt{q_{r1}^2 + q_{r2}^2 + q_{r3}^2} \tag{14}$$

Using these values of consecutive models from $q_r(t)$, we can assemble a vector **w**[n] by selecting $N$ samples from the signals as in (15) [15], where $t + N\Delta t$ refers to the sample of the rotation obtained.

$$\mathbf{w}[n] = [|q_r(t)|, |q_r(t+\Delta t)|, |q_r(t+2\Delta t)| \ldots |q_r(t+N\Delta t)|] \tag{15}$$

Statistical analysis of **w**[n] is essential for quantitatively characterizing the models and defining diagnostic value ranges for each BRB condition. Following the workflow in Figure 1, the mean ($\mu$) was selected as the statistical measure with the best-fitting performance. The mean of **w**[n] reflects the evolution of signals over time and is calculated according to (16).

$$\mu = \frac{1}{N}\sum_{n=1}^{N} \mathbf{w}[n] \tag{16}$$

Each test file for each BRB condition contains 29,999 samples, providing 29,998 moduli of $q_r(t)$. The window **w**[n] utilizes $N$ values from these 29,998 moduli to compute $\mu$. By shifting the window **w**[n] across the test file, multiple values of $\mu$ can be calculated. This approach enables calculating and evaluating polynomial and Fourier models that describe BRB behavior, as shown in Section 2 of Figure 1.

### *2.2. Fitting and Evaluation*

The values of $\mu$ are derived from test files corresponding to a healthy motor, one BRB, two BRBs, and three BRBs to model the function $f(\mu)$ using polynomial regression and Fourier series. This function quantitatively assesses the BRB damage level in the induction motor. Polynomial regressions and the Fourier series were calculated in the second to ninth order, which is the range supported by Matlab's function capabilities. Results from the second to sixth order are presented, as higher-order fits produce similar algebraic expressions and accuracy, making them unnecessary for further consideration.

The remaining files are evaluated in $f(\mu)$ by calculating $\mu$ to determine the extent of BRB damage. Figure 3 displays the fitted functions generated through polynomial and Fourier series methods, comparing these fitted functions with the actual data samples. The boxplot graphs present position results from one file for each fault state, analyzed

using a fitted function. They distinctly showcase the minimum and maximum values, as well as the mean, providing clear insights into the data. As anticipated, the estimated curves closely align with the observed data, achieving the accuracy required for reliable damage assessment.

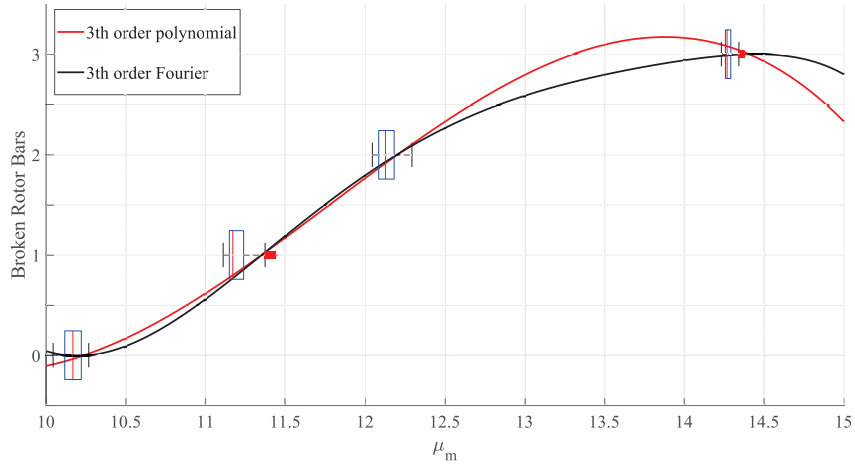


**Figure 3.** Polynomial and Fourier regressions.

### *2.3. Experimental Setup*

Our work is tested with a dataset of the workbench presented in [27] to validate its effectiveness. The experimental setup, illustrated in Figure 4, includes a three-phase induction motor and a direct current machine acting as a generator to simulate load torque. They are connected by a shaft with a rotary torque wrench. Additionally, various sensors are connected at different locations within the setup.

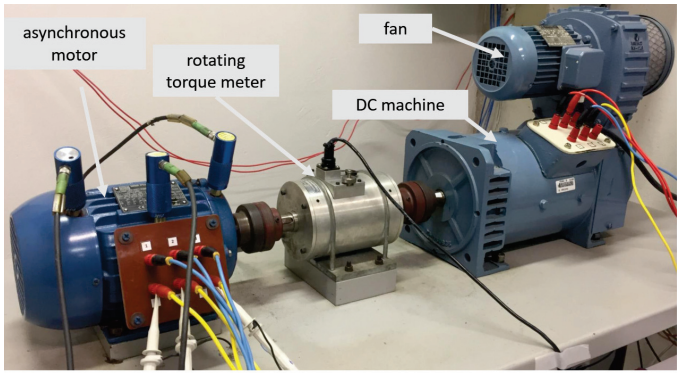


**Figure 4.** Experimental setup of the induction motor with one, two, and three BRBs [27].

The workbench consists of vibration, current, and voltage measurements from which we selected four vibration measurements. These are taken from various induction motor parts to analyze its mechanical behavior. This analysis enables the adaptation of four signals into a quaternion format. In past studies [22,23], a combination of current and mechanical vibration signals was utilized due to a scarcity of signals. However, this work aims to use signals of the same type for a more consistent analysis.

These four signals are acquired by four vibrocontrol uniaxial accelerometers model PU2001, located on the housing, on the driven side, and on the non-driven side to obtain tangential, radial, and axial vibration. The sensors present a sensitivity of 10 mV/mm/s, with a frequency range from 5 to 2000 Hz. The data acquisition system utilized in the experimental setup is a National Instruments (Austin, TX, USA) data acquisition card, model NI DAQmx PCIe-6259. This card features 32 analog input channels, each with a

resolution of 16 bits and an acquisition rate of 1.25 MHz. Additionally, it includes four channels of 16-bit analog output, operating at a speed of 2.8 MHz, and 48 digital I/O channels capable of functioning at a clock frequency of up to 10 MHz.

The signals $V_h$, $V_d$, $V_a$, and $V_s$ are acquired from a three phase induction motor of the W22 standard line from manufacturer WEG, with 1 hp, 220 V/380 V, 3.02 A/1.75 A, four poles, 34 rotor bars in the squirrel cage rotor, a rated speed of 1715 rpm, and a nominal torque of 4.1 Nm. The database includes two additional vibration signals. These signals were tested using various combinations, but the resulting statistics were insufficient for proper characterization. Therefore, the signals that yielded the best results were those recorded from the engine chassis. Different directional measurements were selected to enhance the results. The placement of the sensors and the orientation of the signals are shown in Figure 5.

The induction motor is driven by a control panel, for which the type of drive can be selected as star or triangle, and the type of supply as direct mains voltage or via a three-phase inverter. A shaft containing a rotary torque wrench Transtec model MT-103 (Arlington, VA, USA) connects the motor with a direct-current machine, simulating the load in the motor of 100% of full load in all tests.

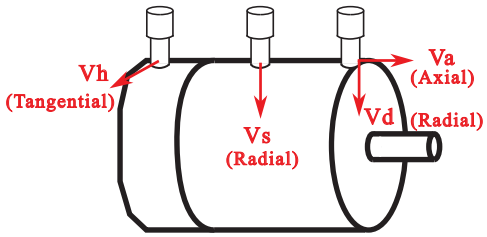


**Figure 5.** The position of the sensors and the orientation of the signals.

The workbench shows between one and four adjacent rotor bar failures caused by 6 mm diameter drilling in the squirrel cage rotor to ensure that the rotor bar was completely drilled alongside the healthy state by means of a bench drill mounted with the tip centered at half the longitudinal length of the rotor, as is shown in Figure 6.

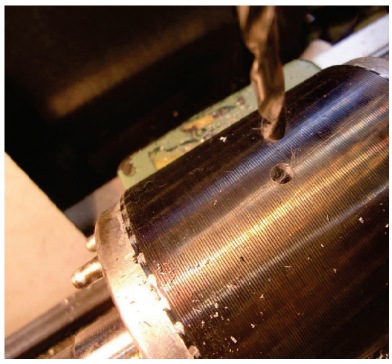

**Figure 6.** Provoked BRB drilling [27].

We selected the sets of healthy and from one to three BRBs because they presented a gradual increase in the results, while the four BRB states provoked regressions with instability.

The dataset presents ten repetitions of each state acquired during 18 s with a sample rate of 8.326 kHz. We selected thirty thousand samples in a steady state of the four vibration signals to test.

## 3. Results

In the experimental tests, a random test file from each rotor state was selected to create a sub-workbench for calculating $f(\mu_w)$. Our method then adapts one sample from each of the four vibration signals to construct the current quaternion $q(t)$ and determines the rotation $q_r(t)$ based on the previous quaternion sample $q_d(t)$, as shown in (12). By calculating the modulus of $q_r(t)$ for each delayed quaternion sample, we obtain a total of 29,999 samples.

Multiple shifted windows $\boldsymbol{w}[n]$—utilizing 4000, 6000, 8000, 10,000, 12,000, 14,000, and 20,000 samples—are employed to calculate the mean ($\mu$) for each window, forming a function $f(\mu)$ that characterizes fault behavior. This model function is then evaluated on the remaining test files (excluding those used in model formation). The dispersion of data points around the fitted function can be measured by root mean square error (RMSE), allowing us to evaluate how closely the data are concentrated around the fitted function [28]. We consider this measurement to be a metric to record the joint accuracy of our method across different rotor states. The process is repeated forty times using the original dataset with polynomial regression and Fourier series. The mean RMSE values from these forty trials are analyzed across polynomial orders from second to sixth.

Figure 7 shows the average of the RMSE values obtained from the forty tests, with the different window samples tested along with multiple orders of the predictive wear functions. Analyzing the graph mentioned above, it is observed that as window size increases, the mean RMSE values remain relatively stable for each polynomial order, indicating that sample size has minimal impact on the efficiency of our method at a given order.

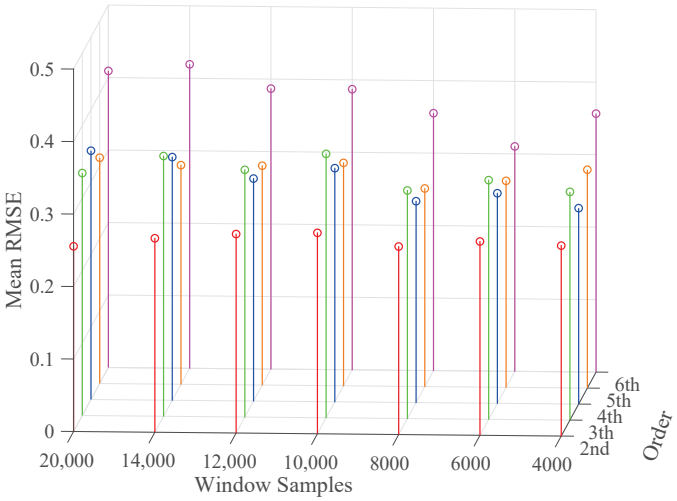


**Figure 7.** Mean RMSE behavior with polynomial modeling.

Table 1 presents the average of the RMSE for each window size and polynomial order, along with the minimum and maximum RMSE values across repetitions. The lowest average of the RMSE observed is 0.256, achieved with 20,000 window samples in the second order, though a comparable result is obtained with 8000 samples, yielding a mean RMSE of 0.259 in the same order. In the sixth order, mean RMSE increases in all cases due to a broader spread in minimum and maximum values. Polynomial regression demonstrates consistent behavior, largely unaffected by sample size or polynomial order.

Similarly, we calculated the mean of forty RMSE results to examine the behavior of the Fourier series as a regression method, ranging from the second to the sixth order. Figure 8 illustrates these results, showing that the method's efficiency is impacted by sample size,

particularly from the fourth to the sixth order. While the Fourier series modeling displays consistent behavior at lower orders, its performance varies as the order increases.

**Table 1.** Mean, minimum, and maximum RMSE in each order using polynomial modeling.

| Window Samples | Order 2 | 3 | 4 | 5 | 6 |
|---|---|---|---|---|---|
| | *Mean (min, max)* | *Mean (min, max)* | *Mean (min, max)* | *Mean (min, max)* | *Mean (min, max)* |
| 4000 | 0.263 (0.22, 0.39) | 0.315 (0.22, 0.47) | 0.270 (0.17, 0.47) | 0.301 (0.20, 0.56) | 0.357 (0.17, 1.29) |
| 6000 | 0.267 (0.21, 0.34) | 0.330 (0.21, 0.66) | 0.290 (0.19, 0.56) | 0.285 (0.18, 0.66) | 0.310 (0.15, 0.66) |
| 8000 | 0.259 (0.22, 0.32) | 0.315 (0.20, 0.80) | 0.278 (0.17, 0.74) | 0.273 (0.17, 0.68) | 0.355 (0.17, 0.88) |
| 10,000 | 0.277 (0.22, 0.47) | 0.364 (0.21, 0.78) | 0.322 (0.18, 0.79) | 0.308 (0.18, 0.65) | 0.387 (0.15, 1.41) |
| 12,000 | 0.274 (0.22, 0.47) | 0.341 (0.21, 0.83) | 0.307 (0.18, 0.85) | 0.303 (0.18, 0.68) | 0.387 (0.18, 1.08) |
| 14,000 | 0.268 (0.21, 0.50) | 0.359 (0.20, 0.71) | 0.335 (0.19, 0.76) | 0.302 (0.18, 0.59) | 0.419 (0.14, 0.93) |
| 20,000 | 0.256 (0.21, 0.43) | 0.334 (0.20, 0.81) | 0.343 (0.17, 0.86) | 0.312 (0.18, 0.79) | 0.409 (0.17, 0.96) |

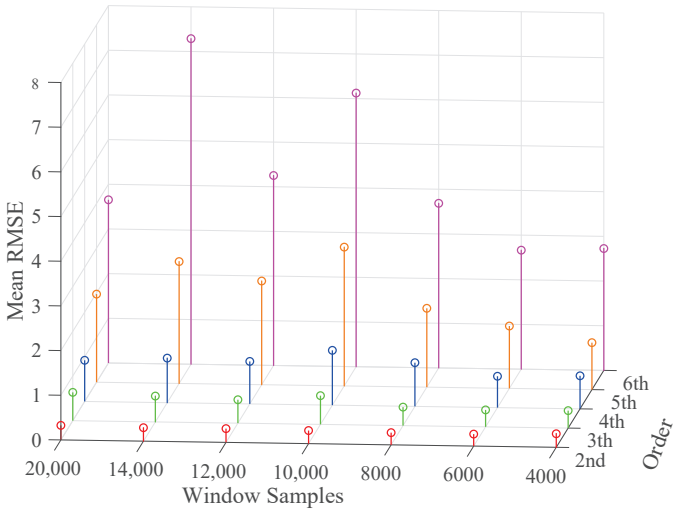


**Figure 8.** Mean RMSE behavior with Fourier series modeling.

Table 2 presents the mean RMSE for each window size and modeling order, along with the minimum and maximum RMSE values across forty repetitions. The lowest mean RMSE observed in the table is 0.268, achieved with 6000 window samples in the second order. It has been observed that the difference between the minimum and maximum values of orders is greater than the fourth order increases when using Fourier series modeling. Additionally, the average values of the RMSE for these orders change differently compared to those using polynomial modeling. This indicates that the functions derived from the Fourier series have less adaptation to the verification values.

Comparing the average of the RMSE values in Tables 1 and 2 reveals that increasing the number of samples minimally impacts the mean RMSE across each order. However, polynomial modeling consistently yields a lower mean RMSE, indicating that the function $f(\mu)$ achieves a closer fit to the original values and exhibits stable results as the order and window sample parameters increase. The polynomial method yields more stable values. Therefore, even when different samples are used to create the function that describes the behavior of the bars, the resulting functions adapt more effectively compared to those generated by the Fourier series. While a lower order in Fourier series with fewer samples may produce similar values in variation, the polynomial method generally demonstrates better adaptability.

**Table 2.** Mean, minimum, and maximum RMSE in each order from two to six using Fourier series modeling.

| Window | Order | | | | |
|---|---|---|---|---|---|
| | 2 | 3 | 4 | 5 | 6 |
| **Samples** | ***Mean (min, max)*** | ***Mean (min, max)*** | ***Mean (min, max)*** | ***Mean (min, max)*** | ***Mean (min, max)*** |
| 4000 | 0.303 (0.16, 0.66) | 0.391 (0.16, 1.28) | 0.739 (0.18, 3.06) | 1.051 (0.17, 4.48) | 2.727 (0.07, 19.73) |
| 6000 | 0.268 (0.19, 0.53) | 0.379 (0.17, 1.34) | 0.702 (0.16, 3.11) | 1.396 (0.18, 6.00) | 2.663 (0.12, 36.69) |
| 8000 | 0.273 (0.16, 0.69) | 0.414 (0.15, 2.45) | 0.978 (0.23, 7.26) | 1.765 (0.14, 12.63) | 3.684 (0.12, 68.57) |
| 10,000 | 0.293 (0.17, 0.70) | 0.643 (0.16, 3.60) | 1.227 (0.18, 4.69) | 3.107 (0.21, 26.46) | 6.125 (0.11, 81.33) |
| 12,000 | 0.308 (0.18, 0.74) | 0.524 (0.17, 4.67) | 0.951 (0.18, 8.13) | 2.321 (0.15, 26.73) | 4.252 (0.10, 80.28) |
| 14,000 | 0.301 (0.17, 0.64) | 0.579 (0.14, 3.13) | 0.998 (0.16, 4.89) | 2.728 (0.17, 20.43) | 7.288 (0.09, 162.18) |
| 20,000 | 0.325 (0.18, 0.70) | 0.634 (0.15, 3.37) | 0.921 (0.15, 5.55) | 1.972 (0.15, 21.71) | 3.653 (0.09, 29.71) |

A lower order results in fewer operations during modeling and the QSA method demonstrates that a higher order is not necessary to achieve good adaptation results with the functions. Additionally, it has been shown that, given a sampling rate of 8.326 kHz, a duration of less than one second is sufficient in a real-world scenario to obtain a diagnosis of the wear degree in rotor bars.

## 4. Conclusions

Few studies have developed methodologies to quantify gradual levels of faults, such as BRB faults, in induction motors. The method presented here accurately quantifies BRB failure severity using Quaternion Signal Analysis (QSA), polynomial regression, and Fourier series modeling. This approach provides incremental records of motor behavior, enabling precise estimation and timely prevention of severe faults in the time domain.

The mean RMSE results indicate consistent performance across regression orders, window sample sizes, and modeling techniques. Polynomial modeling, in particular, demonstrates that changes in function order and window size have minimal impact on method effectiveness. This robustness allows for low-order and low-sample implementations, which are computationally efficient as they rely solely on fundamental addition and multiplication operations, unlike Fourier series, which require sine and cosine harmonics.

Future work will test this methodology by expanding the number of BRB conditions to detect partial BRBs and validating it with breaks in the junction between the bar and the side rings. In addition, we are interested in applying our development to assess wear levels in various rotating machine components, such as bearings and gearboxes, to validate their performance across diverse failure sources.

The QSA method was designed to adapt to different load conditions in induction motors; however, this adaptability needs to be validated. Consequently, we will conduct an analysis to examine how the ability to detect fault signatures depends on various load levels in the induction motor.

**Author Contributions:** Conceptualization, J.L.C.-H. and M.A.I.-M.; methodology, J.L.C.-H. and D.L.A.-O.; software, J.L.C.-H.; validation, D.L.A.-O. and R.C.-S.; formal analysis, J.L.C.-H. and M.A.I.-M.; investigation, J.L.C.-H.; resources, M.A.I.-M.; data curation, D.L.A.-O.; writing—original draft preparation, J.L.C.-H.; writing—review and editing, D.L.A.-O. and M.A.I.-M.; visualization, J.L.C.-H. and R.C.-S.; supervision, R.C.-S.; funding acquisition, M.A.I.-M. All authors have read and agreed to the published version of the manuscript.

**Funding:** The APC was funded by the Electronic Engineering Department of Universidad de Guanajuato under POA 2024.

**Institutional Review Board Statement:** Not applicable.

**Informed Consent Statement:** Not applicable.

**Data Availability Statement:** The original contributions presented in the study are included in the article, further inquiries can be directed to the corresponding author.

**Acknowledgments:** The authors thank the University of Guanajuato for the facilities and support to develop this project. Special thanks to the DAIP CIIC 048/2024 project: "Implementation of an Automatic Braking System for Electric Vehicles for People with Disabilities" (valid from 1 January to 31 December 2024) for its financial and technical support.

**Conflicts of Interest:** The authors declare no conflicts of interest. The funders had no role in this study's design, in the collection, analyses, or interpretation of data, in the writing of the manuscript, or in the decision to publish the results.

## Abbreviations

The following abbreviations are used in this manuscript:

| | |
|---|---|
| BRB | Broken Rotor Bar |
| FFT | Fast Fourier Transform |
| MUSIC | Multiple Signal Classification |
| DTFT | Digital Taylor–Fourier Transform |
| MP | Matching Pursuit |
| KNN | k-Nearest Neighbor |
| SVM | Support Vector Machine |
| DWT | Discrete Wavelet Transform |
| QEWT | Quaternion Empirical Wavelet Transform |
| ART | Adaptive Resonance Theory |
| MAP | Mapping |
| MLP | Multi-Layer Perceptron |
| QSA | Quaternion Signal Analysis |
| $V_h$ | Tangential mechanical vibration speed in the housing |
| $V_a$ | Axial mechanical vibration speed on the driven side |
| $V_s$ | Radial mechanical vibration speed on the non-driven side |
| $V_d$ | Radial mechanical vibration speed on the driven side |
| $q(t)$ | Quaternion signal in time domain |
| $q_d(t)$ | Delayed quaternion in time domain |
| $q_r(t)$ | Rotated quaternion in time domain |
| $\mathbf{w}[n]$ | Windows vector |
| $\mu$ | Mean |
| RMSE | Root Mean Square Error |

## References

1. Aguayo-Tapia, S.; Avalos-Almazan, G.; Rangel-Magdaleno, J.d.J.; Ramirez-Cortes, M.J. Physical variable measurement techniques for fault detection in electric motors. *Energies* **2023**, *16*, 4780. [CrossRef]
2. Chen, J.; Wang, J.; Zhu, J.; Lee, T.H.; de Silva, C.W. Unsupervised Cross-Domain Fault Diagnosis Using Feature Representation Alignment Networks for Rotating Machinery. *IEEE ASME Trans. Mech.* **2021**, *26*, 2770–2781. [CrossRef]
3. Zheng, H.; Wang, R.; Yin, J.; Li, Y.; Lu, H.; Xu, M. A new intelligent fault identification method based on transfer locality preserving projection for actual diagnosis scenario of rotating machinery. *Mech. Syst. Signal Process.* **2020**, *135*, 106344. [CrossRef]
4. Altaf, S.; Ahmad, S.; Zaindin, M.; Huda, S.; Iqbal, S.; Soomro, M.W. Multiple industrial induction motors fault diagnosis model within powerline system based on wireless sensor network. *Sustainability* **2022**, *14*, 10079. [CrossRef]
5. Gu, B.G. Development of broken rotor bar fault diagnosis method with sum of weighted fourier series coefficients square. *Energies* **2022**, *15*, 8735. [CrossRef]
6. Gangsar, P.; Tiwari, R. Signal-based condition monitoring techniques for fault detection and diagnosis of induction motors: A state-of-the-art review. *Mech. Syst. Signal Process.* **2020**, *144*, 106908. [CrossRef]

7. Aguayo-Tapia, S.; Avalos-Almazan, G.; Rangel-Magdaleno, J.d.J.; Paternina, M.R.A. Broken bar fault detection using taylor-fourier filters and statistical analysis. *Entropy* **2023**, *25*, 44. [CrossRef] [PubMed]
8. Ibrahim, A.; Anayi, F.; Packianather, M.; Alomari, O.A. New hybrid invasive weed optimization and machine learning approach for fault detection. *Energies* **2022**, *15*, 1488. [CrossRef]
9. Yaman, O. An automated faults classification method based on binary pattern and neighborhood component analysis using induction motor. *Measurement* **2021**, *168*, 108323. [CrossRef]
10. Godoy, W.F.; da Silva, I.N.; Goedtel, A.; Palácios, R.H.C.; Lopes, T.D. Application of intelligent tools to detect and classify broken rotor bars in three-phase induction motors fed by an inverter. *IET Electr. Power Appl.* **2016**, *10*, 430–439. [CrossRef]
11. Nascimento, N.M.M.e.; Medeiros, C.M.S.; Filho, P.P.R. A comparison of machine learning methods to identify broken bar failures in induction motors using statistical moments. *Adv. Intell. Syst. Comput.* **2018**, *736*, 124–133. [CrossRef]
12. Martinez-Herrera, A.L.; Ferrucho-Alvarez, E.R.; Ledesma-Carrillo, L.M.; Mata-Chavez, R.I.; Lopez-Ramirez, M.; Cabal-Yepez, E. Multiple fault detection in induction motors through homogeneity and kurtosis computation. *Energies* **2022**, *15*, 1541. [CrossRef]
13. Singh, M.; Shaik, A.G. Entropy-based broken rotor-bar fault detection and estimation of its severity in a three-phase induction motor. In Proceedings of the 2020 IEEE International Conference on Power Electronics, Drives and Energy Systems, Jaipur, India, 16–19 December 2020; pp. 1–6. [CrossRef]
14. Bejaoui, I.; Bruneo, D.; Xibilia, M.G. Remaining useful life prediction of broken rotor bar based on data-driven and degradation model. *Appl. Sci.* **2021**, *11*, 7175. [CrossRef]
15. Kartiwa, A.; Supriatna, A.K.; Rusyaman, E.; Sulaiman, J. Review of quaternion differential equations: Historical development, applications, and future direction. *Axioms* **2023**, *12*, 483. [CrossRef]
16. Huang, C.; Li, J.; Gao, G. Review of quaternion-based color image processing methods. *Mathematics* **2023**, *11*, 2056. [CrossRef]
17. Abbassi, R.; Jerbi, H.; Kchaou, M.; Simos, T.E.; Mourtas, S.D.; Katsikis, V.N. Towards higher-order zeroing neural networks for calculating quaternion matrix inverse with application to robotic motion tracking. *Mathematics* **2023**, *11*, 2756. [CrossRef]
18. Li, J.; Chen, P.; Chang, Z.; Zhang, G.; Guo, L.; Zhao, C. Trajectory tracking control of quadrotor based on fractional-order s-plane model. *Machines* **2023**, *11*, 672. [CrossRef]
19. Rikam, L.E.; Bitjoka, L.; Nketsa, A. Quaternion Fourier transform spectral analysis of electrical currents for bearing faults detection and diagnosis. *Mech. Syst. Signal Process.* **2022**, *168*, 108656. [CrossRef]
20. Zhang, K.; Deng, Y.; Chen, P.; Ma, C.; Xu, Y. Quaternion empirical wavelet transform and its applications in rolling bearing fault diagnosis. *Measurement* **2022**, *195*, 111179. [CrossRef]
21. Contreras-Hernandez, J.L.; Almanza-Ojeda, D.L.; Ledesma-Orozco, S.; Garcia-Perez, A.; Romero-Troncoso, R.J.; Ibarra-Manzano, M.A. Quaternion Signal Analysis Algorithm for Induction Motor Fault Detection. *IEEE Trans. Ind. Electron.* **2019**, *66*, 8843–8850. [CrossRef]
22. Contreras-Hernandez, J.L.; Almanza-Ojeda, D.L.; Ledesma, S.; Garcia-Perez, A.; Castro-Sanchez, R.; Gomez-Martinez, M.A.; Ibarra-Manzano, M.A. Geometric analysis of signals for inference of multiple faults in induction motors. *Sensors* **2022**, *22*, 2622. [CrossRef] [PubMed]
23. Contreras-Hernandez, J.L.; Almanza-Ojeda, D.L.; Ibarra-Manzano, M.A.; Amezquita-Sanchez, J.P.; Valtierra-Rodriguez, M.; Camarena-Martinez, D. Short-Circuit Damage Diagnosis in Transformer Windings Using Quaternions: Severity Assessment through Current and Vibration Signals. *Appl. Sci.* **2023**, *13*, 12622. [CrossRef]
24. Cardenas-Cornejo, J.J.; Ibarra-Manzano, M.A.; González-Parada, A.; Castro-Sanchez, R.; Almanza-Ojeda, D.L. Classification of inter-turn short-circuit faults in induction motors based on quaternion analysis. *Measurement* **2023**, *222*, 113680. [CrossRef]
25. Sinha, A.K.; Das, S.; Chatterjee, T.K. Empirical relation for broken bar determination in scim. *COMPEL-Int. J. Comput. Math. Electr. Electron. Eng.* **2018**, *37*, 242–265. [CrossRef]
26. Talebi, S.P.; Werner, S.; Mandic, D.P. Quaternion-valued distributed filtering and control. *IEEE Trans. Autom. Control* **2020**, *65*, 4246–4257. [CrossRef]
27. Treml, A.E.; Flauzino, R.A.; Suetake, M.; Maciejewski, N.A.R. Experimental database for detecting and diagnosing rotor broken bar in a three-phase induction motor. *IEEE Dataport* **2020**. [CrossRef]
28. Ren, T.; Kang, X.; Sun, W.; Song, H. Study of Dynamometer Cards Identification Based on Root-Mean-Square Error Algorithm. *Int. J. Pattern Recognit. Artif. Intell.* **2018**, *32*, 1850004. [CrossRef]


**Disclaimer/Publisher's Note:** The statements, opinions and data contained in all publications are solely those of the individual author(s) and contributor(s) and not of MDPI and/or the editor(s). MDPI and/or the editor(s) disclaim responsibility for any injury to people or property resulting from any ideas, methods, instructions or products referred to in the content.

*applied sciences*

MDPI

*Article*

# Inter-Turn Fault Diagnosis of Induction Motors Based on Current Vector Pattern Analysis in Stationary Coordinate Frame

**Inyeol Yun [1], Hyunwoo Kim [2], Ju Lee [1] and Sung-Gu Lee [3,*]**

[1] Department of Electrical Engineering, Hanyang University, Seoul 04763, Republic of Korea
[2] Elmore Family School of Electrical and Computer Engineering, Purdue University, West Lafayette, IN 47907, USA; kim4852@purdue.edu
[3] Department of Electrical Engineering, Dong-A University, Busan 49315, Republic of Korea
* Correspondence: sunggu@dau.ac.kr

**Abstract:** In this study, a current vector pattern is analyzed for inter-turn fault (ITF) diagnosis of induction machines (IMs), and an ITF diagnosis algorithm is proposed. When an ITF occurs in IMs, a negative-sequence current is generated due to fault resistance, even though a positive-sequence voltage is applied to IMs. Based on the mathematical model of IMs with an ITF, the current vector patterns in the stationary coordinate frame are analyzed. The superposition of positive- and negative-sequence components results in an elliptical current vector trajectory, and its orientation varies depending on the fault conditions. The co-simulation using finite element analysis and circuit simulation is implemented to analyze the current vector pattern of IMs with an ITF. The ITF diagnosis is proposed based on the current vector pattern. A 12 kW, four-pole, three-phase IM and terminal box, which was used to implement an ITF, is manufactured, and an experiment setup is established to verify the ITF algorithm. The effectiveness of the proposed ITF algorithm is validated through experimental verification of the manufactured IM and terminal box.

**Keywords:** co-simulation; current vector analysis; induction motor; inter-turn fault diagnosis (ITF); negative-sequence current

## 1. Introduction

In recent years, transportation electrification has advanced at an astonishing pace, driven by increasing environmental concerns, regulatory pressures, and rapid technological innovation. Governments around the world are introducing stringent emission standards and providing financial incentives to encourage the adoption of eco-friendly mobility solutions [1,2]. At the same time, advances in battery technology, power electronics, and lightweight materials have made electric drivetrains more practical and economical than ever before. As a result, electric vehicles (EVs), hybrid electric vehicles (HEVs), and other electric mobility solutions are rapidly replacing conventional internal combustion engine vehicles in markets around the world [3,4]. While transportation electrification brings about improvements in energy efficiency and reductions in carbon emissions, it also places increasing demands on the reliability and resilience of the underlying propulsion system.

As a core component of transportation electrification, electric motors, especially those used for traction, must have reliability and the ability to detect failures to ensure safe and reliable operation [5]. Among the various types of electric motors, induction motors (IMs) have maintained their dominance in traction and industrial applications [6,7]. Their simple structure, lack of permanent magnets, and cost-effectiveness make them a favorable choice for many commercial systems [8]. However, the reliability of IMs is becoming

an increasingly important concern, especially in failure-prone environments. As electric vehicles become more widespread, ensuring the robust operation of these motors under a variety of conditions is becoming increasingly important [9].

There are various types of motor faults that can occur during operation, and the appropriate diagnostic method depends on the fault type. In general, motor faults are classified into electrical, magnetic, and mechanical categories [10]. Among these, stator-related faults in IMs account for more than 30% of all failures [11]. An inter-turn fault (ITF) in IMs occurs when the insulation between adjacent stator windings deteriorates, leading to a localized short circuit. This fault induces an unbalanced magnetic field, resulting in localized overheating and magnetic flux distortion. If not detected at an early stage, the fault may evolve into more severe conditions such as phase-to-phase or phase-to-ground faults, ultimately causing complete winding burnout and system failure [12–15].

Several studies have investigated methods to diagnosis ITFs in IMs; these methods include transient-response-based methods [16–18], motor current signature analysis (MCSA) [19–25], and machine learning-based methods [24–32]. In [17–19], the transient characteristics of IMs with an ITF are analyzed, and fault diagnosis methods are proposed based on measured physical properties such as current or temperature. Fault diagnosis based on MCSA has been widely adopted due to its simplicity and cost-effectiveness, as it only relies on current sensors. MCSA can be conducted based on the time domain (e.g., current envelope analysis) [19,20], frequency domain (e.g., Fast Fourier transform) [21,22], and time–frequency domain (e.g., Hilbert transform, Discrete Wavelet transform, and Short-Time Fourier Transform) [23–25]. Machine learning-based methods, such as Support Vector Machine (SVM), have been employed for ITF detection [24–28]. These techniques utilize features derived from a mathematical model and frequency-domain characteristics of the IM under ITF. Although these methods demonstrate high diagnostic performance, their reliance on high sampling rates and considerable computational resources may limit their feasibility for implementation in embedded systems. Recently, fault monitoring of inverter-fed IMs has been proposed using differential-mode (DM) and common-mode (CM) impedance analysis [5,29–32]. In [29,30], DM and CM impedance modeling and measurement methods are presented to facilitate high-frequency impedance analysis for stator health monitoring. The influence of stator faults on DM impedance was investigated, and variations in DM noise were accurately predicted [31]. In contrast, CM impedance measured at specific frequencies has proven to be effective for detecting ITFs. This approach is particularly advantageous because it does not require direct electrical connections to the motor terminals [32]. Instead, it relies on externally injected radio-frequency sinusoidal signals, offering high reliability and robustness, as it remains unaffected by the supply voltage quality. Although impedance analyzers can measure up to 120 MHz [33], additional equipment, such as inductive couplers and impedance analyzers, is necessary for implementation.

In this paper, a fault diagnosis algorithm based on the current vector pattern is proposed for detecting ITFs in IMs. When an ITF occurs in IM, the fault resistance occurs in the parallel connection of the faulted phase in the IM. Based on a mathematical model of an IM with an ITF, the current in the steady state is analyzed. Due to the faulted phase, a negative-sequence current is generated, even though a positive-sequence voltage is applied to the IM. Since both positive- and negative-sequence currents are generated, the current vector pattern in the stationary coordinate frame has a specific shape, which can be obtained from the mathematical model. Furthermore, the co-simulation with a finite element analysis (FEA) and circuit simulation is implemented to analyze the current vector pattern, and an ITF diagnosis algorithm is proposed based on the current vector analysis. An experimental setup is implemented using a 12 kW, four-pole, three-phase IM, inverter, fault resistance,

and terminal box for winding connection. The effectiveness of the proposed ITF diagnosis algorithm is validated through experiments conducted under the fault conditions.

The rest of this paper is organized as follows. The current vector analysis of an IM with an ITF based on a mathematical model is discussed in Section 2. Based on the current vector analysis, an ITF diagnosis algorithm is proposed, and the co-analysis is described in Section 3. Section 4 presents experimental verification using the 12 kW, four-pole, three-phase IM and terminal box. Section 5 provides the conclusion of this study.

## 2. Current Vector Analysis of IMs with ITF

### *2.1. Mathematical Model for ITF*

Figure 1 shows the mathematical model for an induction motor with an ITF in Phase A. Since the fault resistance is connected to the fault phase parallelly, the voltage equation is expressed as follows [34]:

$$\begin{aligned} [v_s] &= [R_s][i_s] + \tfrac{d}{dt}[\lambda_s] - [\mu R_s \ 0 \ 0]^T \ i_f \\ R_f i_f &= \mu R_s \left( i_{as} - i_f \right) + \tfrac{d}{dt}\lambda_{as2} \\ 0 &= [R_r][i_r] + \tfrac{d}{dt}[\lambda_r] \end{aligned} \tag{1}$$

where

$$\begin{aligned} [v_s] = [v_{as} \ v_{bs} \ v_{cs}]^T, \ [i_s] &= [i_{as} \ i_{bs} \ i_{cs}]^T \\ [\lambda_s] = [L_{ss}][i_s] + [L_{sr}][i_r] + \mu[-(L_{ls} + L_{ms}) \ L_{ms}/2 \ L_{ms}/2]^T i_f, \\ [\lambda_r] = [L_{rs}][i_s] + [L_{rr}][i_r] - \mu L_{ms}[\cos\theta_e \ \cos(\theta_e + 2\pi/3) \ \cos(\theta_e - 2\pi/3)]^T i_f, \\ \lambda_{as2} = -\mu[-(L_{ls} + L_{ms}) \ L_{ms}/2 \ L_{ms}/2][i_s] \\ + \mu L_{ms}[\cos\theta_r \ \cos(\theta_r - 2\pi/3) \ \cos(\theta_r + 2\pi/3)][i_r] - \mu(L_{ls} + \mu L_{ms}) i_f, \end{aligned}$$

$v_{as}$, $v_{bs}$, and $v_{cs}$ are the phase voltages; $i_{as}$, $i_{bs}$, and $i_{cs}$ are the phase currents; $i_r$ is the rotor current; $i_f$ is the fault current; $\lambda_s$ and $\lambda_r$ are the flux linkages of the stator and rotor, respectively; $L_{ss}$ and $L_{rr}$ are the self-inductances of the stator and rotor, respectively; $L_{sr}$ and $L_{rs}$ are the mutual inductances between the stator and rotor; $R_s$ and $R_r$ are the resistances of the stator and rotor, respectively; $L_{ls}$ and $L_{ms}$ are the leakage and magnetize inductance, respectively; $\mu = N_{fault}/N_{ph}$ is the ratio of the number of turns in the fault winding; and $\theta_e$ is the electrical angle.

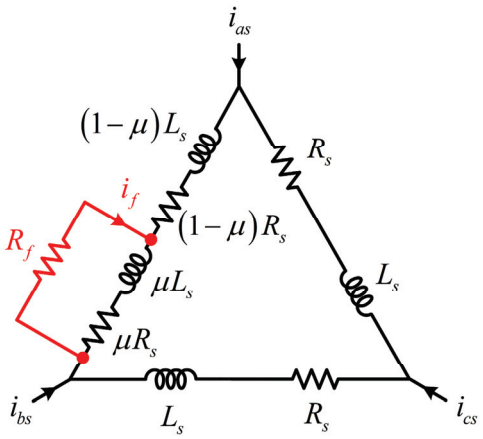


**Figure 1.** Configuration of ITF in IM with Δ connection.

To analyze the current vector pattern in the stationary coordinate frame (the $\alpha\beta$-axis plane), the coordinate transformation is considered as illustrated in Figure 2. From Figure 2, the coordinate transformation can be expressed as follows:

$$\left[C_{abc\to\alpha\beta}\right] = \frac{2}{3}\begin{bmatrix} 1 & -\frac{1}{2} & -\frac{1}{2} \\ 0 & \frac{\sqrt{3}}{2} & -\frac{\sqrt{3}}{2} \end{bmatrix}, \quad \left[C_{\alpha\beta\to abc}\right] = \begin{bmatrix} 1 & -\frac{1}{2} & -\frac{1}{2} \\ 0 & \frac{\sqrt{3}}{2} & -\frac{\sqrt{3}}{2} \end{bmatrix}^T \tag{2}$$

where $[C_{abc\to\alpha\beta}]$ is the coordinate transformation from abc to $\alpha\beta$, and $[C_{\alpha\beta\to abc}]$ is the coordinate transformation from $\alpha\beta$ to abc. From Equation (2), three-phase components are transformed into stationary coordinate frame as shown in Equation (3).

$$\left[f_{\alpha\beta}\right] = \left[C_{abc\to\alpha\beta}\right]\left[f_{abc}\right], \left[f_{abc}\right] = \left[C_{\alpha\beta\to abc}\right]\left[f_{\alpha\beta}\right] \tag{3}$$

where $[f_{abc}]$ is the physical value, such as the voltage and current, in *abc*, and $[f_{\alpha\beta}]$ is the physical value, such as the voltage and current, in $\alpha\beta$. By subtracting Equation (3) from Equation (1), the voltage equations in the stationary coordinate frame can be obtained using the stationary coordination transformations:

$$\begin{array}{l} \left[v_{\alpha\beta s}\right] = \left[R_s\right]\left[i_{\alpha\beta s}\right] + \frac{d}{dt}\left[\lambda_{\alpha\beta s}\right] - \frac{2}{3}\mu R_s i_f \\ 0 = \left[R_r\right]\left[i_{\alpha\beta r}\right] + \frac{d}{dt}\left[\lambda_{\alpha\beta r}\right] - j\omega_e\left[\lambda_{\alpha\beta r}\right] \end{array} \tag{4}$$

where

$$\left[\lambda_{\alpha\beta s}\right] = \left[L_s\right]\left[i_{\alpha\beta s}\right] + \left[L_m\right]\left[i_{\alpha\beta r}\right] - \frac{2}{3}\mu\begin{bmatrix} L_s \\ 0 \end{bmatrix} i_f, \left[\lambda_{\alpha\beta r}\right] = \left[L_m\right]\left[i_{\alpha\beta s}\right] + \left[L_r\right]\left[i_{\alpha\beta r}\right] - \frac{2}{3}\mu\begin{bmatrix} L_m \\ 0 \end{bmatrix} i_f,$$

$[v_{\alpha\beta s}]$ is the voltage in the stationary coordinate frame; $[i_{\alpha\beta s}]$ and $[i_{\alpha\beta r}]$ are the current of the stator and rotor in the stationary coordinate frame, respectively; $[\lambda_{\alpha\beta s}]$ and $[\lambda_{\alpha\beta r}]$ are the flux linkage of the stator and rotor in the stationary coordinate frame, respectively; and $\omega_e$ is the electrical speed.

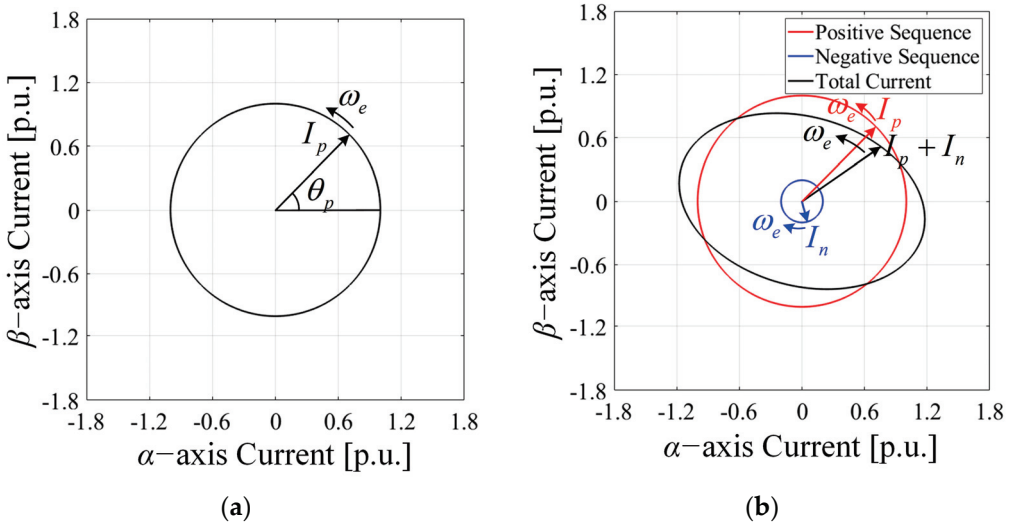


**Figure 2.** Current vector pattern: (**a**) health condition; (**b**) fault condition.

In a steady-state IM, the voltage and current can be expressed as a complex form:

$$\mathbf{V}_s = V_{ps}e^{j\omega_e t} + V_{ns}e^{-j\omega_e t}, \ \mathbf{I}_s = I_{ps}e^{j\omega_e t} + I_{ns}e^{-j\omega_e t}, \ \mathbf{I}_r = I_{pr}e^{js\omega_e t} + I_{nr}e^{-js\omega_e t} \tag{5}$$

where vs is the phase form of the voltage; $\mathbf{I}_s$ is the phase form of the stator current; $\mathbf{I}_r$ is the phase form of the rotor current; $V_{ps}$ and $V_{ns}$ are the positive and negative sequences of the voltage, respectively; $I_{ps}$ and $I_{ns}$ are the positive and negative sequences of the stator current, respectively; and $I_{pr}$ and $I_{nr}$ are the positive and negative sequences of the rotor current, respectively.

By subtracting Equation (5) from Equation (4), the phase equation in terms of the positive and negative sequences can be expressed as follows:

$$\begin{aligned} V_{ps} &= (R_s + j\omega_e L_s)\left(I_{ps} - \tfrac{2}{3}\mu I_f\right) + j\omega_e L_m I_{pr} \\ V_{ns} &= (R_s + j\omega_e L_s)\left(I_{ns} - \tfrac{2}{3}\mu I_f\right) + j\omega_e L_m I_{nr} \\ 0 &= \left(\tfrac{R_r}{s} + j\omega_e L_r\right) I_{pr} + j\omega_e L_m\left(I_{ps} - \tfrac{2}{3}\mu I_f\right) \\ 0 &= \left(\tfrac{R_r}{2-s} + j\omega_e L_r\right) I_{nr} + j\omega_e L_m\left(I_{ns} - \tfrac{2}{3}\mu I_f\right) \\ \mu\left(V_{sp} + V_{sn}\right) &= \mu\left(1 - \tfrac{2}{3}\mu\right)(R_s + j\omega_e L_{ls}) I_f + R_f I_f \end{aligned} \tag{6}$$

From Equation (6), the stator current can be expressed as follows:

$$\begin{bmatrix} I_{ps} \\ I_{ns} \end{bmatrix} = \begin{bmatrix} Y_{pp} & Y_{pn} \\ Y_{np} & Y_{nn} \end{bmatrix} \begin{bmatrix} V_{ps} \\ V_{ns} \end{bmatrix} \tag{7}$$

where

$$\begin{aligned} Y_{pp} &= \frac{1}{R_s + j\omega_e L_s - \frac{\omega_e^2 L_m^2}{R_r/s + j\omega_e L_r}} + Y_{pn}, \\ Y_{nn} &= \frac{1}{R_s + j\omega_e L_s - \frac{\omega_e^2 L_m^2}{R_r/(2-s) + j\omega_e L_r}} + Y_{np}, \\ Y_{pn} = Y_{np} &= \frac{2}{3}\frac{\mu^2}{R_f + \mu\left(1 - \frac{2\mu}{3}\right)(R_s + j\omega_e L_{ls})}, \end{aligned} \tag{8}$$

$Y_{pp}$ and $Y_{nn}$ are the admittances of the positive and negative sequences, respectively, and $Y_{pn}$ and $Y_{np}$ are the admittances between the positive and negative sequences.

If the positive-sequence voltage is applied to the IM, the positive and negative currents can be expressed as shown in Equation (7) because the negative-sequence voltage is zero.

$$I_{ps} = Y_{pp} V_{ps},\ I_{ns} = Y_{np} V_{ps} \tag{9}$$

When a fault occurs in Phase A, the admittance between the positive and negative sequences becomes non-zero due to the presence of $\mu$ in Equation (8). As a result, the negative-sequence current is induced by the applied positive-sequence voltage and is influenced by fault parameters such as the fault resistance and the ratio of shorted turns. The presence of a negative-sequence component under fault conditions changes the current vector pattern differently from that of a healthy condition.

### *2.2. Current Vector Pattern Analysis*

Under ITF conditions in the IM, both positive- and negative-sequence currents are generated, even when only a positive-sequence voltage is applied. These sequence currents can be represented as phasors in the complex plane.

$$I_{ps} = I_p e^{j\theta_p},\ I_{ns} = I_n e^{-j\theta_n},\ I_p = Y_{pp} V_{ps},\ I_n = Y_{np} V_{ps} \tag{10}$$

where $I_p$ and $I_n$ are the magnitudes of the positive- and negative-sequence currents, respectively, and $\theta_p$ and $\theta_n$ are the phase angles of the positive- and negative-sequence currents.

The total current, comprising both positive- and negative-sequence components, can be expressed as follows:

$$\begin{aligned} I_t &= I_{ps}e^{j\omega_e t} + I_{ns}e^{-j\omega_e t} \\ I_\alpha + jI_\beta &= I_p e^{j(\omega_e t+\theta_p)} + I_n e^{-j(\omega_e t+\theta_n)} \\ I_\alpha &= I_p\cos\left(\omega_e t+\theta_p\right) + I_n\cos(\omega_e t+\theta_n) \\ I_\beta &= I_p\sin\left(\omega_e t+\theta_p\right) - I_n\sin(\omega_e t+\theta_n) \end{aligned} \tag{11}$$

From Equation (9), the relationship between the $\alpha\beta$-axis current can be expressed as follows:

$$AI_\alpha^2 + BI_\alpha I_\beta + CI_\beta^2 = \left(I_p^2 - I_n^2\right)^2 \tag{12}$$

where

$$\begin{aligned} A &= I_p^2 + I_n^2 - 2I_pI_n\cos\left(\theta_p-\theta_n\right) \\ B &= -4I_pI_n\sin\left(\theta_p-\theta_n\right) \\ C &= I_p^2 + I_n^2 + 2I_pI_n\cos\left(\theta_p-\theta_n\right). \end{aligned} \tag{13}$$

Equation (12) represents a quadratic form, where the relationship between the $\alpha$- and $\beta$-axis currents is governed by the coefficients defined in Equation (13). These coefficients in Equation (12) satisfy the following relationships:

$$B^2 - 4AC = -4\left(I_p^2 - I_n^2\right)^2 < 0. \tag{14}$$

In the quadratic form presented in Equation (12), the $\alpha$- and $\beta$-axis currents exhibit an elliptical relationship if the condition given in Equation (14) is satisfied. Under healthy operating conditions, Equation (12) simplifies to a circular form, as the negative-sequence current becomes zero according to Equations (8) and (9).

$$I_\alpha^2 + I_\beta^2 = I_p^2 \tag{15}$$

Therefore, the current vector pattern can be represented as a circle under healthy conditions and as an ellipse under ITF conditions, as illustrated in Figure 2. Moreover, both the magnitude and phase of the current vector are influenced by the fault conditions. Although the ITF conditions are analyzed using Equations (8), (9) and (12), accurately calculating the admittance between the positive and negative sequences is challenging due to the coupling between the stator and rotor currents. To address this, the next section presents a fault diagnosis approach based on current vector pattern analysis using co-simulation with FEA and circuit simulation under various fault conditions.

## 3. ITF Diagnosis Based on Current Vector Pattern

As shown in Section 2, the current vector pattern is analyzed when an ITF occurs in Phase A. Due to the negative-sequence current, the current vector pattern has an ellipse shape. In this section, the current vector pattern is analyzed based on the co-analysis with FEA and circuit simulation using ANSYS Maxwell 2024R1 and Simplorer 2024R1.

### *3.1. FEA Model*

To construct the FEA model, the 12 kW, four-pole, three-phase IM used in the RENAULT TWIZY is considered, as summarized in Table 1. Figure 3a presents the FEA model, in which an ITF is introduced in Phase A by incorporating a fault resistance connected in parallel with the faulted winding. To implement the ITF condition, co-simulation is conducted using ANSYS Simplorer 2024R1, as shown in Figure 3b. The stator winding configuration is a $\Delta$-connection, and the fault resistance is connected in parallel with the

winding of the faulted phase. The co-simulation model includes a three-phase inverter, an FEA-based IM block, a stationary coordinate transformation block, and a V/f control block. The V/f control applies a positive-sequence voltage to the IM through the three-phase inverter. Based on the measured stator currents, the $\alpha\beta$-axis currents are calculated using the stationary coordinate transformation block.

**Table 1.** Specification of IM for Twizy.

| Content | Value | Unit |
|---|---|---|
| Rated power | 12 | kW |
| Rated speed | 2010 | rpm |
| Maximum speed | 7250 | rpm |
| Rated frequency | 70 | Hz |
| DC voltage | 52 | V |
| Rated voltage | 20 | $V_{rms}$ |
| Rated current | 248 | $A_{rms}$ |
| DC link voltage | 48 | V |
| Switching frequency | 10 | kHz |
| Modulation method | SVPWM | - |
| Stator outer/inner diameter | 200/125 | mm |
| Rotor outer/inner diameter | 124/36 | mm |
| Airgap length | 0.5 | mm |
| Stack length | 120 | mm |
| Number of poles/slots | 4/36 | - |
| Total series turns | 13 | |
| Number of parallel branches | 4 | - |
| Core material | 35PN230 | - |

### *3.2. FEA Results*

As discussed in Section 2, the current vector exhibits an elliptical pattern under ITF conditions in an IM, primarily due to the presence of negative-sequence currents. These negative-sequence currents are influenced by fault parameters such as the fault resistance, the number of shorted turns, and the specific faulted phase. To investigate the current vector pattern under various fault conditions, co-simulations are conducted. Figure 4 illustrates the current vector patterns for each faulted phase. Under healthy conditions, the current vector forms a circle. However, in the presence of an ITF, the pattern transitions into an ellipse due to the unbalanced impedance introduced by the fault resistance. The main axis of the ellipse varies depending on the faulted phase. Specifically, when Phase A is faulted, the ellipse's main axis appears between $0^\circ$ and $60^\circ$; if Phase B is faulted, it appears between $-60^\circ$ and $0^\circ$; and if Phase C is faulted, it appears between $-120^\circ$ and $-60^\circ$. This main axis of the ellipse corresponds to a $30^\circ$ angular displacement between the ellipse main axis and the magnetic motive force center of the faulted phase, as depicted in Figure 4. In the case of a Y-connected winding instead of a $\Delta$-connected one, the current phase lags by $30^\circ$, which shifts the main axis. In this case, the main axis of the ellipse for Phase A lies between $-30^\circ$ and $30^\circ$; for Phase B, it lies between $30^\circ$ and $90^\circ$; and for Phase C, it lies between $-90^\circ$ and $-30^\circ$. A summary of the main axis angle for each faulted phase is provided in Table 2. The magnitude of the negative-sequence current is influenced by the fault parameters, such as the number of shorted turns and the fault resistance, as illustrated in Figure 5a,b. As the number of shorted turns increases or the fault resistance decreases, the elliptical distortion becomes more pronounced, indicating a higher degree of current imbalance. Furthermore, the positive- and negative-sequence currents are influenced by the speed and slip, as shown in Equation (8). The current vector pattern is analyzed for speed and slip, as illustrated in Figure 5c,d. Although the magnitude of the current vector

depends on the speed and slip, the main axis of the ellipse appears between 0° and 60°. These trends are consistently observed across all simulation scenarios, confirming that the proposed method not only detects the occurrence of faults but also provides insights into their severity.

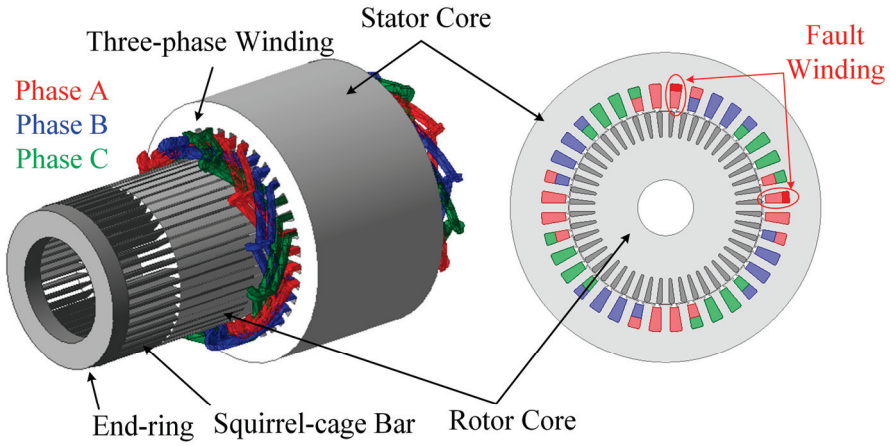


(**a**)

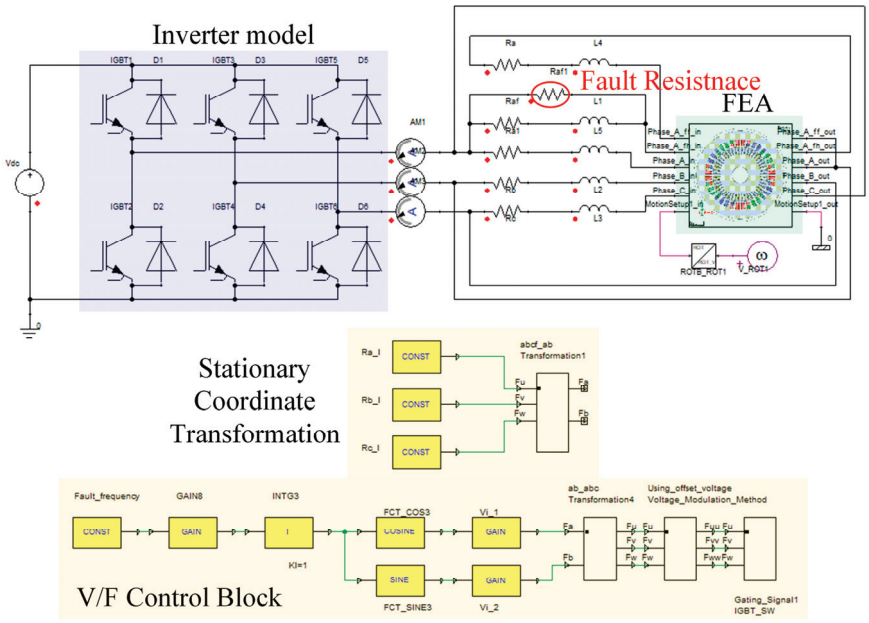


(**b**)

**Figure 3.** Co-analysis used in analysis of the current vector pattern in an ITF in an IM: (**a**) IM model (right: 3D view; left: 2D view); (**b**) circuit model for implementing the ITF.

**Table 2.** The angle of the maximum current vector for the fault phase and winding connection.

| Winding Connection | Fault Phase | The Angle of the Maximum Current Vector |
|---|---|---|
| Δ | A | 0–60° & 180–240° |
| | B | 300–360° & 120–180° |
| | C | 240–300° & 60–120° |
| Y | A | 0–30° & 150–210° & 330–360° |
| | B | 270–300° & 90–150° |
| | C | 30–90° & 210–270° |

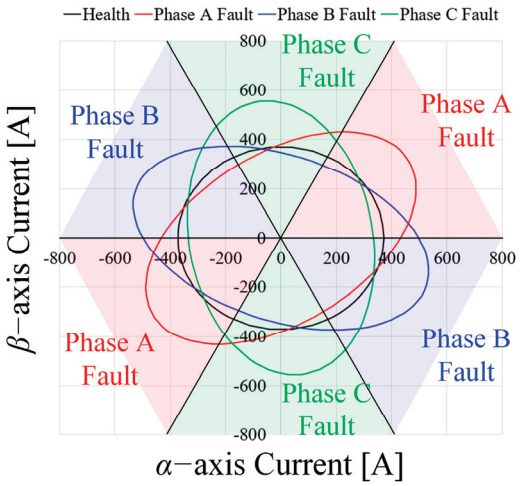


**Figure 4.** Current vector pattern for healthy and faulty conditions.

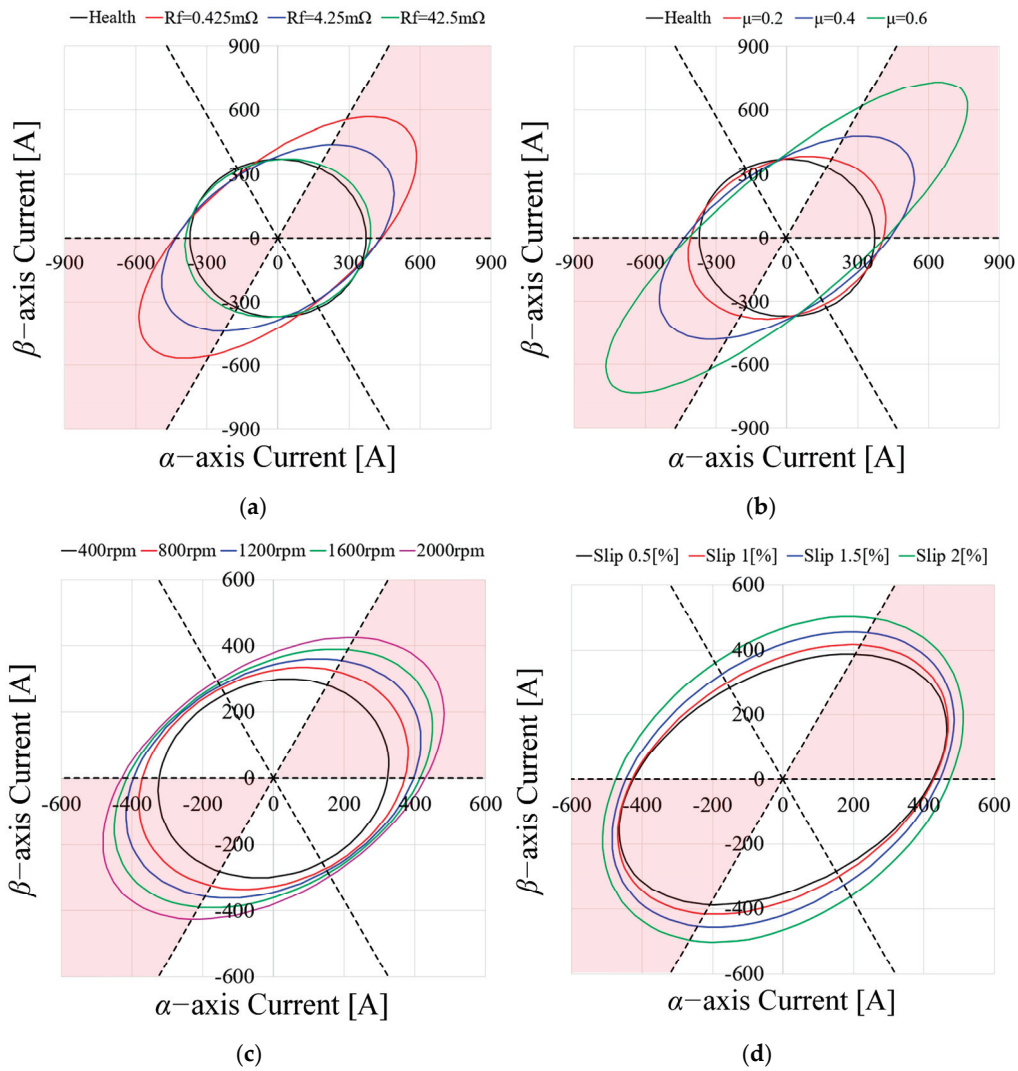


**Figure 5.** Current vector pattern for the fault resistance and number of fault turns when the ITF occurs in Phase A: (**a**) fault resistance; (**b**) the ratio of shorted turns; (**c**) speed; (**d**) slip.

### *3.3. Fault Diagnosis Algorithm*

Through the co-simulation of the FEA model and circuit analysis, the current vector pattern under ITF conditions is analyzed, and a fault diagnosis algorithm is proposed.

Based on the co-simulation results, an ITF diagnosis algorithm tailored for Δ-connected windings is developed, as illustrated in Figure 6. In this approach, a positive-sequence voltage is applied to the IM, and the stator current in the stationary coordinate frame is obtained using the measured three-phase currents. Since the stationary coordinate transformation is employed, the use of an encoder is not required, which simplifies the implementation of the diagnostic method. The angle of the maximum current vector is calculated from the stationary-frame current, and fault detection is performed based on this angle. As summarized in Table 2 and illustrated in Figure 6, the proposed algorithm enables effective identification of the faulted phase without the need for complex signal processing or rotor position information.

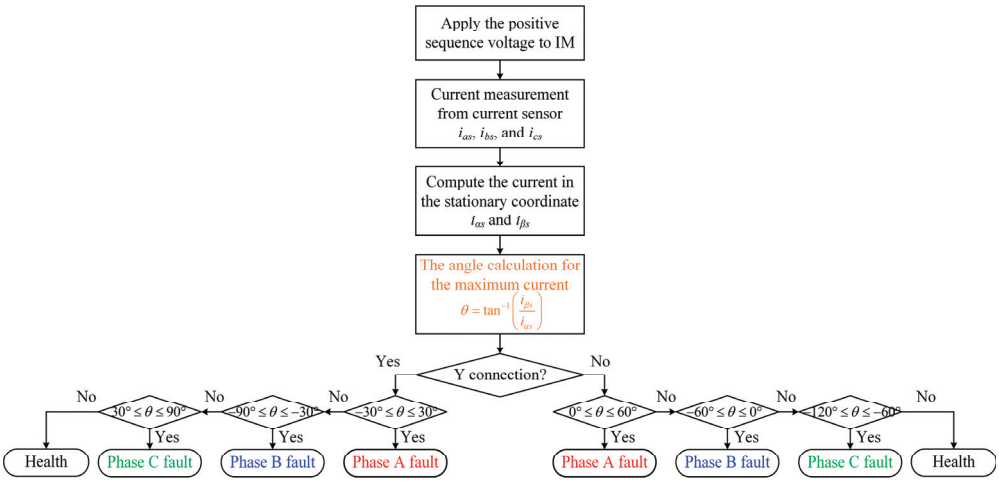


**Figure 6.** ITF diagnosis based on the current vector pattern.

## 4. Experimental Verification

To validate the proposed ITF diagnosis method, experiments were conducted using a 12 kW, four-pole, three-phase IM with both Y and Δ winding configurations. Figure 7a shows the manufactured machine. The stator windings were separated to allow for fault injection in each phase as shown in Figure 7b, and the winding connections were configured via a terminal box as shown in Figure 7a. A TELEDYNE oscilloscope (Teledyne Technologies, Thousand Oaks, CA, USA) was used to capture the current waveforms, while a control desk was employed to manage the inverter and IM operation. The inverter utilized in the experiments was equipped with an SPS600GB10S6 dual-pack MOSFET module from SEMI POWEREX (Seattle, WA, USA). A digital signal processor (DSP), specifically the TMS320F28069, was employed to compute the $\alpha$- and $\beta$-axis current based on the measured three-phase currents, as shown in Figure 8a. The three-phase currents were digitized using an analog-to-digital converter (ADC), and the resulting $\alpha\beta$-axis currents were obtained through coordinate transformation on the DSP. The α- and β-axis currents were converted to analog signals through a digital-to-analog converter (DAC) and monitored using the oscilloscope. The manufactured IM was coupled with a dynamometer to conduct the fault experiment during motor operation, as shown in Figure 8b. ITFs were implemented at the terminal box by connecting a fault resistance (TGHGCR0050FE from OHMITE, Warrenville, IL, USA) in parallel with the fault phase of the IM. Although the nominal value of the fault resistor is 0.5 mΩ, the total resistance increased to approximately 3.5 mΩ due to additional lead wire resistance. To activate the fault during motor operation, an electrical relay was connected in series with the fault resistance and the faulted phase winding, as illustrated in Figure 8c. Figure 8d presents the measured current waveforms before and after the fault through the electrical relay. The experimental parameters, including operating speed,

switching frequency, and motor specifications, are shown in Table 3. The experiments were conducted under low-speed conditions, approximately 200 rpm, to guarantee safety. For each fault phase, the stator currents were measured using the current sensor and observed from the oscilloscope. The current vector patterns during the steady-state operation are illustrated in Figures 9 and 10 for Y and Δ connections, respectively. Under healthy conditions, the current vector formed a nearly circle pattern as shown in Figures 9a and 10a. Upon implementing the faulty condition, the current vector pattern distorted into an ellipse, consistent with the FEA and simulation results, as illustrated in Figures 9b–d and 10b–d. The main axis of the ellipse varied with the faulted phase, demonstrating the algorithm's capability to distinguish not only between healthy and faulty conditions, but also to accurately identify the specific faulted phase. These results validate that the current vector pattern-based fault diagnosis method is effective across different winding configurations.

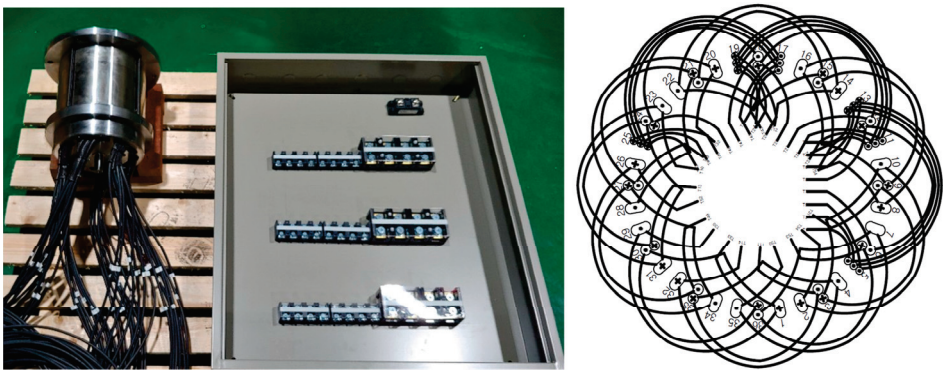

(**a**) (**b**)

**Figure 7.** Manufactured machine: (**a**) IM and terminal box; (**b**) winding configuration.

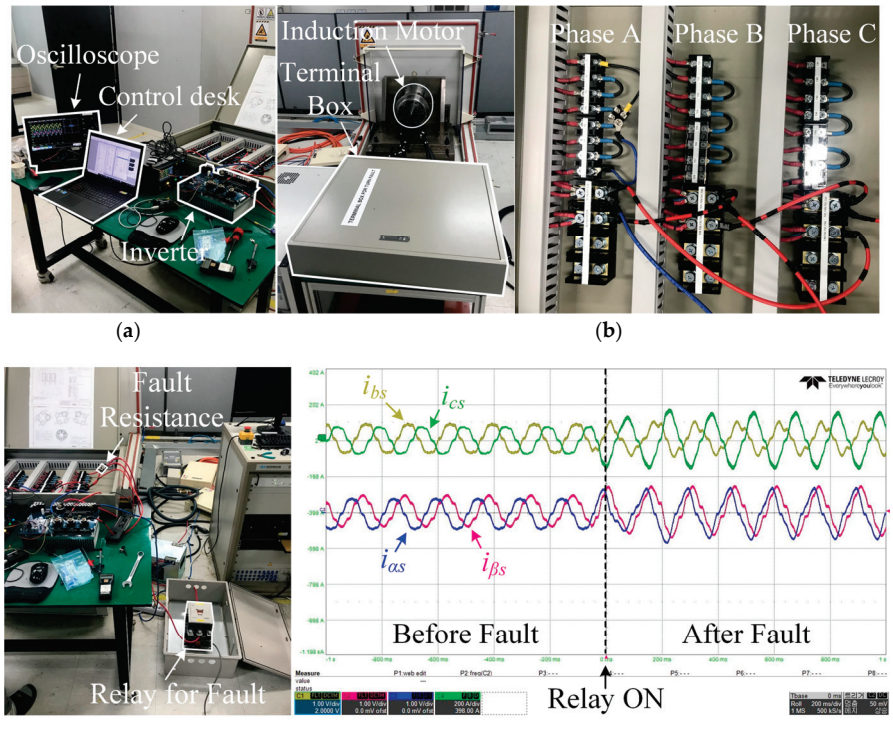


(**a**) (**b**)

(**c**) (**d**)

**Figure 8.** Experiment environment: (**a**) inverter, control desk, and oscilloscope; (**b**) IM, terminal box, and winding; (**c**) fault resistance and relay; (**d**) current waveform.

**Table 3.** Experimental parameters.

| Content | Value | Unit |
|---|---|---|
| Operating speed | 200 | rpm |
| Switching frequency | 500 | Hz |
| Phase resistance | 11.5 | mΩ |
| Phase inductance | 0.6 | mH |
| Fault resistance wo/w lead wire | 0.5/3.5 | mΩ |

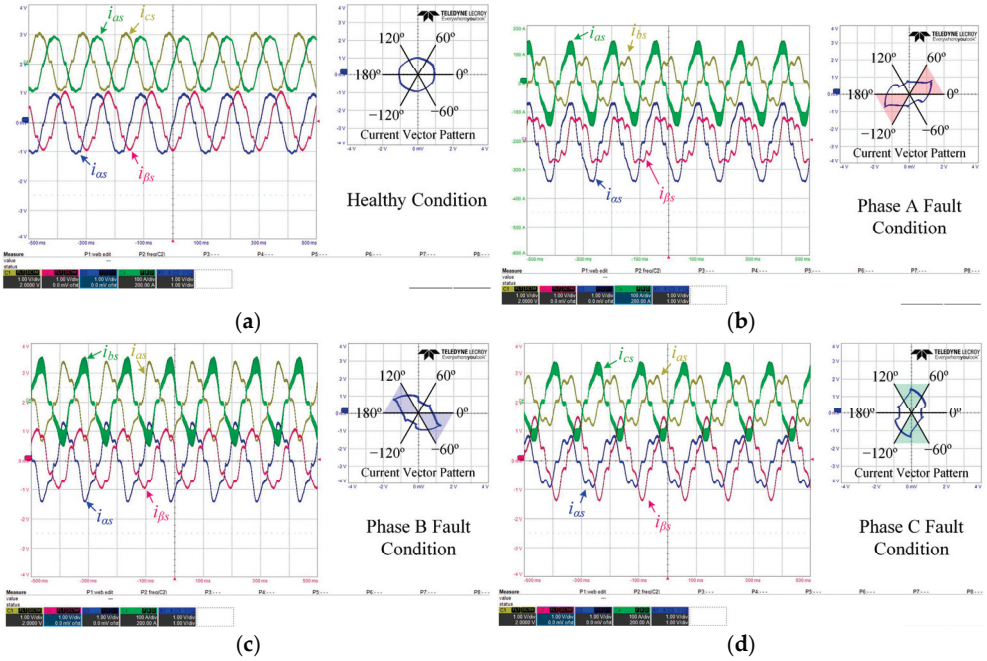


**Figure 9.** Experiment results of IM with Δ connection: (**a**) health condition; (**b**) Phase A fault condition; (**c**) Phase B fault condition; (**d**) Phase C fault condition.

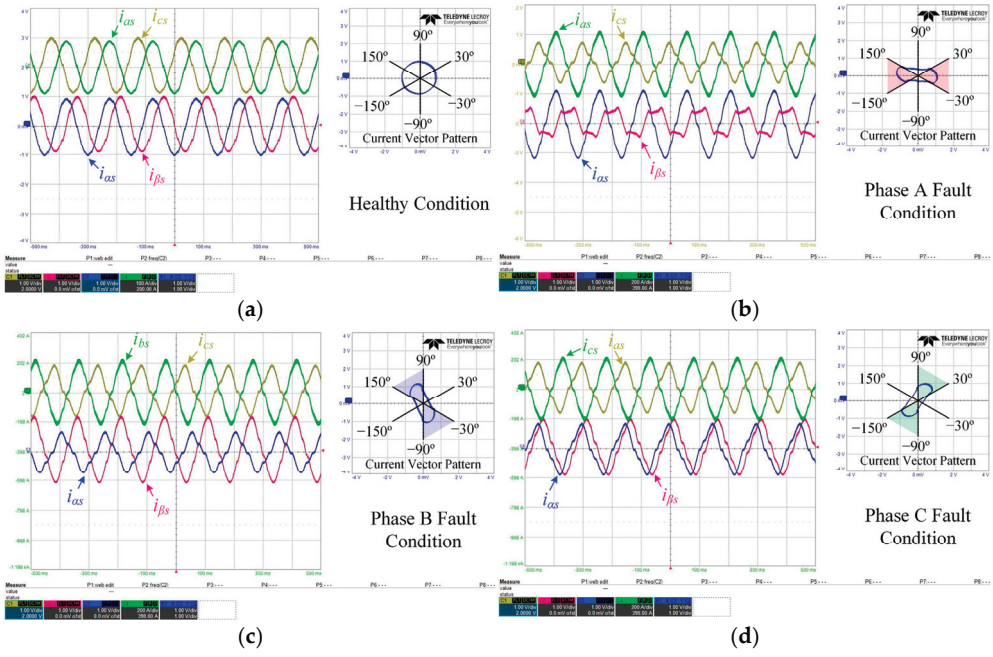


**Figure 10.** Experiment results of IM with Y connection: (**a**) health condition; (**b**) Phase A fault condition; (**c**) Phase B fault condition; (**d**) Phase C fault condition.

## 5. Conclusions

In this study, the current vector patterns of IM with the ITF were analyzed based on a mathematical model, co-simulation, and experiment. When an ITF occurs in an IM, a negative-sequence current is generated, even though only a positive-sequence voltage is applied. The superposition of positive- and negative-sequence components results in an elliptical current vector pattern, which is characteristic of ITFs. The co-simulation with the FEA and circuit simulation was established to analyze the current vector pattern for an ITF in an IM. The angle of the maximum current vector depends on the fault phase and parameters. Based on this relationship, a fault diagnosis algorithm was proposed, which identifies the faulted phase by detecting the angle of the major axis in the stationary coordinate frame. An experimental setup was established using a 12 kW, four-pole, three-phase IM from a RENAULT Twizy and a terminal box for implementing the winding connections to verify the ITF diagnosis algorithm. The current in the stationary coordinate frame was computed in the DSP based on the measured current from current sensor. The current vector pattern was observed using the DAC and ACD of DSP and oscilloscope. The ITF conditions were implemented through the terminal box, and the current vector pattern was analyzed for the fault phase. As a result, the fault diagnosis algorithm was verified by the co-simulation and experimental results. This approach provides an ITF diagnosis during the operation of the IM, and the position sensor, such as encoder and resolver, is not needed because the stationary coordinate transformation is used. Although current vector pattern analysis has been employed for the diagnosis of ITFs in IMs, the detection of other types of faults also requires further investigation. Therefore, future research will focus on extending current pattern analysis methodologies to encompass various fault conditions in IMs, with consideration of the high-frequency IM model and constraints of motor drive systems. In addition, machine learning-based methods will be explored to improve fault classification accuracy, particularly for distinguishing between ITFs, broken rotor bars, and turn-to-turn faults, by utilizing features extracted from current vector patterns.

**Author Contributions:** Conceptualization, I.Y. and H.K.; methodology, H.K.; software, I.Y., S.-G.L. and H.K.; validation, I.Y., S.-G.L. and H.K.; formal analysis, S.-G.L. and H.K.; investigation, I.Y.; resources, I.Y. and J.L.; data curation, I.Y. and H.K.; writing—original draft preparation, I.Y. and H.K.; writing—review and editing, S.-G.L., J.L. and H.K.; visualization, I.Y.; supervision, J.L. and H.K.; project administration, J.L. and H.K.; funding acquisition, J.L. All authors have read and agreed to the published version of the manuscript.

**Funding:** This work was supported by the Korea Institute of Energy Technology Evaluation and Planning (KETEP) grant funded by the Korea government (MOTIE) (No. RS-2023-00237024: Development and Demonstration of Medium-Sized Variable Speed High-Power Motor).

**Institutional Review Board Statement:** Not applicable.

**Informed Consent Statement:** Not applicable.

**Data Availability Statement:** The original contributions presented in this study are included in the article. Further inquiries can be directed to the corresponding author.

**Conflicts of Interest:** The authors declare no conflicts of interest.

## References

1. Xue, C.; Zhou, H.; Wu, Q.; Wu, X.; Xu, X. Impact of Incentive Policies and Other Socio-Economic Factors on Electric Vehicle Market Share: A Panel Data Analysis from the 20 Countries. *Sustainability* **2021**, *13*, 2928. [CrossRef]
2. Zaino, R.; Ahmed, V.; Alhammadi, A.M.; Alghoush, M. Electric Vehicle Adoption: A Comprehensive Systematic Review of Technological, Environmental, Organizational and Policy Impacts. *World Electr. Veh. J.* **2024**, *15*, 375. [CrossRef]

3. Teske, S.; Bratzel, S.; Tellermann, R.; Stephan, B.; Vargas, M. Net Zero: The Remaining Global Market Volume for Internal Combustion Engines in Light-Duty Vehicles under a 1.5 °C Carbon Budget Trajectory. *Energies* **2022**, *15*, 8037. [CrossRef]
4. Memon, M.; Rossi, C. A Review of EV Adoption, Charging Standards, and Charging Infrastructure Growth in Europe and Italy. *Batteries* **2025**, *11*, 229. [CrossRef]
5. Issa, R.; Clerc, G.; Hologne-Carpentier, M.; Michaud, R.; Lorca, E.; Magnette, C.; Messadi, A. Review of Fault Diagnosis Methods for Induction Machines in Railway Traction Applications. *Energies* **2024**, *17*, 2728. [CrossRef]
6. Joksimović, G.; Zajec, P.; Tessarolo, A.; Ambrožič, V.; Rihar, A. Stator Current Spectral Content of Inverter-Fed Cage Rotor Induction Motor. *IEEE Access* **2022**, *10*, 23112–23121. [CrossRef]
7. Asad, B.; Vaimann, T.; Belahcen, A.; Kallaste, A.; Rassõlkin, A.; Ghafarokhi, P.S.; Kudelina, K. Transient Modeling and Recovery of Non-Stationary Fault Signature for Condition Monitoring of Induction Motors. *Appl. Sci.* **2021**, *11*, 2806. [CrossRef]
8. Park, D.-H.; Song, C.-H.; Won, Y.-J.; Park, J.-C.; Kim, H.-S.; Park, H.-R.; Yoon, Y.-D.; Lim, M.-S. Magnetizing Inductance Estimation Method of Induction Motor for EV Traction Considering Magnetic Saturation Changes According to Current and Slip Frequency. *IEEE Trans. Magn.* **2024**, *60*, 1–5. [CrossRef]
9. Yatsugi, K.; Pandarakone, S.E.; Mizuno, Y.; Nakamura, H. Common Diagnosis Approach to Three-Class Induction Motor Faults Using Stator Current Feature and Support Vector Machine. *IEEE Access* **2023**, *11*, 24945–24952. [CrossRef]
10. Jin, L.; Wang, X.; Mao, Y.; Lu, L.; Wang, Z. Online Attribute Matching Based Few-Sample Data-Driven Diagnosis of Electrical Faults in PMSM Drive. *IEEE Trans. Power Electron.* **2024**, *39*, 2620–2631. [CrossRef]
11. Rengifo, J.; Moreira, J.; Vaca-Urbano, F.; Alvarez-Alvarado, M.S. Detection of Inter-Turn Short Circuits in Induction Motors Using the Current Space Vector and Machine Learning Classifiers. *Energies* **2024**, *17*, 2241. [CrossRef]
12. Allal, A.; Lammouchi, Z.; Khechekhouche, A.; Mohamed, N.; Alqunun, K.; Alghadhban, A.; Marouani, I.; Guesmi, T. Advanced Residual Optimal Mapping Approach for Precise Detection of Stator Faults in Induction Motors. *IEEE Access* **2024**, *12*, 143515–143530. [CrossRef]
13. Aswad, R.A.K.; Jassim, B.M.H.; Zahawi, B.; Gadoue, S. Hybrid Model-Based Fuzzy Logic Diagnostic System for Stator Faults in Three-Phase Cage Induction Motors. *IEEE Access* **2023**, *11*, 75707–75714. [CrossRef]
14. Dybkowski, M.; Bednarz, S. Modified Rotor Flux Estimators for Stator-Fault-Tolerant Vector Controlled Induction Motor Drives. *Energies* **2019**, *12*, 3232. [CrossRef]
15. Goh, Y.J.; Kim, O. Linear Method for Diagnosis of Inter-Turn Short Circuits in 3-Phase Induction Motors. *Appl. Sci.* **2019**, *9*, 4822. [CrossRef]
16. Singh, G.; Anil Kumar, T.C.; Naikan, V.N.A. Induction motor inter turn fault detection using infrared thermographic analysis. *Infrared Phys. Technol.* **2016**, *77*, 277–282. [CrossRef]
17. Chen, L.; Shen, J.; Xu, G.; Chi, C.; Feng, Q.; Zhou, Y.; Deng, Y.; Wen, H. Induction Motor Stator Winding Inter-Tern Short Circuit Fault Detection Based on Start-Up Current Envelope Energy. *Sensors* **2023**, *23*, 8581. [CrossRef]
18. Zaparoli, I.O.; Rabelo Baccarini, L.M.; Lamim Filho, P.C.M.; Batista, F.B. Transient envelope current analysis for inter-turn short-circuit detection in induction motor stator. *J. Braz. Soc. Mech. Sci. Eng.* **2020**, *42*, 97. [CrossRef]
19. Niu, G.; Dong, X.; Chen, Y. Motor Fault Diagnostics Based on Current Signatures: A Review. *IEEE Trans. Instrum. Meas.* **2023**, *72*, 1–19. [CrossRef]
20. da Silva, A.M.; Povinelli, R.J.; Demerdash, N.A.O. Induction Machine Broken Bar and Stator Short-Circuit Fault Diagnostics Based on Three-Phase Stator Current Envelopes. *IEEE Trans. Ind. Electron.* **2008**, *55*, 1310–1318. [CrossRef]
21. Ghanbari, T.; Mehraban, A.; Farjah, E. Inter-Turn Fault Detection of Induction Motors Using a Method Based on Spectrogram of Motor Currents. *Measurement* **2022**, *205*, 112180. [CrossRef]
22. Surya, G.N.; Khan, Z.J.; Ballal, M.S.; Suryawanshi, H.M. A simplified frequency-domain detection of stator turn fault in squirrel-cage induction motors using an observer coil technique. *IEEE Trans. Ind. Electron.* **2017**, *64*, 1495–1506. [CrossRef]
23. Rajan Babu, W.; Senthil Kumar, R.; Satheesh Kumar, R. Rigorous investigation of stator current envelope of an induction motor using Hilbert spectrum analysis. *Mater. Today Proc.* **2021**, *45*, 2474–2478. [CrossRef]
24. Almounajjed, A.; Sahoo, A.K.; Kumar, M.K. Diagnosis of stator fault severity in induction motor based on discrete wavelet analysis. *Measurement* **2021**, *182*, 109780. [CrossRef]
25. Jung, J.-H.; Lee, J.-J.; Kwon, B.-H. Online diagnosis of induction motors using MCSA. *IEEE Trans. Ind. Electron.* **2006**, *53*, 1842–1852. [CrossRef]
26. Saucedo-Dorantes, J.J.; Jaen-Cuellar, A.Y.; Perez-Cruz, A.; Elvira-Ortiz, D.A. Detection of Inter-Turn Short Circuits in Induction Motors under the Start-Up Transient by Means of an Empirical Wavelet Transform and Self-Organizing Map. *Machines* **2023**, *11*, 958. [CrossRef]
27. Morales-Perez, C.J.; Camarena-Martinez, D.; Amezquita-Sanchez, J.P.; Rangel-Magdaleno, J.D.J.; Ramírez, E.E.S.; Valtierra-Rodriguez, M. Early Detection of Inter-Turn Short Circuits in Induction Motors Using the Derivative of Stator Current and a Lightweight 1D-ResNet. *Computation* **2025**, *13*, 140. [CrossRef]

28. Cardenas-Cornejo, J.J.; Almanza-Ojeda, D.L.; Gonzáalez-Parada, A.; Hernandez-Ramirez, V.; Ibarra-Manzano, M.A. Complex Signal Analysis for Inter-Turn Short-Circuits Faults on Induction Motors. *IEEE Sens. J.* **2025**, *25*, 13433–13440. [CrossRef]
29. Creux, J.; Haje Obeid, N.; Boileau, T.; Meibody-Tabar, F. Online High Frequency Impedance Identification Method of Inverter-Fed Electrical Machines for Stator Health Monitoring. *Appl. Sci.* **2024**, *14*, 10911. [CrossRef]
30. Vinayak, B.A.; Alam, M.F.; Jagadanand, G.; Anand, K.A. Stator Inter Turn Fault Diagnosis by High-Frequency Modeling of Inverter Fed Induction Motor. In Proceedings of the 2020 IEEE International Conference on Power Electronics, Smart Grid and Renewable Energy (PESGRE2020), Cochin, India, 2–4 January 2020; pp. 1–5.
31. Zhao, Z.; Fan, F.; Wang, W.; Liu, Y.; See, Y.K. Detection of Stator Interturn Short-Circuit Faults in Inverter-Fed Induction Motors by Online Common-Mode Impedance Monitoring. *IEEE Trans. Instrum. Meas.* **2021**, *70*, 1–10. [CrossRef]
32. Fan, F.; Zhao, Z.; Jie, H.; Sun, Q.; Tu, P.; Shu, Z.; Wang, W.; See, K.Y. Impact of Motor Stator Winding Faults on Motor Differential-Mode Impedance and Mode Transformation. *Chin. J. Electr. Eng.* **2022**, *8*, 12–21. [CrossRef]
33. Jie, H.; See, K.Y.; Chang, Y.; Gao, R.X.-K.; Fan, F.; Zhao, Z. Enhancing motor impedance measurements: Broadening the spectrum from low to high frequencies. *Meas. Sci. Technol.* **2024**, *35*, 86008. [CrossRef]
34. Tallam, R.M.; Habetler, T.G.; Harley, R.G. Transient Model for Induction Machines with Stator Winding Turn Faults. *IEEE Trans. Ind. Appl.* **2002**, *38*, 632–637. [CrossRef]


**Disclaimer/Publisher's Note:** The statements, opinions and data contained in all publications are solely those of the individual author(s) and contributor(s) and not of MDPI and/or the editor(s). MDPI and/or the editor(s) disclaim responsibility for any injury to people or property resulting from any ideas, methods, instructions or products referred to in the content.

*applied sciences*

MDPI

*Article*

# Impedance-Based Inter-Turn Fault Diagnosis in Integrated Induction Motor and Drive Systems Using Space Voltage Vectors

**Jungho Ahn [1], Ju Lee [1] and Hyunwoo Kim [2,*]**

[1] Department of Electrical Engineering, Hanyang University, Seoul 04763, Republic of Korea; ahnleo@hanyang.ac.kr (J.A.); julee@hanyang.ac.kr (J.L.)
[2] Elmore Family School of Electrical and Computer Engineering, Purdue University, West Lafayette, IN 47907, USA
* Correspondence: kim4852@purdue.edu

**Abstract:** In this paper, a winding inter-turn fault (ITF) diagnosis algorithm for electrical machines in integrated motor and drive (IMD) systems is proposed based on impedance analysis using space voltage vectors. An ITF alters the stator resistance, causing an imbalance in the motor's impedance depending on the phase connection. This impedance asymmetry can be effectively utilized for fault diagnosis. However, in IMD systems, direct impedance measurement through mechanical terminal access is difficult due to the integrated structure. To address this, the impedance of the induction motor is analyzed electrically, without the need for physical disconnection, allowing practical implementation within integrated systems. The specific phase angle of the space voltage vector in the three-phase inverter is analyzed to replicate the electrical conditions of mechanical terminal configurations. Based on this approach, a fault diagnosis algorithm was developed by analyzing the variation in stator current and impedance with respect to space voltage vector angles. The effectiveness of the proposed method was verified through experimental validation using a 12kW three-phase induction motor and terminal box.

**Keywords:** fault diagnosis; integrated motor and drive (IMD); intern-turn fault (ITF); three-phase inverter; space voltage vector

## 1. Introduction

With the recent rapid growth of the electric vehicle (EV) industry, integrated motor and drive (IMD) systems, which simultaneously provide high power density and efficiency, have attracted significant attention across various industrial sectors [1,2]. IMD systems offer several advantages, including reduced installation space, lower wiring losses, suppression of electromagnetic interference, and improved overall system efficiency [3,4]. Furthermore, an IMD system enables the elimination of components such as transformers and filters and offers the benefits of an optimized cooling structure and modular design, making it particularly well suited for EV applications that demand high power density [5,6]. In line with this trend, extensive research has been conducted on compact, high-frequency IMD systems that employ PCB-based stators and GaN-based switching devices. Integrated designs incorporating GaN devices capable of operating at frequencies above 1 MHz have emerged as promising solutions for both reducing system size and suppressing current ripple [7,8].

Electrical faults such as inter-turn faults (ITFs), bearing failures, and insulation breakdowns in motors—critical components in EV systems—can lead to system shutdowns, fires,

and serious safety incidents during operation. As a result, diagnostic technologies, including fault-tolerant design approaches, have become increasingly important [9]. In particular, autonomous driving systems require immediate fault response and sustained control system stability due to the limited possibility of driver intervention [10,11]. Recent studies have applied hybrid optimization algorithms for fault diagnosis and parameter estimation in power systems and electrical drives. These approaches offer improved robustness and accuracy in noisy or nonlinear environments [11,12].

Motor faults that can occur during operation are diverse, and diagnostic approaches and countermeasures vary depending on the fault type. In general, motor faults are categorized into electrical, magnetic, and mechanical faults [13]. Electrical faults include inter-turn short circuits (ITSCs), phase-to-phase short circuits, and phase-to-ground faults [14–17]. Magnetic faults consist of demagnetization and magnetic asymmetry [18,19], while mechanical faults include bearing failures, rotor eccentricity, broken rotor bars, and air-gap asymmetry. Other possible faults include sensor failures and inverter faults [20–22]. Among these, ITSC faults are considered the most severe, as they can lead to total winding failure within a short period and generate significant torque ripple [23,24]. This occurs because a localized short between turns produces extremely high circulating currents, resulting in severe overheating, insulation breakdown, and ultimately catastrophic motor failure or even fire [25,26]. In particular, ITFs can rapidly destroy the entire winding and, in the case of permanent magnet (PM) motors, may even cause magnet demagnetization, posing a serious threat to overall system reliability [27,28].

Various methods have been developed to diagnose ITFs due to their severity. These methods are considered to be among the most critical aspects of motor fault diagnosis [28–33]. In [28–30], the widely adopted approach of motor current signature analysis (MCSA) is introduced. MCSA techniques are generally categorized into FFT-based spectrum analysis, time–frequency analysis (e.g., wavelet transform and Hilbert–Huang transform), and other methods. However, spectrum-analysis-based methods are highly sensitive to high-frequency noise and load variations, which can degrade diagnostic reliability. In [27], artificial intelligence (AI)-based diagnostic techniques, including neural networks and support vector machines (SVMs), have also been actively explored. However, AI-based approaches require large amounts of labeled fault data for effective training, and acquiring sufficient and diverse fault data under various operating conditions remains a major challenge in real-world industrial environments. Furthermore, conventional model-based methods require complex mathematical modeling and are susceptible to uncertainties in motor parameters [31,32].

ITF diagnosis based on impedance analysis in induction motors (IMs) was introduced in a previous study [33]. The impedance characteristics of six winding connections were analyzed, and the phase of impedance was calculated to diagnose the ITF. The six winding connections are required to calculate the phase of impedance for ITF diagnosis. Although the introduced ITF diagnosis method is simplified compared to other methods, it presents practical limitations when applied to real industrial systems such as electric vehicles (EVs), which commonly utilize IMD systems. In these systems, the physical disconnection of the inverter from the motor is required to perform offline measurements, which significantly limits the applicability of the approach in IMD systems.

This paper proposes an offline ITF diagnosis algorithm for IMD systems based on impedance analysis and the space voltage vector control of a three-phase inverter. The proposed method enables fault detection without mechanical separation between the motor and the inverter, making it highly suitable for IMD-based applications. Assuming an ITF occurs in phase A, the terminal impedances are analyzed and compared to identify the maximum and minimum impedance values. Although ITFs can be diagnosed through

terminal resistance measurements, the terminal configuration in IMD systems differs due to the integrated structure of the motor and inverter. Therefore, the space voltage vector of the three-phase inverter is analyzed for each switching state. A fault diagnosis algorithm is proposed based on both the impedance characteristics and the space voltage vector analysis. To validate the proposed algorithm, an experimental setup was constructed using a 12 kW three-phase induction motor (IM), an inverter, fault resistance, and a terminal box for winding connections. The algorithm was verified for both Y and Δ connections without requiring access to mechanical terminal connections.

Here, we provide a summary of the main contributions of our work:

(1) To diagnose the ITF, the impedance of electrical machine is analyzed for the terminal connection. The terminal connection is implemented electrically through the space vector control of the three-phase inverter, eliminating the need for inverter disconnection or access to terminal connections when the ITF of the electrical machine is diagnosed.

(2) The proposed method does not require the tracking of time-varying operational parameters, thereby simplifying implementation compared to online diagnostic approaches. Furthermore, a low-complexity algorithm based on phase impedance comparison across six space voltage vectors is employed, enhancing compatibility with embedded systems and real-time control platforms.

(3) A 12 kW three-phase IM was manufactured, and an experimental environment was implemented to verify the proposed algorithm for ITF diagnosis. The proposed ITF diagnosis algorithm was verified through the measurement of impedance for the space voltage vector for Y and Δ connections.

This paper is organized as follows: Section 2 describes the analysis of the impedance characteristics under ITF conditions in phase A for both Y and Δ connections. Section 3 presents the space voltage vector analysis corresponding to inverter switching states and proposes the ITF diagnosis algorithm based on impedance variation. Section 4 describes the experimental validation using the fabricated IM and terminal box. Section 5 concludes the paper.

## 2. Impedance Analysis of Inter-Turn Fault of Induction Motor

### *2.1. Mathematical Model of Induction Motor with Inter-Turn Fault*

Figure 1 shows the configuration of an induction motor under ITF conditions with Y and delta connections. In the event of an ITF in phase A, fault resistance appears in parallel with the winding of the faulty phase. This additional parallel path results in reduced impedance in the fault phase, leading to an imbalance in the per-phase impedance of the stator. The resulting asymmetry in impedance can be effectively utilized as a diagnostic feature for identifying ITF in induction motors. The impedance of healthy and fault phases can be expressed as follows:

$$Z_h = R_a + j\omega L_a \tag{1}$$

$$Z_f = \frac{R_f(R_{a1} + j\omega L_{a1})}{R_{a1} + j\omega L_{a1} + R_f} + R_{a2} + j\omega L_{a2} \tag{2}$$

where

$$R_a = R_{a1} + R_{a2}, \;\; L_a = L_{a1} + L_{a2}, \tag{3}$$

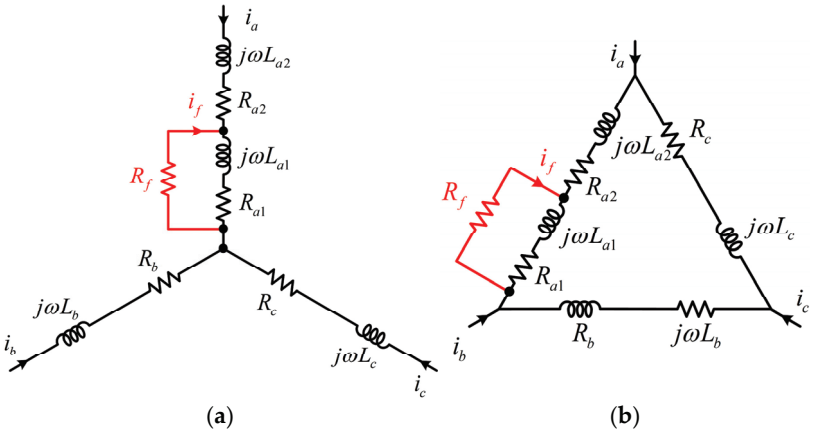


**Figure 1.** Configuration of inter-turn fault in IM: (**a**) Y connection; (**b**) Δ connection.

$Z_h$ and $Z_f$ denote the impedances of healthy and fault phases, respectively. $R_a$ and $L_a$ represent the phase resistance and inductance of the healthy phase, respectively. $R_{a1}$ and $L_{a1}$ are the resistance and inductance of the fault phase with the fault resistance connected in parallel. $R_{a2}$ and $L_{a2}$ denote the resistance and inductance of the fault phase without the fault resistance. $R_f$ is the fault resistance, and $\omega$ is the electrical angular speed. By subtracting Equation (3) from Equation (2), the impedance of the fault phase is expressed as follows:

$$\begin{aligned} Z_f &= \frac{R_f(R_{a1}+j\omega L_{a1})}{R_{a1}+j\omega L_{a1}+R_f} + R_a - R_{a1} + j\omega(L_a - L_{a1}) \\ &= Z_h - \frac{(R_{a1}+j\omega L_{a1})\left(R_{a1}+j\omega L_{a1}-R_f\right)}{R_{a1}+j\omega L_{a1}+R_f}. \end{aligned} \tag{4}$$

Since the fault resistance is connected in parallel with the phase impedance, the fault phase impedance becomes lower than that of the healthy phase, as shown in Equation (4). This indicates that impedance imbalance occurs under ITF conditions, and the impedance of the fault phase is lower than that of the healthy phase. In the next subsection, the impedance analysis of the motor connection is provided to propose the fault diagnosis.

### *2.2. Impedance Analysis with Y Connection*

When an ITF occurs in phase A, the terminal connection is considered to analyze the impedance for the Y connection, as shown in Figure 2. The impedance analysis is conducted for the terminal connection configuration. When the two phases are connected as shown in Figure 2a–c, the terminal impedance can be expressed as follows:

$$Z_{a-b} = Z_{c-a} = Z_f + Z_h, \quad Z_{b-c} = 2Z_h \tag{5}$$

where $Z_{a\text{-}b}$, $Z_{c\text{-}a}$, and $Z_{b\text{-}c}$ denote the terminal impedances corresponding to the connections between phases A and B, C and A, and B and C, respectively. Since the fault impedance is lower than the healthy impedance, as shown in Equation (4), the terminal impedance comparison is as follows.

$$Z_{a-b} - Z_{b-c} = Z_f - Z_h < 0 \;\; \rightarrow \;\; Z_{a-b} = Z_{c-a} < Z_{b-c} \tag{6}$$

From Equation (6), the specific terminal impedance is greater than the other terminal impedances. If an ITF occurs in a different phase, the specific terminal impedance increases when the two corresponding phases are connected.

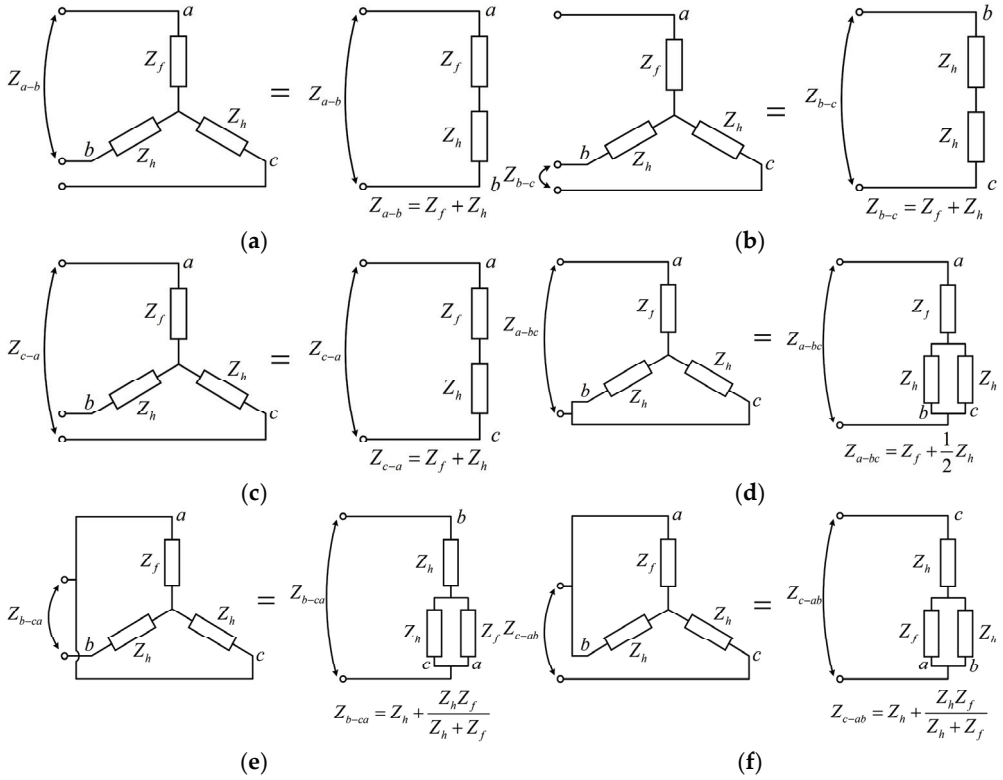


**Figure 2.** Impedance analysis for a Y connection with a phase A fault: (**a**) *a-b*; (**b**) *b-c*; (**c**) *c-a*; (**d**) *a-bc*; (**e**) *b-ca*; (**f**) *c-ab*.

The impedance for the terminal connection between phase A and the midpoint of phases B and C, denoted as $Z_{a\text{-}bc}$ and shown in Figure 2f, is calculated as in Equation (7).

$$Z_{a-bc} = Z_f + Z_h \,||\, Z_h = Z_f + \frac{1}{2}Z_h \tag{7}$$

Similarly, the impedances for connections *b-ca* and *c-ab*, represented in Figure 2d,e, are given by Equation (8).

$$Z_{b-ca} = Z_{c-ab} = Z_h + Z_f \,||\, Z_h = Z_h + \frac{Z_f Z_h}{Z_f + Z_h} \tag{8}$$

A comparison between (7) and (8) reveals that the impedance of the *a-bc* configuration is greater than those of the *b-ca* and *c-ab*, as summarized in Equation (9).

$$\begin{aligned} &Z_{a-bc} - Z_{b-ca} = \frac{\left(Z_f - Z_h\right)\left(2Z_f + Z_h\right)}{2\left(Z_f + Z_h\right)} < 0 \\ &Z_{a-bc} < Z_{b-ca} = Z_{c-ab} \end{aligned} \tag{9}$$

From Equation (9), the specific impedance of a given terminal connection configuration is lower than that of the other configurations. If a fault occurs in phase B or C, the impedance becomes either maximum or minimum, depending on the specific terminal connection. Table 1 presents the maximum and minimum impedance values for each fault phase and terminal connection when an ITF occurs in phase A with the Y connection.

**Table 1.** Impedance analysis results for a Y connection with a phase A fault.

| Fault Phase | Maximum Impedance among $Z_{a\text{-}b}$, $Z_{b\text{-}c}$, and $Z_{c\text{-}a}$ | Minimum Impedance among $Z_{a\text{-}bc}$, $Z_{b\text{-}ca}$, and $Z_{c\text{-}ab}$ |
|---|---|---|
| A | $Z_{b\text{-}c}$ | $Z_{a\text{-}bc}$ |
| B | $Z_{c\text{-}a}$ | $Z_{b\text{-}ca}$ |
| C | $Z_{a\text{-}b}$ | $Z_{c\text{-}ab}$ |

### *2.3. Impedance Analysis with Δ Connection*

Figure 3 illustrates the terminal configuration of an IM with a Δ connection when an ITF occurs in phase A. As shown in Figure 3, three terminals are available, enabling various inter-terminal connection configurations. Depending on the selected terminal pair, the measured impedance varies due to the presence of fault resistance in the affected phase. The impedance measured between phases A and B, as shown in Figure 3a, is expressed in Equation (10).

$$Z_{a-b} = Z_f \,||\, 2Z_h = \frac{2Z_f Z_h}{Z_f + 2Z_h} \tag{10}$$

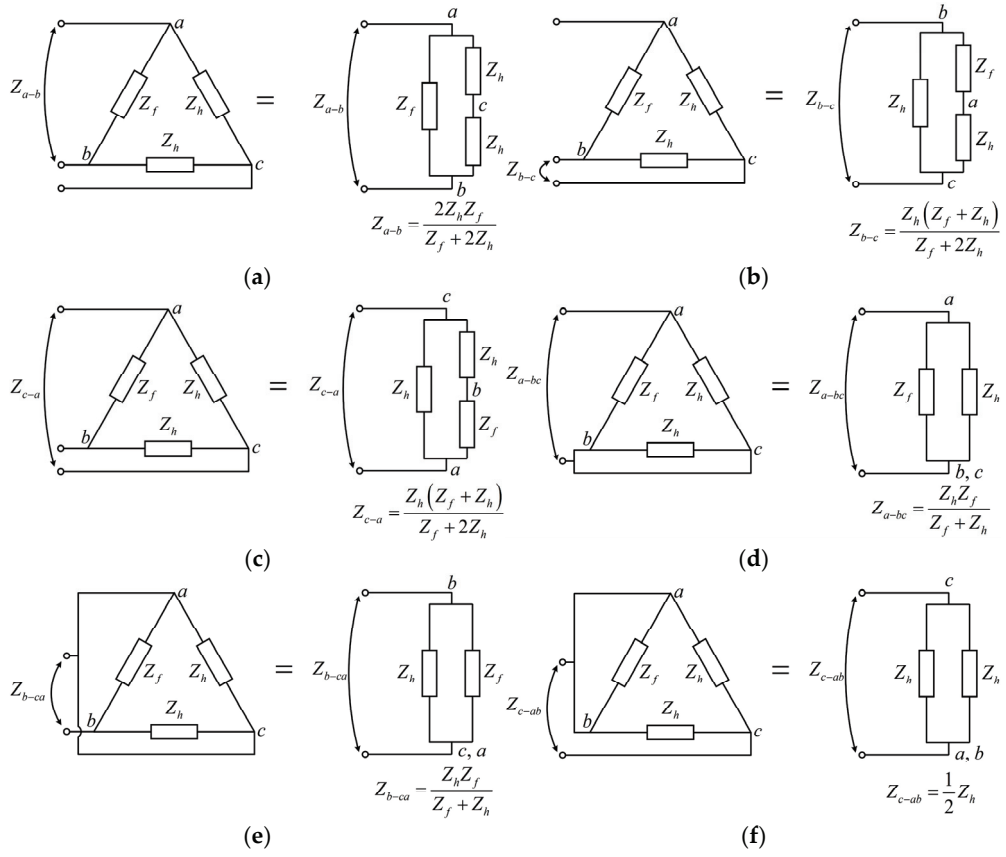


**Figure 3.** Impedance analysis for a Δ connection with a phase A fault: (**a**) *a-b*; (**b**) *b-c*; (**c**) *c-a*; (**d**) *a-bc*; (**e**) *b-ca*; (**f**) *c-ab*.

In the same way, the impedance values for terminal pairs *b-c* and *c-a*, corresponding to Figure 3b,c, are described in Equation (11).

$$Z_{b-c} = Z_{c-a} = Z_h \,||\, (Z_f + Z_h) = \frac{Z_h(Z_f + Z_h)}{Z_f + 2Z_h} \tag{11}$$

Under ITF conditions, the impedance of the fault phase decreases due to the fault resistance being placed in parallel with the stator winding. As a result, the impedance of

the *a-b* connection becomes lower than those of the *b-c* and *c-a* connections, as demonstrated in Equation (12).

$$\begin{aligned} Z_{a-b} - Z_{b-c} &= \frac{Z_h(Z_f - Z_h)}{Z_f + 2Z_h} < 0 \\ Z_{a-b} &< Z_{b-c} = Z_{c-a} \end{aligned} \tag{12}$$

The impedance for the terminal connection between c and the midpoint of *a-b*, denoted as *c-ab* and shown in Figure 3f, is calculated as in Equation (13).

$$Z_{c-ab} = Z_h \,||\, Z_h = \frac{1}{2} Z_h \tag{13}$$

Likewise, the impedances for connections *a-bc* and *b-ca*, represented in Figure 3d,e, are given by Equation (14).

$$Z_{a-bc} = Z_{b-ca} = Z_f \,||\, Z_h = \frac{Z_f Z_h}{Z_f + Z_h} \tag{14}$$

A comparison of Equations (13) and (14) reveals that the impedance of the *c-ab* configuration is greater than those of the *a-bc* and *b-ca* connections, as summarized in Equation (15).

$$\begin{aligned} Z_{c-ab} - Z_{a-bc} &= \frac{Z_h}{2} \frac{Z_h - Z_f}{Z_f + Z_h} > 0 \\ Z_{c-ab} &> Z_{a-bc} = Z_{b-ca} \end{aligned} \tag{15}$$

When a fault occurs in phase B or C, the impedance becomes either a maximum or a minimum, depending on the specific terminal connection. Table 2 presents the maximum and minimum impedance values for each fault phase and terminal configuration. This information enables effective ITF diagnosis based on impedance characteristics.

**Table 2.** Impedance analysis results for Δ connection with phase A fault.

| Fault Phase | Minimum Impedance among $Z_{a\text{-}b}$, $Z_{b\text{-}c}$, and $Z_{c\text{-}a}$ | Maximum Impedance among $Z_{a\text{-}bc}$, $Z_{b\text{-}ca}$, and $Z_{c\text{-}ab}$ |
|---|---|---|
| A | $Z_{a\text{-}b}$ | $Z_{c\text{-}ab}$ |
| B | $Z_{b\text{-}c}$ | $Z_{a\text{-}bc}$ |
| C | $Z_{c\text{-}a}$ | $Z_{b\text{-}ca}$ |

However, in IMD systems, such as those used in electric vehicles, mechanical access to motor terminals is often limited or impractical. A diagnostic approach based on space voltage vector control is proposed to address this limitation by emulating terminal connection conditions electrically, without physical rewiring.

## 3. Inter-Turn Fault Diagnosis of Integrated Motor and Drive Systems

As shown in Section 2, impedance is analyzed for the terminal configuration when an ITF occurs in phase A with both Y and Δ connections. Physical terminal access is required to measure impedances. However, such access is often limited or impractical in IMD systems. In this section, the space voltage vector method is employed to analyze the impedance.

### *3.1. Space Voltage Vector in Three-Phase Inverter*

There are six switching components in a three-phase inverter, as shown in Figure 4a. Each phase has two switching states (ON and OFF), resulting in three possible configurations: (1) upper switch ON, lower switch OFF: '1'; (2) upper switch OFF, lower switch

ON: '0'; (3) both switches OFF: '-'. In a three-phase inverter, the possible voltage states are expressed as shown in Figure 4b. The space voltage vector is defined as follows:

$$\mathbf{V} = V_m e^{j\theta_m} \tag{16}$$

where $\mathbf{V}$ is the space voltage vector, $V_m$ is the magnitude of the space voltage vector, and $\theta_m$ is the phase angle of the space voltage vector. The space voltage vector is determined by the switch states for each phase. Table 3 shows the phase angles of the space voltage vector corresponding to each switching state.

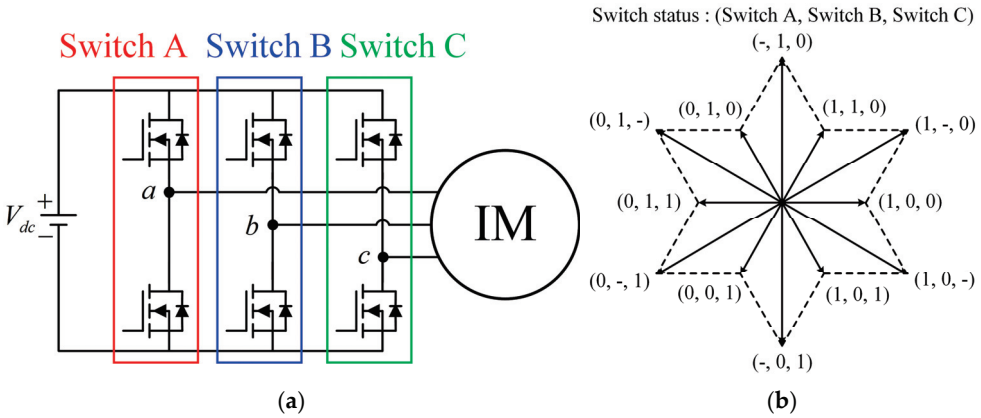


**Figure 4.** Three-phase inverter configuration and space voltage vectors for switching conditions: (**a**) integrated motor and drive system; (**b**) space voltage vectors based on switching conditions for each phase.

**Table 3.** Phase of space voltage vector for switching conditions.

| Phase A Switch | Phase B Switch | Phase C Switch | Phase of Voltage Vector [°] |
|---|---|---|---|
| 1 | 0 | 0 | 0 |
| 1 | - | 0 | 30 |
| 1 | 1 | 0 | 60 |
| - | 1 | 0 | 90 |
| 0 | 1 | 0 | 120 |
| 0 | 1 | - | 150 |
| 0 | 1 | 1 | 180 |
| 0 | - | 1 | 210 |
| 0 | 0 | 1 | 240 |
| - | 0 | 1 | 270 |
| 1 | 0 | 1 | 300 |
| 1 | 0 | - | 330 |

### *3.2. Terminal Connection for Space Voltage Vector*

Since the space voltage vector is determined by the switching states for each phase, as shown in Figure 4 and Table 3, the terminal connection is implemented for the space voltage vector as shown in Figure 5. In the phase with a space voltage vector of 0° the resulting terminal connection corresponds to *a-bc*, as illustrated in Figure 5a. At 30°, the configuration results in a terminal connection equivalent to *c-a*, as shown in Figure 5b. In the same way, each space voltage vector position shown in Figure 5 yields an electrical connection that corresponds directly to a specific mechanical terminal connection described in Figures 2 and 3. Table 4 summarizes the relationship between the phase of the space voltage vector and the equivalent terminal connections. This correspondence demonstrates

that terminal connections can be realized based on the space voltage vector in the three-phase inverter. The alternating voltage is applied to the motor for the space voltage vector, and the calculated impedance from the measured phase current can be used in the fault diagnosis, as shown in Section 2. As a result, ITF diagnosis can be achieved electrically without the need for the physical reconnection of motor terminals in IMD systems.

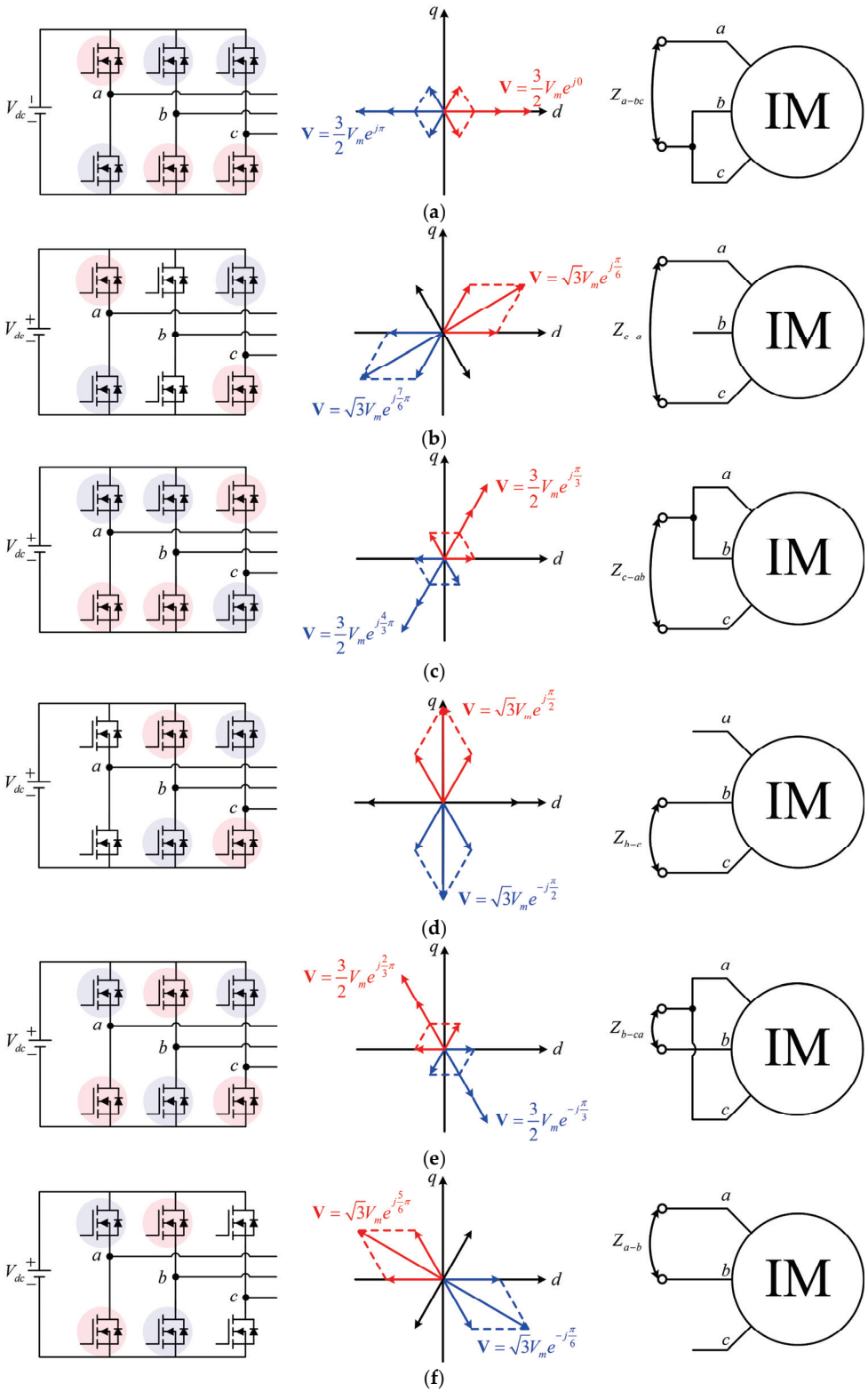


**Figure 5.** Switching status, space voltage vector, and terminal connection in IMD with three-phase inverter: (**a**) 0°; (**b**) 30°; (**c**) 60°; (**d**) 90°; (**e**) 120°; (**f**) 150°.

**Table 4.** Terminal connections for phases of space voltage vector.

| Phase of Space Voltage Vector [°] | Terminal Connection |
|---|---|
| 0 and 180 | *a-bc* |
| 30 and 210 | *c-a* |
| 60 and 240 | *c-ab* |
| 90 and 270 | *b-c* |
| 120 and 300 | *b-ca* |
| 150 and 330 | *a-b* |

### *3.3. Fault Diagnosis Algorithm*

The terminal connections are implemented based on the space voltage vector by the three-phase inverter. Based on the impedance and space voltage vector, the ITF algorithm is proposed as shown in Figure 6. The alternating voltage is applied to the motor according to the phase of the space voltage vector through the three-phase inverter. The impedances corresponding to each phase of the space voltage vector are calculated from the input voltage and measured phase currents. The fault diagnosis is performed by identifying the maximum and minimum impedances associated with each phase of the space voltage vector. For example, when an ITF occurs in phase A with the Δ connection, the phases of the space voltage vector corresponding to the maximum and minimum impedance values are 60° and 150°, respectively, as shown in Figure 6b. In the same way, when the ITF occurs in phase B or C, the fault diagnosis can be performed as shown in Figure 6.

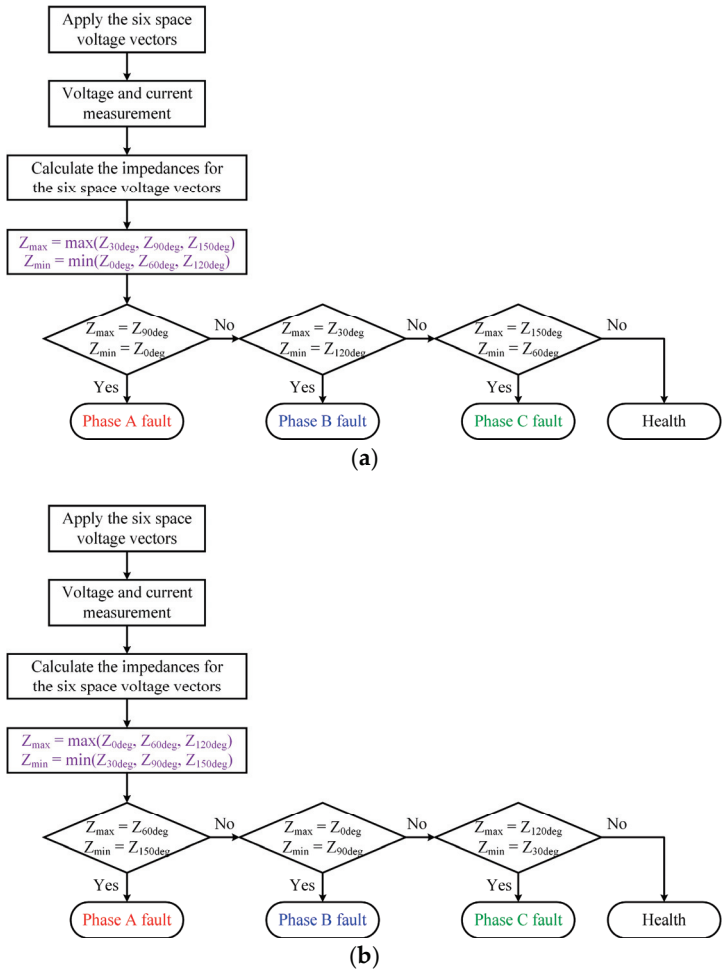


**Figure 6.** Inter-turn fault diagnosis algorithm: (**a**) Y connection; (**b**) Δ connection.

## 4. Experimental Verification

This section presents the experimental verification of the proposed fault diagnosis algorithm. A 12 kW three-phase IM from RENAULT TWIZY, used for EV applications, is described in Table 5. The motor parameters and fault resistance were measured using the impedance analyzer. The phase resistance of the IM was 11.5 mΩ, and a fault resistance of 3.6 mΩ was considered. Figure 7 shows the manufactured IM and terminal box used to implement the winding connections and simulate fault conditions. The windings of the IM were separated, as shown in Figure 8, and connected through the terminal box. The experimental setup for ITF diagnosis is shown in Figure 9. The test motor was coupled to a dynamometer system, and both Y and Δ connections were implemented through the terminal box. A three-phase inverter was used to apply the space voltage vector to the IM. Fault diagnosis was conducted with both Y and Δ connections, as illustrated in Figure 10. The fault resistance was connected in parallel with the faulty phase. The voltage and current were measured using voltage and current sensors, such as the HAH1DR series from LEM, and the impedance was calculated for each space voltage vector. The measured voltage and current were converted to digital values using an analog-to-digital converter in a digital signal processor (DSP), specifically the TMS320F28069, to enable impedance calculation. Moreover, the calculated impedance, the phase of the space voltage vector, and the diagnostic status were converted back to analog signals via the DSP's digital-to-analog converter and displayed on an oscilloscope. The experimental results for the Y and Δ connections are shown in Figures 11 and 12, respectively. As shown in Figure 11, when an ITF occurs in phase A, the impedance reaches its maximum at a phase angle of 90° and its minimum at 0°, corresponding to the specific phase angles of the space voltage vector in the three-phase inverter. When the fault occurs in phase B, the maximum impedance is observed at 30° and the minimum at 120°. Similarly, for a fault in phase C, the impedance is maximized at 150° and minimized at 60°. As demonstrated in Figure 12, the measured impedance values for each fault condition were analyzed based on measured currents. By comparing the impedance at each space voltage vector phase, the presence and location of the fault are determined based on the fault diagnosis algorithm shown in Figure 6. As shown in Figures 11 and 12, the fault diagnosis algorithm was verified and conducted within 3.5 s.

**Table 5.** Specification of test motor.

| Contents | Value | Unit |
|---|---|---|
| DC voltage | 52 | V |
| Power | 12 | kW |
| Current | 248 | Arms |
| Phase resistance | 11.5 | mΩ |
| Phase inductance | 0.6 | mH |
| Fault resistance | 3.6 | mΩ |
| Frequency of space voltage vector | 500 | Hz |

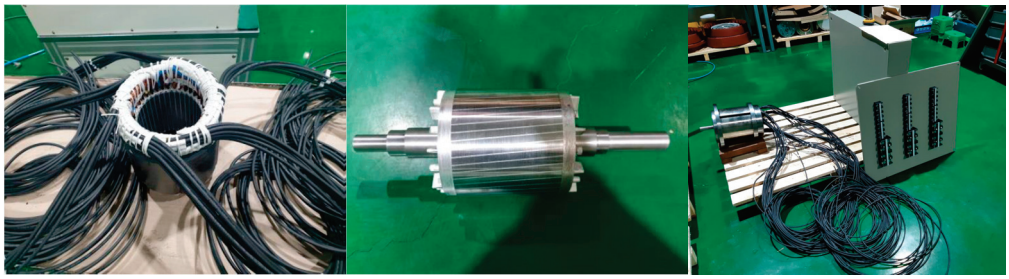

(**a**) (**b**) (**c**)

**Figure 7.** Manufacture and experimental environment: (**a**) stator; (**b**) rotor; (**c**) terminal box.

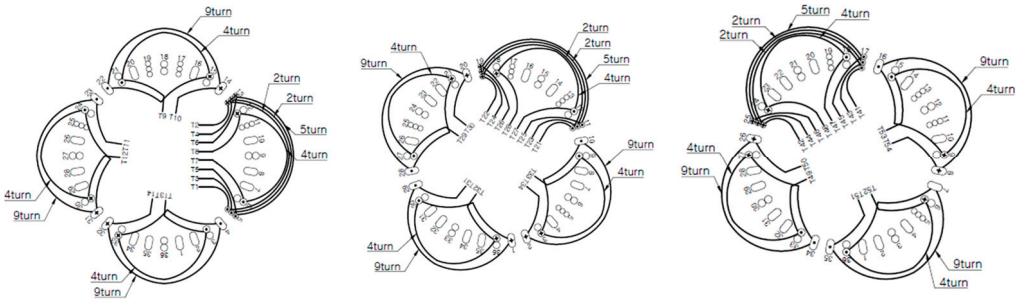


(**a**) (**b**) (**c**)

**Figure 8.** Winding configuration for validation of inter-turn fault algorithm: (**a**) phase A; (**b**) phase B; (**c**) phase C.

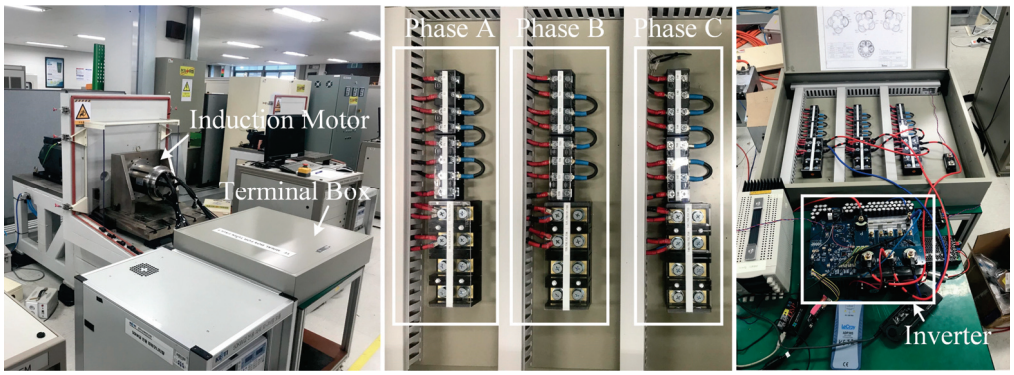


(**a**) (**b**) (**c**)

**Figure 9.** Experimental environment for inter-turn fault diagnosis: (**a**) motor and terminal box; (**b**) fault situation; (**c**) inverter for fault diagnosis.

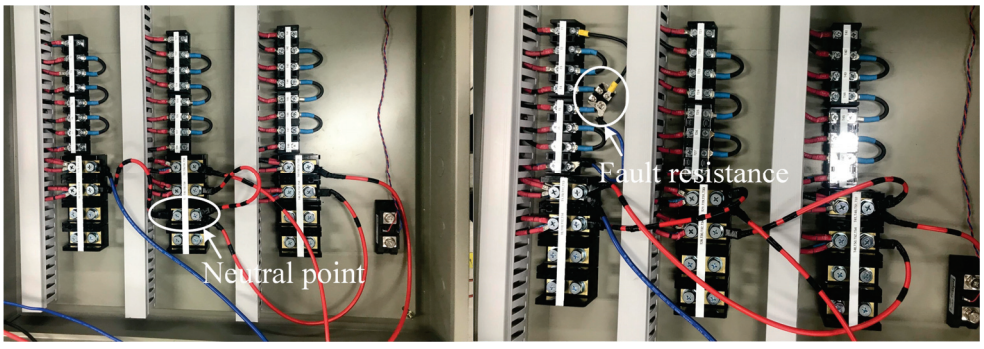


(**a**) (**b**)

**Figure 10.** Connections for experiment: (**a**) Y connection; (**b**) Δ connection.

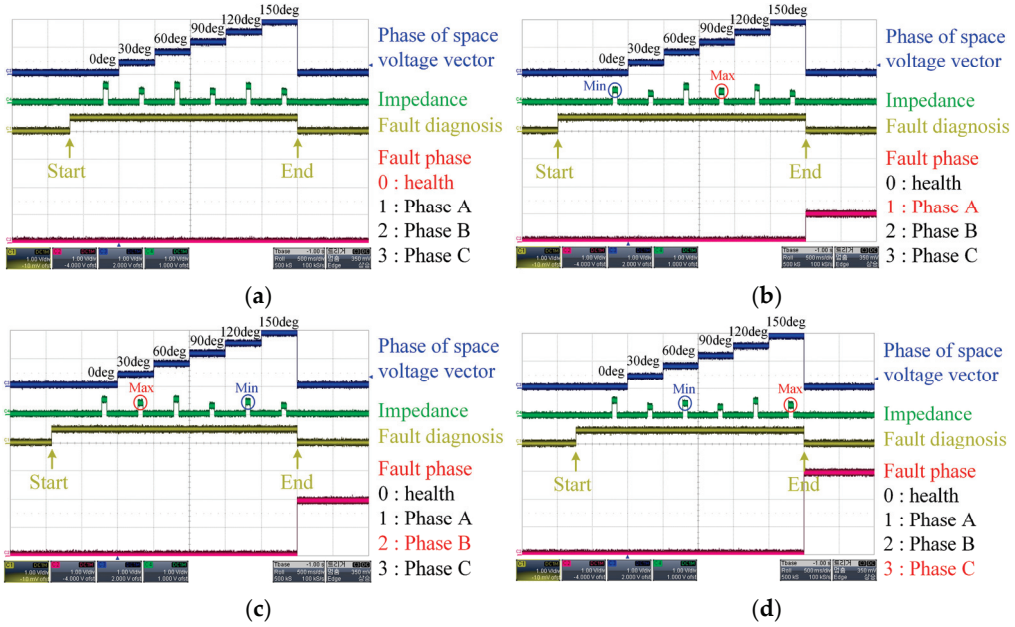


**Figure 11.** Experiment results for Y connection: (**a**) healthy; (**b**) fault phase A; (**c**) fault phase B; (**d**) fault phase C.

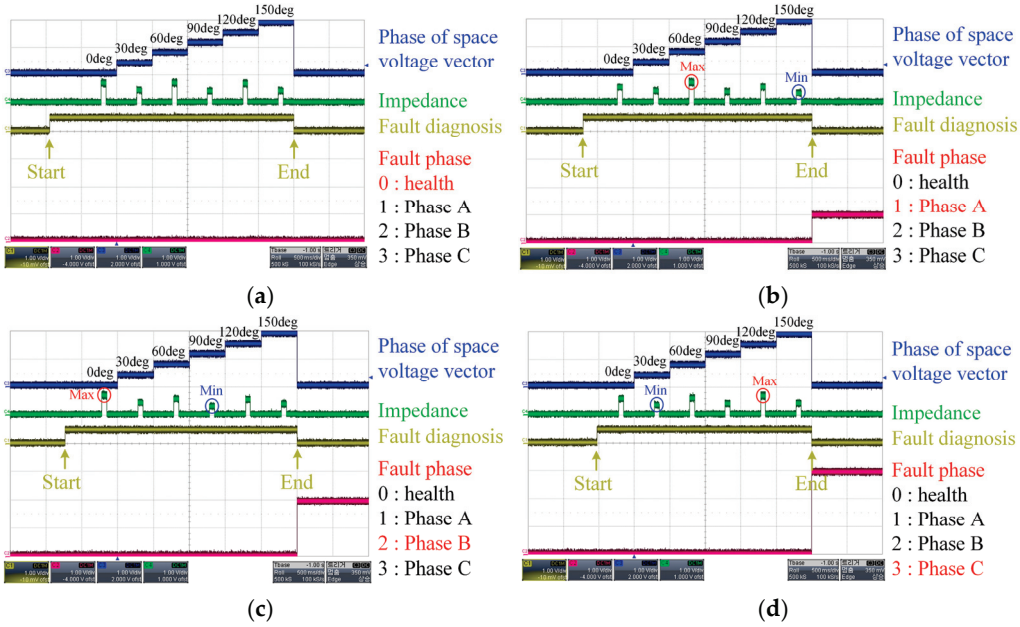


**Figure 12.** Experiment results for Δ connection: (**a**) healthy; (**b**) fault phase A; (**c**) fault phase B; (**d**) fault phase C.

## 5. Conclusions

In this paper, an inter-turn fault diagnosis algorithm is proposed based on impedance analysis and space voltage vector control for IMD systems. The terminal impedances when an inter-turn fault occurs in phase A are analyzed, revealing specific maximum and minimum impedance patterns with both Y and Δ connections. The space voltage vectors of a three-phase inverter are also analyzed according to the switching states of each phase. A fault diagnosis algorithm is proposed by associating the terminal connections with the phases of the space voltage vector. An experimental setup, including a 12 kW three-phase induction motor from RENAULT TWIZY and a terminal box for winding connections, was implemented to validate the proposed algorithm. The impedances for each space voltage

vector were calculated using a DSP (TMS320F28069) based on measured current and voltage and they were displayed on the oscilloscope using the processor's DAC. Inter-turn faults and various winding connections were implemented through the terminal box to emulate different fault conditions. The proposed diagnosis algorithm was verified through the experimental results for faults in each phase for both Y and Δ connections, and the fault diagnosis was conducted within 3.5 s. This approach provides a practical and reliable solution for fault detection in highly integrated EV drive systems where mechanical access to motor terminals is restricted. Furthermore, the proposed ITF diagnosis does not require prior information about the electrical machine, such as healthy impedance, as it relies on the maximum and minimum impedance values associated with six space voltage vectors. Future research will focus on analyzing the frequency dependence of measured impedance to determine the optimal frequency range for reliable fault detection. To enhance diagnostic robustness, meta-heuristic techniques, such as genetic algorithms for optimization and support vector machines for classification, will also be investigated.

**Author Contributions:** Conceptualization, J.A. and H.K.; methodology, H.K.; software, J.A.; validation, J.A. and H.K.; formal analysis, H.K.; investigation, J.A.; resources, J.L.; data curation, J.A.; writing—original draft preparation, J.A. and H.K.; writing—review and editing, J.L. and H.K.; visualization, J.A.; supervision, J.L. and H.K.; project administration, H.K.; funding acquisition, J.L. All authors have read and agreed to the published version of the manuscript.

**Funding:** This work was supported by the Korea Institute of Energy Technology Evaluation and Planning (KETEP) grant funded by the Korea government (MOTIE) (RS-2023-00237024, Development and demonstration of medium-sized variable speed high-power motor).

**Institutional Review Board Statement:** Not applicable.

**Informed Consent Statement:** Not applicable.

**Data Availability Statement:** Data are contained within the article.

**Conflicts of Interest:** The authors declare no conflicts of interest.

## References

1. Azab, M. A Review of Recent Trends in High-Efficiency Induction Motor Drives. *Vehicles* **2025**, *7*, 15. [CrossRef]
2. Zhang, B.; Song, Z.; Liu, S.; Huang, R.; Liu, C. Overview of Integrated Electric Motor Drives: Opportunities and Challenges. *Energies* **2022**, *15*, 8299. [CrossRef]
3. Wu, X.; Geng, Y.; Li, M.; Wang, W.; Tu, M. Inter-Turn Short Circuit Diagnosis of Permanent Magnet Synchronous Motor Based on Siamese Convolutional Neural Network Under Small Fault Samples. *IEEE Sensors J.* **2024**, *24*, 26982–26993. [CrossRef]
4. Bahrami-Fard, M.; Chen, T.; Winchell, E.; Fahimi, B. Integrated Induction Motor Drive for Variable Speed Industrial Applications. *IEEE Trans. Power Electron.* **2025**, *40*, 7176–7188. [CrossRef]
5. Gulsuna, O.; Tokgoz, F.; Karakaya, F.; Keysan, O. Design and Analysis of a GaN-Based Megahertz Integrated Motor Drive for a PCB Motor. *IEEE Trans. Ind. Electron.* **2024**, *71*, 15435–15444. [CrossRef]
6. Zhang, J.; Zhang, X.; Gu, C.; Li, J.; Zhang, H.; Zhao, H. Characterizations of PM Synchronous Motor with an Integrated Common-Mode Voltage Filter. *IEEE Trans. Ind. Appl.* **2024**, *60*, 353–366.
7. Nam, D.W.; Hong, M.K.; Jo, N.R.; Jung, D.H.; Kim, W.H. Design of Coil Patterns for an Axial Flux Permanent Magnet Synchronous Motor with PCB Stator. *IEEE Access* **2025**, *13*, 12936–12944. [CrossRef]
8. Naradhipa, A.M.; Kim, S.; Yang, D.; Choi, S.; Yeo, I.; Lee, Y. Power Density Optimization of 700 kHz GaN-Based Auxiliary Power Module for Electric Vehicles. *IEEE Trans. Power Electron.* **2021**, *36*, 5610–5621. [CrossRef]
9. Hwang, K.Y.; Kim, S.I.; Song, B.K. Single Winding Type Determination of Dual Winding Three-Phase Motor Considering Overheat Problem in Integrated Electric Braking System of Autonomous Vehicles. *IEEE Trans. Transp. Electrific.* **2023**, *9*, 656–666. [CrossRef]
10. Sun, X.; Song, C.; Zhang, Y.; Sha, X.; Diao, N. An Open-Circuit Fault Diagnosis Algorithm Based on Signal Normalization Preprocessing for Motor Drive Inverter. *IEEE Trans. Instrum. Meas.* **2023**, *72*, 3513712. [CrossRef]
11. Orlowska-Kowalska, T.; Wolkiewicz, M.; Pietrzak, P.; Skowron, M.; Ewert, P.; Tarchala, G.; Krzysztofiak, M.; Kowalski, C.T. Fault Diagnosis and Fault-Tolerant Control of PMSM Drives–State of the Art and Future Challenges. *IEEE Access* **2022**, *10*, 59979–60024. [CrossRef]

12. Gupta, V.; Sultana, M.; Khanna, A. Hybrid optimization-based approach for transmission line parameter identification in the presence of noise. *Data Anal. J.* **2023**, *9*, 100182.
13. Jin, L.; Wang, X.; Mao, Y.; Lu, L.; Wang, Z. Online Attribute Matching Based Few-Sample Data-Driven Diagnosis of Electrical Faults in PMSM Drive. *IEEE Trans. Power Electron.* **2024**, *39*, 2620–2631. [CrossRef]
14. Tokgoz, F.; Gülsuna, Ö.; Karakaya, F.; Cakal, G.; Keysan, O. Mechanical and Thermal Design of an Optimized PCB Motor for an Integrated Motor Drive System with GaNFETs. *IEEE Trans. Energy Convers.* **2023**, *38*, 653–661. [CrossRef]
15. Wang, S.; Sun, Y.; Huang, Z.; Mu, S. Analysis of Stator Internal Phase-to-Phase Short Circuit in the 12-Phase Synchronous Generator with Rectifier-Load System. *IEEE Trans. Energy Convers.* **2018**, *33*, 299–311. [CrossRef]
16. Yuan, W.; Li, Y.; Xu, L.; Li, T.; Chen, X. A Fast Faulty Phase Selection Method Considering Fault Tolerance for Single Phase to Ground Fault in Distribution Networks. *IEEE Trans. Instrum. Meas.* **2023**, *72*, 3533212. [CrossRef]
17. Yuan, J.; Feng, C.; Ji, Y.; Liu, X.; Dong, X.; Liu, J. Faulty Feeder Detection for Successive Single Phase-to-Ground Faults Based on Line Model Recognition and Correlation Comparison. *IEEE Trans. Power Del.* **2025**, *40*, 750–763. [CrossRef]
18. Gao, C.; Gao, B.; Xu, X.; Si, J.; Hu, Y. Automatic Demagnetization Fault Location of Direct-Drive Permanent Magnet Synchronous Motor Using Knowledge Graph. *IEEE Trans. Instrum. Meas.* **2024**, *73*, 3502312. [CrossRef]
19. Bonet-Jara, J.; Pons-Llinares, J.; Gyftakis, K.N. Comprehensive Analysis of Principal Slot Harmonics as Reliable Indicators for Early Detection of Interturn Faults in Induction Motors of Deep-Well Submersible Pumps. *IEEE Trans. Ind. Electron.* **2023**, *70*, 11692–11702. [CrossRef]
20. Choi, J.; Kim, S.H.; Lee, W.K.; Lee, J.S. Rapid Control Prototyping and Analysis of a Fault Diagnosis and Amplifying Algorithm for Broken Rotor Bar Induction Motor Drives. *IEEE Access* **2025**, *13*, 19064–19074. [CrossRef]
21. Kang, Y.; Yao, L. Fault Diagnosis for Permanent Magnet Synchronous Motor with Demagnetization Fault and Sensor Fault. *IEEE Trans. Instrum. Meas.* **2024**, *73*, 3533311. [CrossRef]
22. Ma, J.; Bai, X.; Ma, F.; Zhuo, S.; Sun, B.; Li, C. Convolutional Neural Network Design Based on Weak Magnetic Signals and Its Application in Aircraft Bearing Fault Diagnosis. *IEEE Sens. J.* **2024**, *24*, 36031–36043. [CrossRef]
23. Niu, G.; Dong, X.; Chen, Y. Motor Fault Diagnostics Based on Current Signatures: A Review. *IEEE Trans. Instrum. Meas.* **2023**, *72*, 3520919. [CrossRef]
24. Lang, W.; Hu, Y.; Gong, C.; Zhang, X.; Xu, H.; Deng, J. Artificial Intelligence-Based Technique for Fault Detection and Diagnosis of EV Motors: A Review. *IEEE Trans. Transp. Electrific.* **2022**, *8*, 384–406. [CrossRef]
25. Chen, C.S.; Lin, C.J.; Yang, F.J.; Lin, F.C. Model Design of Inter-Turn Short Circuits in Internal Permanent Magnet Synchronous Motors and Application of Wavelet Transform for Fault Diagnosis. *Appl. Sci.* **2024**, *14*, 9570. [CrossRef]
26. Qin, Y.; Li, G.J.; Jia, C.; McKeever, P. Investigation of Inter-Turn Short-Circuit Fault of PM Machines Using PWM Voltage-Based Modeling. *IEEE Trans. Transp. Electrific.* **2024**, *10*, 1324–1334. [CrossRef]
27. Cui, R.; Fan, Y.; Li, C. On-Line Inter-Turn Short-Circuit Fault Diagnosis and Torque Ripple Minimization Control Strategy Based on OW Five-Phase BFTHE-IPM. *IEEE Trans. Energy Convers.* **2018**, *33*, 2200–2209. [CrossRef]
28. Chen, Q.; Han, X.; Liu, G.; Zhao, W.; Shi, H. Inter-Turn Fault Diagnosis and Control for Five-Phase PMSMs by Disturbance Observer. *IEEE Trans. Ind. Electron.* **2024**, *71*, 13901–13909. [CrossRef]
29. Dongare, U.V.; Umre, B.S.; Ballal, M.S.; Dongare, V.P. Online Inter-Turn Fault Detection in Wound Rotor Induction Motors Based on VI Loci Pattern. *IEEE Trans. Ind. Appl.* **2024**, *60*, 411–425. [CrossRef]
30. Asad, B.; Vaimann, T.; Belahcen, A.; Kallaste, A.; Rassõlkin, A.; Ghafarokhi, P.S.; Kudelina, K. Transient Modeling and Recovery of Non-Stationary Fault Signature for Condition Monitoring of Induction Motors. *Appl. Sci.* **2021**, *11*, 2806. [CrossRef]
31. Zhang, J.; Zhan, W.; Ehsani, M. Fault-Tolerant Control of PMSM with Inter-Turn Short-Circuit Fault. *IEEE Trans. Energy Convers.* **2019**, *34*, 2267–2275. [CrossRef]
32. Asad, B.; Vaimann, T.; Belahcen, A.; Kallaste, A.; Rassõlkin, A.; Iqbal, M.N. The Cluster Computation-Based Hybrid FEM-Analytical Model of Induction Motor for Fault Diagnostics. *Appl. Sci.* **2020**, *10*, 7572. [CrossRef]
33. Gu, B.-G. Offline Interturn Fault Diagnosis Method for Induction Motors by Impedance Analysis. *IEEE Trans. Ind. Electron.* **2018**, *65*, 5913–5920. [CrossRef]


**Disclaimer/Publisher's Note:** The statements, opinions and data contained in all publications are solely those of the individual author(s) and contributor(s) and not of MDPI and/or the editor(s). MDPI and/or the editor(s) disclaim responsibility for any injury to people or property resulting from any ideas, methods, instructions or products referred to in the content.

*applied sciences*

MDPI

*Article*

# Online High Frequency Impedance Identification Method of Inverter-Fed Electrical Machines for Stator Health Monitoring

**Jérémy Creux [1,2], Najla Haje Obeid [1], Thierry Boileau [2,*] and Farid Meibody-Tabar [2]**

[1] IFP Energies Nouvelles, Institut Carnot IFPEN Transports Energie, 1 et 4 Avenue de Bois-Préau, 92852 Rueil-Malmaison, France; jeremy.creux@ifpen.fr (J.C.); najla.haje-obeid@ifpen.fr (N.H.O.)
[2] Université de Lorraine, CNRS, LEMTA, F-54000 Nancy, France; farid.meibody-tabar@univ-lorraine.fr
* Correspondence: thierry.boileau@univ-lorraine.fr

**Abstract:** In electric powertrain traction applications, the adopted trend to improve the performance and efficiency of electromechanical power conversion systems is to increase supply voltages and inverter switching frequencies. As a result, electrical machine conductors are subjected to ever-increasing electrical stresses, leading to premature insulation degradation and eventual short-circuits. Winding condition monitoring is crucial to prevent such critical failures. Based on the scientific literature, several methods can be used for early identification of aging. A first solution is to monitor partial discharges. This method requires the use of a specific measurement device and an undisturbed test environment. A second solution is to monitor the inter-turn winding capacitance, which is directly related to the condition of the insulation and can cause a change in the stator impedance behavior. Several approaches can be used to estimate or characterize this impedance behavior. They must be performed on a machine at standstill, which limits their application. In this paper, a new characterization method is proposed to monitor the high-frequency stator impedance evolution of voltage source inverter-fed machines. This method can be applied at any time without removing the machine from its operating environment. The range and accuracy of the proposed frequency characterization depend in particular on the supply voltage level and the bandwidth of the measurement probes. The effects of parameters such as temperature, switching frequency, and DC voltage amplitude on the impedance characteristic were also studied and will be presented. Tests carried out on an automotive traction machine have shown that the first two series and parallel resonances of the high-frequency impedance can be accurately identified using the proposed technique. Therefore, by monitoring these resonances, it is possible to predict the aging rate of the conductor.

**Keywords:** winding health monitoring; frequency response analysis; online characterization; impedance; high-frequency behavior; inverter-fed electrical machines

## 1. Introduction

The health monitoring of stator windings in electrical machines is one of the most important challenges in the automotive traction industry. Increasing supply voltages and inverter switching frequencies lead to accelerated aging of these windings [1]. Such aging is characterized by the degradation of insulation layers between conductors. Factors such as the duration and level of exposure to electrical stress influence the quality of these insulators [2]. In order to reduce the risks of premature insulation degradation and to increase winding robustness, several techniques can be considered: improving the conductor impregnation or using enamels that are particularly resistant to partial discharge phenomena [3]; promoting the design of hairpin winding machines that help reduce vibration phenomena in the winding heads [4]. However, it remains essential to monitor the health of these windings to identify their aging as early as possible. Therefore, if a given signature were to exceed a certain threshold, preventive maintenance could be considered to protect the system and reduce maintenance and repair costs and times [5,6].

There are several approaches to monitoring the health of an electrical machine winding. First, partial discharge measurement can be highlighted [7–9]. Some strategies use insulation resistance measurement and polarization index calculation to perform the diagnosis [10,11]. Estimation of equivalent phase-to-ground or interturn capacitance [12,13] may also be conducted. The main drawback of these methods is that they are usually performed on a machine at standstill, disconnected from the power supply. In some applications, particularly industrial applications, these test conditions cannot be met, making aging monitoring impossible. Furthermore, resistance tests can give an indication of windings state of health [14], but since these tests are destructive, they cannot be applied industrially. Statistical studies are used in [15] to estimate the remaining useful life (RUL) of a system. Finally, in recent literature, many aging monitoring methods are based on the analysis of systems frequency response to determine the winding condition. The various approaches used are usually based on the variation of the frequency signatures of the machine impedance characteristic [16–19]. This characterization over a wide frequency band takes into account leakage and magnetization inductances, iron and eddy current losses, as well as interturn and phase-to-ground capacitive couplings. As a result, the different resonance frequencies reflect these different phenomena.

It has been shown in [12] that the decrease of the winding breakdown voltage correlates with an increase of the machine equivalent capacitance. Furthermore, ref. [16] explains that this equivalent capacitance is particularly impacted by the evolution of the capacitance between windings. It can therefore be concluded that its monitoring will help to detect the aging of a machine inter-turn insulator at an early stage. Finally, the model developed in [20] shows that this inter-turn capacitance has a strong influence on the impedance frequency behavior of the machine. As a result, this characteristic will evolve as the machine age. Ref. [16] emphasizes that the first resonance frequency of the impedance characteristic decreases with time, indicating degradation of the winding insulation. It has also been observed in [18] when the windings are subjected to adverse environmental stresses, such as an exposure to a corrosive substance on their insulators. The resonance frequency decreases with prolonged exposure to the corrosive agent. The amplitude of this resonance also decreases as the conductors age. All of these results demonstrate the benefits of monitoring the evolution of frequency impedance over time to assess the aging of electrical machine windings.

Based on the above considerations, we decided to develop an online characterization and diagnostic method for monitoring the health of stator windings of electric traction machines. The advantage of an online approach is that it provides a continuous flow of information within the functional environment of the drive and without interrupting its operation. In particular, this approach can be used to estimate the "remaining useful life" (RUL) of the winding [21–23]. Therefore, an accurate and efficient condition-based maintenance strategy can be established to ensure the availability of the system.

This paper is organized as follows: Section 2 presents a review of the different types of impedance measurements in electrical machines and the associated characterization methods. Section 3 focuses on the broadband frequency behavior of these machines and reviews the different approaches found in the literature to model their high-frequency (HF) behavior. Section 4 explains the online strategy we have developed to characterize this frequency response without removing the machine from its operating environment. Section 5 examines the impact of various factors, such as operating temperature, supply voltage level, and the presence of the rotor in the machine, on the impedance frequency response of the machine. Finally, Section 6 draws conclusions from the paper and discusses future works.

## 2. Impedance Measurement in Electrical Drive Systems

### *2.1. Electrical Machine Impedance Definition*

Several types of impedance measurements can be performed on a permanent magnet synchronous machine (PMSM). The most common types in the literature are common-

mode (CM) and differential-mode (DM) measurements. On an electrical machine with a star-connected winding, these CM and DM measurements are carried out by connecting the different phases of the machine, as shown in Figure 1a,b. For condition monitoring purposes and to locate the fault in the windings, it is possible to successively analyze the behavior of two of the machine phases, as shown in Figure 1c. Finally, with access to the neutral point, it is possible to characterize the behavior of each phase individually, as described in Figure 1d.

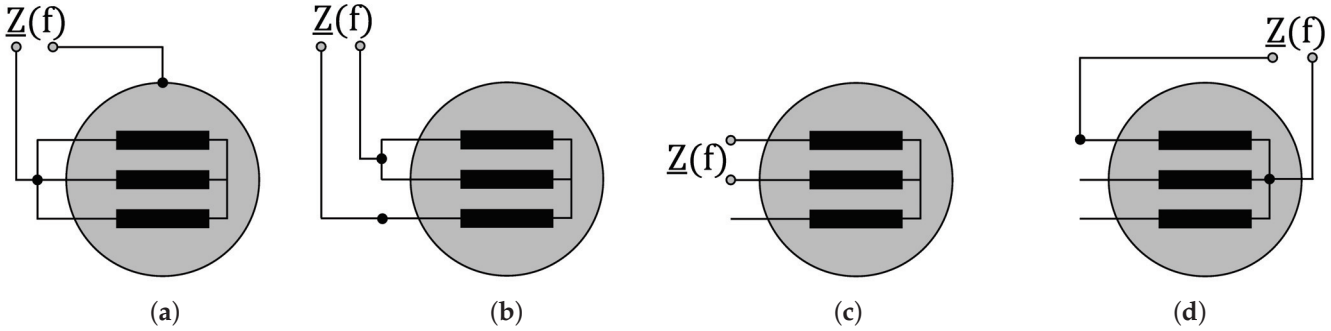


**Figure 1.** Connection and measurement circuit for CM (**a**), DM (**b**), phase-to-phase (**c**), and phase-to-neutral (**d**) impedance characterization in a star-connected three-phase machine.

Similarly, for machines with delta-connected windings, the CM and DM impedance behaviors are measured by connecting the machine phases as shown in Figure 2a,b. Figure 2c describes the connection scheme for characterizing the impedance behavior of each of the machine phases.

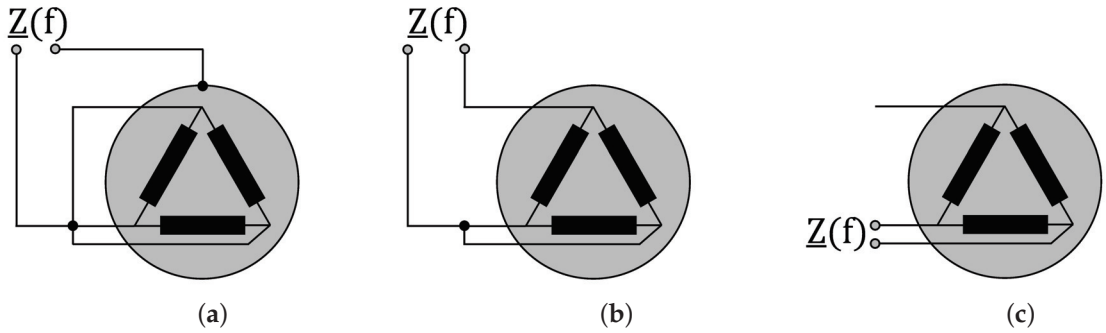


**Figure 2.** Connection and measurement circuit for CM (**a**), DM (**b**), and phase-to-phase (**c**) impedance characterization in a delta-connected three-phase machine.

Finally, in the case of an open-end winding, the behavior of each machine phase can be straightforwardly characterized according to the measurement scheme of Figure 3.

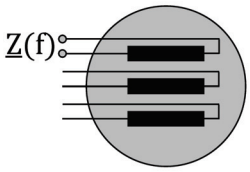


**Figure 3.** Connection and measurement circuit for phase-to-phase impedance characterization in an open-end winding three-phase machine.

*2.2. Impedance Characterization Methods*

Impedance measurement is traditionally performed on a stationary machine disconnected from any power source using an impedance analyzer [24–27], i.e., a measurement device dedicated to characterizing the winding impedance. Multiple instruments are

usually required to cover a wide frequency range. The reason for this is that different calculation approaches must be implemented for certain frequency ranges in order to guarantee the best possible accuracy. It should be noted that the calibration process is a very important step in obtaining consistent and accurate results. The vector network analyzer we used in our study performs a so-called "Gain/Phase" calculation over a frequency range [5 Hz–30 MHz] to determine the impedance characteristic of a machine [28]. The approach consists of the application of a sine wave excitation and the measurement of voltages at two different points of a system to evaluate the impedance of a circuit at a given frequency. The instrument then scans multiple excitation frequencies while storing the various input and output signals obtained in order to construct a Bode diagram of the impedance over the selected frequency range.

Another approach to offline characterization of stator windings requires an oscilloscope to measure the amplitudes of the voltage across a winding and the current flowing through it, as well as the temporal phase shift between these two signals. Then, by applying Ohm law, we can calculate the amplitude and the phase of the winding impedance at a given frequency [17]. The winding must be connected to a low-frequency voltage generator (LFVG), which provides a sweep of frequencies from 1 kHz to 30 MHz to extract the Bode diagram of this impedance. The connection and measurement scheme of this method are shown in Figure 4. This approach can therefore be implemented using fairly common electrical engineering equipment. However, it is a time-consuming process that is difficult to automate and requires numerous measurement points, especially for frequencies above megahertz, to ensure the same accuracy as the results obtained with the impedance analyzer. Moreover, the accuracy of the characterization around certain resonances may be limited by the current amplitude that the LFVG can deliver.

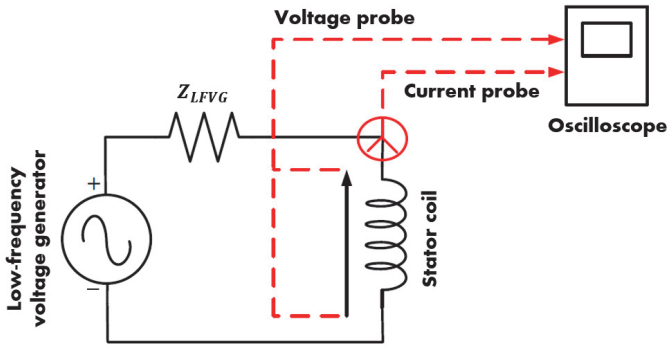


**Figure 4.** Connection and measurement scheme for impedance characterization, using a LFVG and an oscilloscope—redraw from [17].

The main disadvantage of these characterization methods is that they must be performed on a machine that is disconnected from the power supply. This can be particularly challenging in an industrial application. However, online approaches have the advantage of providing continuous information measurement without interrupting the drive's nominal operation. When monitoring the health of windings in an electrical machine, behavioral deviations synonymous with aging can therefore be identified as early as possible. The online approach to impedance characterization most widely used in the literature involves superimposing an HF voltage signal on the machine's main power supply. For this purpose, active [29,30], passive [31,32], or inductive [33] coupling systems are used. An equivalent circuit of the injection and measurement principle taken from [29] is shown in Figure 5.

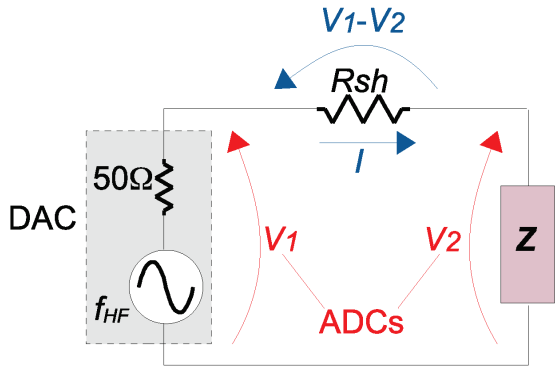


**Figure 5.** Equivalent circuit for online impedance measurement and characterization, using HF signal injection—taken from [29].

Based on Kirchhoff laws, the impedance for each excitation frequency can be calculated. The derived expression is given by (1).

$$Z = \frac{V_2}{I} = R_{sh} \cdot \frac{V_2}{V_1 - V_2} \tag{1}$$

where $Z$ is the impedance amplitude of the system to be characterized, $V_1$ and $V_2$ are the voltage amplitudes measured at the HF generator and machine terminals respectively and $R_{sh}$ is the shunt resistor used to determined the amplitude of the current $I$.

One of the disadvantages of this approach is its invasiveness, as external HF injection has a significant impact on the nominal operation of the machine and can even accelerate the aging of its windings.

## 3. Broadband Stator Model for Data Storage

For health monitoring, comparison of a large number of data sets is needed. This requires the ability to store them in the form of models with a limited number of parameters. This would allow to reconstruct the impedance characteristic and keep only the essential information for aging assessment. In this section, the impedance frequency response will be first displayed to highlight the information that needs to be stored. Then, the various models suitable for condition monitoring that meet the aforementioned conditions are detailed.

### *3.1. Impedance Frequency Response*

As mentioned in the previous section, common-mode and differential-mode impedance behaviors are generally characterized and modeled. These works address electromagnetic interference and compatibility issues [34–36], particularly during the interconnection of the various subsystems that form an electromechanical powertrain. The impedance characteristics outlined are intended to evaluate the CM and DM currents that will circulate and then to size the components that will limit them. However, there are also approaches to characterize the impedant or admittant behavior of the machine, carried out from a health monitoring perspective [17,37].

The impedant behavior is generally displayed as a Bode diagram over a wide frequency range (from hundreds of hertz to several tens of megahertz), as shown in the example in Figure 6 taken from [25]. In this example, the low-frequency behavior of CM is purely capacitive, while that of DM is mostly inductive. Moreover, at higher frequencies, there are numerous resonant frequencies that represent the wealth of the information provided by this characteristic.

Ref. [24] explains that the impedance characteristics of mechatronic systems are largely impacted by parasitic effects such as inductive loops, capacitive couplings, or dissipative phenomena. Consequently, it is difficult to accurately predict and model this behavior during the design phase of these systems because there are too many manufacturing

uncertainties. Therefore, most studies are based on actual measurements of the impedance behavior and attempt to capture and represent it in a simplified manner.

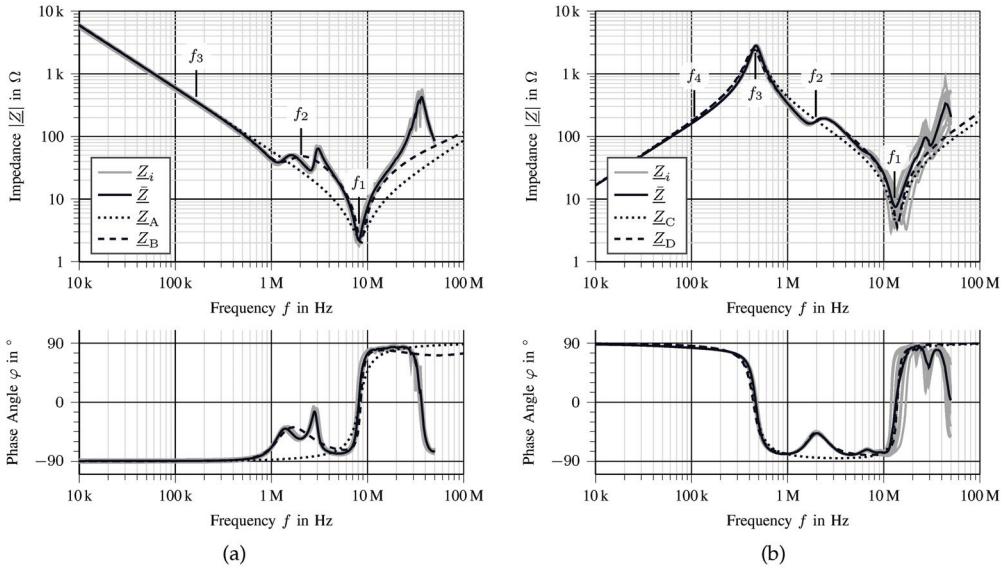


**Figure 6.** Example of Bode diagram depicting CM (**a**) and DM (**b**) impedance behaviors—taken from [25].

### *3.2. High-Frequency Modeling of PMSM*

Classical electrical equivalent circuit (EEC) models of electrical machines, either sound [38,39] or tailored to the study of interturn short-circuit faults [40], are external machine models. They can also be described as "low-frequency", since high-frequency phenomena, which are of less importance for the purpose of the modeling, are generally neglected. As mentioned in the previous section and recalled in [41], the HF behavior is particularly sensitive to "parasitic" effects linked to the quality of the conductor insulation, which means that it must be properly modeled to monitor the evolution of the winding state of health. There are several approaches in the literature to model and/or characterize the HF behavior of a PMSM. These have interesting properties for identifying behavioral deviations associated with insulator aging. They can be divided into two categories: those based on a physical model of the machine phases and those based on an experimental frequency response of the machine behavior. The most popular are HF EEC models [19,25,34,42–45]. There are many such methods in the literature, mainly because they can be used to evaluate either overvoltages at the terminals of inverter-fed machines [46], CM currents circulating through bearings [47], or electromagnetic interference phenomena within power conversion chains [35]. The accuracy of these methods depends on their complexity, i.e., the number of parameters to be evaluated. Depending on the purpose of the model and the accuracy required, these parameters are calculated using hybrid methods that combine analytical and numerical calculations with experimental characterization of the machine behavior [48].

There are also transfer function approaches to the impedance frequency response of PMSM, as presented in [17,35]. Finally, there is an HF approach based on the physical design of the machine phases, which takes into account capacitive coupling phenomena between coils and with the machine ground [13].

The next parts will describe these different HF modeling approaches in detail.

#### 3.2.1. PMSM HF Electrical Equivalent Circuit Model

This HF approach of EEC models is similar to conventional low-frequency circuits, but the proposed EEC models are much more complex and take into account a number of phenomena that are considered parasitic and which are neglected in the standard approach. Thus, the complex association of electrical components (resistance, inductance,

and capacitance) connected in series or in parallel means that the following phenomena can be taken into account:

- Interturn capacitive couplings;
- Phase-to-ground capacitive couplings;
- Leakage inductances in the first turns of the windings;
- Magnetizing inductances;
- Iron and eddy current losses.

The model complexity is determined by the purpose of the modeling and the accuracy required. The first approaches identified in the literature are based on $\pi$ modeling of each machine phase, similar to what is used to describe the behavior of transmission lines [49]. For example, we can identify the HF EEC models developed in [34,43,50] and presented in Figure 7.

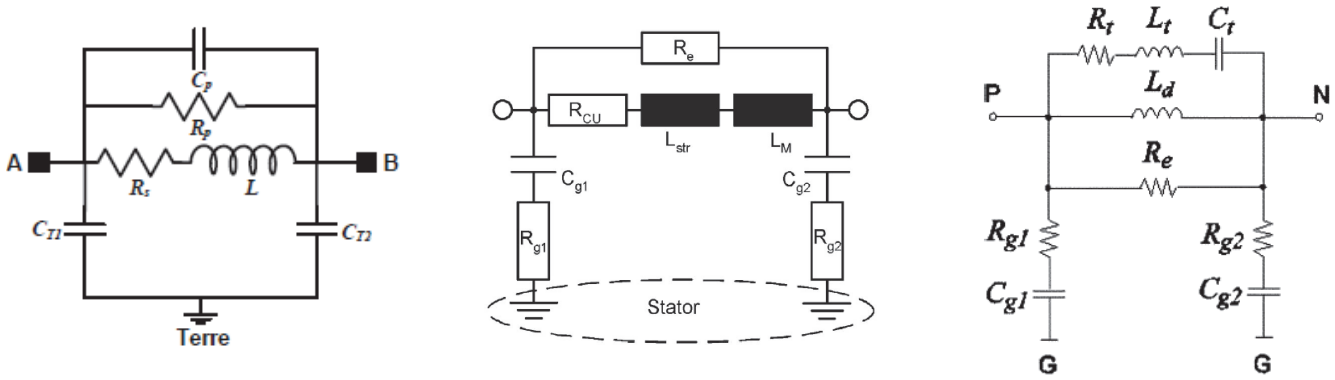


(**a**) (**b**) (**c**)

**Figure 7.** Examples of $\pi$-based HF EEC models of machine phases—taken from [50] (**a**), [34] (**b**), and [43] (**c**).

Figure 8a compares the impedance frequency response estimated using the model presented in Figure 7a with its experimental profile for the three parallelized phases of the 750 W induction machine studied in [50]. Figure 8b compares the experimental and estimated frequency response characteristics, using the model described in Figure 7b of the CM (curve with the lowest mean impedance over the considered frequency range) and DM (curve with the highest mean impedance over the considered frequency range) impedances, of the 15 kW induction machine tested in [34]. Finally, Figure 8c compares the experimental and estimated CM (left curve) and DM (right curve) impedance profiles calculated using the model shown in Figure 7c for the 2.2 kW electric machine studied in [43]. It should be noted that the accuracy of the various models presented remains rather limited and does not perfectly characterize the impedant frequency behavior of these machines over the entire frequency range considered. Building on this postulate, more recent work has sought to construct more complex HF EEC models capable of taking into account more HF phenomena. This is particularly the case in [44,51], whose models have been improved in [45].

Figure 9 shows the complete HF EEC model developed in [45] to characterize the impedant frequency behavior of an 8 kW, star-connected PMSM. Note the following in this model:

- $R_g$ is the resistance of each phase.
- $C_{gi}$ represents the parasitic capacitances between the windings and the stator frame.
- "EMF" blocks describe the electromotive forces generated in each of the machine phases during operation.
- "Part 0" blocks characterize the CM and the DM behavior around resonance and anti-resonance frequencies at very high frequencies (between one and a few tens of megahertz).
- "Part 1" blocks characterize the CM and the DM behavior around resonance and anti-resonance frequencies at high frequency (between 10 kHz and 1 MHz).

- "Part 2" blocks model magnetizing inductances and eddy-current losses in the ferromagnetic core.
- "Part 3" blocks characterize the DM impedant behavior at high frequencies (between 10 kHz and 1 MHz).
- "Part 4" blocks model the effects of leakage inductances in the first turns of coils.

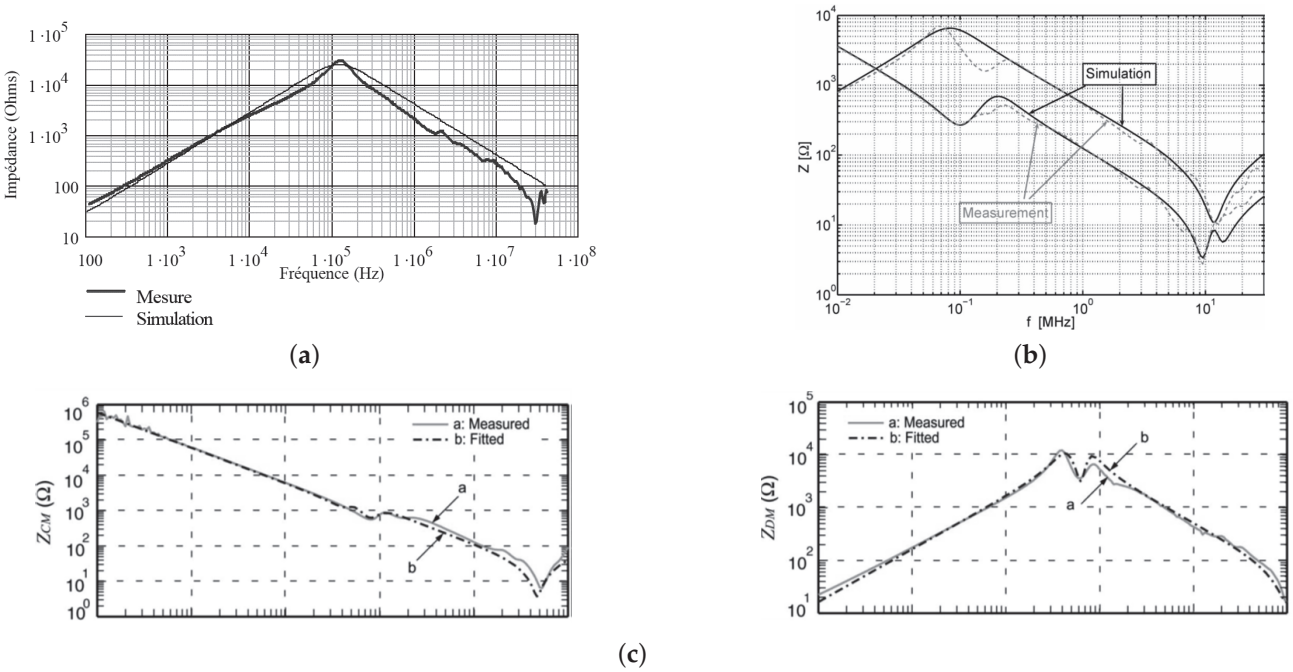


**Figure 8.** Experimental and modeled impedance frequency response of three parallel phases in [50] (**a**), of CM and DM in [34] (**b**), and of CM and DM in [43] (**c**).

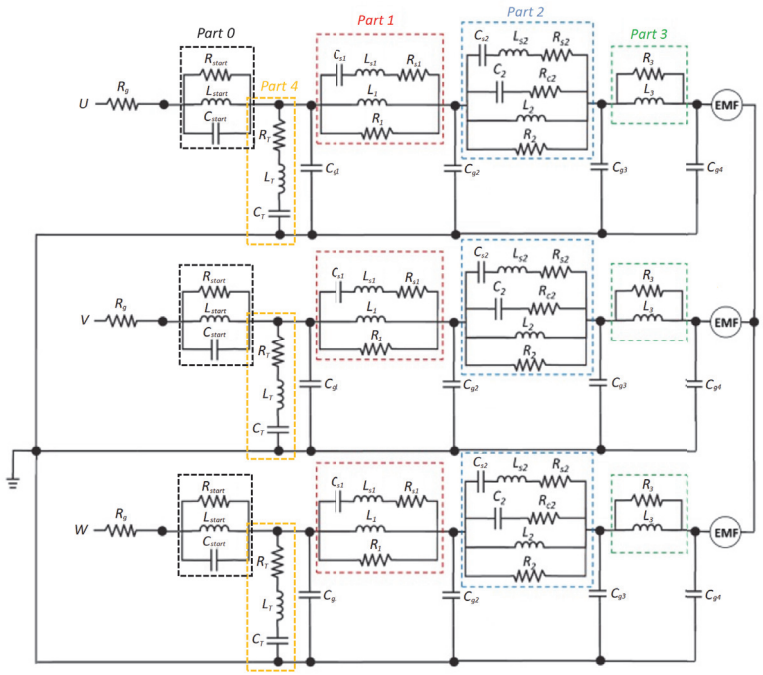


**Figure 9.** Example of a complete HF EEC model of a star-connected PMSM—taken from [45].

Figure 10 compares the experimental and estimated frequency response of the CM (a) and DM (b) impedances of the machine studied in [45], using the model shown in Figure 9.

Comparing the accuracy of these plots with those of Figure 8, a much better correlation of the impedance behavior is observed over the entire frequency range considered, especially at very high frequencies (beyond the megahertz). The various resonances are perfectly described, both in terms of frequency and amplitude.

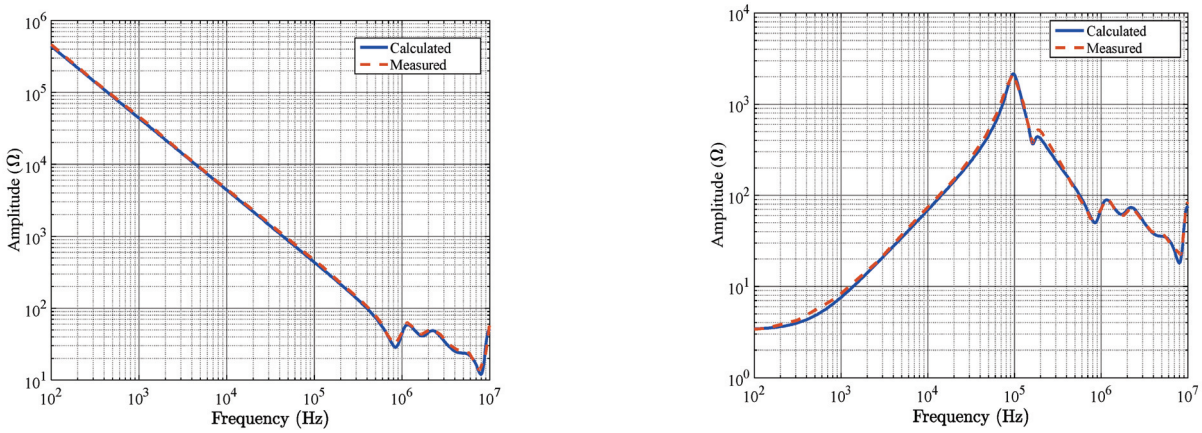


**Figure 10.** Comparison of experimental and modeled CM (**a**) and DM (**b**) impedance frequency behavior—taken from [45].

To evaluate the different parameters of the models presented in Figures 7 and 9, the usual approach is to experimentally characterize the impedance frequency response of the machine under test, then to simplify certain frequency ranges according to the assumptions made, and finally to estimate the various equivalent parameters, as explained by M. Schinkel in [34]. Such a model cannot be considered generic and must be developed for each machine topology. Finally, when the model becomes more complex, it may be necessary to couple this approach with analytical and/or numerical calculations in order to evaluate all the different parameters of the HF EEC model designed [45,48].

3.2.2. Transfer Function Approach to PMSM Behavior

In the interest of early diagnosis of interturn short-circuit faults in PMSM, N. Haje Obeid proposes in [52] to develop a transfer function multi-model to accurately model the behavior of a machine stator winding over a wide frequency range from a few kilohertz to over ten megahertz. The idea is to determine the transfer function that matches the experimental behavior of the winding. The method is based on a graphical model that uses the experimental admittance plot (inverse of the impedance) to determine the linear, time-invariant transfer function characteristic of the machine behavior. The transfer function of such a system is described by the Equation (2) below:

$$H(s) = \frac{a_n s^n + a_{n-1} s^{n-1} + \cdots + a_0}{b_m s^m + b_{m-1} s^{m-1} + \cdots + b_0} \quad (2)$$

where $n$ and $m$ are the order of the numerator and denominator polynomials, respectively, while the coefficients $a_i$ and $b_j$ that characterize the frequency response are calculated by solving an optimization problem.

In the example developed in [52], the optimization problem is solved using a genetic algorithm. This type of algorithm uses the principle of natural selection to ensure that the initial population of the problem evolves towards the best possible solution after a given number of generations $N_g$. To find an optimal solution, the order of the transfer function is increased if the transfer function of the best individual from the previous generation does not satisfy the system frequency response. The solution is adopted when this condition is satisfied. It should be noted that if the optimization problem is solved by a relatively high-order transfer function, it is possible to split the study into two different

frequency ranges in order to obtain simpler solutions that describe the desired behavior as accurately. The resulting multi-model transfer function can then be stored and reused in a diagnostic process.

Another approach is to use vector fitting techniques to extract a generic transfer function for characterizing the CM impedance of an electrical machine [53]. This transfer function is defined by the relation (3).

$$H(s) = A + B.s + \sum_{k=1}^{N} \frac{r_k}{s - p_k} \tag{3}$$

where $A$ denotes a resistive behavior, $B$ refers to an inductance type of behavior, $N$ is a natural integer that characterizes the order of the polynomial, and $r$ and $p$ are the various residues and poles of the transfer function, respectively.

To go further, ref. [35] proposes to use this transfer function as a basis for an equivalent circuit model, where the number of parameters to be estimated depends on the order of the resulting transfer function. Two approaches are then considered to evaluate these parameters:

- A constrained optimization, to minimize the error between the model and the experimental measurement of the machine CM impedance [35];
- An analytical calculation of the various parameters, taking into account the type and design of the winding as well as the material and method of impregnation of the conductors [24].

The author argues that for the machine studied, a 4th-order transfer function satisfies the conditions to accurately model the CM impedance behavior. The resulting model is compared in Figure 11 with the impedance frequency response measured on the machine.

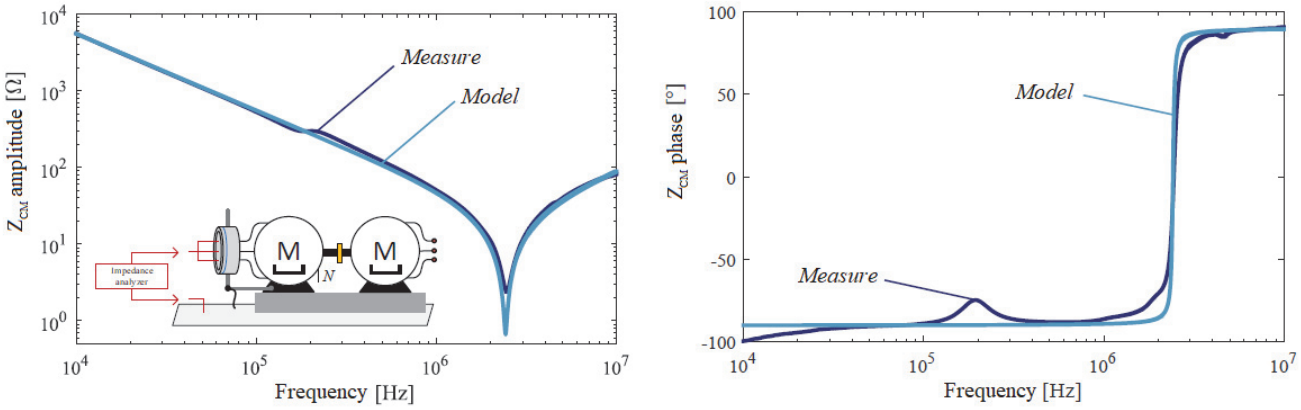


**Figure 11.** Comparison of the experimental frequency response and the proposed transfer function model of CM impedance—taken from [35].

### 3.2.3. HF Approach Based on PMSM Phase Design

The approach based on the machine phase design developed in [13] takes into account capacitive coupling phenomena between the coils and with the machine ground, which are neglected when building a traditional EEC model. The consideration of these couplings increases the accuracy of the model. Furthermore, the formulation in state equations makes the numerical resolution of the problem fast and straightforward. Finally, because the model is based on a portion of the winding, its symmetry properties provide a simple and effective tool for representing the behavior of a single coil or of the entire stator winding by placing state models in series or in parallel.

W. Liu explains in [13] the problem formulation for three healthy turns of a winding. The drawing of the studied structure helps to consider the different phenomena encountered (capacitive phase-to-ground couplings, couplings between two adjacent turns, and inductive couplings between adjacent half-turns). This structure is described in Figure 12.

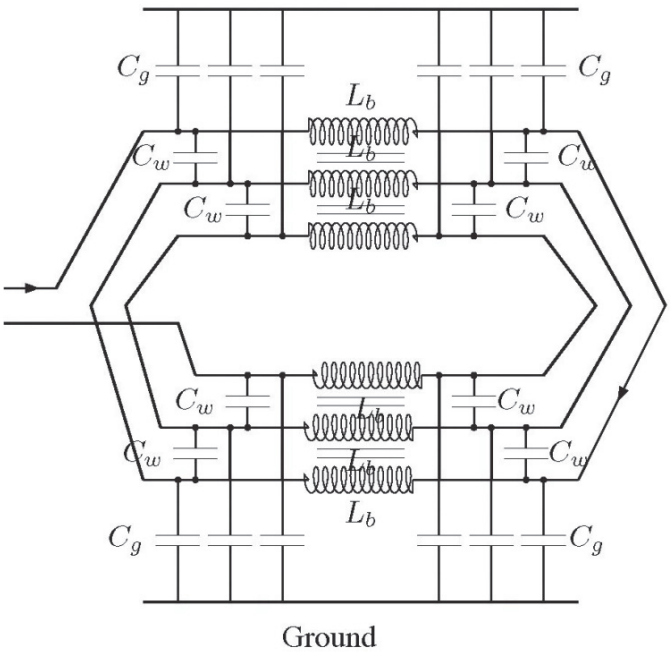


**Figure 12.** Structure of a three-turn coil model with inductive and capacitive couplings—taken from [13].

To simplify the formulation, an equivalent circuit of the three machine turns is defined. Then, the state variables of the model are the voltages across the equivalent capacitors and the currents flowing in each of the equivalent inductances. For a three-turn coil, as in [13], there are 13 such variables. The state vector aggregates these different variables, allowing us to formulate the problem as (4). Finally, after linear transformations, we obtain a state model (5) capable of describing the behavior of 3 inductively and capacitively coupled PMSM turns.

$$\dot{X} = G.\dot{X} + H.X + K.U \tag{4}$$

$$\begin{cases} \dot{X} = A.X + B.U \\ Y = C.X + D.U \end{cases} \tag{5}$$

where $X$ is the state vector, $Y$ is the output vector, and $U$ is the input vector.

Therefore, thanks to this state–space formulation of the behavior of the coupled turns, the precise behavior of both the low-frequency and high-frequency behavior of the complete MSAP can be evaluated with fast numerical resolution. The intermediate step is the estimation of the various model parameters. This estimation is done in [13] using an output error optimization algorithm. The advantage of this formulation, which is based on the machine design, is that it takes into account the winding topology and capacitive couplings, which are generally neglected. As explained earlier, these couplings are representative of the quality of the insulation between the conductors and consequently characteristic of the winding aging and the development of interturn short circuits.

## 4. Proposed Online Method for Impedance Characterization of Electrical Machines

The impedance characterization method developed in this section has been designed to monitor the aging of windings in electrical machines powered by voltage inverters. The aim of this online approach is to observe, at each moment of the machine operation, the

evolution of the different resonance frequencies, which are typical of insulation degradation [16,18]. To do this, we assumed that a supply through a voltage source inverter would intrinsically excite the stator windings of electric machines over a very wide frequency range. Actually, as W. Chen points out in [54], every multiple of the switching frequency is found in the voltage signal applied to the machine terminals. Therefore, unlike the online methods presented in Section 2.2, the proposed method does not require any dedicated HF injection device. However, for accurate broadband impedance characterization of the windings, it relies on wideband gap probes and a dedicated data acquisition system.

In the following, we will present the system under study and the different measurements required for the characterization. Then, we will describe the proposed characterization process, step by step, to obtain the information needed to monitor the winding state of health.

### *4.1. Studied System and Measurements*

The system under investigation is described in Figure 13. The electrical machine is powered by a voltage source inverter (VSI), made of SiC power components, and driven by pulse–width modulation (PWM). The only variables required for frequency impedance characterization are the voltages at machine terminals and the currents circulating in the windings. As mentioned above, these signals are evaluated using wideband gap probes and processed to calculate the frequency response of the windings. Finally, the resistance value of each machine phase is also required to implement the proposed method.

The experimental test bench used in this study is shown in Figure 14. The prototype in our experimental setup is star-connected. Also, we have made the neutral point accessible in order to measure the voltage at this point of the winding. Therefore, two types of characterization presented in Section 2.1 can be undertaken with our method: phase-to-phase impedance and phase-to-neutral impedance.

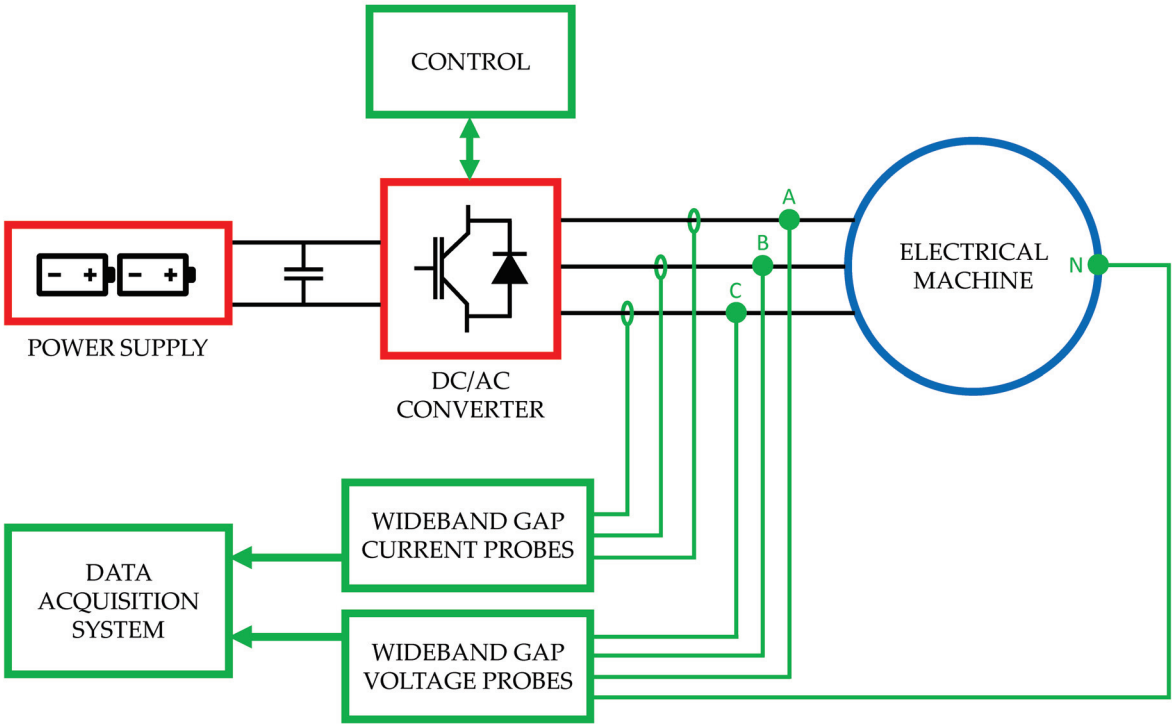


**Figure 13.** System description and measured signals.

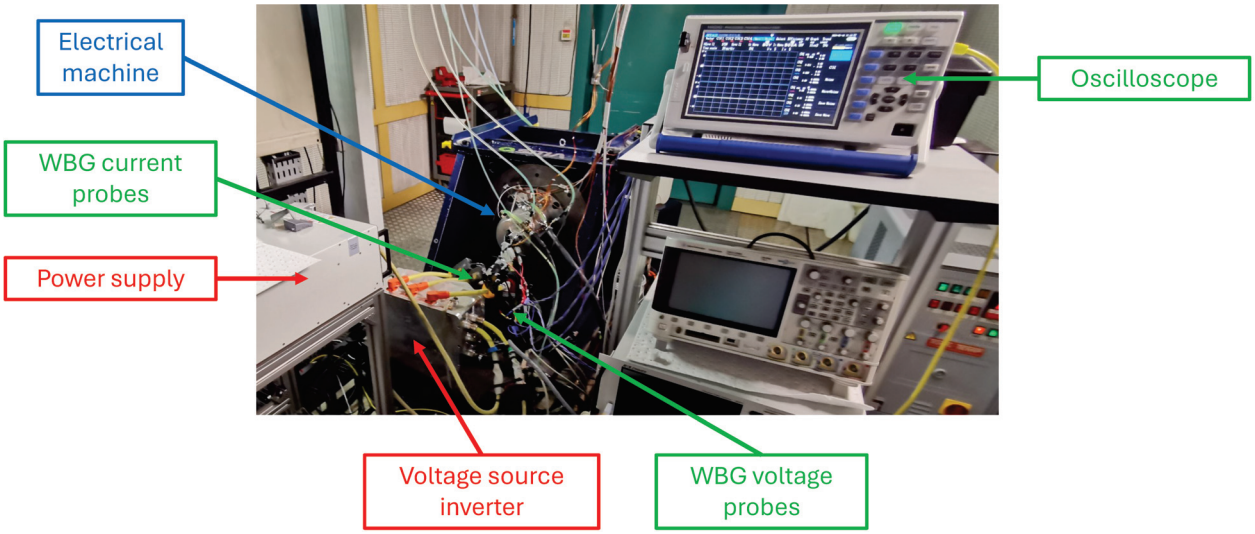


**Figure 14.** Experimental test bench.

*4.2. Flow Chart of the Proposed Characterization Method*

The online impedance characterization method developed in this work is based on the flowchart presented in Figure 15.

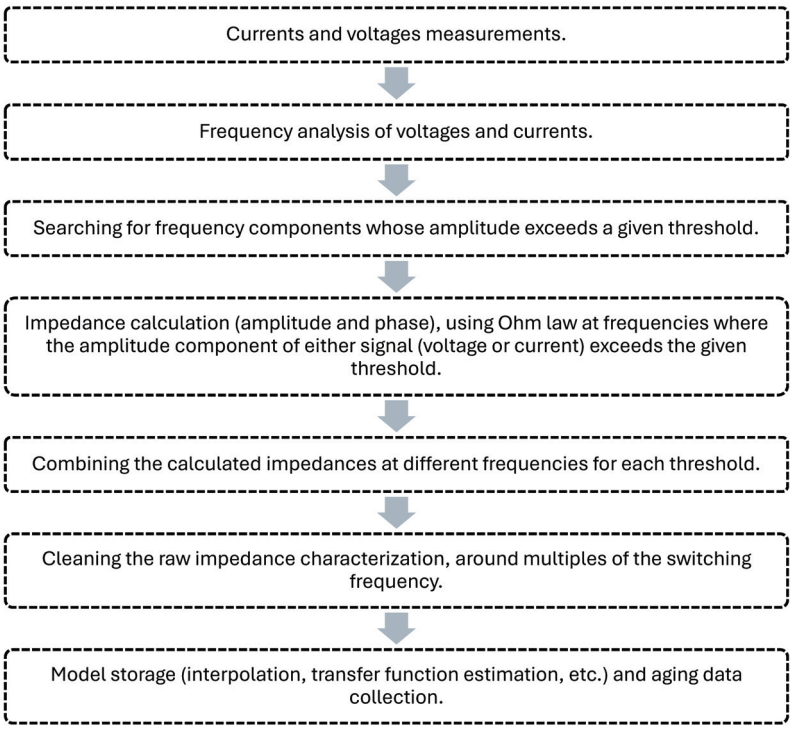


**Figure 15.** Flowchart of the proposed characterization method.

The various steps in this process are detailed in the following paragraphs.

**Step 1—Measurements**

Voltages are measured at points A, B, and C (and N, if the neutral point is accessible) of the system described in Figure 13. The currents flowing in each phase of the machine are also measured. It should be noted that the frequency range of the characterization depends directly on the bandwidth (BW) of these sensors. In our study, their BW is [12 Hz, 50 MHZ]. To measure these data, the acquisition is performed using an oscilloscope with a sampling frequency of 62.5 MHz. Therefore, the Nyquist theorem states that only

frequency components up to 31.25 MHz ($f_{max}$) are properly displayed in the discrete signals obtained [55].

The machine under test is fed by a VSI with a switching frequency between 10 kHz and 35 kHz. The electrical fundamental frequency ($f_e$) of this traction machine is in the frequency range [100 Hz, 500 Hz]. Also, in these applications, the DC bus voltage ranges from 300 V to 750 V. When the neutral point is not accessible, we can consider a simple voltage system by applying the relation 6.

$$V_{abc} = \frac{U_{abc}}{\sqrt{3}} \tag{6}$$

where $U_{abc}$ are phase-to-phase voltages and $V_{abc}$ are simple voltages.

Note that the proposed method can be performed with simple voltages or phase-to-phase voltages. For the remainder of this study, we will only consider simple voltages. Figure 16 depicts the waveforms of the simple voltages (a) and the currents circulating in the stator windings (b), respectively. Per unit has been used for confidentiality reasons. For time variables, the signal amplitude is divided by the amplitude of the fundamental component. However, for frequential spectrums, the signal amplitude is divided by the maximum amplitude over the considered frequency range.

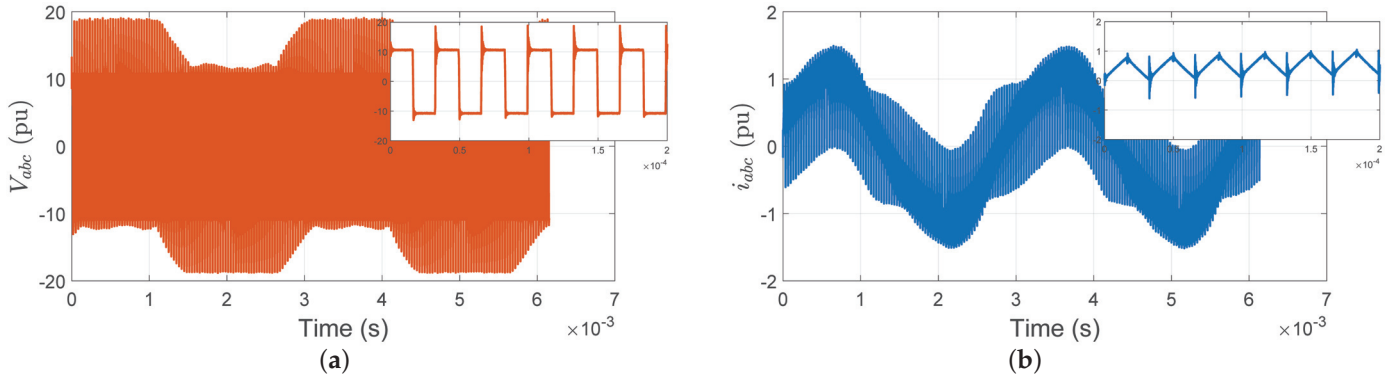


**Figure 16.** Waveforms of the simple voltages (**a**) and measured currents (**b**).

**Step 2—Frequency analysis**

To perform the frequency analysis of voltages and currents, we considered these signals to be stationary, i.e., measured on a machine in steady-state operation. Therefore, we decided to use the Fast Fourier Transform (FFT) to extract their frequency spectrum. However, under transient conditions, time–frequency transformations should be used to extract the frequency spectrum of these signals. These include Short-Time Fourier Transform (STFT); Wavelet Transform (WT); Wigner-Ville Distribution (WVD); Choi-Williams Distribution (CWD); Hilbert-Huang Transform (HHT); etc.

This transformation is expressed mathematically by the relation 7 [56].

$$\left[ \quad f[n] = \frac{2n}{N\Delta t} \quad , \quad y[n] = \sum_{k=0}^{\frac{N}{2}-1} x[k].e^{-j\frac{4\pi}{N}kn} \quad \right] \tag{7}$$

where $f[n]$ is the frequency associated with the nth point of the transform, $y[n]$ is the result at the nth point of the transform, $N$ is the maximum number of points of the transform to satisfy the Nyquist criterion, and $\Delta t$ is the sampling period of the measured time signal.

The frequency content of the various signals analyzed is shown in Figure 17. The logarithmic scale on the x-axis and the transformation of the processed signal into decibel amplitude have been used for visual clarity.

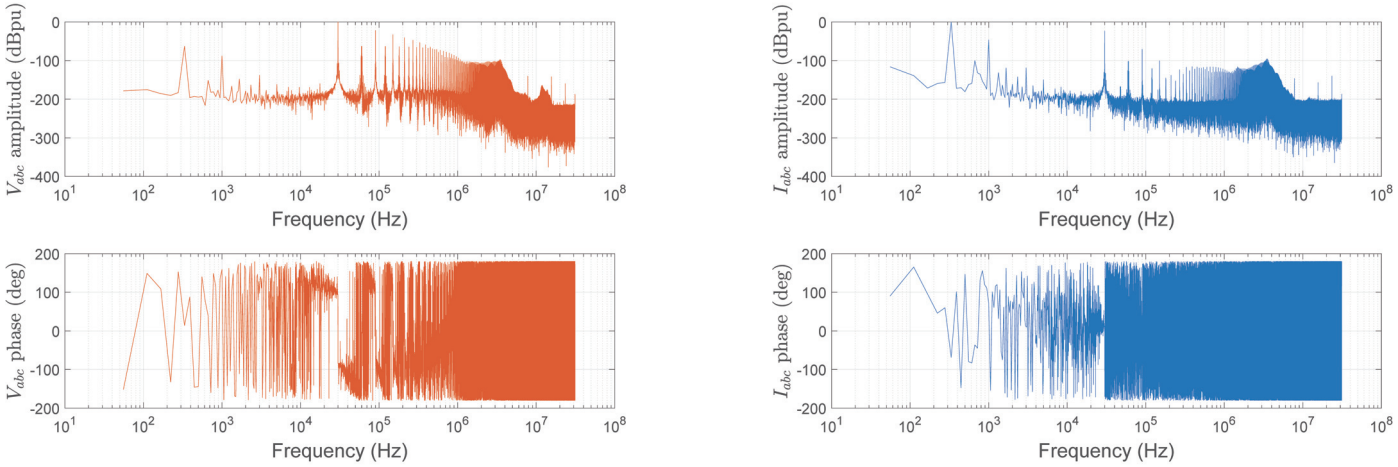


**Figure 17.** Frequential analysis of the simple voltages (**a**) and measured currents (**b**).

**Step 3—Search for dominant frequency components**

Then, the idea is to extract the frequency components whose amplitude is predominant depending on the frequency range considered. For this purpose, we have defined adaptive thresholds for the frequency spectrum of voltages and currents. These thresholds are characterized by relations (8) and (9), respectively. The graphical representation of this search for the dominant frequency components is explained for the simple voltages in Figure 18. Note that these thresholds have been defined using the DC bus voltage ($U_{DC}$, which for this excitation corresponds to the amplitude at the switching frequency) and the maximum sampling frequency (to satisfy the Nyquist criterion).

$$S_V(f) = \frac{U_{DC}}{\sqrt{3}} . \frac{f_{max}}{f_{PWM}} . \frac{1}{f} \tag{8}$$

$$S_I(f) = S_V(f) . R_{ph} \tag{9}$$

where $S_V$ and $S_I$ are the thresholds for simple voltages and currents, respectively, $f$ is the given frequency, $U_{DC}$ is the DC bus voltage, $f_{max}$ is the maximum sampling frequency, $f_{PWM}$ is the switching frequency, and $R_{ph}$ is the electrical resistance of the machine phases.

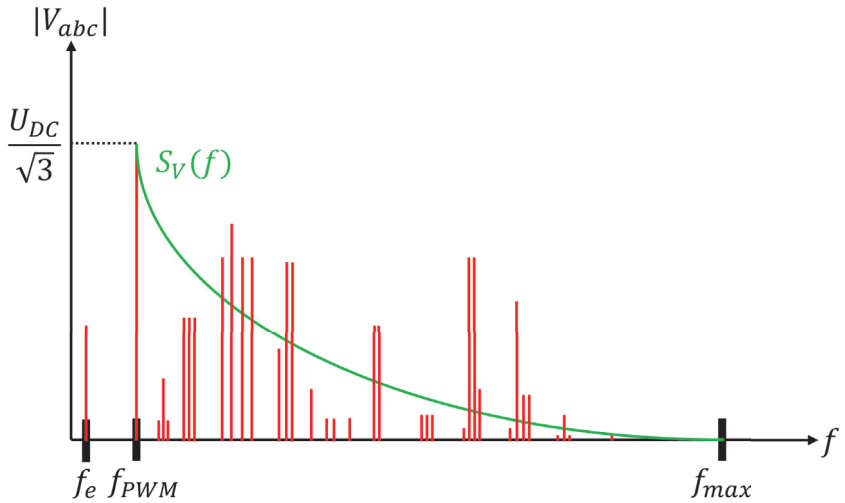


**Figure 18.** Graphical representation of the adaptive threshold defined to extract the predominant frequency components within single voltages.

Finally, for each of the processed signals (simple voltages and currents), once the amplitude of the given component exceeds the threshold set at a given frequency ($f_{prep}$), the following quintet is stored:

$$Q = \left[ f_{prep} \, , \, |V_{abc}(f_{prep})| \, , \, |I_{abc}(f_{prep})| \, , \, \angle V_{abc}(f_{prep}) \, , \, \angle I_{abc}(f_{prep}) \right]$$

**Step 4—Impedance calculation**

To characterize the impedance behavior as a function of the excitation frequency, we must determine the corresponding impedance for each frequency $f_{prep}$ contained in the vectors $Q_V$ and $Q_I$. The Ohm law is used to calculate the amplitude and the phase of this impedance, as described in Equations (10) and (11).

$$|Z(f_{prep})| = \frac{|V_{abc}(f_{prep})|}{|I_{abc}(f_{prep})|} \tag{10}$$

$$\angle Z(f_{prep}) = \angle V_{abc}(f_{prep}) - \angle I_{abc}(f_{prep}) \tag{11}$$

The raw impedance characteristics obtained independently from the two thresholding methods are shown in Figure 19. In particular, it can be seen that the point densities are not evenly distributed depending on the threshold used. On the one hand, around the so-called "parallel" resonances, i.e., when the inductive reactance is equal to the capacitive reactance, the current amplitude is minimal and its signal is in phase with the applied voltage. This results in a local impedance maximum and more points with the threshold at simple voltages. On the other hand, around the so-called "series" resonances, the applied AC voltage generates the maximum current amplitude. These two signals are then in phase. This results in a local impedance minimum and more points with the threshold at the currents.

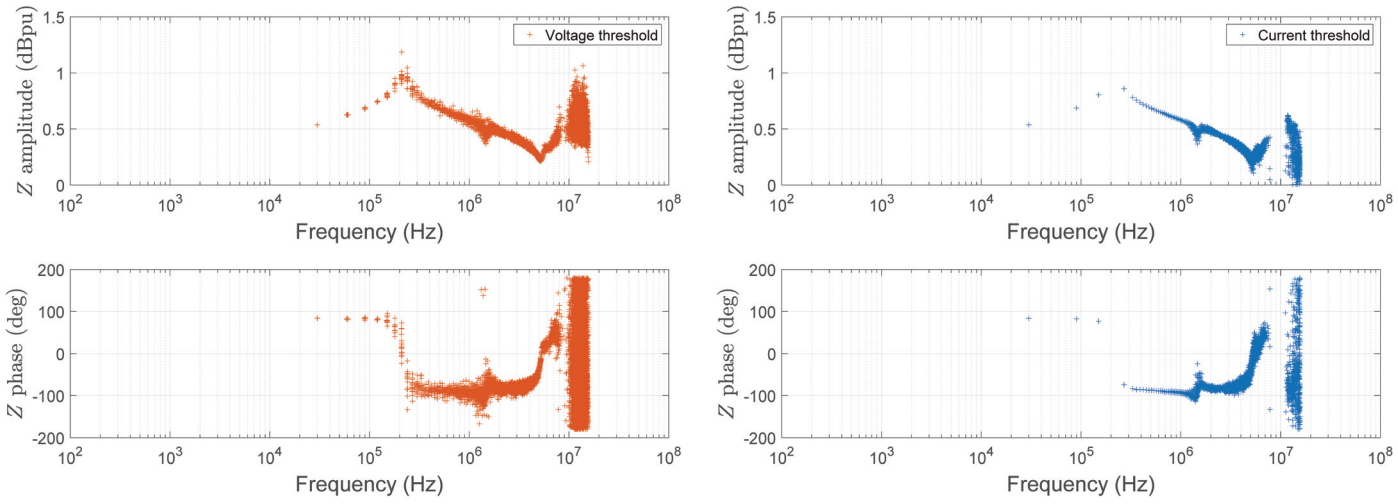


(**a**) (**b**)

**Figure 19.** Raw frequency impedance characterization obtained by thresholding simple voltages (**a**) and currents (**b**).

Also, as expected, the maximum frequency of these characteristics is equal to $\frac{f_{max}}{2}$, i.e., around 15.6 MHz. Finally, these two profiles are particularly noisy at very high frequencies (over a dozen megahertz).

**Step 5—Combining impedances**

To take advantage of the precision of both plots around the different resonance frequencies, we will concatenate these two characterizations. The superposition of the two curves is shown in Figure 20. Despite the relative clarity of the full impedance characteri-

zation, we can see that it remains fairly noisy, which is why it is necessary to perform a cleanup step on the raw data.

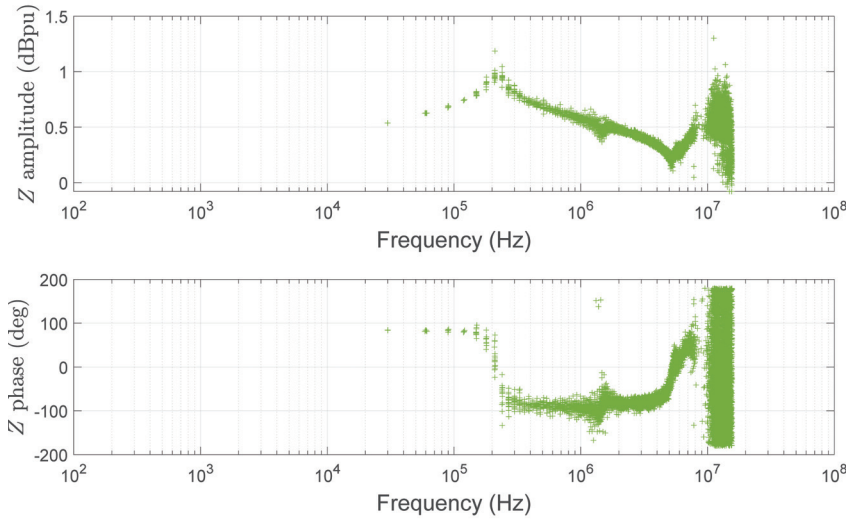


**Figure 20.** Complete raw frequency impedance characterization.

**Step 6—Cleaning the raw impedance characterization**

To extract a more precise impedance characteristic from the raw pattern generated in the previous step, we need to perform a "cleaning" step. The strategy adopted is to cluster the various points gravitating around multiples of the switching frequency. In this study, an interval of 5% on either side of these multiples was considered. Thus, the impedance amplitude and phase for each of these multiples is defined as the average of the values within this interval. If no point is close to one of the switching frequency multiples, then no value is assigned to it.

By applying this strategy to the raw impedance characterization obtained in Figure 20, we obtain a much cleaner frequency spectrum, especially at very high frequencies. To complete the resulting spectrum, the value of the impedance calculated at the fundamental excitation frequency ($f_e$) is added. This new characterization is shown in Figure 21.

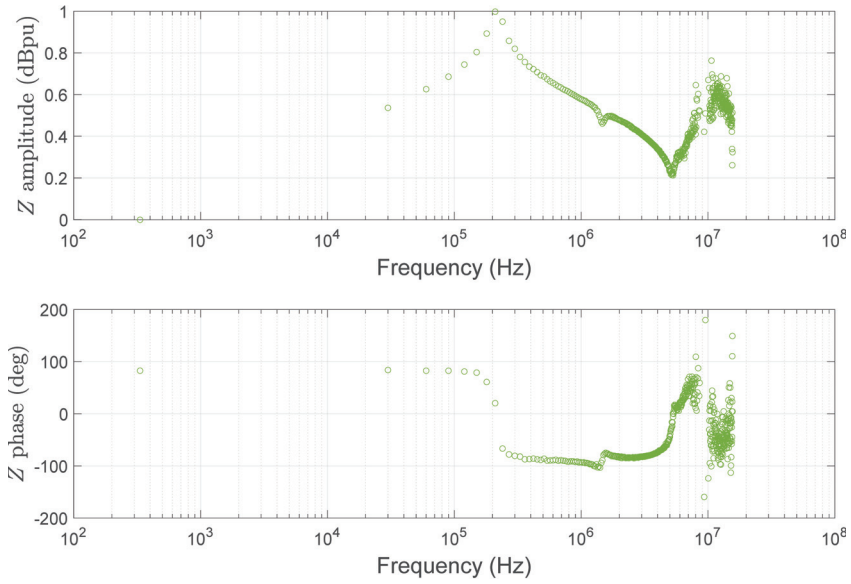


**Figure 21.** Improved frequency impedance characterization.

**Step 7—Model storage and aging data collection**

Finally, for aging monitoring purposes, it is essential to accurately evaluate the various parallel and series resonances of this improved impedance characterization. Since each point represents a multiple of the switching frequency, it is not possible to precisely assess these resonance values. There are two ways to recover these informations. The first is to interpolate these profiles and extract local extremes in order to analyze their evolution. The second is to model the impedance frequency behavior of the machine phases using the various approaches presented in Section 3.2 and look for behavioral deviations synonymous with aging.

Figure 22 shows the impedance behavior obtained by interpolating the improved characterization calculated in step 6. The type of interpolation used is the "Akima spline" [57]. The first two parallel and series resonances can be properly characterized, and data can be stored to monitor the health of the winding. Finally, the overall behavior at very high frequencies is more erratic and fails to accurately identify the other resonances.

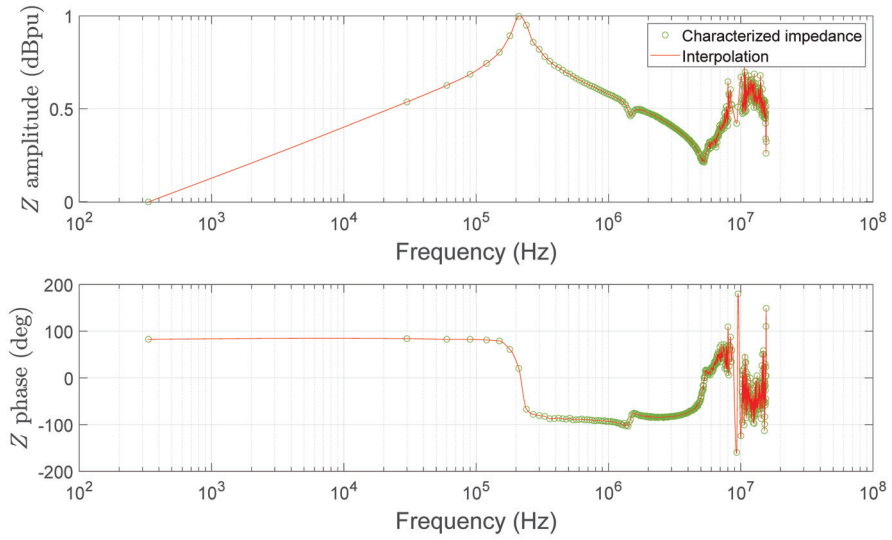


**Figure 22.** Interpolation of the impedance frequency response.

### *4.3. Validation and Interest of the Proposed Method*

The objective was to verify the reliability and consistency of our strategy. For this purpose, we performed about 15 measurements on the same test machine at different times during its operation (at different operating points and on different days). Interpolation was used to determine the amplitude and the frequency of the various resonances found.

Figure 23 shows the different characteristics acquired during these tests. It can be seen that the different profiles are superimposed regardless of the machine operating point. The first two resonances can be identified. Based on the different results, we highlight that the uncertainty to characterize the first parallel resonance is less than or equal to 12.33 kHz and 4.4 dBΩ (<3%). The frequency uncertainty to characterize the first series resonance is identical to that observed for the first parallel resonance. However, in terms of amplitude, it is less than or equal to 233 kHz.

Furthermore, in order to validate the proposed online characterization approach, we compared the resulting plot with that measured offline using a vector network analyzer. The results are shown in Figure 24.

There is a strong correlation between the two frequency behaviors. The relative difference between the two characteristic frequencies of the first parallel resonance is less than 10%. In terms of amplitude, the two approaches give the same result. On the other hand, there is a deviation between the behavior observed with our online method and with the impedance analyzer around the first series resonance. This is intrinsically related to the use of fixture adapters and a measurement cable between the impedance analyzer and the test machine, as explained in [58] and confirmed by Figure 25, which compares the impedance response of a traction machine as a function of the cable used. Based on these results, it is essential to emphasize the importance of using the same measurement

conditions if we want to properly exploit the results of these frequency analyses and draw the correct conclusions about the health of the windings.

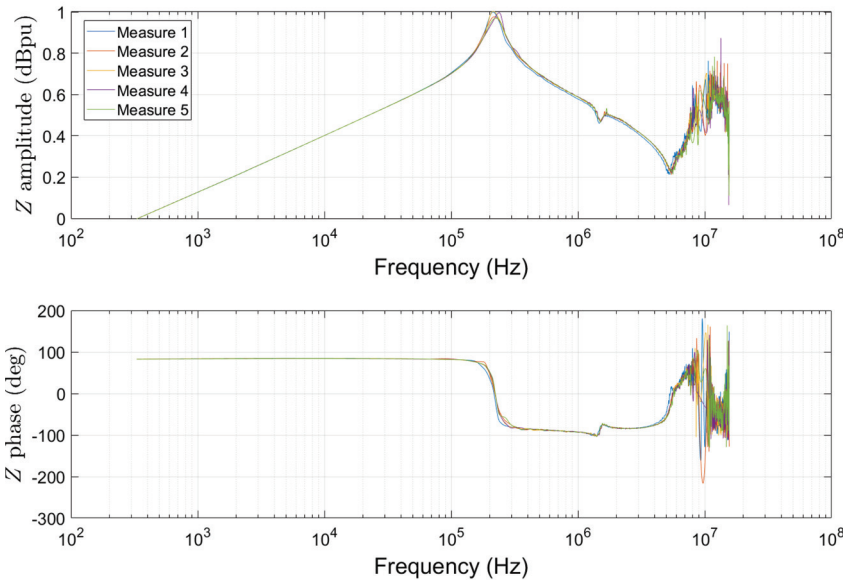


**Figure 23.** Comparison of impedance interpolations obtained at different times and operating points.

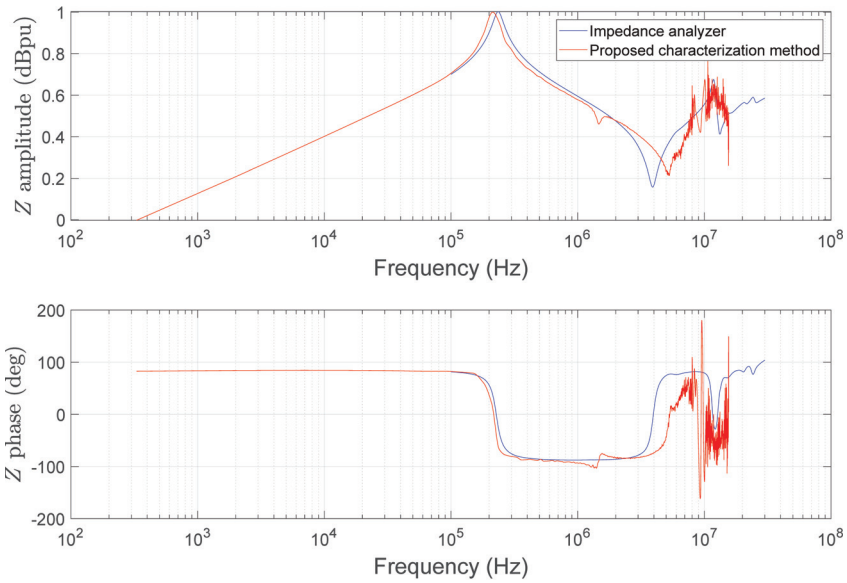


**Figure 24.** Comparison of impedance characterizations obtained with the proposed online method and with an impedance analyzer.

Finally, the benefits of this online impedance characterization approach can be summarized in three points:

- The HF excitation is naturally provided by the voltage source inverter. The method is therefore non-invasive and has no effect on actuator operation or aging.
- No measurement cables or fixture adapters are required, eliminating the need for a calibration phase and making the characterization process highly reliable.
- Finally, health monitoring is performed at all times without removing the machine from its operating environment, allowing early detection of insulation degradation in the windings.

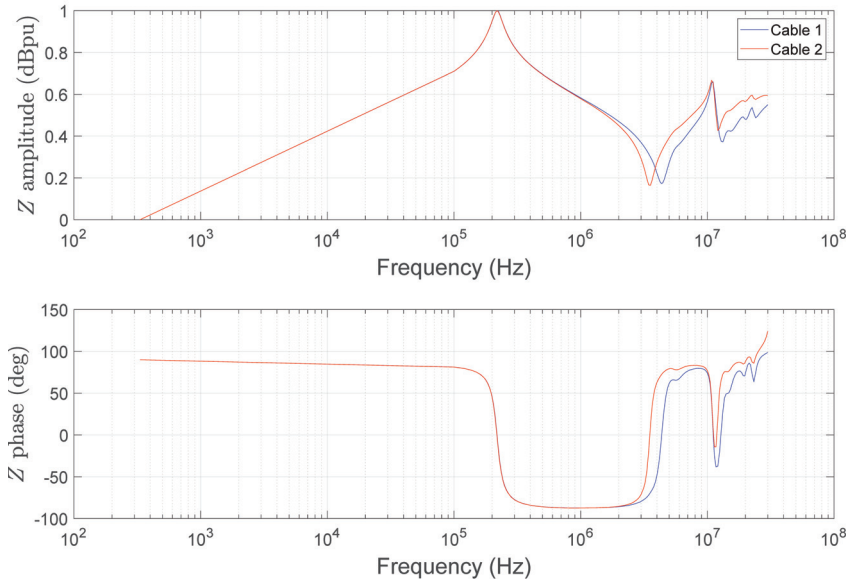


**Figure 25.** Measurement cable effect on the frequency response measured by the impedance analyzer.

## 5. Parameters Influencing Impedance Frequency Response

To extend our study, we wanted to understand the influence of some parameters on the impedance characteristics obtained using the proposed strategy. The three parameters investigated are the machine operating temperature, the inverter switching frequency, and the DC bus voltage amplitude. Findings are discussed below.

### *5.1. Temperature*

To investigate the effect of temperature on the HF impedance frequency response of the machine, we carried out two characterizations at different temperatures. The first at room temperature ($T$ = 25 °C), after a few moments of operation, and the second after a few tens of minutes of circulating a current in the windings, so that the thermal regime is established. The second test was performed at a temperature of 80 °C. The results are shown in Figure 26. From the characterization plot after cleaning, as well as its interpolation, we can see that the HF impedance behavior remains identical, regardless of the operating temperature.

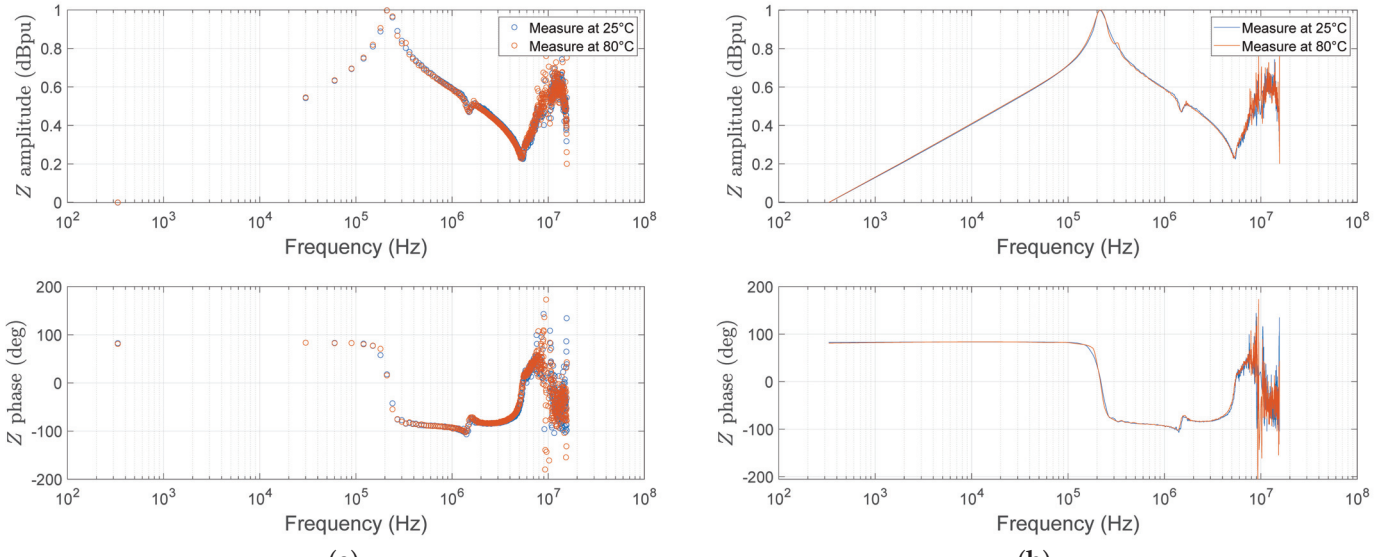


**Figure 26.** Comparison of the impact of the operating temperature on the cleaned impedance characteristic (**a**) and its interpolation (**b**).

### *5.2. Switching Frequency*

We have also studied the influence of the inverter switching frequency on the accuracy of the proposed impedance identification method. Since it is the various multiples of the switching frequency that are intrinsically excited, this means that for a fixed measurement frequency range, the characteristic obtained is enriched or depleted, depending on the switching frequency used. This assertion is confirmed by comparing the cleaned impedance characteristics shown in Figure 27a, obtained with $f_{PWM} = 15$ kHz and $f_{PWM} = 30$ kHz. The number of blue points is twice as high when the switching frequency is set to 15 kHz.

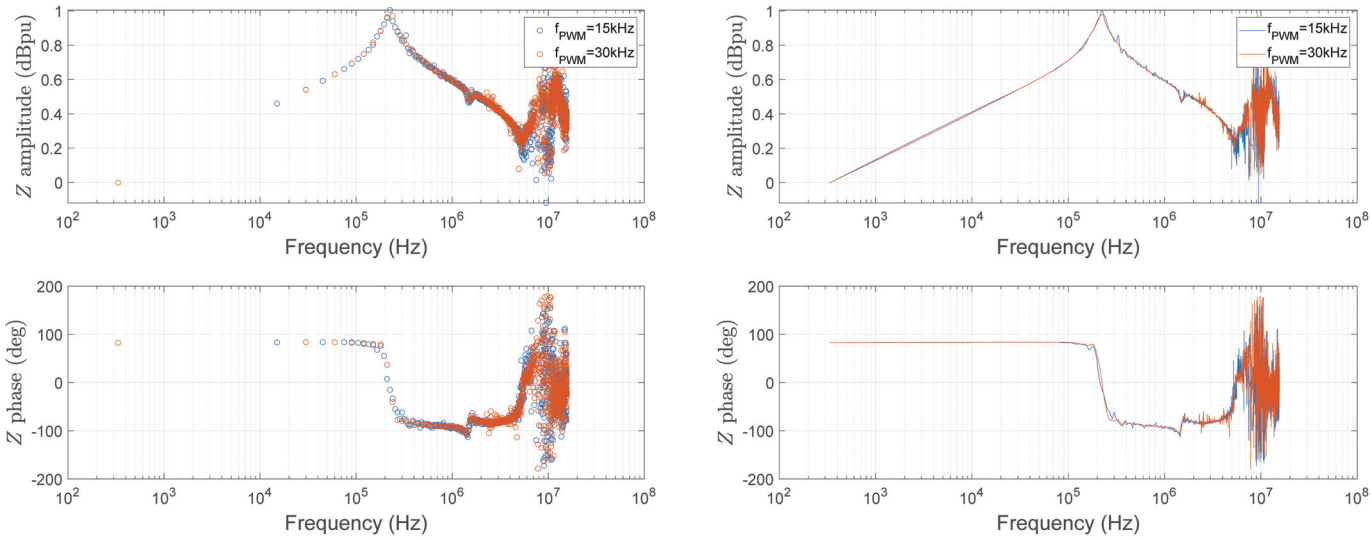


**Figure 27.** Comparison of the impact of the switching frequency on the cleaned impedance characteristic (**a**) and its interpolation (**b**).

This increased point density provides a better approximation of the different series and parallel resonance frequencies. As a result, their estimation is all the more accurate and reliable. However, the interpolations presented in Figure 27b show that the difference in accuracy obtained with these two switching frequencies is not significant enough to bias the characterization, as the deviation is less than 3% (the uncertainty range calculated in Section 4.3 during reliability tests of the method).

### *5.3. DC Voltage*

Finally, we have investigated the impact of the DC bus voltage on the impedance frequency response of the machine. For this purpose, we performed two characterizations with $U_{DC} = 300$ V and $U_{DC} = 600$ V. The results presented in Figure 28 show that the amplitude of the DC bus voltage has little effect on the accuracy of the impedance frequency response method. The reason for this lies in the very definition of the proposed method, since the adaptive threshold used to identify the various dominant frequency components that are used to derive the frequency characterization is defined using this parameter. The approach is therefore inherently independent of the DC bus voltage amplitude.

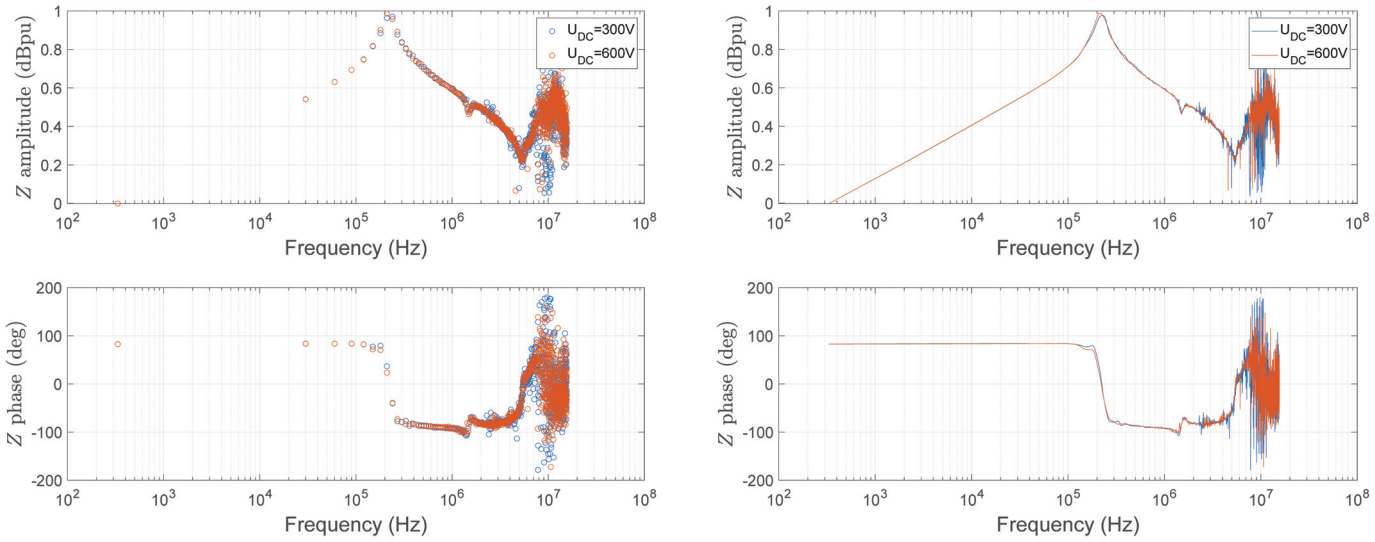


**Figure 28.** Comparison of the impact of the DC bus voltage on the cleaned impedance characteristic (**a**) and its interpolation (**b**).

## 6. Conclusions

In this paper, after reviewing the state of the art in frequency characterization and modeling of stator winding impedance behavior in electrical machines, we have presented the online characterization principle we have developed for monitoring conductor aging. This characterization method is applicable to any machine fed by a voltage inverter. When the inverter is controlled by PWM, it naturally excites all the multiples of its switching frequency up to very high frequencies (i.e., above tens of megahertz), and thus we are able to extract the impedance frequency response of the machine phases using time measurements of voltages and currents.

The proposed method consists of several steps. First, a frequency analysis of the signals is performed. Then we look for frequency components whose amplitude is above a defined threshold. Then, using these data, we apply Ohm law to calculate the impedance amplitude and phase for each highlighted frequency. To reduce noise and uncertainties around multiples of the switching frequency, we must refine the raw characterization. Finally, modeling or interpolation is performed to store this impedance behavior and thus gather useful information for aging monitoring (frequencies and amplitudes of the first parallel and series resonances).

We have demonstrated the reliability and accuracy of our characterization method compared with other offline approaches available in the literature. We have also studied the influence of various parameters, such as operating temperature, inverter switching frequency, or DC bus voltage, on the impedance frequency response of the machine windings.

Finally, the advantage of the proposed broadband impedance characterization approach designed for aging monitoring lies in the fact that unlike other online methods in the literature, it does not require any additional injection system to excite the windings. The invasiveness of the method is therefore limited since it does not affect the operation or aging of the machine. Calibration is the most critical step to ensure good data analysis when using an impedance analyzer. Our approach eliminates this step, making it all the more reliable. Finally, aging monitoring can be done at any time without removing the machine from its operating environment, allowing early detection of insulation degradation in the windings.

**Author Contributions:** Conceptualization, J.C. and N.H.O.; methodology, J.C., N.H.O., T.B. and F.M.-T.; software, J.C.; validation, J.C., N.H.O., T.B. and F.M.-T.; formal analysis, J.C. and N.H.O.; investigation, J.C. and N.H.O.; resources, N.H.O.; data curation, J.C.; writing—original draft prepa-

ration, J.C.; writing—review and editing, N.H.O., T.B. and F.M.-T.; visualization, J.C.; supervision, N.H.O., T.B. and F.M.-T.; project administration, N.H.O., T.B. and F.M.-T.; funding acquisition, N.H.O., T.B. and F.M.-T. All authors have read and agreed to the published version of the manuscript.

**Funding:** This research received no external funding.

**Institutional Review Board Statement:** Not applicable.

**Informed Consent Statement:** Not applicable.

**Data Availability Statement:** The data presented in this study are available on request from the corresponding author. The data are not publicly available due to privacy concerns for the participants involved in the study.

**Conflicts of Interest:** The authors declare no conflicts of interest.

## References

1. Bose, B. *Power Electronics and Motor Drives*, 2nd ed.; Academic Press: Cambridge, MA, USA, 2020; ISBN 978-0-12-821360-5.
2. Manns, D.; Galioto, S.; Weeber, K.; Yagielski, J.High frequency life testing of stator coil insulation. In Proceedings of the 2008 IEEE International Symposium on Electrical Insulation, Vancouver, BC, Canada, 9–12 June 2008.
3. Guastavino, F.; Ratto, A.; Torello, E.; Biondi, G. Aging tests on nanostructured enamels for winding wire insulation. *IEEE Trans. Ind. Electr.* **2014**, *61*, 5550–5557. [CrossRef]
4. Gerlach, M.E.; Weber, S.; Ponick, B. Influence of Hairpin winding and insulation on the vibration behavior of electric machines. *IEEE Trans. Ind. Appl.* **2024**, *60*, 206–214.
5. Besnard, F.; Bertling, L. An approach for condition-based maintenance optimization applied to wind turbine blades. *IEEE Trans. Sustain. Energy* **2010**, *1*, 77–83. [CrossRef]
6. Rafiee, K.; Feng, Q.; Coit, D.W. Condition-based maintenance for repairable deteriorating systems subject to a generalized mixed shock model. *IEEE Trans. Reliab.* **2015**, *64*, 1164–1174. [CrossRef]
7. Kaufhold, M.; Borner, G.; Eberhardt, M.; Speck, J. Failure mechanism of the interturn insulation of low voltage electric machines fed by pulse-controlled inverters. *IEEE Electr. Ins. Mag.* **1996**, *12*, 9–16. [CrossRef]
8. Hudon, C.; Amyot, N.; Lebey, T.; Castelan, P.; Kandev, N. Testing of low-voltage motor turn insulation intended for pulse-width modulated applications. *IEEE Trans. Dielectr. Electr. Insul.* **2000**, *7*, 783–789.
9. Stone, G.C. Partial discharge diagnostics and electrical equipment insulation condition assessment. *IEEE Trans. Dielectr. Electr. Insul.* **2005**, *12*, 891–903. [CrossRef]
10. Boileau, T. *3rd Year Engineering Cycle*; Lecture on diagnosis and fault detection in PMSM; ENSEM: Vandoeuvre-lès-Nancy, France, 2019.
11. IEEE Standard 43-2013. Recommended Practice for Testing Insulation Resistance of Rotating Machinery. 2014. Available online: https://ieeexplore.ieee.org/document/836297 (accessed on 4 February 2023).
12. Werynski, P. Vieillissement des Diélectriques et Surveillance in situ des Machines Electriques. Ph.D. Thesis, Université d'Artois (LSEE), Arras, France, 2006. Available online: https://www.researchgate.net/publication/272857976 (accessed on 28 January 2021).
13. Liu, W.; Schaeffer, E.; Loron, L.; Chanemouga, P. High Frequency modelling of stator windings dedicated to machine insulation diagnosis by parametric identification. In Proceedings of the 2007 IEEE International Symposium on Diagnostics for Electric Machines Power Electronics and Drives, Cracow, Poland, 6–8 September 2007.
14. Yang, J.; Kang, T.-J.; Kim, B.; Lee, S.B.; Yoon, Y.-W.; Kang, D.; Cho, J.; Kim, H. Experimental evaluation of using the surge PD test as a predictive maintenance tool for monitoring turn insulation quality in random wound AC motor stator windings. *IEEE Trans. Dielectr. Electr. Insul.* **2012**, *19*, 53–60. [CrossRef]
15. Lahoud, N.; Nguyen, M.Q.; Maussion, P.; Malec, D.; Mary, D. Lifetime model of the inverter-fed motors secondary insulation by using a design of experiments. *IEEE Trans. Dielectr. Electr. Insul.* **2015**, *22*, 3170–3176. [CrossRef]
16. Perisse, F.; Mercier, D.; Lefevre, E.; Roger, D. Robust diagnostics of stator insulation based on high frequency resonances measurements. *IEEE Trans. Dielectr. Electr. Insul.* **2009**, *16*, 1496–1502. [CrossRef]
17. Haje Obeid, N. Contribution à la Détection des Défauts Statoriques des Actionneurs à Aimants Permanents—Application à la Détection d'un Défaut Inter-Spires Intermittent et au suivi de Vieillissement. Ph.D. Thesis, Université de Lorraine (GREEN), Nancy, France, 2016. Available online: https://tel.archives-ouvertes.fr/tel-01530619/ (accessed on 1 December 2020).
18. Jameson, N.J.; Azarian, M.H.; Pecht, M. Impedance-based condition monitoring for insulation systems used in low-voltage electromagnetic coils. *IEEE Trans. Ind. Electr.* **2017**, *64*, 3748–3757. [CrossRef]
19. Zou, Z.; Liu, S.; Kang, J. Degradation mechanism and online electrical monitoring techniques of stator winding insulation in inverter-fed machines. *World Electr. Veh. J.* **2024**, *15*, 444–466.[CrossRef]
20. Perisse, F.; Werynski, P.; Roger, D. A new method for AC machine turn insulation diagnostic based on high frequency resonances. *Trans. Dielectr. Electr. Insul.* **2007**, *14*, 1308–1315. [CrossRef]

21. Ahmadzadeh, F.; Lundberg, J. Remaining useful life estimation: review. *Int. J. Syst. Assur. Eng. Manag.* **2014**, *5*, 461–474. [CrossRef]
22. Nguyen, V.; Seshadrinath, J.; Wang, D.; Nadarajan, S.; Vaiyapuri, V. Model-based diagnosis and RUL estimation of induction machines under interturn fault. *IEEE Trans. Ind. Appl.* **2017**, *53*, 2690–2701. [CrossRef]
23. Venkatesan, S.; Manickavasagam, K.; Tengenkai, N.; Vijayalakshmi, N. Health monitoring and prognosis of electric vehicle motor using intelligent-digital twin. *IET Electr. Power Appl.* **2019**, *13*, 1328–1335. [CrossRef]
24. Ramos Chavez, J.I. Design of High Frequency Operating Mechatronic Systems: Tools and Methods of Characterization of Electromagnetic Couplings Between Electromechanic Converters and Power Electronics Converters. Ph.D. Thesis, Institut National Polytechnique de Toulouse (ENIT-LGP), Toulouse, France, 2016. Available online: https://www.theses.fr/2016INPT0075 (accessed on 25 January 2023).
25. Hoffmann, A.; Ponick, B. Statistical deviation of high-frequency lumped model parameters for stator windings in three-phase electrical machines. In Proceedings of the 2020 International Symposium on Power Electronics, Electrical Drives, Automation and Motion, (SPEEDAM), Sorrento, Italy, 24–26 June 2020.
26. Al-Ameri, S.M.; Abdul-Malek, Z.; Salem, A.A.; Noorden, Z.A.; Alawady, A.A.; Yousof, M.F.M.; Mosaad, M.I.; Abu-Siada, A.; Thabit, H.A. Frequency response analysis for three-phase star and delta induction motors—Pattern recognition and fault analysis using statistical indicators. *Machines* **2023**, *11*, 106–123. [CrossRef]
27. Ranzinger, L.; Uhrig, S.; Tenbohlen, S. Analysis and modeling the frequency response of rotating machines regarding fault diagnosis using SFRA. *IEEE Trans. Energy Convers.* **2024**, *39*, 1–10. [CrossRef]
28. Keysight Technologies Incorporation. E5061B ENA Vector Network Analyzer—Data Sheet. 2021. Available online: https://www.keysight.com/us/en/assets/7018-02242/data-sheets/5990-4392.pdf (accessed on 4 July 2024).
29. Sant'Ana, W.C.; Lambert-Torres, G.; Bonaldi, E.L.; Gama, B.R.; Zacarias, T.G.; Areias, I.A.; Arantes, D.; Assuncao, F.O.; Campos, M.M.; Steiner, F.M. Online frequency response analysis of electric machinery through an active coupling system based on power electronics. *Sensors* **2021**, *21*, 8057. [CrossRef]
30. Gama, B.R.; Sant'ana, W.C.; Lambert-Torres, G.; Salomon, C.P.; Bonaldi, E.L.; Borges-Da-Silva, L.E.; Carvalho, R.B.B.; Steiner, F.M. FPGA prototyping using the STEMlab board with application on frequency response analysis of electric machinery. *IEEE Access* **2021**, *9*, 26822–26838. [CrossRef]
31. Sant'Ana, W.C.; Salomon, C.P.; Lambert-Torres, G.; Da Borges Silva, L.E.; Bonaldi, E.L.; Lacerda Oliveira, L.E.; Da Borges Silva, J.G. Early detection of insulation failures on electric generators through online Frequency Response Analysis. *Electr. Power Syst. Res.* **2016**, *140*, 337–343. [CrossRef]
32. Bucci, G.; Ciancetta, F.; Fioravanti, A.; Fiorucci, E.; Mari, S.; Silvestri, A. Online SFRA for reliability of power systems. *Sensors* **2023**, *23*, 2583. [CrossRef] [PubMed]
33. Rathnayaka, S.B.; See, K.Y. Early detection of induction motor's defects using an inductively coupled impedance extraction method. In Proceedings of the 2017 IEEE International Electric Machines and Drives Conference (IEMDC), Miami, FL, USA, 21–24 May 2017.
34. Schinkel, M.; Weber, S.-P.; Guttowski, S.; John, W.; Reichl, H. Efficient HF modeling and model parameterization of induction machines for time and frequency domain simulations. In Proceedings of the 21st Annual IEEE Applied Power Electronics Conference and Exposition, (APEC), Dallas, TX, USA, 19–23 March 2006.
35. Dos Santos, V. Modélisation des émissions Conduites de mode Commun D'une Chaîne électromécanique—Optimisation Paramétrique de l'Ensemble Convertisseur Filtres sous Contraintes CEM. Ph.D. Thesis, Institut National Polytechnique de Toulouse (LAPLACE), Toulouse, France, 2019. Available online: https://www.theses.fr/2019INPT0021 (accessed on 5 December 2022).
36. Chen, H.; Yan, Y.; Zhao, H. Extraction of Common-Mode impedance of an inverter-fed induction motor. *IEEE Trans. Electr. Comp.* **2016**, *58*, 599-–606. [CrossRef]
37. Zheng, D.; Lu, G.; Zhang, P. A noninvasive interturn insulation condition monitoring method based on the Common-Mode impedance spectrum of inverter-fed machines. *IEEE Trans. Ind. Appl.* **2021**, *57*, 4786–4795. [CrossRef]
38. Grenier, D.; Labrique, F.; Buyse, H.; Matagne, E. *Electromécanique—Convertisseurs D'énergie et Actionneurs*, 1st ed.; Dunod: Paris, France, 2001; ISBN 978-2-10-005325-4.
39. Fudeh, H.R.; Ong, C.-M. Modeling and analysis of induction machines containing space harmonics - Part I: Modeling and Transformation. *IEEE Trans. Power App. Syst.* **1983**, *PAS-102*, 2608–2615. [CrossRef]
40. Boileau, T. Contribution à la Continuité de Service des Actionneurs Synchrones à Aimants Permanents. Tolérance au Défaut de Capteur Mécanique: Détection de Défauts électriques. Ph.D. Thesis, Institut National Polytechnique de Lorraine (GREEN), Nancy, France, 2010. Available online: https://hal.univ-lorraine.fr/tel-01749443 (accessed on 1 December 2020).
41. Ruiz-Sarrio, J.E.; Antonino-Daviu, J.A.; Navarro-Navarro, A.; Biot-Monterde, V. A review of broadband frequency techniques for insulation monitoring and diagnosis in rotating electrical machines. *IEEE Trans. Ind. Appl.* **2024**, *60*, 6092–6102. [CrossRef]
42. Weber, S.-P.; Hoene, E.; Guttowski, S.; John, W.; Reichl, H. Modeling induction machines for EMC-Analysis. In Proceedings of the IEEE 35th Annual Power Electronics Specialists Conference, Aachen, Germany, 20–25 June 2004.
43. Wang, L.; Ngai-Man Ho, C.; Canales, F.; Jatskevich, J. High-Frequency modeling of the long-cable-fed induction motor drive system using TLM approach for predicting overvoltage transients. *IEEE Trans. Power Electr.* **2010**, *25*, 2653–2664. [CrossRef]

44. Wu, Y.; Bi, C.; Jia, K.; Jin, D.; Li, H.; Yao, W.; Liu, G. High-frequency modelling of permanent magnet synchronous motor with star connection. *IET Electric Power Appl.* **2018**, *12.4*, 539–546. [CrossRef]
45. Rahimi, A.; Kanzi, K. Improved High-Frequency modeling of PMSM using 3-D finite element analysis. In Proceedings of the 2019 International Power System Conference (PSC), Teheran, Iran, 9–11 December 2019.
46. Ferreira, R.S.; Ferreira, A.C. Transient model to study voltage distribution in electrical machine windings considering the rotor. *Electric Power Syst. Res.* **2021**, *195*, 107155–107162. [CrossRef]
47. Vidmar, G.; Miljavec, D. A universal high-frequency three-phase electric-motor model suitable for the delta- and star-winding connections. *IEEE Trans. Power Electr.* **2015**, *30*, 4365–4376. [CrossRef]
48. Moreno, Y.; Almandoz, G.; Egea, A.; Arribas, B.; Urdangarin, A. Analysis of permanent magnet motors in High Frequency—A review. *Appl. Sci.* **2021**, *11*, 6334. [CrossRef]
49. Yang, Z. PI-based simulation modeling for performance testing of the power transmission line. *Energy* **2024**, *301*, 131753. [CrossRef]
50. Revol, B. Modélisation et Optimisation des Performances CEM D'une Association Variateur de Vitesse—Machine Asynchrone. Ph.D. Thesis, Université Joseph Fourier (Laboratoire d'électrotechnique de Grenoble), Grenoble, France, 2003. Available online: https://theses.hal.science/tel-00006396v1 (accessed on 17 March 2024).
51. Toulabi, M.S.; Wang, L.; Bieber, L.; Filizadeh, S.; Jatskevich, J. A universal High-Frequency induction machine model and characterization method for arbitrary stator winding connections. *IEEE Trans. Energy Conv.* **2019**, *34*, 1164–1177. [CrossRef]
52. Haje Obeid, N.; Boileau, T.; Nahid-Mobarakeh, B. Comparison of high frequency winding modeling for stator health monitoring. In Proceedings of the 14th International Symposium on Diagnostics for Electrical Machines, Power Electronics and Drives (SDEMPED), Chania, Greece, 28–31 August 2023.
53. Gustavsen, B.; Semlyen, A. Rational approximation of frequency domain responses by vector fitting. *IEEE Trans. Power Del.* **1999**, *14*, 1052–1061. [CrossRef]
54. Chen, W.; Sun, H.; Gu, X.; Xia, C. Synchronized space-vector PWM for three-level VSI with lower harmonic distortion and switching frequency. *IEEE Trans. Power Electr.* **2016**, *31*, 6428–6441. [CrossRef]
55. Mishali, M.; Eldar, Y. Sub-Nyquist Sampling. *IEEE Signal Proc. Mag.* **2011**, *28*, 98–124. [CrossRef]
56. Cottet, F. *Traitement du Signal*, 1st ed.; Dunod: Paris, France, 2005; ISBN 978-2-10-049690-5.
57. Akima, H. A new method of interpolation and smooth curve fitting based on local procedures. *J. ACM* **1970**, *17*, 589–602. [CrossRef]
58. Jie, H.; See, K.Y.; Chang, Y.; Gao, R.X.-K.; Fan, F.; Zhao, Z. Enhancing motor impedance measurements: broadening the spectrum from low to high frequencies. *Meas. Sci. Technol.* **2024**, *35*, 86008. [CrossRef]


**Disclaimer/Publisher's Note:** The statements, opinions and data contained in all publications are solely those of the individual author(s) and contributor(s) and not of MDPI and/or the editor(s). MDPI and/or the editor(s) disclaim responsibility for any injury to people or property resulting from any ideas, methods, instructions or products referred to in the content.

*applied sciences*

MDPI

*Article*

# Demagnetization Fault Location of Direct-Drive Permanent Magnet Synchronous Motor Based on Search Coil Data-Driven

**Caixia Gao [1], Zhen Jiang [1], Xiaozhuo Xu [1,*] and Jikai Si [2]**

[1] School of Electrical Engineering and Automation, Henan Polytechnic University, Jiaozuo 454150, China; gcx@hpu.edu.cn (C.G.); 13137176411@163.com (Z.J.)
[2] College of Electrical Engineering, Zhengzhou University, Zhengzhou 450000, China; sijikai@zzu.edu.cn
* Correspondence: xxz@hpu.edu.cn

**Abstract**

Demagnetization faults in direct-drive permanent magnet synchronous motors (DDPMSM) can cause significant performance degradation and unplanned downtime. Traditional fault location methods, which rely on manual feature extraction, exhibit limited accuracy and efficiency in complex and variable operating conditions. To address these limitations, this study presents a demagnetization fault location method based on a search coil employing a data-driven one-dimensional convolutional neural network (1D-CNN). Firstly, the arrangement of search coils was determined, and a partitioned mathematical model was established, using the residual back electromotive force (back-EMF) of the search coil over a single electrical cycle as the fundamental unit. Secondly, the residual back-EMF in the search coil is analyzed under various demagnetization parameters and operating conditions to assess the robustness of the proposed method. Furthermore, a 1D-CNN-based fault location model was developed using residual back-EMF signals as the input and targeting the identification of demagnetized permanent magnet types. Simulation and experimental results demonstrate that the proposed method can effectively detect and locate demagnetization faults across different operating conditions. When the demagnetization degree is not less than 10%, the fault location accuracy reaches 99.58%, and the minimum detectable demagnetization degree is 8%. The approach demonstrates excellent robustness and generalization, offering an intelligent solution for demagnetization fault location in PMSMs.

**Keywords:** direct-drive permanent magnet synchronous motor; convolutional neural network; demagnetization fault location; search coil; residual electromotive force

## 1. Introduction

With its direct load connection eliminating mechanical transmission, the direct-drive permanent magnet synchronous motor (DDPMSM) offers key advantages, including direct drive, high power density, and a compact structure. These merits have led to its broad adoption in aerospace, rail transport, industrial automation, and other fields [1,2]. However, motors are subject to the combined effects of electrical, thermal, and mechanical stresses and other factors during operation, posing a risk of fault. Common fault types include demagnetization, inter-turn short circuits, eccentricity, etc. As the core excitation component of a PMSM, permanent magnets can lead to a decline in motor output torque when they undergo an irreversible demagnetization fault. Under the constant load torque constraints, to maintain stable torque output from the motor, the armature current needs

to increase simultaneously to compensate for the weakening of the excitation magnetic field. At this point, the motor temperature will gradually rise, which not only exacerbates the demagnetization fault but also damages the winding insulation and induces winding short-circuit faults. If the motor operates in this state for a long time, it will result in motor burnout, cause unscheduled downtime, and even cause catastrophic accidents. Therefore, achieving timely detection and accurate location of demagnetization faults not only facilitates early warning but also provides an important basis for post-fault operation and maintenance strategies formulation and accident prevention, thereby effectively ensuring the stable operation of the motor system. Furthermore, for DDPMSM, with a larger number of magnetic poles, the precise location of faulty magnetic poles becomes more challenging. Therefore, conducting in-depth research on demagnetization fault detection and location methods holds significant theoretical and practical engineering value.

Currently, online demagnetization detection methods have primarily relied on spectral analysis of signals, such as current [3,4], voltage [5–7], torque [8], and noise [9,10]. However, the characteristic harmonics in these signals that indicate demagnetization are mostly suitable for local demagnetization and are less sensitive to uniform demagnetization. Moreover, most methods can only achieve fault detection but struggle with precise location. This limitation stems primarily from their reliance on characteristic harmonics for analysis, which are susceptible to interference from factors such as motor winding configuration, structural design, and fault type. Consequently, the reliability of these methods is often compromised in complex and variable real-world industrial environments for diagnosis.

To address the limitations of spectral analysis, some researchers have proposed detection strategies based on magnetic signals. Demagnetization faults lead to alterations in the air gap magnetic flux density distribution, and such variations are measurable through detection coils installed in the motor. Search coils offer advantages such as low cost and simple structure (made solely of fine copper wire winding) and have been widely used for demagnetization fault diagnosis via induced voltage. By winding search coils around stator teeth, localized and uniform demagnetization can be detected based on the induced voltage; however, fault location remains unachievable [11]. To improve location capabilities, researchers have attempted to install independent coils on each stator tooth, extracting tooth flux to diagnose the quantity of demagnetized permanent magnets and decouple the induced electromotive force to determine their positions [12,13]. However, these methods currently only study the fault mode of a single demagnetized PM, and the installation of multiple coils results in complex system structures and high invasiveness. To balance location accuracy, implementation invasiveness, and early fault detection capability, our previous research proposed a detection solution based on toroidal yoke search coils [14]. This method involves placing three coils in stator slots to generate three positioning signals and determining the demagnetization location by matching with predefined waveforms. However, the multi-coil structure and reliance on multiple signals also lead to high algorithm complexity.

With the aim of coil reduction and diagnostic system simplification, a novel demagnetization fault diagnosis strategy is proposed in this paper, utilizing only two series-connected toroidal yoke search coils, with their residual voltage serving as the fault characteristic [15]. By matching the measured waveform with predefined waveforms in a fault dictionary, precise identification of the demagnetization type and location is achieved. Although the method effectively reduces the number of coils and simplifies the process, its performance still heavily relies on the accurate setting of predefined waveform templates and manual thresholds. Therefore, an intelligent approach capable of autonomously adapting to varying operating conditions and automatically extracting features is required.


https://doi.org/10.3390/app16020870

In recent years, artificial intelligence algorithms have been widely applied in fault diagnosis, primarily attributed to their powerful capabilities in feature learning and pattern recognition. In traditional machine learning, the Support Vector Machine (SVM) is suitable for small-sample classification tasks but has limitations such as weak interpretability and reliance on manual feature extraction [16]. On the other hand, shallow neural networks can realize automatic feature learning. The Probabilistic Neural Network (PNN) is appropriate for pattern classification and offers fast training speed, but its classification accuracy is highly affected by the choice of the smoothing factor [17,18]. Backpropagation Neural Network (BPNN) has excellent function approximation capabilities but exhibits instability in classification tasks and tends to fall into local optima [19]. Shallow neural networks generally lack sufficient representation capability, whereas deep learning models like Recurrent Neural Network (RNN), Long Short-Term Memory (LSTM) network, and CNN significantly improve feature representation by increasing network depth and structural complexity. RNNs excel in long-time-series prediction but face challenges in spatiotemporal feature extraction and are prone to gradient vanishing or explosion, making it hard to establish effective long-term dependencies [20]. LSTM networks address these issues through gating mechanisms and strengthen the ability of long-term dependency modeling; however, they have high computational resources and longer training times [21]. CNNs, leveraging their structural advantages, reduce sequence dimensionality while preserving key information, leading to improved training efficiency [22]. Notably, as an effective feature extractor, CNN is capable of extracting high-level abstract features directly from raw signals, providing a more accurate characterization of fault features compared to raw data [23–27].

To address the issues of traditional methods relying on precise threshold setting and the high computational complexity and poor real-time performance of intelligent algorithms, this paper proposes a fault location method based on 1-D CNN. The main contributions and innovations of this study are as follows:

(1) A precise method for demagnetization fault localization in DDPMSM based on the back-EMF signal of the search coil is proposed. This method utilizes the sensitivity of the residual back-EMF signal to changes in the internal magnetic field of the motor, significantly enhancing the sensitivity of fault location.
(2) This study adopts a CNN to construct an end-to-end fault diagnosis model. This approach avoids the reliance on manual feature extraction and threshold setting in traditional methods, thereby improving the development efficiency of the diagnostic system.
(3) In response to the raw one-dimensional time series signals as input and the need for real-time diagnosis, this paper proposes a lightweight 1D-CNN structure. The model directly processes the original one-dimensional time series signals, avoiding complex feature engineering and two-dimensional image conversion steps, thereby reducing computational complexity and enhancing the real-time processing performance of the location system.

This article is organized as follows: Section 2 establishes a mathematical model for the search coil residual back-EMF and analyzes the influence patterns of different fault types, operating conditions, and severity levels affect signal characteristics based on the model. Section 3 details the construction process of building a comprehensive fault sample database. and elaborates on the architecture and operational principles of the proposed one-dimensional CNN diagnostic network. Section 4 presents experimental validation and a comparative analysis of the proposed method's effectiveness, conducted on a developed experimental platform. Finally, Section 5 concludes the article.


https://doi.org/10.3390/app16020870

## 2. Analysis of Search Coil Residual Back-EMF Under Demagnetization Fault

### *2.1. Search Coil Arrangement*

The demagnetization fault in PMSM weakens the magnetic field of the demagnetized magnet, a change detectable via stator-mounted coils. The waveform of the coil's back-EMF, being directly dependent on the magnetic state of its coupled permanent magnet, carries substantial demagnetization fault information and is therefore ideal for demagnetization diagnosis. To accurately locate the demagnetized magnet, a search coil configuration is employed, consisting of two identical toroidal yoke coils. These coils are installed within the stator slots of the PMSM and connected in forward series to constitute a search coil, as shown in Figure 1. Each of the toroidal yoke coils is arranged in the inner and outer stator slots of the PMSM. The two yoke coils should be spaced approximately one pole pitch apart to enhance the signal amplitude, which improves the Signal-to-Noise Ratio (SNR). The operating mechanism of the novel searching coil will be analyzed in the following section.

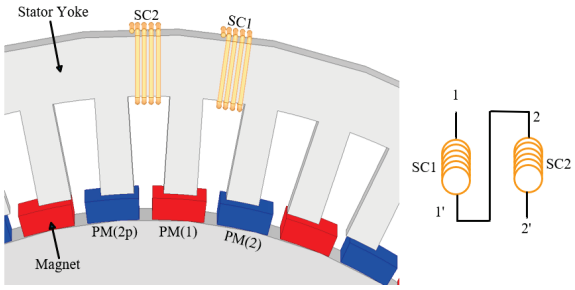


**Figure 1.** The arrangement of the search coil.

### *2.2. Residual Back-EMF Model of SC*

The search coil's back-EMF arises from the time-varying magnetic flux linked with the coil. Under no-load conditions, the spatial distribution of this magnetic field is primarily determined by the arrangement of PMs. For analytical convenience, the PMs are sequentially numbered from 1 to 2p, as illustrated in Figure 1. To achieve synchronous sampling over the entire mechanical cycle, the initial data acquisition point is defined when PM1 and PM2p are positioned such that their geometric centers are alignment with the geometric center of coil SC1. The back-EMFs of SC1 and SC2 for a full motor rotation cycle are collected, and they are subtracted from those under healthy conditions to obtain the residuals of these EMFs. The residual back-EMFs induced by PM$_i$ in SC1 and SC2 are defined as:

$$e_{1-\mathrm{PM}i-\mathrm{rs}} = N_\mathrm{s} l_\mathrm{st} v k_\mathrm{demi} B_{\mathrm{g-i-h}} \tag{1}$$

$$e_{2-\mathrm{PM}i-\mathrm{rs}} = N_\mathrm{s} l_\mathrm{st} v k_\mathrm{demi} B_{\mathrm{g-i-h}} e^{j\theta_\mathrm{s}} \tag{2}$$

where $N_\mathrm{s}$ denotes toroidal yoke coil turns, $l_\mathrm{st}$ represents the motor stack length, and $v$ is the motor rotational speed. $k_\mathrm{demi}$ is the demagnetization severity coefficient, and $k_\mathrm{demi} \in [0, 1]$, which is 0 when the PM$i$ is healthy and is 1 when the PM$i$ is totally demagnetized. As the severity of demagnetization increases, $k_\mathrm{demi}$ approaches 1. $B_\mathrm{g\text{-}i\text{-}h}$ is the airgap flux density produced by the healthy permanent magnet PM$i$. The residual back-EMF induced by PM$_i$ in SC2 is calculated by phase shifting (1). $\theta_\mathrm{s}$ is the electrical angle between SC1 and SC2, and this angle equals or nearly approximates one pole pitch.


https://doi.org/10.3390/app16020870

The SC is obtained by summing the residual EMFs from SC1 and SC2. The SC for PMi demagnetization (eSC-PMi) is obtained by subtracting (2) from (1) as:

$$\begin{cases} e_{SC-\mathrm{PM}i} = N_\mathrm{s} l_\mathrm{st} v k_\mathrm{demi} B_\mathrm{g-i-h}(1 + e^{j\theta_\mathrm{s}}) \\ i\pi \le \alpha \le i\pi + \theta_\mathrm{s} + \theta_\mathrm{pm} \end{cases} \tag{3}$$

where $\alpha$ denotes the electrical angle relative to the coordinate origin. $\theta_\mathrm{pm}$ is the electrical angle corresponding to the surface angle of PM, and it is close to $\pi$.

For simplicity, the residual EMF is assumed to be a sinusoidal wave. Based on Fourier series decomposition, $e_{SC\text{-}\mathrm{PM}i}$ may be simplified as:

$$\begin{cases} e_{SC-\mathrm{PM}i} = (-1)^{i-1} E_1 \mathrm{Sin}(\alpha - (i-1)\pi) \\ i\pi \le \alpha \le (i+2)\pi \end{cases} \tag{4}$$

where $E_1$ denotes the amplitude of $e_{sc\text{-}\mathrm{PM}i}$'s fundamental component.

Reliable fault location features must effectively distinguish fault locations under various demagnetization modes. Therefore, aiming to acquire more reliable location information, this paper investigates the influence of various demagnetization modes on SC residual back-EMF. Considering the alternating arrangement of N and S poles in permanent magnet motors, the same fault pattern exhibits similar characteristics across different electrical cycles. For this reason, this paper adopts one electrical cycle of the SC as the fundamental unit for analysis and segments the signal accordingly. The $k$th interval of the SC ($SC_k$) corresponds to the [$(2k-2)\ \pi$, $2k\pi$]. According to (4), the waveform of $SC_k$ is determined by the demagnetization state of PM($2k$), PM($2k-1$), and PM($2k-2$). Specifically, if $k$ satisfies $k$ = 1, then the PM($2k-2$) corresponds to PM2p. Based on the superposition principle, the model for the kth electrical period ($\mathrm{SC}_k$) is expressed as:

$$\begin{cases} SC_k = e_{SC-\mathrm{PM}(2k)} + e_{SC-\mathrm{PM}(2k-1)} + e_{SC-\mathrm{PM}(2k-2)} \\ (2k-2)\pi \le \alpha \le 2k\pi \end{cases} \tag{5}$$

where $k$ indicates the number of electrical cycles.

This model reveals the core mapping correlation between the SC signal and the condition of the PMs. This relationship establishes a theoretical foundation for analyzing the impact of different demagnetization patterns (including the quantity, position, and severity of demagnetized PMs) on the SC signals, thereby providing a theoretical basis for precisely locating demagnetized PMs.

### *2.3. Analysis of Demagnetization Faults on the Residual Back-EMF of SC*

For exploring the influence of the quantity, location, and severity of demagnetized PMs on the residual back-EMF of search coils, a prototype equipped with search coils is established via Infolytica Magnet (R2017) under preconfigured healthy states and demagnetization fault scenarios. The key parameters of the prototype for testing are listed in Table 1.


https://doi.org/10.3390/app16020870

**Table 1.** Main structure parameters of the DDPMSM.

| Items | Values | Unit |
|---|---|---|
| Number of stator slots | 48 | |
| Number of pole pairs | 22 | |
| Stator outer-diameter | 270 | mm |
| Rotor outer-diameter | 201 | mm |
| Stator inter-diameter | 230 | mm |
| Rotor inter-diameter | 176 | mm |
| Axial length | 100 | mm |
| Thickness of PM | 4.5 | mm |
| Rated frequency | 66 | Hz |
| Rated speed | 180 | rpm |
| Rated power | 1.5 | kW |
| Number of coils | 24 | / |
| Coil turns | 70 | / |
| Magnet type | N45M | / |

Based on the analytical model of SC in Section 2.2, the residual back-EMF waveform of the search coil over one electrical cycle is affected by three consecutive PMs. According to the combination of the three PMs' conditions, there are one healthy and seven demagnetized types, as presented in Table 2.

**Table 2.** Combination of demagnetization fault types for three PMs coupled with residual back-EMF of SC.

| | Health Condition and Demagnetization Fault Modes | PM Numbers and Their Corresponding Condition | | |
|---|---|---|---|---|
| | | $2k$ | $2k-1$ | $2k-2$ |
| The $k$th Electrical Period | Health | 0 | 0 | 0 |
| | Type 1 | 0 | 1 | 1 |
| | Type 2 | 1 | 0 | 0 |
| | Type 3 | 1 | 1 | 0 |
| | Type 4 | 0 | 0 | 1 |
| | Type 5 | 0 | 1 | 0 |
| | Type 6 | 1 | 0 | 1 |
| | Type 7 | 1 | 1 | 1 |

As shown in Table 2, 0 represents a healthy condition of the PM, and 1 represents the demagnetized condition. For instance, Type 6 means PM($2k$) and PM($2k-2$) exhibit demagnetization, while PM($2k-1$) remains healthy.

In this study, the 8th electrical period of SC is a case for analysis, which is subject to the health and fault conditions of PM14, PM15, and PM16. Demagnetization faults are simulated through uniform reduction in the PMs' coercivity, and the demagnetization degree is set to 10% for each faulty PM. The simulation of search coil residual back-EMF under healthy conditions and different fault types is illustrated in Figure 2.

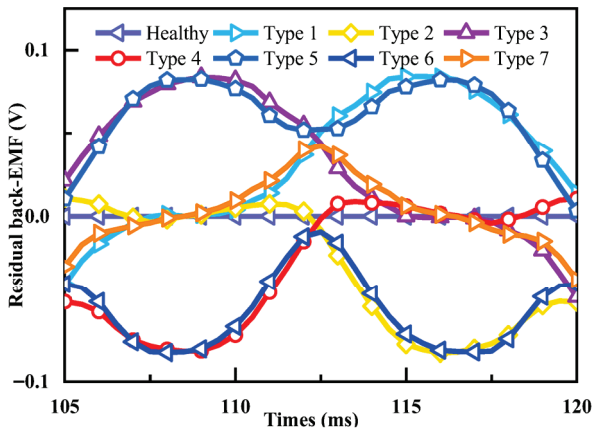


**Figure 2.** Residual back-EMF of SC in healthy condition and seven demagnetization fault types.


https://doi.org/10.3390/app16020870

As illustrated in Figure 2, the partitioned residual back-EMF provides distinct signatures that enable reliable discrimination among the healthy condition and all seven demagnetization fault types.

### *2.4. Robustness Analysis of Demagnetization Fault Characteristic Signal*

(1) Effect of fault severity on the characteristic signal of demagnetization fault.

For exploring the influence of fault severity on the residual back-EMF of SC, five demagnetization fault severities are considered, which include 10%, 30%, 50%, 70%, and 100% demagnetization. Taking Type 1 as an example, the residual back-EMF of SC with different levels of severity is illustrated in Figure 3.

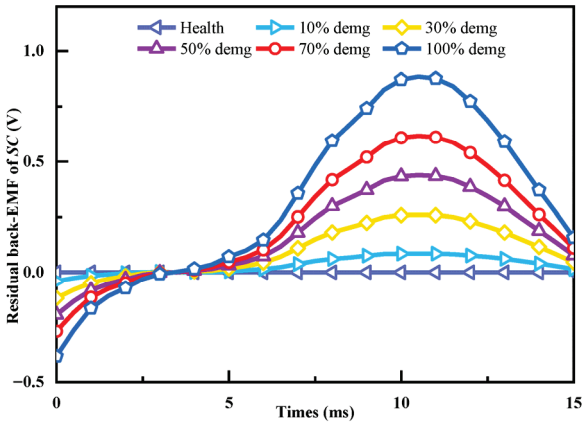


**Figure 3.** Residual back-EMF of SC under Type 1 with different demagnetization degrees.

As illustrated in Figure 3, the residual back-EMF of SC increases proportionally with the severity of the demagnetization fault. In Type 1, the search coil back-EMF at different fault severities has identical waveform morphology, with only amplitude variations. Therefore, the fault severity does not affect the ability to distinguish between demagnetization fault types.

(2) Effect of load on the characteristic signal of demagnetization fault.

For exploring the influence of rated load on SC residual back-EMF, six loads of demagnetization fault are considered under constant speed, which include 0%, 25%, 50%, 75%, 100%, and 125% load. Taking Type 3 as an example, the residual back-EMF of SC with different rated loads is illustrated in Figure 4.

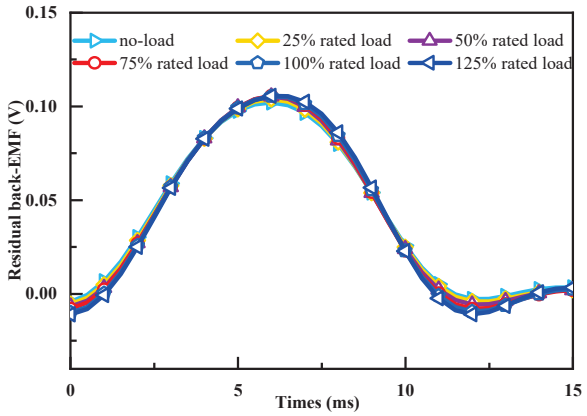


**Figure 4.** Residual back-EMF of SC under Type 3 with different loads.

As illustrated in Figure 4, the back-EMF in the SC exhibits minimal variation under different load conditions for demagnetization faults of identical severity. In Type 3, both


https://doi.org/10.3390/app16020870

the waveform morphology and amplitude remain largely consistent across the tested load range. Therefore, the load condition has a negligible impact on the detection of demagnetization faults.

(3) Effect of speed on the characteristic signal of demagnetization fault.

For exploring the influence of speed on the residual back-EMF of the SC, four speed conditions are considered under rated conditions, which include 90 rpm, 144 rpm, 180 rpm, and 216 rpm. The back-EMF of the SC1 in a healthy motor under different rotational speeds is illustrated in Figure 5.

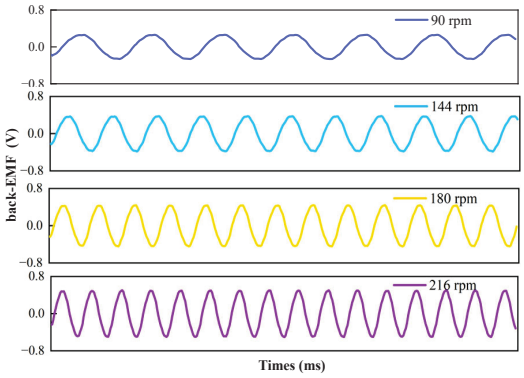


**Figure 5.** Back-EMF waveforms of SC1 at different speeds.

As illustrated in Figure 5, the back-EMF waveforms of a healthy SC1 at different rotational speeds exhibit significant variations in both amplitude and period with speed: The amplitude difference stems from the proportionality between back-EMF and speed (as given in Equation (1)), while the period variation results from the use of a fixed sampling frequency under varying speeds. These discrepancies complicate the selection of a unified reference signal for differential-based analysis, thereby limiting the diagnostic model's generalization capability.

To overcome this limitation, equiangular resampling and amplitude normalization were applied to the SC1 back-EMF signal. Following resampling, as shown in Figure 6, the angular-domain waveforms exhibit consistent periods across speeds, eliminating period-related discrepancies. For amplitude normalization, the measured signal was multiplied by a normalization coefficient $k_v$, given by

$$k_v = V / V_n \tag{6}$$

where $V_n$ is the rated speed, and $V$ is the actual motor speed.

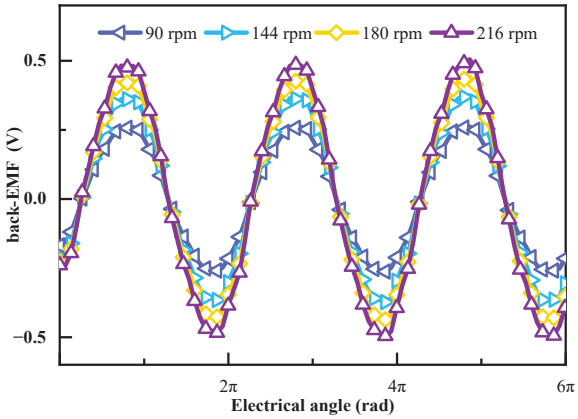


**Figure 6.** The back-EMF waveform of SC1 after equiangular resampling.


https://doi.org/10.3390/app16020870

After these processing steps, both the amplitude and waveform of the SC1 back-EMF become independent of speed, endowing the proposed diagnostic method with robustness against speed fluctuations.

## 3. Permanent Magnet Fault Diagnosis Based on CNN

Extracting fault features from characteristic signals is a crucial step in fault diagnosis. However, traditional fault diagnostic methods rely on manually extracting features based on signal processing techniques, with diagnostic performance constrained by expert expertise and exhibit limited generalization capability. In contrast, deep learning techniques possess a remarkable ability to extract discriminative features adaptively and have been widely adopted in various equipment fault diagnosis applications. Among these, the CNN, as one of the most representative architectures in deep learning, has achieved outstanding performance in motor fault diagnosis scenarios. Therefore, this study proposes an intelligent diagnosis method based on CNN. The workflow can be generally split into data processing and CNN model design, as illustrated in Figure 7. Specifically, it consists of three main steps: (1) constructing an enhanced fault sample library by injecting noise; (2) designing a CNN architecture suitable for residual sequences of search coils back-EMF; and (3) conducting model training and performance evaluation. Each step is detailed in the subsequent subsections.

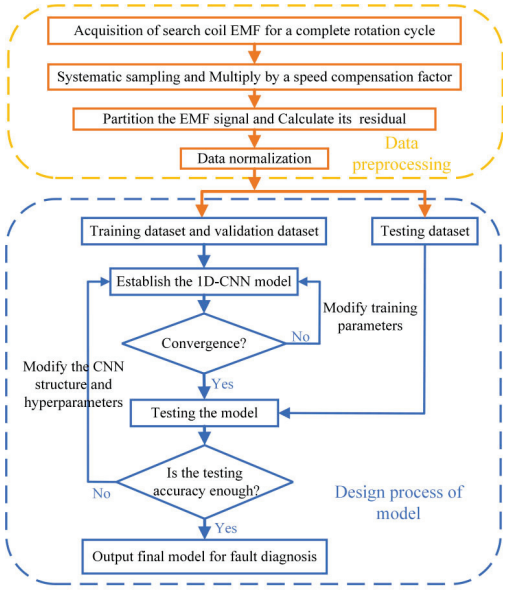


**Figure 7.** Flowchart of the 1-D CNN model design process.

### *3.1. Fault Sample Database Construction with Noise Injection*

The limited availability of experimental samples (only one healthy prototype and one with a Type 5 demagnetization fault) restricted the comprehensive coverage of fault types, severity levels, and locations. To overcome this constraint, we employed finite element simulations to generate 720 samples for establishing a comprehensive initial sample library.

This sample library encompasses eight operational states (one healthy and seven fault Types, Type1-Type7), six load levels (0%, 25%, 50%, 100%, 125% of rated load), four speed conditions (40%, 60%, 80%, 100% rated speed), and five fault severity levels (10%, 30%, 50%, 70%, 100% demagnetization). A full-factorial design was used to evaluate all combinations of these states and conditions. Both healthy and faulty samples cover identical ranges of load and speed, with data in each group being mutually independent and non-overlapping.

Since motors are susceptible to external environmental noise during actual operation, a factor not considered in finite element model simulations. To validate the model's


https://doi.org/10.3390/app16020870

robustness, Gaussian white noise is injected into the simulated data. This type of noise is widely adopted for CNN robustness testing due to its flat power spectral density (simulates random interference) and computational efficiency. To better emulate real-world noise conditions, SNR levels of 5 dB and 15 dB are applied, representing strong electromagnetic interference (5 dB) and moderate background noise (15 dB), respectively. The noise intensity is quantified by the SNR, defined as:

$$SNR = 10 \times \log_{10}(\frac{P_s}{P_n}) \tag{7}$$

where $P_s$ and $P_n$ denote the average power of the signal component and noise component, respectively, within a specified time interval.

The resampled signal x($m$) constitutes a discrete sequence of length $L_m$. The average power $P_x$ of this discrete signal x($m$) is computed as follows:

$$P_x = \frac{1}{L_m} \times \sum_0^{L_m-1} x(m)^2 \tag{8}$$

The discrete SC fault signal s(m) were substituted into Equation (8) to obtain the original signal power ($P_s$). Substituting the predefined SNR threshold and Ps into Equation (7) yields the target noise power ($P_n$). Gaussian white noise with a power of $P_n$ is generated via Equation (9).

$$N_{oise} = \sqrt{P_{noise}} \times randn(1, L_m) \tag{9}$$

where the *randn* () function generates random samples drawn from a standard normal distribution, and noise represents the synthesized noise data.

The generated noise was superimposed onto all raw signals to produce noise-contaminated signals at the target SNRs. Taking Type 2 as an example, the residual back-EMF of the search coil under different SNRs is illustrated in Figure 8.

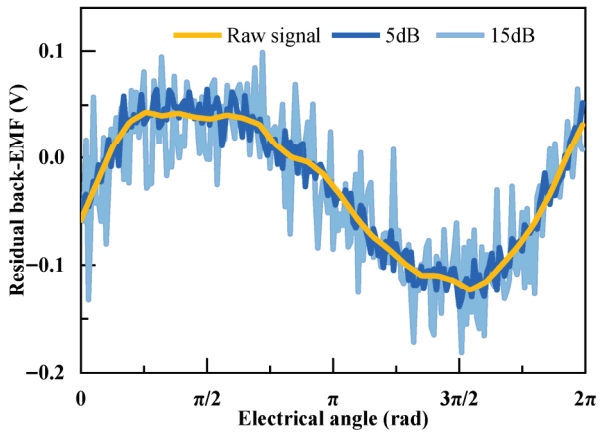


**Figure 8.** Residual back-EMF of the SC at different SNRs.

As shown in Figure 8, the raw signal is the residual back-EMF waveform without noise interference, exhibiting a smooth and continuous trend with stable periodic characteristics. After adding noise, the smoothness of the residual back-EMF waveform significantly decreases and waveform amplitude fluctuation intensifies. As the SNR decreases, the signal quality deteriorates significantly, the smoothness of the waveform further decreases, and the amplitude fluctuation becomes more severe, and the greater the deviation from the raw signal trend. Under strong noise interference, if the fault feature is weak, it will be difficult to effectively extract, which is prone to misdiagnosis and seriously affects the accuracy of diagnosis.


https://doi.org/10.3390/app16020870

To facilitate analysis of these reliable fault features, a fault sample library was developed using experimental data from healthy and faulty prototypes as well as finite element simulation data, as detailed in Table 3.

**Table 3.** Fault sample.

| Category Label | Type | Details | SNR (dB) | Sample Quantity |
|---|---|---|---|---|
| 1 | Healthy | Speed(r/min): 90/144/180/216 Load(A): 0/1/2/3/4/5 Demagnetization Degree: - | - | 240 |
| 2 | Type 1 | | 5/15 | 240 |
| 3 | Type 2 | Speed(r/min): | 5/15 | 240 |
| 4 | Type 3 | 90/144/180/216 | 5/15 | 240 |
| 5 | Type 4 | Load(A): 0/1/2/3/4/5 | 5/15 | 240 |
| 6 | Type 5 | Demagnetization Degree: | - | 240 |
| 7 | Type 6 | 10%/30%/50%/70%/100% | 5/15 | 240 |
| 8 | Type 7 | | 5/15 | 240 |

### *3.2. Proposed 1D-CNN Model Design*

Based on the established dataset, this study focuses on the core component of the intelligent diagnostic model: a 1-D CNN architecture for end-to-end demagnetization fault diagnosis. When designing the CNN, the following concepts were adhered to: uniform filter size, the number of filters should increase layer by layer, and each convolutional layer must be followed by an activation function and a pooling layer. Therefore, we propose a CNN that adjusts parameters based on the above principles, relying on experience and previous experimental tuning. After experimental tuning, the finalized CNN architecture generally comprises one input layer, two convolutional layers, two max-pooling layers, one fully connected layer, and one output layer, as illustrated in Figure 9.

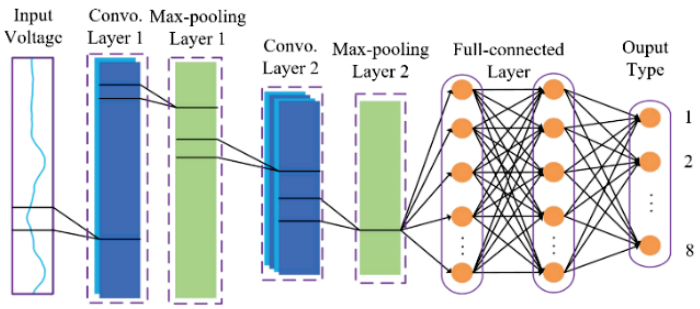


**Figure 9.** The basic structure of 1-D CNN.

(1) The input layer is configured to receive a 200 × 1 residual signal from the search coil. This dimension was selected because, firstly, the features of demagnetization faults are most distinctly exhibited over one full electrical cycle; Secondly, integer-period sampling was employed to eliminate spectral leakage. This requires the number of samples N to satisfy $N = f_s/f_0$. Consequently, with a fundamental frequency $f_0$ of 66 Hz and a sampling frequency fs of 13.2 kHz, N is determined to be 200. This approach can retain the complete information of the phase and amplitude, thereby providing input data for the convolutional layers to learn the essential discriminative features.

(2) The convolution layer utilizes the convolution operation to automatically extract features from the output of the preceding layer or the original signal. The convolution operation is given by

$$x_j^l = f\left(\sum_{x \in M_j} x_i^{l-1} * k_j^l + b_j^l\right) \quad (10)$$


https://doi.org/10.3390/app16020870

where $x_i^{l-1}$ indicates the input data for the $l$th layer and $*$ represents the convolution operation, $x_j^l$ is the output of layer l, $M_j$ denotes the set of input features, $k_j^l$ and $b_j^l$ represent the convolutional kernel weight and bias corresponding to the $j$th kernel in the lth convolutional layer, respectively. where $f(\cdot)$ refers to a nonlinear activation function, applied to enhance the network's nonlinear expression capability.

The ReLU activation function is commonly used to accelerate the convergence of the model during its training process, as given by

$$\mathrm{ReLU}(x) = \max(0, x) \tag{11}$$

After determining the basic network composition, the effectiveness of feature extraction primarily depends on two key architectural parameters: convolutional depth and kernel size. These parameters collectively determine the receptive field size and the granularity of feature extraction, which are essential to accurately extracting the local patterns exhibited by demagnetization faults in residual back-EMF sequences. Therefore, this study adopts a stepwise systematic optimization strategy: first determining the optimal network depth, and then optimizing the kernel size based on this foundation.

First, network depth optimization was conducted. Considering the limited length of the input sequence ($200 \times 1$) and the need to precisely capture the localized pulse signatures characteristic manifested in the residual back-EMF under demagnetization faults, this study employed a small initial convolutional kernel (kernel size = 3, stride = 1) to preserve the temporal details of the input signal. With this configuration, this study evaluated architectures with 1 to 4 convolutional layers. The different convolutional layers' diagnostic accuracy is presented in Table 4. The results indicated that the two-layer network achieved significantly higher diagnostic accuracy compared to the single-layer model. However, increasing the depth to 3 or 4 layers yielded no substantial improvement in accuracy. This suggests that the two-layer structure already provides a sufficient receptive field to capture fault characteristics, while deeper structures increase the risks of vanishing/exploding gradients. Consequently, a two-layer architecture was identified as optimal, employing 16 and 32 filters in its first and second layers, respectively.

**Table 4.** Diagnostic accuracy with different convolutional layers.

| Layer | 1 | 2 | 3 | 4 |
|---|---|---|---|---|
| Accuracy | 98.20% | 99.50% | 99.60% | 99.62% |

Subsequently, within the two-layer framework, this study compared four kernel sizes ($2 \times 1$, $3 \times 1$, $5 \times 1$, $7 \times 1$). The results indicate that CNN models with different kernel sizes all achieve classification accuracy of approximately 99%. The kernel size has minimal impact on the classification accuracy of the CNN model. Balancing computational efficiency and result accuracy, this paper selects a $3 \times 1$ kernel size for the model design.

(3) The pooling layer is placed after the convolutional layer to reduce the dimension of the extracted features. The pooling operation is treated as a down-sampling operation. This reduces the computational and parametric overhead, thereby mitigating overfitting and improving model generalization capability. The most widely used in CNN is maximum pooling. The mathematical expression is

$$P_i^{l+1} = \underset{(j-1)W+1<t<jW}{max} \{q_i^l(t)\} \tag{12}$$


https://doi.org/10.3390/app16020870

where $P_i^{l+1}$ represents the output value of the $(l+1)$th layer, $W$ refers to the width of the pooling window. $q_i^l(t)$ represents the output of the $t$th neurons in the $i$th channel of the l layer.

Following the convolutional operation, a max pooling layer (kernel size = 2, stride = 2) is employed to downsample the feature maps. This configuration is specifically optimized for 1-D residual back-EMF time-series signals, with its key advantages being: First, its compact receptive field preserves fine-grained temporal features more effectively than larger kernels, maintaining essential structural details during down-sampling. Second, a stride of 2 halves the length of the feature maps, reducing computational complexity and memory consumption in subsequent layers by approximately 50%. Finally, for an input sequence length of 200, this stride ensures non-overlapping and complete coverage of the entire sequence, preventing information loss at the boundaries. In summary, this empirically validated configuration achieves an optimal balance between computational efficiency and feature preservation.

(4) The purpose of a fully connected layer is to project the feature space to the sample label space; the features are converted into 1-D vectors. Each neuron in this layer is fully connected to all neurons in the preceding layer. The output vector of the $l$ layer is

$$x_j^l = f(\sum_{i=1}^{M} x_i^{l-1} \times w_{ij}^l + b_j^l), j = 1,\ 2,\ \ldots,\ N \tag{13}$$

where $M$ is the input feature dimensionality, and $N$ is the output vector dimensionality. $w_{ij}^l$ denotes the weight of the connection between the $i$th neuron of the $(l-1)$ th layer and the $j$th neuron of the $l$th layer, and $b_j^l$ indicates the bias term of the $j$th neuron of the lth layer.

The SoftMax is connected after the fully connected layer and acts as a classifier. The SoftMax function calculates the probability that the input data belongs to each class. The output expression of SoftMax regression is

$$p(x_j^l) = \frac{e^{x_j^{l-1}}}{\sum_{k=1}^{N} e^{x_k^{l-1}}} \tag{14}$$

where $N$ is the number of classes, $x_j^{l-1}$ is the output of the upper layer, and $p\left(x_j^l\right)$ is the output probability.

The classification module, comprising fully connected layers and an output layer, utilizes the Softmax activation function, maps the high-dimensional features to a probability distribution over fault classes, enabling detection and location of demagnetization faults. The model's detailed architecture is specified in Table 5.

**Table 5.** Network architecture and parameters.

| Layer | Parameter | Output Dim |
|---|---|---|
| Input Layer | \ | $200 \times 1$ |
| Convolution Layer(C1) | 16 filters, kernel = $3 \times 1$ | $200 \times 1 \times 16$ |
| Activation Function | ReLU | \ |
| Maximum Pooling | Kernel = 2 Stride = 2 | $100 \times 1 \times 16$ |
| Convolution Layer(C2) | 32 filters, kernel = $3 \times 1$ | $100 \times 1 \times 32$ |
| Activation Function | ReLU | \ |
| Maximum Pooling | Kernel = 2 Stride = 2 | $50 \times 1 \times 32$ |
| Fully connected Layer | \ | $1 \times 1 \times 8$ |
| SoftMax Layer | \ | $1 \times 1 \times 8$ |
| Output Layer | \ | $1 \times 1 \times 8$ |


https://doi.org/10.3390/app16020870

### *3.3. Model Training and Performance Evaluation*

To evaluate the performance and generalization capability of the designed 1D-CNN model, we employed the comprehensive fault database detailed in Table 3. The dataset was partitioned randomly into training, validation, and test sets at a 2:1:1 proportion to ensure an unbiased model evaluation process, then fed into a CNN model constructed with the MATLAB 2024a Deep Learning Toolbox for training. Training of the 1D-CNN model was using the Adaptive Moment Estimation (Adam) optimizer. Key hyperparameters are set as follows: 0.01 for the learning rate, 40 for the maximum epochs, and 64 for the batch size. The training and validation progress are illustrated in Figure 10, and the confusion matrix corresponding to the 1D-CNN test results is illustrated in Figure 11.

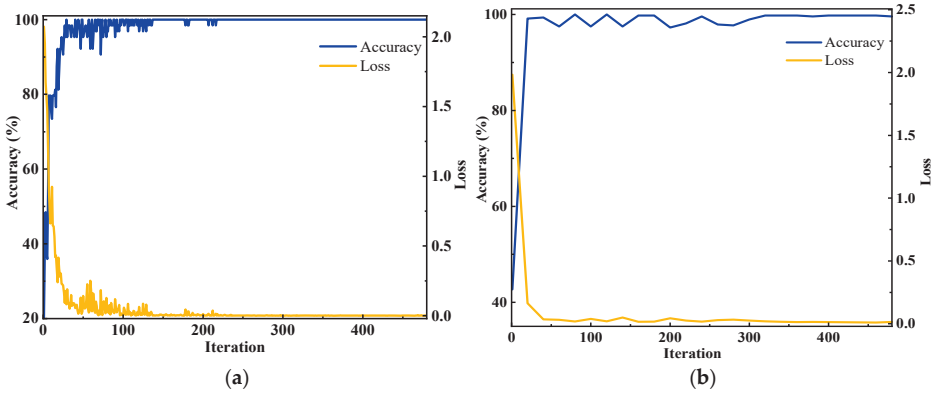


**Figure 10.** Accuracy and loss curves during training and validation. (**a**) Training process. (**b**) Validation process.

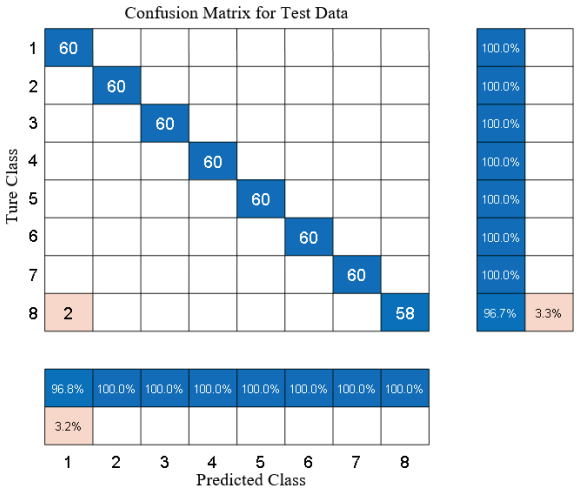


**Figure 11.** Confusion matrix of the 1D-CNN test results.

As shown in Figure 10, the model approached convergence after approximately 300 iterations. Both training and validation accuracy exceeded 99%. Furthermore, the training and validation losses decreased consistently and stabilized around 0.001. These results suggest that the model exhibits strong convergence and generalization performance.

As illustrated in Figure 11, the model demonstrated excellent performance on the test set, achieving an overall accuracy of 99.5% and a classification accuracy exceeding 96.5% for all eight fault states. However, confusion matrix analysis revealed one misclassification: a small number of samples from Type 7 (uniform demagnetization of three permanent magnets within the same electrical cycle) were incorrectly identified as normal. This misclassification can be attributed to the preservation of magnetic field symmetry in Type 7, which only causes variations in signal amplitude without waveform distortion.


https://doi.org/10.3390/app16020870

In contrast, demagnetization of single or dual permanent magnets disrupts magnetic symmetry, resulting in more distinguishable features.

Notably, all misclassifications of Type 7 occurred at the 10% demagnetization level. At this early stage, the fault feature closely resembles normal conditions, making differentiation difficult. From an engineering safety perspective, a 10% demagnetization degree generally does not immediately cause system failure or severe performance degradation, thus providing enough maintenance time before performance deteriorates.

## 4. Experimental Result

### *4.1. Experimental Setup*

The experimental platform is illustrated in Figure 12. It primarily comprises two comparative prototypes (healthy and defective, with key parameters summarized in Table 1). During the experiment, the driver powers the test prototype while an independent motor provides the load. Both prototypes were mechanically coupled to a torque transducer for simultaneous speed and torque measurement. Search coils (diameter: 0.5 mm, turns per coil: 5) were installed in the test prototype to sense the back-EMF. The back-EMF data, recorded by the acquisition card, is routed to the computer via USB. An oscilloscope, connected to the search coils via probes in parallel, provided visual monitoring of the back-EMF. To simulate demagnetization faults, permanent magnets PM9 and PM31 were detached from the test prototype. These magnets were symmetrically positioned relative to the center line, thereby avoiding potential eccentricity effects.

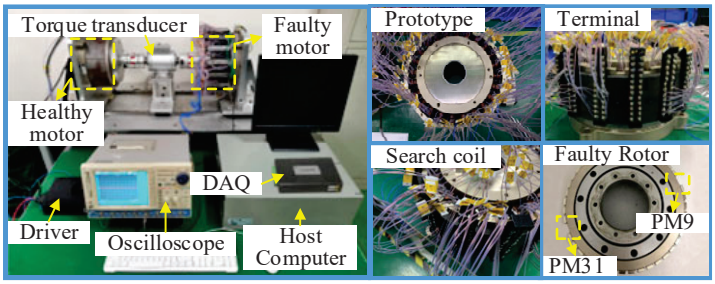


**Figure 12.** Experiment platform.

### *4.2. Experimental Results and Analysis*

To verify the proposed location method, the experimental back-EMF signals from the healthy prototype under rated load conditions were compared with the corresponding simulation results. A low-pass filter realized in MATLAB was applied to process the measured back-EMF signal. The back-EMF signals of SC1, SC2, and SC for the healthy prototype under rated load conditions are illustrated in Figure 13.

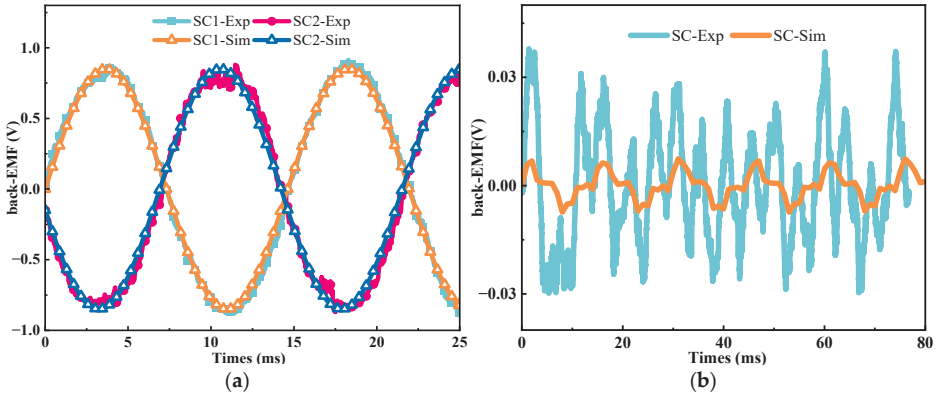


**Figure 13.** Experimental results of search coil back-EMF (**a**) SC1 and SC2 back-EMF, (**b**) SC back-EMF.


https://doi.org/10.3390/app16020870

As illustrated in Figure 13a, the experimental back-EMF results for search coils agree well with the theoretical predictions, with a maximum relative error of 4.4% between the actual and theoretical peak values. As illustrated in Figure 13b, the maximum discrepancy between simulated and experimental results of SC was 0.04 V. This discrepancy stems from environmental noise, PMSM magnetic field non-uniformity, and stator winding imbalances, inherent phenomena present in both healthy and faulty states. However, these minor discrepancies have a negligible impact on diagnostic outcomes, as the 1-D CNN model is not dependent on precise peak-value measurements. Instead, it utilizes an end-to-end learning approach to extract discriminative features directly from the raw signal data.

After verifying the reliability of the healthy baseline measurements under rated load, the influence of load variations on diagnostic signals was further analyzed. The SC waveforms of the healthy motor at rated speed under four rated load conditions are illustrated in Figure 14.

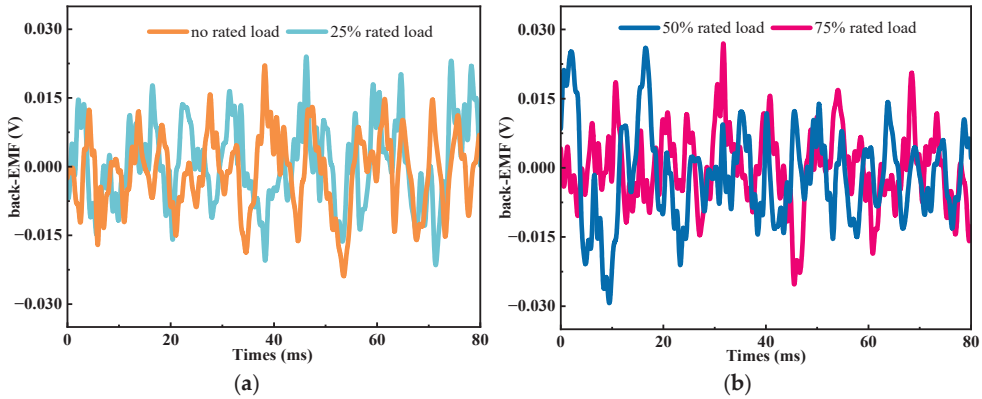


**Figure 14.** Experimental results of SC residual back-EMF for the different loads. (**a**) no rated load and 25% rated load (**b**) 50% rated load and 75% rated load.

As shown in Figure 14, the SC signal of the healthy motor is largely independent of load variations, and these minor differences do not affect the diagnostic outcome.

To demonstrate its objective of fault diagnosis, the method was subsequently applied to fault location experiments. In the faulty prototype, permanent magnets PM9 and PM31 were completely removed. The fault location signal exhibits distinct features at the 5th and 16th electrical cycles, which correspond precisely to the magnetic pole partitions of the removed PMs. The waveforms of the fault location signal measured under rated operating conditions are illustrated in Figure 15.

As illustrated in Figure 15a,b, the simulated and experimental residual back-EMF waveforms obtained from the search coil are in strong agreement. Specifically, both SC1 and SC2 exhibit pronounced signals during the intervals of [60 ms, 75 ms] and [225 ms, 245 ms], which correspond to the 5th and 16th electrical periods, respectively. As illustrated in Figure 15c,d, the SC waveform within these critical intervals displays the same characteristics previously defined for Type 5 and matches the fault signature (0, 1, 0) listed in Table 2. Substituting $k = 5$ and $k = 16$ into the expression $(2k - 2, 2k - 1, 2k)$, the demagnetized permanent magnets are identified as PM9 and PM31.


https://doi.org/10.3390/app16020870

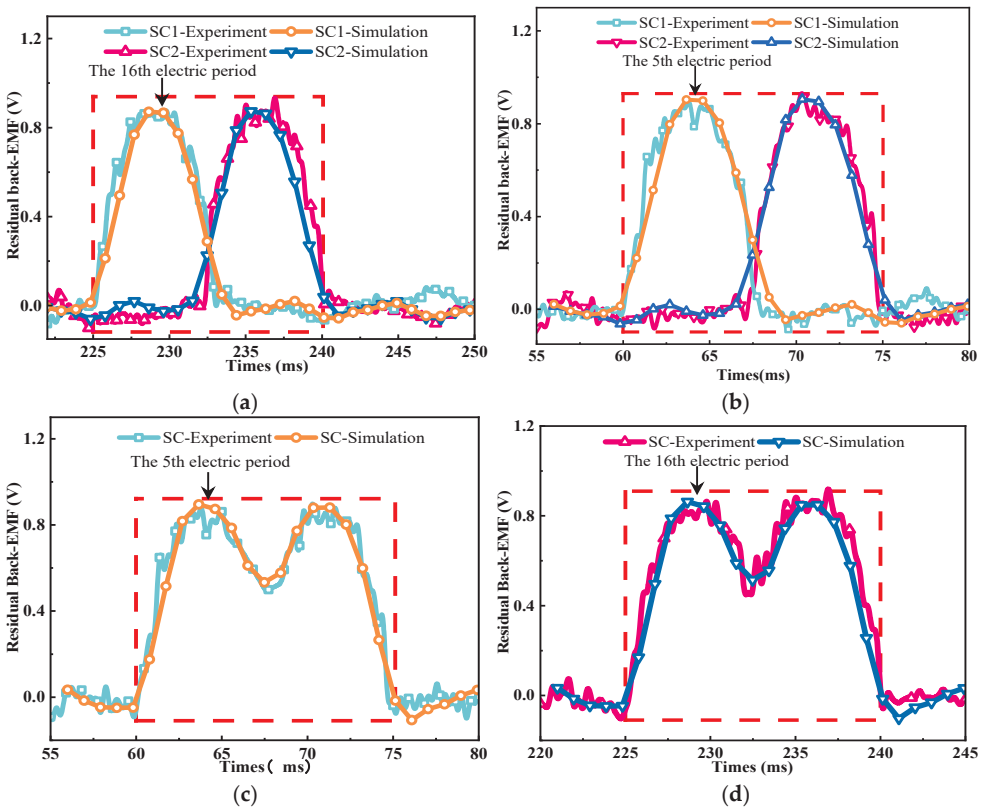


**Figure 15.** Experimental results of search coils' residual back-EMFs for defective prototype. (**a**) Residual back-EMF in the 5th electrical cycle (**b**) Residual EMF of SC1 and SC2 in the 16th electrical cycle (**c**) Residual EMF of SC in the 5th electrical cycle (**d**) Residual EMF of SC in the 16th electrical cycle.

### *4.3. Comparison with Other Methods*

To validate the performance advantages of the 1-D CNN model, LSTM, BPNN, PNN, and SVM are used as comparative models. Meanwhile, to avoid random errors caused by a single test, each model underwent ten independent experiments, with the average classification accuracy serving as the performance evaluation metric. The per-class accuracy of these models is illustrated in Figure 16, and overall accuracy and computational time are summarized in Table 6.

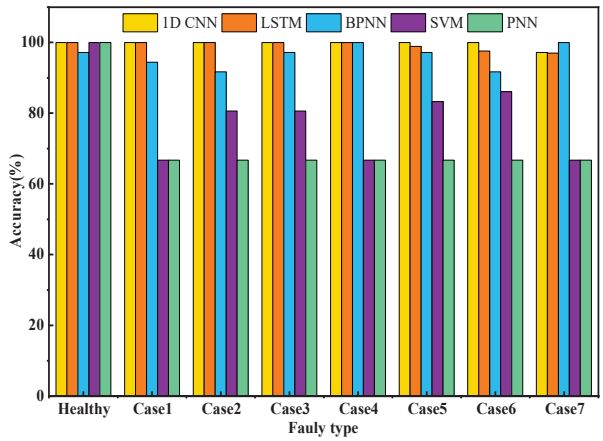


**Figure 16.** Comparison of diagnostic accuracy among different algorithms.


https://doi.org/10.3390/app16020870

**Table 6.** The result of different methods.

| Methods | Testing Accuracy | Time |
|---|---|---|
| 1-D CNN | 99.58% | 3 s |
| LSTM | 98.93% | 9 s |
| BPNN | 96.18% | 12 s |
| PNN | 78.84% | 0.06 s |
| SVM | 70.86% | 0.2 s |

As illustrated in Figure 16, the proposed 1D-CNN model achieved superior performance in classification, with all fault-type accuracies exceeding 96.5%. Although the BPNN marginally outperformed our model in Type 7, the 1D-CNN maintained the highest accuracy across all other fault types.

As summarized in Table 6, the proposed 1D-CNN achieved the highest testing accuracy (99.58%) with a computational time of only 3 s, outperforming other methods. In contrast, the LSTM achieves 98.93% accuracy but requires 9 s for computation, while the BPNN reaches 96.18% accuracy but requires 12 s for computation. Although the PNN and SVM computed faster (0.06 s and 0.2 s), their accuracy was more than 21% lower than the proposed model. This demonstrates that the CNN model holds significant advantages when applied to demagnetization fault detection and location in DDPMSMs.

## 5. Conclusions

This study proposes a 1-D CNN location method based on the residual back-EMF of SC to locate demagnetization faults in DDPMSM. Experiments and simulations corroborated the efficacy and reliability of the proposed method.

(1) SC1 and SC2, two toroidal coils, are installed in corresponding positions within adjacent pole-pairs in the stator slots, connected in series to constitute the SC assembly. This configuration enables fault location through residual back-EMF analysis. This approach significantly reduces intrusiveness and implementation cost compared to conventional methods that involve installing search coils and applies to permanent magnet synchronous motors with any pole-slot combination.

(2) The rotor is partitioned into several sectors based on the pole pairs of the permanent magnets, dividing the full mechanical cycle accordingly. Previous analysis indicates that the residual back-EMF waveform is related to the state of three adjacent permanent magnets. Therefore, by analyzing the location signal waveform within each sector, the magnetic state of the permanent magnets in that sector can be effectively identified, thereby enabling accurate location of the demagnetized permanent magnets.

(3) This paper proposes a precise location method based on a 1D-CNN, which is capable of achieving both detection and location of demagnetization faults. Compared with the other classification approaches, the experimental result shows that the proposed method's fault type location accuracy reaches 99.58%, significantly outperforming methods such as LSTM, BPNN, PNN, and SVM. Although the computational efficiency of this method is slightly lower than that of PNN and SVM, its diagnostic accuracy shows an improvement of over 20%, and both its computational efficiency and comprehensive diagnostic performance are superior to those of BPNN and LSTM.

The proposed method demonstrates strong capabilities in detecting and locating demagnetization faults. While the method is invasive, it applies to safety-sensitive scenarios, including rail transit systems, aerospace power systems, and industrial automation systems.

Future work will primarily focus on the refining and enhancing the existing location model to improve its performance and investigating fault severity assessment methodolo-


https://doi.org/10.3390/app16020870

gies to achieve a comprehensive diagnostic procedure from fault location to severity evaluation.

**Author Contributions:** C.G. supervised the study, reviewed the manuscript, and proposed the research direction of the paper. Z.J. wrote the main manuscript text, prepared the figures and tables, performed coding work, and conducted data processing. X.X. and J.S. supervised the study, reviewed the manuscript. All authors have read and agreed to the published version of the manuscript.

**Funding:** This work was supported by National Natural Science Foundation of China (52177039) and, Natural Science Foundation of Henan Province (252300421328). Fundamental Research Funds for the Universities of Henan Province (NSFRF240306).

**Institutional Review Board Statement:** Not applicable.

**Informed Consent Statement:** Not applicable.

**Data Availability Statement:** The data that support the findings are available from the corresponding author upon reasonable request.

**Conflicts of Interest:** The authors have no conflicts to disclose.

## References

1. Mohamed, Y.A.-R.I. Direct Instantaneous torque control in direct drive permanent magnet synchronous motors—A new approach. *IEEE Trans. Energy Convers.* **2007**, *22*, 829–838. [CrossRef]
2. Mohamed, Y.A.-R.I. A Hybrid-Type variable-structure instantaneous torque control with a robust adaptive torque observer for a high performance direct-drive PMSM. *IEEE Trans. Ind. Electron.* **2007**, *55*, 2491–2499. [CrossRef]
3. Goktas, T.; Zafarani, M.; Akin, B. Discernment of broken magnet and static eccentricity faults in permanent magnet synchronous motors. *IEEE Trans. Energy Convers.* **2016**, *31*, 578–587. [CrossRef]
4. Kao, I.H.; Wang, W.J.; Lai, Y.H.; Perng, J.W. Analysis of permanent magnet synchronous motor fault diagnosis based on learning. *IEEE Trans. Instrum. Meas.* **2018**, *68*, 310–324. [CrossRef]
5. Urresty, J.-C.; Riba, J.-R.; Romeral, L. A back-EMF based method to detect magnet failures in PMSMs. *IEEE Trans. Magn.* **2013**, *49*, 591–598. [CrossRef]
6. Bossio, J.; Ruschett, C.; Bossio, G.; Verucchi, C.; De Angelo, C. Rotor fault diagnosis in permanent magnet synchronous machine using the midpoint voltage of windings. *IET Electr. Power Appl.* **2020**, *14*, 256–261. [CrossRef]
7. Usman, A.; Rajpurohit, B.S. Modeling and classification of stator inter-turn fault and demagnetization effects in BLDC motor using rotor back-EMF and radial magnetic flux analysis. *IEEE Access* **2020**, *8*, 118030–118049. [CrossRef]
8. Ebrahimi, M.; Faiz, J. Demagnetization fault diagnosis in surface mounted permanent magnet synchronous motors. *IEEE Trans. Magn.* **2013**, *49*, 1185–1192. [CrossRef]
9. Zhu, M.; Yang, B.; Hu, W.; Feng, G.; Kar, N.C. Vold–Kalman Filtering Order Tracking Based Rotor Demagnetization Detection in PMSM. *IEEE Trans. Ind. Appl.* **2019**, *55*, 5768–5778. [CrossRef]
10. Barmpatza, A.C.; Kappatou, J.C. Study of the total demagnetization fault of an AFPM wind generator. *IEEE Trans. Energy Convers.* **2021**, *36*, 916–928. [CrossRef]
11. Rafaq, M.S.; Lee, H.; Park, Y.; Lee, S.B.; Zapico, M.O.; Fernandez, D.; Diaz-Reigosa, D.; Briz, F. Airgap search coil based identification of PM synchronous motor defects. *IEEE Trans. Ind. Electron.* **2022**, *69*, 6551–6560. [CrossRef]
12. Zeng, C.; Huang, S.; Lei, J.; Wan, Z.; Yang, Y. Online rotor fault diagnosis of permanent magnet synchronous motors based on stator tooth flux. *IEEE Trans. Ind. Appl.* **2021**, *57*, 2366–2377. [CrossRef]
13. Da, Y.; Shi, X.; Krishnamurthy, M. A New approach to fault diagnostics for permanent magnet synchronous machines using electromagnetic signature analysis. *IEEE Trans. Power Electron.* **2013**, *28*, 4104–4112. [CrossRef]
14. Chen, H.; Gao, C.; Si, J.; Nie, Y.; Hu, Y. A novel method for diagnosing demagnetization fault in PMSM using toroidal-yoke-type search coil. *IEEE Trans. Instrum. Meas.* **2021**, *71*, 750101. [CrossRef]
15. Gao, C.; Li, B.; Chen, H.; Xu, Y.; Xu, X.; Si, J. A less-invasive method for accurately diagnosing demagnetization fault in PMSM using rotor partition. *IEEE Trans. Transp. Electrif.* **2021**, *9*, 2356–2366. [CrossRef]
16. Shi, Q.; Zhang, H. Fault diagnosis of an autonomous vehicle with an improved SVM algorithm subject to unbalanced datasets. *IEEE Trans. Ind. Electron.* **2021**, *68*, 6248–6256. [CrossRef]
17. Guo, F.; Fu, W.; Wang, Y.; Chen, J. Research on fault diagnosis method for photovoltaic array based on model fusion. *Electr. Eng.* **2025**, *107*, 8189–8199. [CrossRef]


https://doi.org/10.3390/app16020870

18. Yang, X.; Chen, W.; Li, A.; Yang, C. A Hybrid machine-learning method for oil-immersed power transformer fault diagnosis. *IEEJ Trans. Electr. Electron. Eng.* **2020**, *15*, 501–507. [CrossRef]
19. Liu, F.; Wu, R.; Teng, F.; Liu, Y.; Lu, S.; Ju, B.; Cao, Z. A Two-stage learning model for track-side acoustic bearing fault diagnosis. *IEEE Trans. Instrum. Meas.* **2021**, *70*, 3516512. [CrossRef]
20. Ma, L.; Dong, J.; Peng, K. A practical root cause diagnosis framework for quality-related faults in manufacturing processes with irregular sampling measurements. *IEEE Trans. Instrum. Meas.* **2022**, *71*, 3511509. [CrossRef]
21. Dao, F.; Zeng, Y.; Qian, J. Fault diagnosis of hydro-turbine via the incorporation of Bayesian algorithm optimized CNN-LSTM neural network. *Energy* **2024**, *290*, 130326. [CrossRef]
22. Skowron, M.; Orlowska-Kowalska, T.; Kowalski, C.T. Detection of permanent magnet damage of PMSM drive based on direct analysis of the Stator phase currents using Convolutional Neural Network. *IEEE Trans. Ind. Electron.* **2022**, *69*, 13665–13675. [CrossRef]
23. Dai, Y.; Zhang, L.; Xu, D.; Chen, Q.; Li, J. Development of deep learning-based cooperative fault diagnosis method for multi-PMSM drive system in 4WID-EVs. *IEEE Trans. Instrum. Meas.* **2024**, *73*, 3506513. [CrossRef]
24. Lv, K.; Wang, D.; Huang, W.; Liu, H.; Jiang, Y.; Hu, J. Multiple fault diagnosis of PMSM based on stator tooth flux and parallel residual convolutional neural network. *IEEE Trans. Transp. Electrif.* **2024**, *10*, 9727–9748. [CrossRef]
25. Eker, M.; Gündogan, B. Demagnetization fault detection of permanent magnet synchronous motor with convolutional neural network. *Electr. Eng.* **2023**, *105*, 1695–1708. [CrossRef]
26. Ni, S.; Wang, H.; Liu, S.; Wang, Y.; Yu, J.; Wang, L. Efficient multimodal motor demagnetization diagnosis framework with half-wave fundamental wave division transformation. *IEEE Trans. Ind. Electron.* **2025**, *74*, 2533116. [CrossRef]
27. Ince, T.; Kiranyaz, S.; Eren, L.; Askar, M.; Gabbouj, M. Real-Time motor fault detection by 1-D convolutional neural network. *IEEE Trans. Ind. Electron.* **2016**, *63*, 7067–7075. [CrossRef]

**Disclaimer/Publisher's Note:** The statements, opinions and data contained in all publications are solely those of the individual author(s) and contributor(s) and not of MDPI and/or the editor(s). MDPI and/or the editor(s) disclaim responsibility for any injury to people or property resulting from any ideas, methods, instructions or products referred to in the content.


https://doi.org/10.3390/app16020870

applied sciences

MDPI

*Article*

# Influence of Temperature on Brushless Synchronous Machine Field Winding Interturn Fault Severity Estimation

**Rubén Pascual [1], Eduardo Rivero [2], José M. Guerrero [3], Kumar Mahtani [1] and Carlos A. Platero [1,*]**

[1] Department of Automation, Electronic and Electrical Engineering and Industrial Informatics, Escuela Técnica Superior de Ingenieros Industriales, Universidad Politécnica de Madrid, 28006 Madrid, Spain; ruben.pascualj@alumnos.upm.es (R.P.); kumar.mahtani@upm.es (K.M.)
[2] ESELEC Ingenieros, 28008 Madrid, Spain; eduribar@hotmail.com
[3] Department of Electrical Engineering, Escuela de Ingeniería de Bilbao, Universidad del País Vasco, 48013 Bilbao, Spain; josemanuel.guerrerog@ehu.eus
* Correspondence: carlosantonio.platero@upm.es

**Abstract:** There are numerous methods for detecting interturn faults (ITFs) in the field winding of synchronous machines (SMs). One effective approach is based on comparing theoretical and measured excitation currents. This method is unaffected by rotor temperature in static excitation SMs. However, this paper investigates the influence of rotor temperature in brushless synchronous machines (BSMs), where rotor temperature significantly impacts the exciter excitation current. Extensive experimental tests were conducted on a special BSM with measurable rotor temperature. Given the challenges of measuring rotor temperature in industrial machines, this paper explores the feasibility of using stator temperature in the exciter field current estimation model. The theoretical exciter field current is calculated using a deep neural network (DNN), which incorporates electrical brushless synchronous generator output values and stator temperature, and it is subsequently compared with the measured exciter field current. This method achieves an error rate below 0.5% under healthy conditions, demonstrating its potential for simple implementation in industrial BSMs for ITF detection.

**Keywords:** AC machines; brushless synchronous machines; condition monitoring; deep learning; fault detection; generators; deep neural networks; rotor temperature; stator temperature; power generation

## 1. Introduction

In power generation applications, brushless synchronous machines (BSMs) usually consist of a main machine and an exciter, mechanically coupled on the same shaft. The exciter's function is to supply the necessary field power to the main machine for its operation. In the conventional topology, the exciter's field winding is rolled around the stator poles, and its armature is an AC winding located on the rotor. The AC output of the exciter armature is converted into the DC excitation input for the main machine by a rotating diode rectifier bridge. The field winding of the main machine is located on the rotor and its armature on the stator.

Currently, several excitation systems for BSMs are identified by the field power source supplied to the exciter [1–3]. The primary advantages of removing brushes and slip rings in the excitation system [4] are reduced maintenance costs and increased operational safety, as no sparks are produced. In some facilities, such as oil refineries and chemical plants, the use of BSMs is mandatory.

The market for BSMs is extensive. High-power BSMs are widely used in nuclear power plants, while low-power units are employed in emergency diesel generators and hydro power plants [5,6]. Furthermore, BSMs can address issues arising from the high penetration of renewable generation plants in the grid, such as the reduction of the short-circuit ratio (SCR). BSMs used as synchronous condensers can help maintain a minimum SCR level in

global grids [7,8], especially those equipped with a PMG as a pilot exciter. Additionally, BSMs can help renewable power plants comply with various grid code requirements, which are largely based on specific standards [9–11].

In all these applications, BSMs must meet industry reliability standards, including protection against faults and abnormal operating conditions [12,13]. BSMs are susceptible to various faults due to their operating conditions. This manuscript focuses on the influence of temperature on estimating the theoretical field exciter excitation current, with the ultimate goal of detecting interturn faults (ITFs) in the field winding of BSMs. The number of ITFs is directly proportional to the severity of the fault [14,15].

The main difficulty in detecting ITFs is that they do not usually result in large overcurrent in the machine, so the machine can operate normally if the interturn fault severity level is lower than a tolerable limit. However, the existence of a magnetic unbalance causes additional mechanical stress on the machine, which can lead to large vibrations that can damage the generator.

The main origin of ITFs is the weakness of the insulation [16,17]. A short-circuit between turns is usually caused by deterioration of the insulation, which is usually caused by the high stresses applied to the insulation. The ITFs cause a drop in the electrical resistance between the poorly insulated turns, which leads to an increase in the excitation current of the generator.

Differences in electrical potential, mechanical stresses due to vibrations and frictions, and thermal stresses due to a temperature gradient are the causes of high stresses in the insulation, which can lead to damage to it. In addition, the presence of fine particles or liquids such as water or acids can increase the likelihood of ITFs.

There are some previous model-based approaches for rotor ITF detection and severity estimation in BSMs [14,15]. Some of these methods are based on the comparison of two variables: the theoretical model estimation obtained from the machine electrical output values and the measured exciter field current. This comparison is very useful for attesting deviations from the healthy condition and for calculating the fault severity level employing the relative difference between both values. So, accurate assessment of the excitation current in BSMs is essential for proper machine characterization. This significance arises from the inherent nature of brushless excited SMs, where the field winding becomes physically inaccessible during operation, making direct measurement of the field current extremely challenging.

Another previous article [18] investigates the idea of implementing deep neural network (DNN) algorithms to detect ITFs in BSMs. The combination of large numbers of experimental data and the use of deep learning methods achieves excellent results for detecting ITFs in BSMs. However, preceding algorithms fail to account for the impact rotor winding temperature may have on field current estimation. During machine operation, a notable increase in rotor winding temperature occurs, gradually causing a decline in the field current. It is interesting to highlight that, while extensive studies have explored field current estimation, limited research investigates temperature-induced alterations in these values. In [19], field current and field winding temperature are estimated using a machine model, and then the estimates are compared with the actual currents measured in the stator and adjusted through a correction mechanism using a Kalman filter, demonstrating efficacy in simulations. In [20], field current and temperature estimation is achieved through the DC link current, initially computed via an algorithm and afterward fed back to the controller and compared with the measured value. The resulting error facilitates temperature estimation refinement, thereby improving both field and DC link current estimates.

Furthermore, due to the difficulty of accurate modeling posed by SMs combined with recent advancements in computational learning, contemporary studies explore methodologies such as neural networks for identifying faults within the field winding. Works such as [18,21] collect healthy machine data alongside post-fault data to use these data for early fault detection. Nonetheless, these methods do not work in the absence of real-time consideration of BSM operating temperatures, as situations may arise where a fault between turns

in a cold machine exhibits field current values like those of a healthy machine operating at high temperatures.

Taking into account this difficulty, the main objective of this work is to demonstrate and verify the influence of temperature on the exciter excitation current estimation algorithm. This will substantially improve the results studied in previous works [18], where a neural network model was presented that allowed the estimation of the excitation correlation of a brushless machine but did not consider the rotor temperature. Considering how the rotor temperature affects the excitation current of the machine, the results obtained by taking into account the machine temperature as input to the model will be much closer to the real machine measurements. The second objective is to validate the use of stator temperature instead of rotor temperature in the estimation algorithm. This is a very important validation because the stator temperature can be measured during operation in industrial BSMs, where it is not possible to measure the rotor temperature.

For this purpose, this paper proposes using DNN architecture algorithms. It was decided to use DNNs to estimate the excitation current because the introduction of artificial intelligence in the field of diagnosis of synchronous machines is on the rise, as can be seen in several recent research works [22–24].

The developed DNN uses voltage, active and reactive power, and temperature ($U$, $P$, $Q$, and $\theta$) as inputs of the model to estimate the field excitation current of the BSM. The proposed method was developed using a special laboratory setup, firstly to collect all the necessary data to train the DNN under healthy conditions.

In Section 2, the influence of temperature is analyzed in different excitation systems of synchronous machines (SMs). It also highlights the importance of considering temperature as an input in developing the theoretical excitation current estimation model of a BSM. The proposed method and the steps to develop the estimation method are discussed in Section 3. Then, Section 4 describes the experimental setup and the experimental tests performed on it under healthy conditions. Finally, Section 5 summarizes the paper's conclusions.

## 2. Influence of Rotor Temperature on Different Excitation Systems of SMs

This section presents the need to consider the rotor temperature in the model to estimate the exciter field current for detecting ITFs in BSMs.

In an SM with static excitation, as shown in Figure 1, the excitation current ($I_f$) is controlled directly by a controlled rectifier which modifies the field winding voltage ($U_f$). As the temperature increases, the excitation field winding resistance increases, and consequently, the excitation voltage must be raised to maintain a constant excitation current.

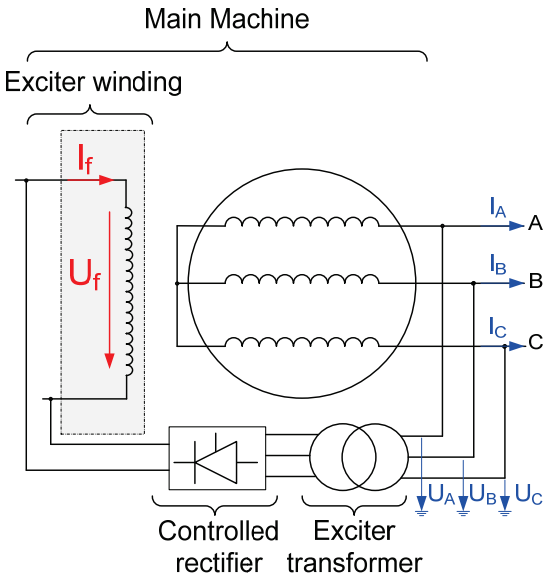


**Figure 1.** Simplified schema of an SM with static excitation under a self-excited topology.

However, in a BSM, as can be seen in Figure 2, the main machine field winding current is regulated through the exciter. When the temperature increases, the resistance of the field winding of the main machine increases, following Equation (1) [25]:

$$R_\theta = R_{\theta_0} \cdot [1 + \alpha \cdot (\theta - \theta_0)] \quad (1)$$

where $R_\theta$ is the resistance at the operating temperature $\theta$, $R_{\theta_0}$ is the resistance at the reference temperature $\theta_0$, and $\alpha$ is the temperature coefficient of resistance for the conductor material.

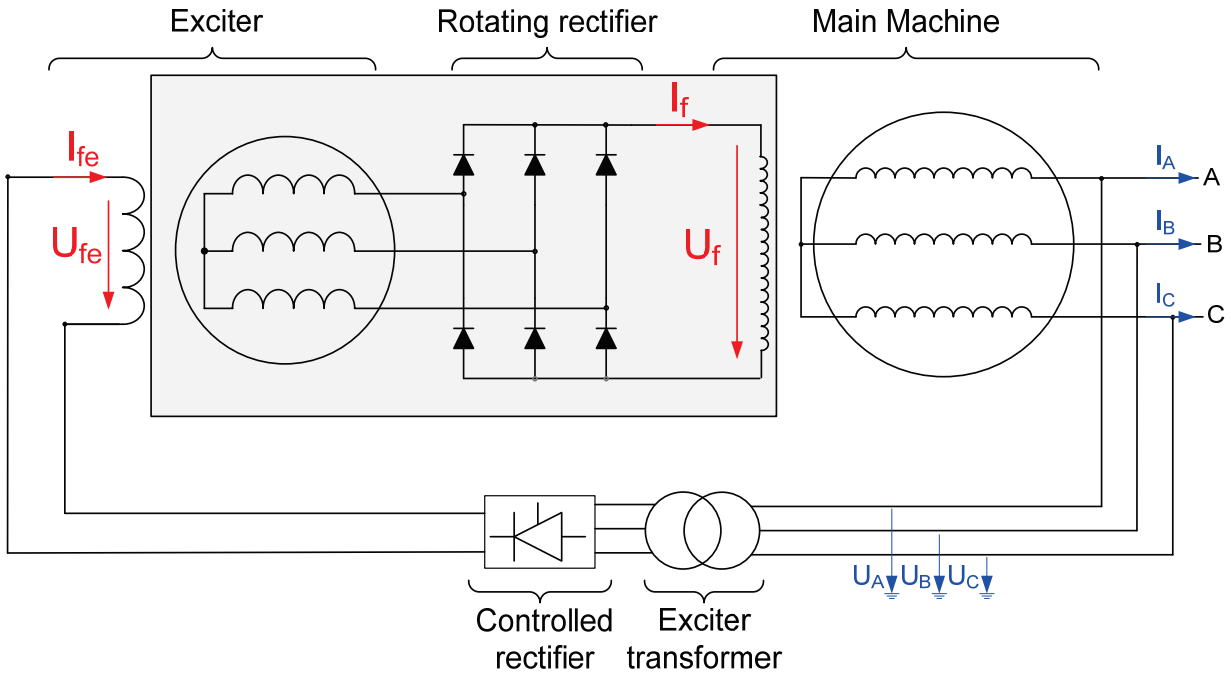


**Figure 2.** Simplified schema of a BSM under a self-excited topology.

This increase in the field winding resistance leads to an increase in the field winding voltage ($U_f$), assuming the excitation current ($I_f$) remains constant. Therefore, to maintain the same operating point ($I_f$ constant), it is necessary to increase the exciter excitation current ($I_{fe}$) to raise the induced voltage in the armature winding of the exciter and consequently the field winding voltage ($U_f$). Additionally, because, as said, the resistance of the exciter field winding increases with the exciter's temperature, this also affects the exciter field voltage ($U_{fe}$).

## 3. Inclusion of Temperature in the DNN Model-Based Method

### *3.1. Foundations*

This section pursues two main objectives. The first is to utilize DNN algorithm architectures to predict the value of the theoretical exciter field current in a BSM, considering the effect of temperature on the machine, with temperature as an additional input. This approach aims to improve the results obtained in other research [18]. The results shown in this previous article are good because of the short-term tests in which the machine did not have time to warm up and the effect of temperature on the estimation of fault severity was not too high. However, in the current work it has been verified that if continuous monitoring of the BSM is to be carried out, the effect of the rotor temperature must be considered, as shown in Section 5.

The second objective is to validate the feasibility of using the stator temperature in the model instead of the rotor temperature, since measuring rotor temperature in industrial BSMs is not possible.

Based on the principles described in [18], the theoretical exciter field current ($I_{fe,cal}$) is estimated using a DNN model under healthy condition calculations. The inputs to this model are a combination of machine output voltage ($U$) and current ($I$) measurements that fully define a [$U$, $P$, $Q$] operating point. In addition to these inputs, the machine temperature measurement ($\theta$) will be included as an input in the present work, following the reasoning presented in Section 3. The comparison of $I_{fe,cal}$ with the actual measured exciter field current ($I_{fe,mea}$) enables ITF severity ($\alpha$) estimation, as the ratio of faulty turns is directly related to the field current increase imposed by the automatic voltage regulator (AVR) with respect to the estimated current. Equation (2) shows the explicit calculation of the severity of the interturn fault in a BSM:

$$\alpha\ [\%] = \frac{N_{Faulty}}{N_{total}} \cdot 100 = \left( \frac{I_{fe,\,cal}}{I_{fe,mea}} - 1 \right) \cdot 100 \tag{2}$$

where $N_{Faulty}$ is the number of equivalent faulty turns with $R_f = 0\ \Omega$, and $N_{total}$ is the total number of turns.

Figure 3 illustrates the simplified layout of the field winding ITF detection and severity estimation technique, with inclusion of the influence of temperature.

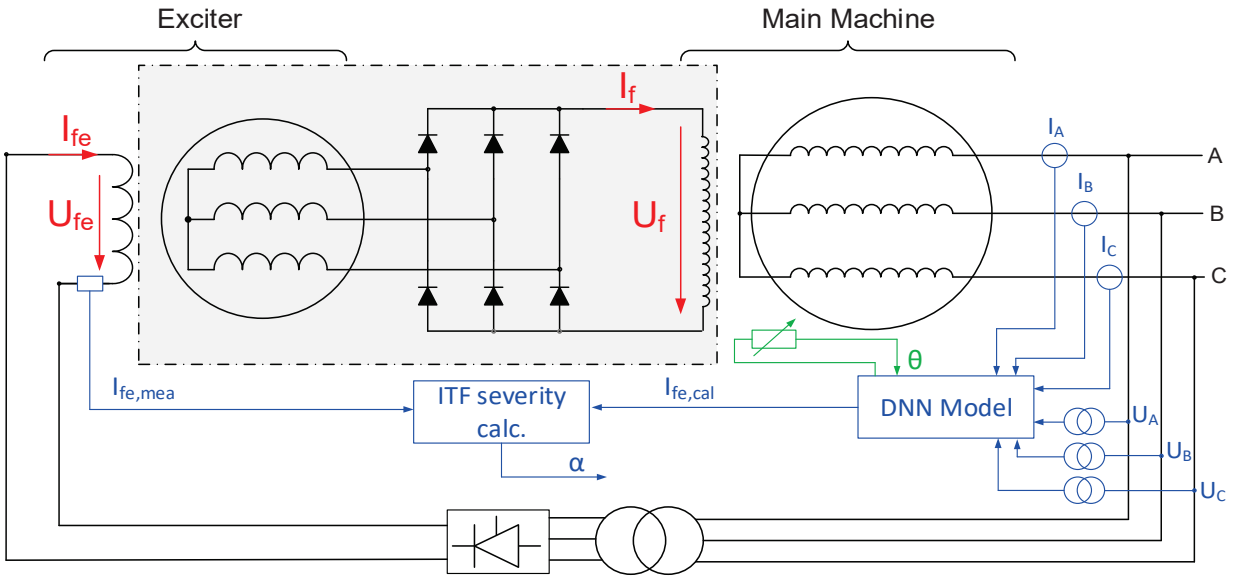


**Figure 3.** Simplified layout of the field winding ITF detection and severity estimation method, with inclusion of the influence of temperature.

The purposely developed DNN allows one to adaptively model the complex relationships among the mentioned variables through approximation of non-linear functions, with a reduced error. In accordance with the complexity of the problem, the DNN model is composed of four neurons in the input layer, one for each input variable ($U$, $P$, $Q$, and $\theta$), and one output neuron which employs the sigmoid as the activation function. The developed DNN has two hidden layers, with their neurons using the rectified linear unit (ReLU) activation function, and was optimized for computational efficiency.

To determine the optimal number of neurons in each hidden layer, the model was trained with all combinations of neurons ranging from 3 to 20 per layer, utilizing the backpropagation method. The backpropagation learning rate was set at 0.001, and the number of epochs was fixed at 40.000. The optimum configuration was selected by evaluating the trained DNNs based on the minimization of the mean square error (MSE) and the minimization of points with errors greater than 5%. The general form of the involved DNN architecture is presented in Figure 4.

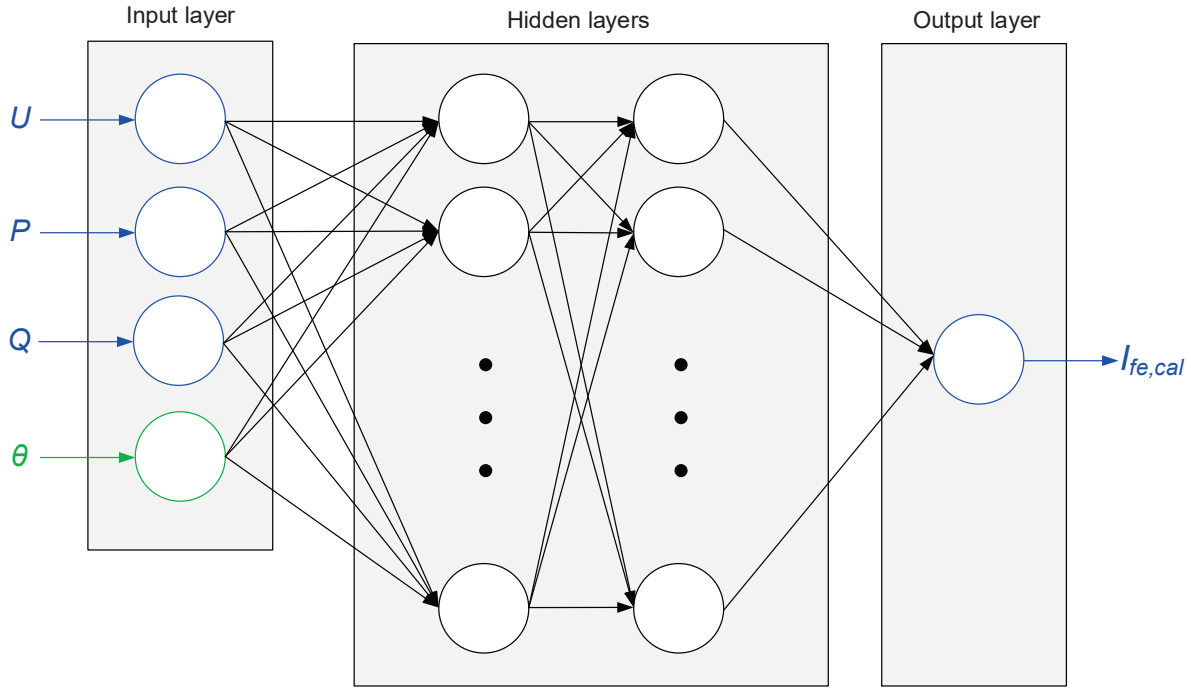


**Figure 4.** Generalized form of the proposed DNN architecture.

The main features of the development stages (data collection and processing, training with validation, and testing) are described in the following subsections.

### 3.2. Data Collection and Processing

The data were obtained through experimental testing on a special laboratory test bench, as described in Section 4, under healthy conditions for BSMs. This dataset was collected by conducting several series of long-term tests, with different grid voltage ($380 \leq U \leq 420$ V), real power ($0 \leq P \leq 3000$ W), and reactive power ($-2000 \leq Q \leq 3000$ var) values.

$V$, $P$, and $Q$ were obtained using a Camile Bauer SINEAX converter M563, and temperatures were measured using $Pt-100$ commercial sensors with converters. The converters of the temperature sensors and the transducer give an output signal proportional to the measured variables in the range of [4–20] mA. To adapt these signals to the measurement range of the Arduino © microcontroller, a series resistor of 249 ohms was connected to each current signal, so the signals are finally in the range [1–5] V, which is a suitable range for the Arduino © microcontroller. Finally, $I_{fe,mea}$ was measured using a Hall effect sensor (INA219) directly compatible with the Arduino © microcontroller.

After acquisition, the data were filtered to remove anomalous measurements. In total, approximately 400,000 refined records were analyzed under healthy conditions. The removed data include transients, anomalous measures, and communication failures.

This data pool was randomly divided into three subsets for training, validation, and testing, as shown in Figure 5.

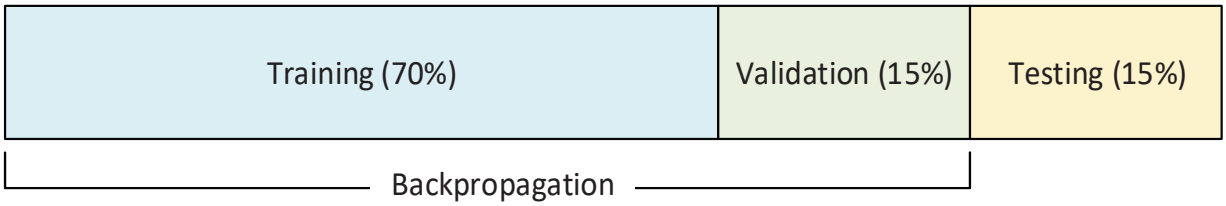


**Figure 5.** Distribution of the refined data pool.

*3.3. Training with Validation*

The feed-forward DNN is trained using the popular backpropagation method [25–27], in order to align the outputs ($I_{fe,cal}$) as closely as possible with the measured values ($I_{fe,mea}$). Backpropagation is an iterative gradient descent optimization technique applied to the network's weight space, enabling the weights to be updated in each iteration and to progressively minimize the cost function (CF).

At the first stage of each epoch, forward propagation is performed, where the inputs ($U$, $P$, $Q$, and $\theta$) are fed to the DNN and the output value is calculated based on those inputs and with the initialization values of the weight, as stated in Equation (3).

$$I_{fe,cal} = F\cdot\left[\sum_{k=1}^{K} w_{F,\,2k} h_{2k}\left(\sum_{j=1}^{J} w_{2k,\,1} h_{1j}\left(w_{1j,U}\cdot U + w_{1j,P}\cdot P + w_{1j,Q}\cdot Q + w_{1j,\theta}\cdot\theta + w_{j,0}\right) + w_{k,0}\right) + w_{F,0}\right] \tag{3}$$

where $wF, 2k$, $w2k, 1$, and $w1j, U$, $w1j, P$, $w1j, Q$, $w1j, \theta$ are the synaptic weights from the neurons of the second hidden layer to the output neuron, from the neurons of the first hidden layer to the second hidden layer, and from the neurons of the input layer to the ones of the first hidden layer, respectively.

To summarize Equation (3), it is better to write the weights vector as in Equation (4):

$$W_t = \left[w_{F,\,2k}\; w_{2k,\,1j}\; w_{1j,\,U}\; w_{1j,\,P}\; w_{1j,\,Q}\; w_{1j,\,\theta}\right] \tag{4}$$

with $j$ from 1 to $J$, and $k$ from 1 to $K$.

At the second stage, the algorithm calculates the value adopted by the CF and subsequently evaluates its gradient by propagating the errors from the output layer back to the input layer through the chain rule. Through stochastic gradient descent, accordingly, moving towards the negative direction of the gradient, the iteration is concluded by updating the weights and biases.

The progressive adjustment of the network is performed by minimizing the mean square error (MSE) between the predicted and the measured exciter field currents, serving as the CF. The cost function calculation is shown in (5).

$$CF = \frac{1}{N}\sum_{n=1}^{N}\left(I_{fe,\,cal} - I_{fe,\,mea}\right)^2 \tag{5}$$

The adaptive moment estimation (ADAM) algorithm, which employs the exponential moving average of both the gradient or first momentum ($\nabla$CF) and the squared gradient or second momentum ($\nabla^2$CF), is used for gradient descent optimization. The diagram of the employed backpropagation method is provided in Figure 6.

Also, the following equations allow the weights vector at epoch $t$ to be determined from the vectors at the previous epoch ($t-1$):

$$W_t = W_{t-1} - l\cdot\frac{\hat{m}_t}{\sqrt{\hat{v}_t + \varepsilon}} \tag{6}$$

$$\hat{m}_t = m_t\cdot\frac{1}{1-\beta_m} \tag{7}$$

$$m_t = \beta_m\cdot m_{t-1} + (1-\beta_m)\cdot\nabla CF \tag{8}$$

$$\hat{v}_t = v_t\cdot\frac{1}{1-\beta_v} \tag{9}$$

$$v_t = \beta_v\cdot v_{t-1} + (1-\beta_v)\cdot(\nabla CF)^2 \tag{10}$$

where $l$ represents the learning rate that allows speeding up of the convergence of the CF to its minimum, $v_t$ and $m_t$ are variables updated in each epoch, and $\varepsilon$, $\beta_m$, and $\beta_v$ are constant.

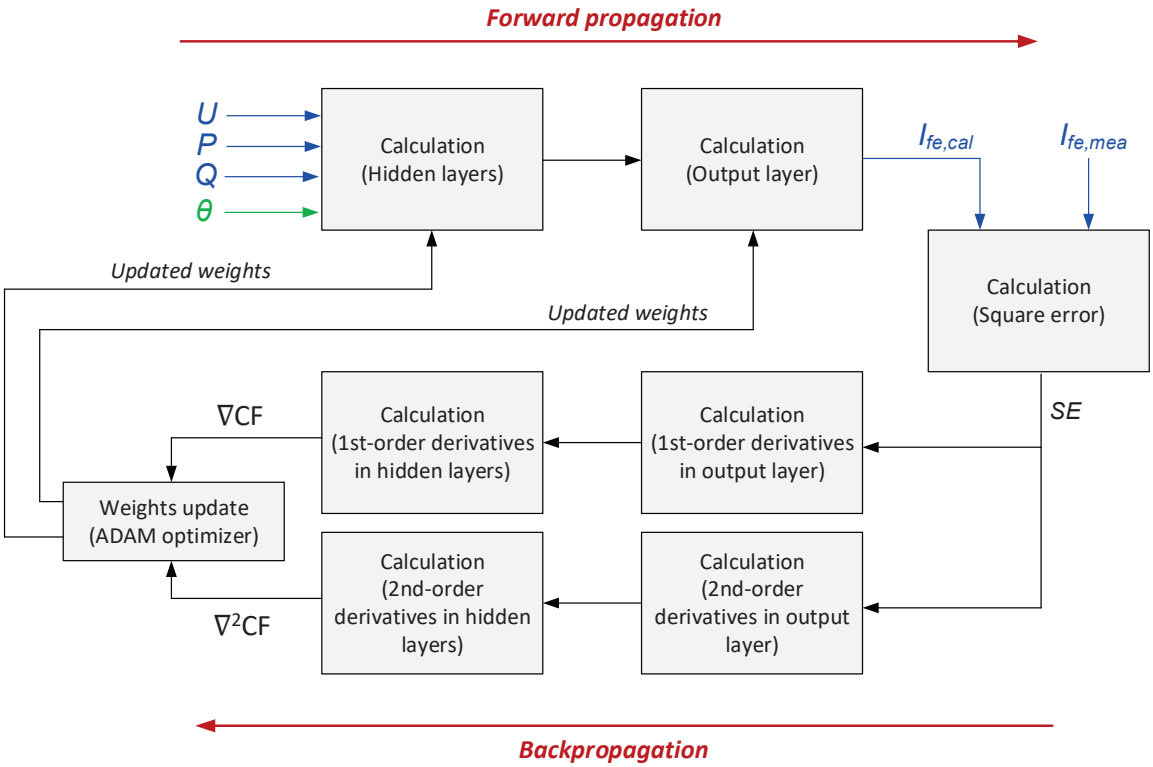


**Figure 6.** DNN training process through backpropagation.

After training, hyperparameter tuning is performed to achieve the best-fitting network. During this validation phase, various neural networks were evaluated to determine the optimal number of hidden layers and nodes in each layer. The network that reduced the maximum absolute error (MAE) to 0.1% was selected.

### 3.4. Tests

After the training and validation process, an unbiased evaluation of the model performance was carried out. The absolute maximum error is approximately 0.5%, so if this method was used to detect ITFs, faults with a severity greater than 0.5% could be detected. In other words, because 0.5% is the smallest severe detectable fault, the tripping limit should never be fixed beneath this value.

Table 1 shows the evaluation results of the DNN network for the machine in healthy conditions, including the value of the mathematical metrics used to evaluate its accuracy: the mean average error (MAE) and the root mean square error (RMSE).

**Table 1.** Results obtained from the DNN predictions under healthy conditions.

| Set of Data | MAE [%] | RMSE [mA] |
|---|---|---|
| Tests under healthy conditions | 0.1 | 0.04 |

The errors obtained through DNN prediction are significantly beneath the errors obtained in previous papers where the temperature was not considered as an input in the model [16]. An MAE of 0.1% shows that the trained DNN has a fairly high overall estimation accuracy, in terms of overall closeness to null error values, while an RMSE of 0.06 implies a fair mean value of prediction dispersion with respect to the actual values, as this metric penalizes outliers or large deviations.

## 4. Experimental Tests

### *4.1. Experimental Setup*

Numerous long-duration tests under constant operation points ($P$, $Q$, and $U$) were carried out on a special 4-salient pole, 5-kVA, 400-V BSM. A simplified diagram of the machine is shown in Figure 7.

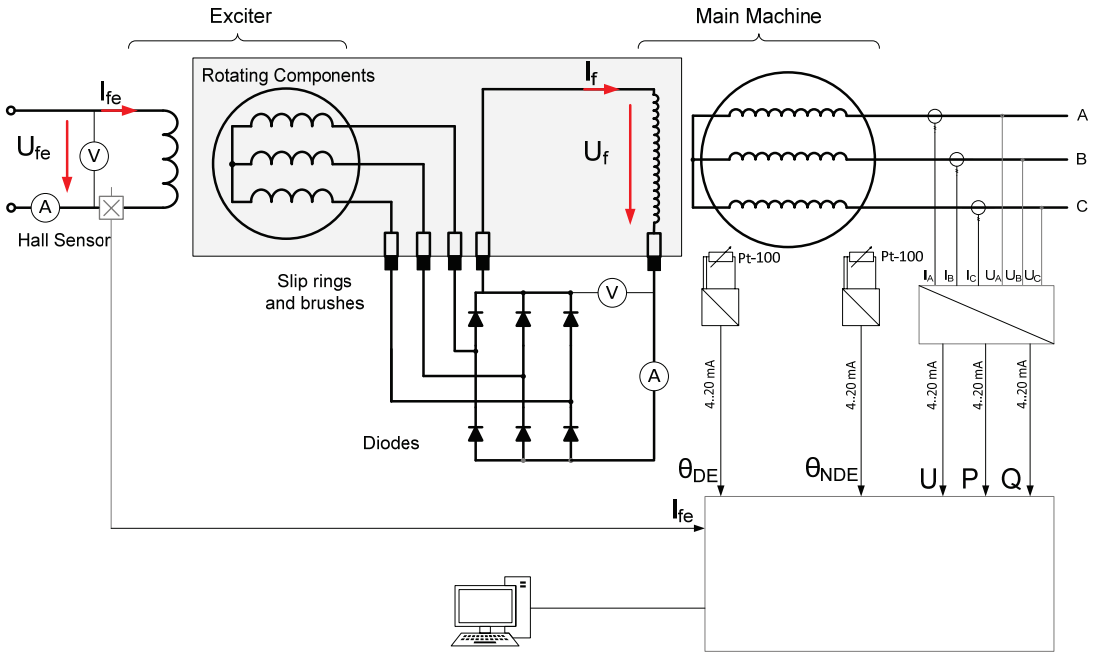


**Figure 7.** Simplified diagram of the experimental setup.

This BSM was modified by adding 5 slip rings and brushes to permit access to the field winding of the main machine and to the "rotating" diodes (which were actually made static in this setup and placed outside of the machine). This modification allows for the measurement of the voltage ($U_f$) and the current ($I_f$) of the field winding of the main machine and consequently the temperature by observing variations in its resistance. Additionally, two Pt−100 type temperature sensors were installed at both ends of the armature windings of the main synchronous machine, and these temperatures were also recorded.

From the armature currents and voltages, the values of stator voltage ($U$), active power ($P$), and reactive power ($Q$) are measured by a commercial 3-channel programmable transducer, SINEAX M563. Finally, the exciter field current is measured using a Hall effect sensor. All these measurements are recorded on a computer through an Arduino© microcontroller, communicating via the COM port of the computer.

During the long-duration test, the temperature of the rotor and the stator of the main synchronous machine increased. To maintain the machine at the same operating point, the exciter excitation current ($I_{fe}$) needs to be increased as the temperature rises.

The ratings of the main machine and the exciter are detailed in Tables 2 and 3, respectively.

There are five slip rings and brushes (4): three are connected to the armature winding of the exciter, and the other two are connected to the main machine's field winding. The voltage and current of the main machine's field winding are measured (5). The temperature of the main machine's armature windings is monitored by two Pt−100 sensors (6). These sensors are placed in the end winding of the machine at both sides of the generator, the non-drive end NDE and the drive end DE. In element 6 of Figure 8, there is a zoom of this area. This is the best non-invasive location of the temperature sensors that allows estimating an average temperature with which to compare the estimations of the DNN.

This modified synchronous machine is actioned by an induction motor (7), which is controlled with a frequency variable converter. A DC source provides the excitation power to the machine, and the machine is connected to the grid.

The experimental laboratory setup is shown in Figure 8. The BSM (1) and the exciter (2) are mechanically coupled with a common shaft. The diodes (3) are located outside the machine in this layout to be accessible.

**Table 2.** Main machine data.

| Alternator Type | Synchronous 3-Phase | |
|---|---|---|
| Rated power | 5 | kVA |
| Rated speed | 1500 | rpm |
| Rated voltage | 400 | V |
| Rated current | 7.2 | A |
| Pole pairs | 2 | |
| Rated frequency | 50 | Hz |
| IP | 21 | |
| Insulation class | F | |
| Rated excitation voltage | 33 | V |
| Rated excitation current | 4.1 | A |

**Table 3.** Exciter data.

| Alternator Type | Synchronous 3-Phase | |
|---|---|---|
| Rated power | 277 | VA |
| Rated speed | 1500 | rpm |
| Rated voltage | 40 | V |
| Rated current | 4 | A |
| Pole pairs | 4 | |
| Rated frequency | 100 | Hz |
| IP | 21 | |
| Insulation class | F | |
| Rated excitation voltage | 33 | V |
| Rated excitation current | 0.61 | A |

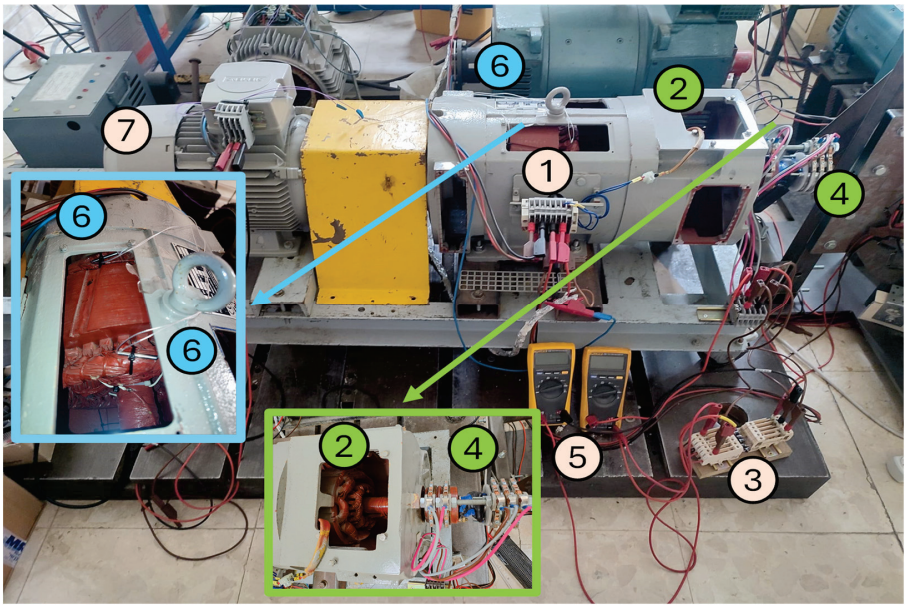


**Figure 8.** Experimental setup: (1) main machine, (2) exciter, (3) diodes, (4) slip rings and brushes, (5) main field winding voltage and current measurement, (6) stator temperature measurement, and (7) driver (induction motor).

*4.2. Experimental Results*

Numerous tests have been conducted to verify that the measured exciter field current ($I_{fe}$) must be significantly increased in BSMs under warm conditions to maintain a constant reactive power delivered by the machine. The tests involve initially setting an operating point for the BSM in terms of active and reactive power, and then allowing the machine to operate as it warms up, while continuously keeping the reactive power constant. To maintain constant $Q$ as the temperature rises, it is necessary to increase the exciter field current ($I_{fe}$).

All the aforementioned electrical variables ($P$, $Q$, $U$, $U_{fe}$, $I_{fe}$, $I_f$, and $U_f$) and the rotor and stator temperatures are continuously monitored. Figure 9 illustrates the increase in the exciter field winding current due to the rising rotor temperature during a test.

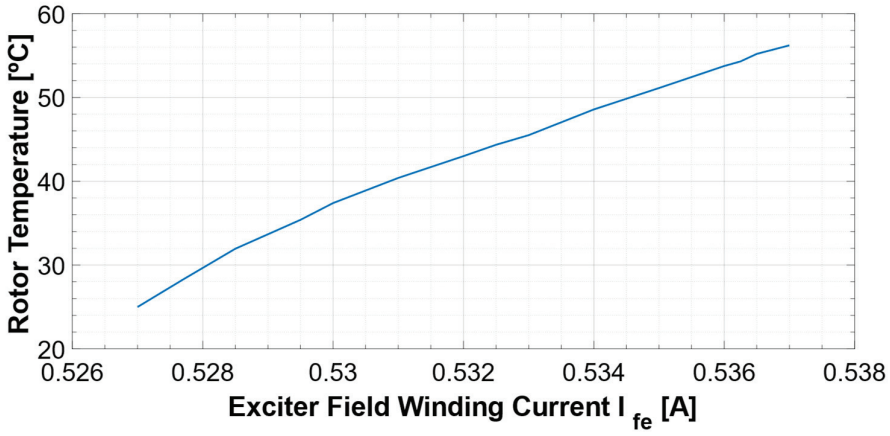


**Figure 9.** Exciter field current ($I_{fe}$) with respect to rotor temperature during a 2 h operation test ($P$ = 2.9 kW, $Q$ = 2.3 kvar, $U$ = 400 V).

Since it is impossible to access the voltage and current of the field winding of the main machine in industrial BSMs and consequently to calculate the rotor temperature, the stator temperature was measured to assess whether it could be used instead of the rotor temperature to estimate the excitation current ($I_{fe}$).

Figures 10 and 11 show the exciter field winding current variation with the increment of the stator and rotor temperatures, respectively. It can be seen that, in this BSM, the exciter field current ($I_{fe}$) consumption increases by 0.75% every 10 K degrees of temperature rise. Thus, to develop a model capable of estimating the excitation current consumption at an electrical operating point of the machine, in the case of BSMs it is necessary to add the machine temperature variable in the estimation model, as said above.

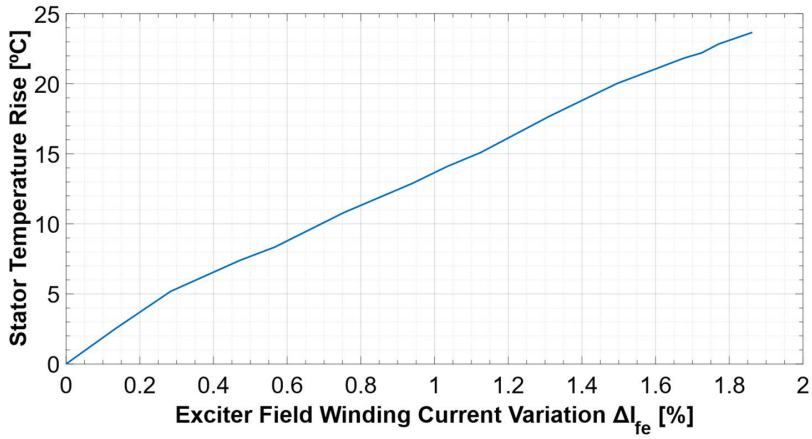


**Figure 10.** Exciter field current rise ($\Delta I_{fe}$) with respect to stator temperature rise during a 2 h operation test ($P$ = 2.9 kW, $Q$ = 2.3 kvar, $U$ = 400 V).

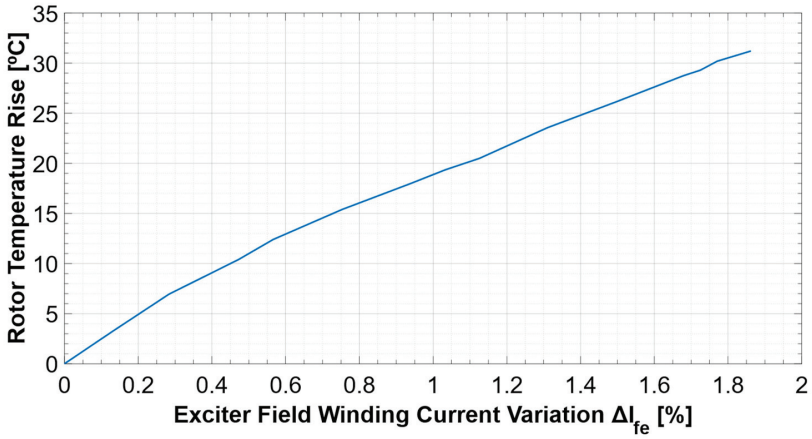


**Figure 11.** Exciter field current rise ($\Delta I_{fe}$) with respect to rotor temperature rise during a 2 h operation test ($P$ = 2.9 kW, $Q$ = 2.3 kvar, $U$ = 400 V).

Comparing Figures 10 and 11, it is verified that the variation in excitation current consumption with increases in stator and rotor temperatures is very similar. Importantly, the slope remains constant with both temperatures, indicating that it is feasible to use the stator temperature in the estimation model.

Additionally, Figure 12 displays the rotor and stator temperatures during a constant reactive power test. The difference between them is also represented. This difference is not constant and varies depending on the machine temperature.

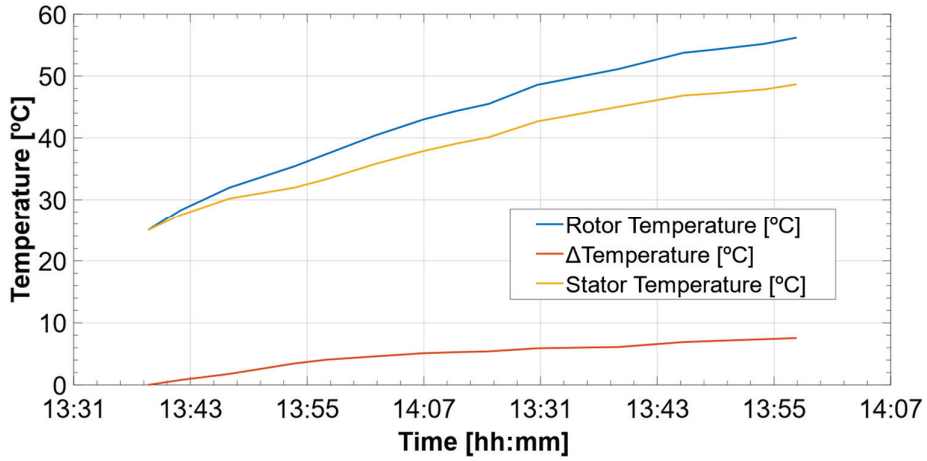


**Figure 12.** Temperature variations during a 2 h operation test ($P$ = 2.9 kW, $Q$ = 2.3 kvar, $U$ = 400 V).

As described in Section 4, to validate that this method is significantly more efficient when using temperature as an input to the model, a DNN was trained with real operating points measured using the experimental system described in the previous subsection.

Figure 13 shows the measured excitation current, $I_{fe,mea}$ (in blue), and the calculated excitation current, $I_{fe,cal}$ (in orange), for all test operational points. The calculated excitation current value is derived from the DNN previously trained with the machine operational data under healthy conditions.

As shown in Figure 13, the DNN excitation current prediction is highly accurate, with a maximum error of 3 mA, which is an error of 1.5%. The MSE obtained is 0.5%, which means that the minimum detectable fault severity is 0.5%, considering the fault severity of Equation (2).

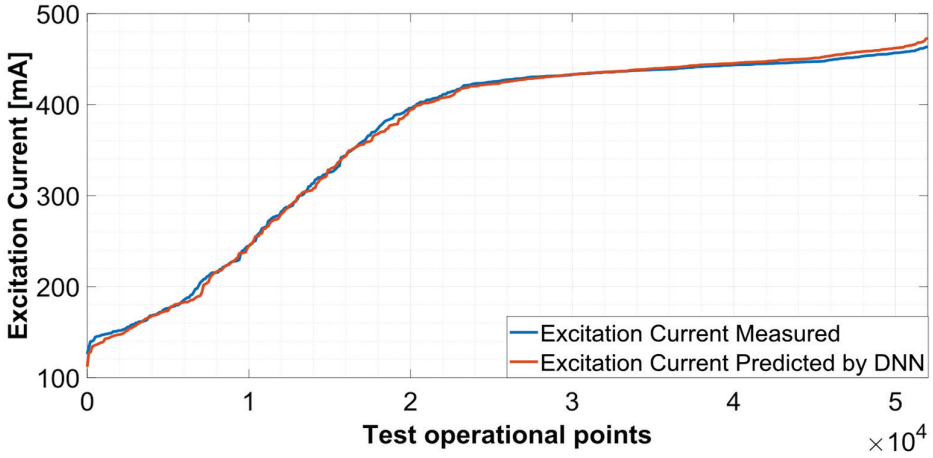


**Figure 13.** Prediction of the excitation current using a DNN.

## 5. Conclusions

In BSMs, rotor temperature is a crucial variable for detecting ITFs based on exciter field current estimation. As the machine heats up, the rotor's resistance increases, necessitating a rise in the rotor field voltage to maintain a constant field current and reactive power. Consequently, the exciter field current must also be increased.

Previous research did not consider the rotor temperature as a variable in the development of the online model-based fault severity estimation algorithm for BSMs. This omission is significant, as the presented results indicate that the exciter excitation current varies by 0.75% for every 10 °C increase in temperature. This could result in errors exceeding 5% in an industrial machine, where the normal operating temperature range can vary from 20 °C in cold conditions to 100 °C in warm conditions. This fact implies that the algorithm could only detect faults from 5% fault severity or higher if unwanted trips are to be avoided.

To enhance the accuracy of the detection method, an alternative online model has been developed for detecting ITFs in BSMs, incorporating the machine's temperature. Given the difficulty of measuring rotor temperature, the use of stator temperature was evaluated as an alternative, yielding satisfactory results.

To validate the equivalence of using rotor versus stator temperature, the variation in the excitation current with different temperatures was compared in several laboratory tests, using 400,000 operational points for training the neural network.

The results obtained in this paper indicate that the DNN using stator temperature as an input can estimate the exciter field current with errors below 0.5%. Consequently, ITFs with a severity of approximately 0.5% or higher can also be detected.

However, this study leaves the gates open to future research, which should focus on carrying out tests with known interturn faults in the brushless generator. Thus, the DNN developed for this article could be used to verify the accuracy of the model as a function of the severity of the fault.

**Author Contributions:** Conceptualization, R.P. and C.A.P.; methodology, R.P., K.M. and C.A.P.; software, R.P. and E.R.; validation, R.P., K.M. and E.R.; formal analysis, J.M.G. and C.A.P.; investigation, R.P. and K.M.; resources, C.A.P.; data curation, R.P.; writing—original draft preparation, R.P. and J.M.G.; writing—review and editing, J.M.G., R.P., K.M., E.R. and C.A.P.; visualization, K.M.; supervision, C.A.P.; project administration, C.A.P.; funding acquisition, C.A.P. All authors have read and agreed to the published version of the manuscript.

**Funding:** This research received no external funding.

**Institutional Review Board Statement:** Not applicable.

**Informed Consent Statement:** Not applicable.

**Data Availability Statement:** The original contributions presented in this study are included in the article; further inquiries can be directed to the corresponding author.

**Conflicts of Interest:** Author Eduardo Rivero was employed by the company ESELEC Ingenieros. The remaining authors declare that the research was conducted in the absence of any commercial or financial relationships that could be construed as a potential conflict of interest.

## References

1. Nøland, J.K.; Nuzzo, S.; Tessarolo, A.; Alves, E.F. Excitation System Technologies for Wound-Field Synchronous Machines: Survey of Solutions and Evolving Trends. *IEEE Access* **2019**, *7*, 109699–109718. [CrossRef]
2. Nuzzo, S.; Bolognesi, P.; Decuzzi, G.; Giangrande, P.; Galea, M. A Consequent-Pole Hybrid Exciter for Synchronous Generators. *IEEE Trans. Energy Convers.* **2021**, *36*, 368–379. [CrossRef]
3. Chakraborty, C.; Basak, S.; Rao, Y.T. Synchronous Generator with Embedded Brushless Synchronous Exciter. *IEEE Trans. Energy Convers.* **2019**, *34*, 1242–1254. [CrossRef]
4. Chapman, S.J. *Electric Machinery Fundamentals*, 5th ed.; McGraw-Hill: New York, NY, USA, 2012; ISBN 9780073529547.
5. *IEEE Std C50.12-2005*; IEEE Standard for Salient-Pole 50 Hz and 60 Hz Synchronous Generators and Generator/Motors for Hydraulic Turbine Applications Rated 5 MVA and Above. IEEE: New York, NY, USA, 2006; pp. 1–45.
6. *IEEE Std C50.13-2014*; IEEE Standard for Cylindrical-Rotor 50 Hz and 60 Hz Synchronous Generators Rated 10 MVA and Above. IEEE: New York, NY, USA, 2014; pp. 1–63.
7. Igbinovia, F.O.; Fandi, G.; Müller, Z.; Švec, J.; Tlustý, J. Optimal location of the synchronous condenser in electric-power system networks. In Proceedings of the IEEE 17th International Scientific Conference on Electric Power Engineering (EPE), Prague, Czech Republic, 16–18 May 2016; pp. 1–6.
8. Marrazi, E.; Yang, G.; Weinreich-Jensen, P. Allocation of synchronous condensers for restoration of system short-circuit power. *J. Mod. Power Syst. Clean Energy* **2018**, *6*, 17–26. [CrossRef]
9. Jiménez, R.P.; Platero, C.A.; Sánchez, M.E.; Barneto, E.R. Synchronous Condenser for European Grid Code Compliance: A Case Study of a PV Power Plant in Spain. *IEEE Access* **2023**, *11*, 54713–54723. [CrossRef]
10. Commission Regulation (EU) 2016/631—Of 14 April 2016—Establishing a Network Code on Requirements for Grid Connection of Generators. Available online: https://op.europa.eu/en/publication-detail/-/publication/1267e3d1-0c3f-11e6-ba9a-01aa75ed71a1/language-en (accessed on 15 May 2024).
11. *IEEE Std 2800-2022*; IEEE Standard for Interconnection and Interoperability of Inverter-Based Resources (IBRs) Interconnecting with Associated Transmission Electric Power Systems. IEEE: New York, NY, USA, 2022; pp. 1–180.
12. Stone, G.; Boulter, E.A.; Culbert, I.; Dhirani, H. *Electrical Insulation for Rotating Machines: Design, Evaluation, Aging, Testing, and Repair*, 4th ed.; Wiley-IEEE Press: Piscataway, NJ, USA, 2004; pp. 1–41.
13. *IEEE Std 56-2016*; IEEE Guide for Insulation Maintenance of Electric Machines. IEEE: New York, NY, USA, 2016; pp. 1–86.
14. Mahtani, K.; Guerrero, J.M.; Beites, L.F.; Platero, C.A. Model-Based On-Line Protection Method for Brushless Synchronous Generators. In Proceedings of the 2021 IEEE 13th International Symposium on Diagnostics for Electrical Machines, Power Electronics and Drives (SDEMPED), Dallas, TX, USA, 22–25 August 2021; pp. 126–132.
15. Mahtani, K.; Guerrero, J.M.; Beites, L.F.; Platero, C.A. Model-Based Field Winding Interturn Fault Detection Method for Brushless Synchronous Machines. *Machines* **2022**, *10*, 1227. [CrossRef]
16. *IEEE Std 1129-2014*; IEEE Guide for Online Monitoring of Large Synchronous Generators (10 MVA and Above). IEEE: New York, NY, USA, 2014; pp. 1–62.
17. Sottile, J.; Trutt, F.C.; Leedy, A.W. Condition Monitoring of Brushless Three-Phase Synchronous Generators with Stator Winding or Rotor Circuit Deterioration. *IEEE Trans. Ind. Appl.* **2006**, *42*, 1209–1215. [CrossRef]
18. Pascual, R.; Mahtani, K.; Rivero, E.; Platero, C.A. Brushless Synchronous Machine Field Winding Interturn Fault Severity Estimation through Deep Neural Networks. *IEEE Trans. Energy Convers.* **2023**, *39*, 1341–1351. [CrossRef]
19. Tang, J.; Liu, Y.; Lundberg, S. Estimation Algorithm for Current and Temperature of Field Winding in Electrically Excited Synchronous Machines with High-Frequency Brushless Exciters. *IEEE Trans. Power Electron.* **2021**, *36*, 3512–3523. [CrossRef]
20. Tang, J.; Jiang, B.; Boscaglia, L.; Chen, H.; Liu, Y. Observations of Field Current and Field Winding Temperature in Electrically Excited Synchronous Machines with Brushless Excitation. In Proceedings of the 2022 International Conference on Electrical Machines (ICEM), Valencia, Spain, 5–8 September 2022; pp. 841–847.
21. Tun, P.P.; Kumar, P.S.; Pratama, R.A.; Shuyong, L. Brushless Synchronous Generator Turn-to-Turn Short Circuit Fault Detection Using Multilayer Neural Network. In Proceedings of the 2018 Asian Conference on Energy, Power and Transportation Electrification (ACEPT), Singapore, 30 October–2 November 2018; pp. 1–8.
22. Ferreira, J.G.; Warzecha, A. An application of machine learning approach to fault detection of a synchronous machine. In Proceedings of the International Symposium on Electrical Machines (SME), Naleczow, Poland, 18–21 June 2017; pp. 1–6.
23. Evangeline, S.I.; Darwin, S.; Raj, E.F.I. A deep residual neural network model for synchronous motor fault diagnostics. *Appl. Soft Comput.* **2024**, *160*, 111683. [CrossRef]
24. Yin, W.; Xia, H.; Huang, X.; Zhang, J.; Miyombo, M.E. A fault diagnosis method for nuclear power plant rotating machinery based on adaptive deep feature extraction and multiple support vector machines. *Prog. Nucl. Energy* **2023**, *164*, 104862. [CrossRef]

25. Ansermet, J.P.; Brechet, S.D. Principles of Thermodynamics. Cambridge University Press: Cambridge, UK, 2019; ISBN 9781108620932.
26. Zhang, X.; Xu, N.; Dai, W.; Zhu, G.; Wen, J. Turbofan Engine Health Prediction Model Based on ESO-BP Neural Network. *Appl. Sci.* **2024**, *14*, 1996. [CrossRef]
27. Taïbi, Z.M.; Hasni, M.; Hamdani, S.; Rahmani, O.; Touhami, O.; Ibtiouen, R. Optimization of the feedforward neural network for rotor cage fault diagnosis in three-phase induction motors. In Proceedings of the 2011 IEEE International Electric Machines & Drives Conference (IEMDC), Niagara Falls, ON, Canada, 15–18 May 2011; pp. 194–199.

**Disclaimer/Publisher's Note:** The statements, opinions and data contained in all publications are solely those of the individual author(s) and contributor(s) and not of MDPI and/or the editor(s). MDPI and/or the editor(s) disclaim responsibility for any injury to people or property resulting from any ideas, methods, instructions or products referred to in the content.

*applied sciences*

MDPI

*Article*

# Detection, Isolation, and Identification of Multiplicative Faults in a DC Motor and Amplifier Using Parameter Estimation Techniques

**Sanja Antić *, Marko Rosić, Branko Koprivica, Alenka Milovanović and Milentije Luković**

Faculty of Technical Sciences Čačak, University of Kragujevac, 32000 Čačak, Serbia; marko.rosic@ftn.kg.ac.rs (M.R.); branko.koprivica@ftn.kg.ac.rs (B.K.); alenka.milovanovic@ftn.kg.ac.rs (A.M.); milentije.lukovic@ftn.kg.ac.rs (M.L.)

* Correspondence: sanja.antic@ftn.kg.ac.rs

**Featured Application: The developed laboratory platform and associated algorithms can be applied in educational and research settings for real-time simulation, detection, and isolation of multiplicative faults in electromechanical systems. Its remote-access capability allows engineering students and researchers to conduct fault diagnosis experiments on DC motor systems without physical presence, supporting distance learning and development of robust FDII methods for safety-critical applications.**

**Abstract:** The increasing complexity of modern control systems highlights the need for reliable and robust fault detection, isolation, and identification (FDII) methods, particularly in safety-critical and industrial applications. The study focuses on the FDII of multiplicative faults in a DC motor and its electronic amplifier. To simulate such scenarios, a complete laboratory platform was developed for real-time FDII, using relay-based switching and custom LabVIEW software 2009. This platform enables real-time experimentation and represents an important component of the study. Two estimation-based fault detection (FD) algorithms were implemented: the Sliding Window Algorithm (SWA) for discrete-time models and a modified Sliding Integral Algorithm (SIA) for continuous-time models. The modification introduced to the SIA limits the data length used in least squares estimation, thereby reducing the impact of transient effects on parameter accuracy. Both algorithms achieved high model output-to-measured signal agreement, up to 98.6% under nominal conditions and above 95% during almost all fault scenarios. Moreover, the proposed fault isolation and identification methods, including a decision algorithm and an indirect estimation approach, successfully isolated and identified faults in key components such as amplifier resistors ($R_1$, $R_9$, $R_{12}$), capacitor ($C_8$), and motor parameters, including armature resistance ($R_a$), inertia ($J$), and friction coefficient ($B$). The decision algorithm, based on continuous-time model coefficients, demonstrated reliable fault isolation and identification, while the reduced Jacobian-based approach in the discrete model enhanced fault magnitude estimation, with deviations typically below 10%. Additionally, the platform supports remote experimentation, offering a valuable resource for advancing model-based FDII research and engineering education.

**Keywords:** fault detection, isolation, and identification; multiplicative faults; DC motor; electronic amplifier; Sliding Window Algorithm; Sliding Integral Algorithm; remote laboratory

## 1. Introduction

As control systems continue to grow in complexity, ensuring their safety and robustness becomes increasingly critical across a wide range of industrial processes. The reliability, robustness, availability, and environmental safety of such systems are often evaluated based on their sensitivity to faults, which may occur randomly during operation. This growing need has resulted in a distinct area within engineering theory and practice–fault detection and isolation (FDI) [1–5].

From a practical engineering standpoint, faults are commonly categorized into additive and multiplicative types. Additive faults are unexpected deterministic inputs (e.g., sudden load change or sensor biases) that affect the system output without altering its internal structure. These faults, which include actuator jamming or sensor drift, are typically absent under normal conditions but produce clear effects on outputs once present [6–12]. Multiplicative faults, by contrast, involve changes in system parameters, such as resistance, inductance, inertia, or friction coefficients. These faults may appear gradually (due to aging or wear) or abruptly (as in structural damage) and are more challenging to detect due to their parameter-driven, indirect, and often masked effects on system output [13–17].

In DC motors, multiplicative faults include misalignment of brushes, wear of the commutator, armature winding faults, variations in armature resistance, and changes in mechanical friction. They may also occur in the accompanying amplifier—making accurate real-time diagnosis a challenging but essential task [18–21].

Various FDI methods have been developed to address these issues, which can be classified into four broad categories:

1. Signal-based techniques rely on analyzing vibration or current signals, often using spectral, statistical, or wavelet-based methods [19,22–25]. While model-free and simple to implement, such methods are generally limited to offline analysis, and their performance deteriorates in low-power or noisy systems. They are also less suitable for detecting multiplicative faults, which often do not generate prominent signal features.
2. Model-based techniques exploit the system's dynamic model and include:
    - Parity equation methods, which compare measured and predicted outputs to generate residuals sensitive to specific faults [3,10,11,26]. These methods are simple to implement and effective for additive fault isolation, but they perform poorly for multiplicative faults due to their reliance on accurate models and sensitivity to noise and parameter uncertainties. Moreover, they typically lack fault identification capability, as they do not quantify fault magnitude.
    - Observer and filter-based methods (e.g., Luenberger observers, Kalman filters, sliding-mode observers) that estimate system states and detect deviations due to faults [7,14,27,28]. Such approaches provide good dynamic tracking and are suitable for real-time use, but they often require precise model tuning and can become unstable or inaccurate in the presence of model uncertainty or high noise.
    - Parameter estimation methods (e.g., Least Squares (LS), Recursive Least Squares (RLS), Extended Kalman Filters (EKF), Unscented Kalman Filters (UKF), Algebraic-Geometric Technique (AGT) [18,26,29–38].
3. Knowledge and data-driven approaches such as fuzzy logic, expert systems, and neural networks can learn or encode relationships between faults and observable features [6,12,18,39,40]. While effective for nonlinear and complex systems, these methods require large training datasets and may lack interpretability.

4. Optimization-based techniques such as Genetic Algorithms (GA), Particle Swarm Optimization (PSO), and Whale Optimization Algorithm (WOA)) that track deviations in estimated parameters, particularly relevant for multiplicative faults [41,42].

Among model-based approaches, parameter estimation techniques offer significant potential for detecting multiplicative faults, as they enable direct monitoring of physical changes within the system. Compared to traditional parameter estimation-based fault detection methods, the advantages of the proposed Sliding Window Algorithm (SWA) [43] and Sliding Integral Algorithm (SIA) [44] become more apparent.

Classical parameter estimation techniques such as LS [18,32,38] and RLS [30,31] are widely used due to their simplicity and low computational requirements. LS is primarily an offline method, as it processes a fixed batch of data and assumes time-invariant parameters during estimation. In contrast, RLS is designed for real-time application, updating estimates recursively as new data become available and using a forgetting factor to adapt to changing system dynamics. However, despite its real-time capability, RLS often struggles with transient disturbances and abrupt parameter changes caused by faults, especially when the forgetting factor is not optimally tuned. These limitations can lead to delayed or inaccurate fault detection in systems subject to abrupt changes [26,30].

Advanced methods such as EKF [29,34,35] and UKF [36,37] offer improved performance in noisy and nonlinear environments. However, their reliance on accurate system models and careful tuning of noise covariances increases implementation complexity and computational burden, limiting their suitability for embedded or real-time applications.

Similarly, algebraic techniques such as the AGT offer analytical insight and enable fault localization. However, they are generally unsuitable for real-time implementation due to their dependence on signal derivatives, symbolic computations, and high sensitivity to measurement noise [33].

Optimization-based techniques such as GA, PSO, and WOA offer global optimization capabilities for parameter estimation, but their high computational complexity makes them impractical for real-time applications [41,42].

In contrast, SWA and SIA offer robust and low-complexity alternatives that preserve interpretability and can be scaled to more complex systems with relative ease. SWA, applied to discrete-time models with short data windows, enhances responsiveness to abrupt faults, while SIA, using continuous-time integral formulations, reduces noise and transient sensitivity—making it suitable for gradual parameter changes. Both methods are non-intrusive, require minimal tuning, and are computationally efficient, making them ideal for embedded real-time applications. Furthermore, by linking estimated model parameters (e.g., $a_1$, $b_0$, $b_1$) to physical quantities (e.g., resistance, inertia), they enable not only fault detection and isolation but also identification of fault severity.

This paper presents a real-time, parameter-estimation-based framework for detection, isolation, and identification (FDII) of multiplicative faults in a DC motor and its amplifier. The system is implemented on a hardware-in-the-loop experimental platform using LabVIEW 2009 and NI CompactRIO CRIO-9075 (National Instruments, Austin, TX, USA), enabling remote access, real-time fault injection, and online testing.

The key contributions include:

1. Development of an interactive laboratory platform for real-time simulation and testing of FDII algorithms, specifically designed to support both practical implementation and engineering education. This is achieved through a hardware-in-the-loop, remotely accessible setup built using LabVIEW and NI CompactRIO, enabling real-time fault injection, detection, isolation, and identification in both the DC motor and its electronic amplifier—representing a significant advancement in applied FDI research and training environments.

2. Comprehensive Evaluation and Comparative Analysis of two complementary parameter estimation methods under identical experimental conditions: a modified Sliding Integral Algorithm (SIA) for continuous-time system modeling, which limits the data window to reduce the influence of transients and improves robustness of parameter estimation; and a Sliding Window Algorithm (SWA) for discrete-time modeling, which enhances responsiveness to abrupt parameter changes. This enables a comparative analysis of their performance and limitations, which is rarely addressed in the existing literature [19–21,33].
3. A modification of the SIA by limiting the data window, which reduces the influence of transients and improves the robustness of parameter estimation.
4. Demonstration of two complementary fault identification approaches that enable quantification of the change in affected physical parameters—a capability rarely addressed in the existing literature [13,14,16,18,19]. In addition to detecting and isolating faults, the proposed methods also estimate fault magnitude, which significantly enhances diagnostic resolution. This is achieved through:
    - A novel decision algorithm, based on the model obtained using SIA, which maps deviations in estimated model parameters to specific physical components;
    - An indirect estimation method, applied in the SWA framework, supported by a selective Jacobian matrix approach that improves the accuracy of physical parameter identification and strengthens the overall diagnostic capability of the system, especially when the relation between model and physical parameters is nonlinear or non-negligible. This overcomes limitations of prior indirect approaches that typically rely on the full Jacobian matrix [3,7].

In summary, this work presents a practical and robust methodology for detecting and identifying multiplicative faults using simple yet effective parameter estimation techniques. Its real-time implementation, experimental validation, and educational applicability make it a valuable contribution to both academic research and industrial practice.

## 2. Materials and Methods

Figure 1 presents the full experimental setup of the measurement equipment, comprising a motor, electronic amplifier, relays, and the CRIO-9075 controller.

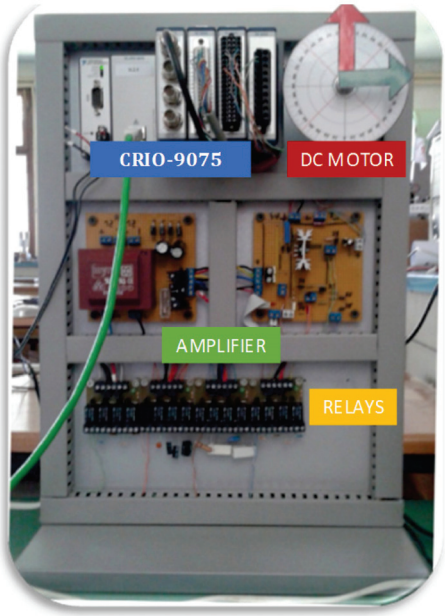


**Figure 1.** Experimental setup of the measuring equipment.

### *2.1. Laboratory Setup*

#### 2.1.1. DC Motor

For the planned experiments, a DC motor with permanent magnets A-max 26 A Ø26 mm Precious Metal Brushes CLL (Maxon Motor AG, Sachseln, Switzerland), 4.5 W was used. Figure 2a shows a DC micro-motor (1) equipped with an MR-128-1000 encoder (2), offering a resolution of 1000 impulses per revolution, and a Gear GP-26-B_144032 gearbox (3) with a gear ratio of 3.8:1.

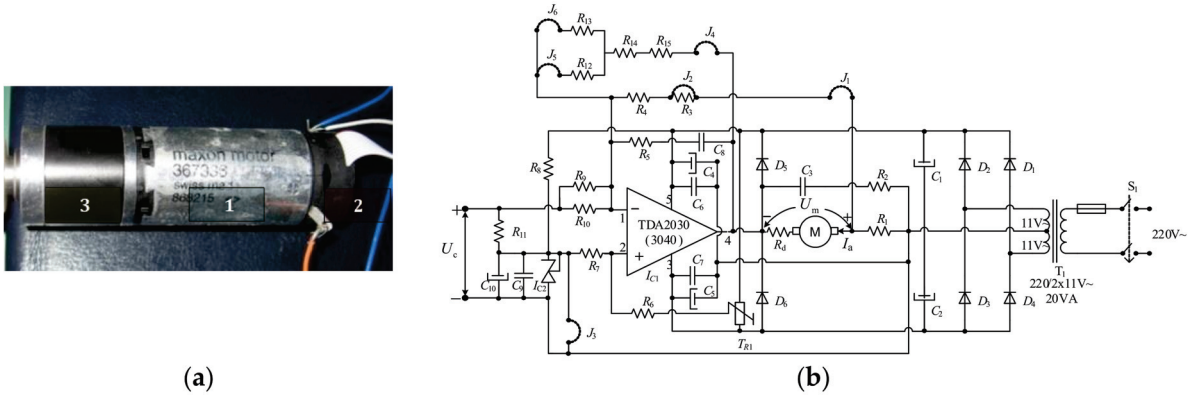


(**a**) (**b**)

**Figure 2.** Main components of the laboratory setup: (**a**) DC micro-motor (1), with encoder (2), and gearbox (3); (**b**) Electronic amplifier-schematic representation.

#### 2.1.2. Electronic Amplifier

The developed amplifier is in the form of a linear electronic converter. It represents a linear electronic circuit whose main component is the operational amplifier TDA2030(A) (STMicroelectronics, Geneva, Switzerland), powered by a DC supply via a single-phase transformer with two secondary windings and a diode rectifier. This amplifier can be used either as a voltage-to-current or voltage-to-voltage converter, for operation in two-quadrant or four-quadrant mode.

Figure 2b shows the electronic schematic of the amplifier used to supply the DC motor. The input voltage of the amplifier represents the control voltage $U_c$. The output of the amplifier is, depending on the mode, either the motor armature current $I_a$ or the reference armature voltage $U_m$.

The gain values of the amplifier are: in current modes $K_{UcIa} = 1/5$ A/V, and in voltage mode $K_{UcUm} = 12/5$ V/V. The accuracy of the amplifier operation is 1% of the range. In the experiments, the electronics were set to voltage-to-voltage, two-quadrant mode. Table 1 presents the data specifications of the DC motor and the amplifier.

**Table 1.** Specifications of the A-max 26 A DC motor (Ø26 mm, 4.5 W, with CLL precious metal brushes) and the amplifier.

| | |
|---|---|
| Nominal armature voltage | $U_{an} = 12$ V |
| Nominal armature current | $I_{an} = 0.629$ A |
| Nominal motor speed | $n_n = 2750$ min$^{-1}$ |
| Motor moment of inertia | $J_m = 1.3 \cdot 10^{-6}$ kgm$^2$ * |
| Gear reducer moment of inertia | $J_{gr} = 0.6 \cdot 10^{-7}$ kgm$^2$ * |
| Encoder moment of inertia | $J_e = 0.7 \cdot 10^{-7}$ kgm$^2$ * |
| Viscous friction coefficient | $B = 1.8 \cdot 10^{-6}$ Nm/rad/s ** |
| Coulomb friction | $M_c = 0.48 \cdot 10^{-3}$ Nm ** |
| Motor torque constant | $K_T = 25.5 \cdot 10^{-3}$ Nm/A |
| Back electromotive force (EMF) constant | $K_e = 25.5 \cdot 10^{-3}$ V/rad/s |
| Armature resistance | $R_a = 7.41$ Ω |

**Table 1.** *Cont.*

| | |
|---|---|
| Armature inductance | $L_a = 0.77 \cdot 10^{-3}$ H |
| Gear ratio | $N = 3.8$ |
| Amplifier resistor $R_1$ | $R_1 = 1\ \Omega$ |
| Amplifier resistor $R_5$ | $R_5 = 1$ kΩ |
| Amplifier resistors $R_9$, $R_{10}$, and $R_{12}$ | $R_9 = R_{10} = R_{12} = 10$ kΩ |
| Amplifier resistors $R_{14}$ and $R_{15}$ | $R_{14} = R_{15} = 1$ kΩ |
| Equivalent resistor $R_{e1}$ | $R_{e1} = R_9 \cdot R_{10}/(R_9 + R_{10}) = 5$ kΩ |
| Equivalent resistor $R_{e2}$ | $R_{e2} = R_{12} + R_{14} + R_{15} = 12$ kΩ |
| Amplifier capacitor $C_8$ | $C_8 = 48$ pF |

* The total moment of inertia of the DC motor is expressed as the sum $J = J_m + J_{gr} + J_e = 1.43 \cdot 10^{-6}$ kgm$^2$. ** This values of $B$ and $M_c$ are not specified in the datasheet for the particular motor but were determined experimentally [45].

### 2.1.3. CompactRIO 9075

The CompactRIO 9075 integrated system consists of a real-time processor and a reconfigurable FPGA (Field-Programmable Gate Array) on the same chassis, enabling control and monitoring capabilities, Figure 1. The CRIO-9075 integrates a 400 MHz industrial real-time processor with an LX25 FPGA and includes four slots for NI C Series I/O modules.

The modules used in the experimental setup are:

- NI 9402 (LVTTL, bidirectional, 4-channel, 55 ns digital input-output module)—for measuring motor speed after the gearbox, based on the frequency of the pulse train from the optical encoder;
- NI 9403 (5 V/TTL, bidirectional, 32-channel, 7 µs digital input-output module)—for controlling the activation of the corresponding relays;
- NI 9205 (32-channel, ±200 mV to ±10 V, 16-bit, 250 kS/s voltage input module)—for measuring the armature voltage of the motor and the armature current (by measuring the voltage across an additional resistor);
- NI 9263 (4-channel, ±10 V, 16-bit voltage output module)—for supplying the control voltage to the amplifier.

### 2.1.4. Relays

In order to develop a real-time FDII system, relays were designed to introduce multiplicative faults into the system by abruptly changing one of the amplifier parameters. Figure 3a shows the electronic schematic of the main part of the relay board used for connecting a resistance $R_i$ ($i$ = 1, 9, 12) into the amplifier circuit.

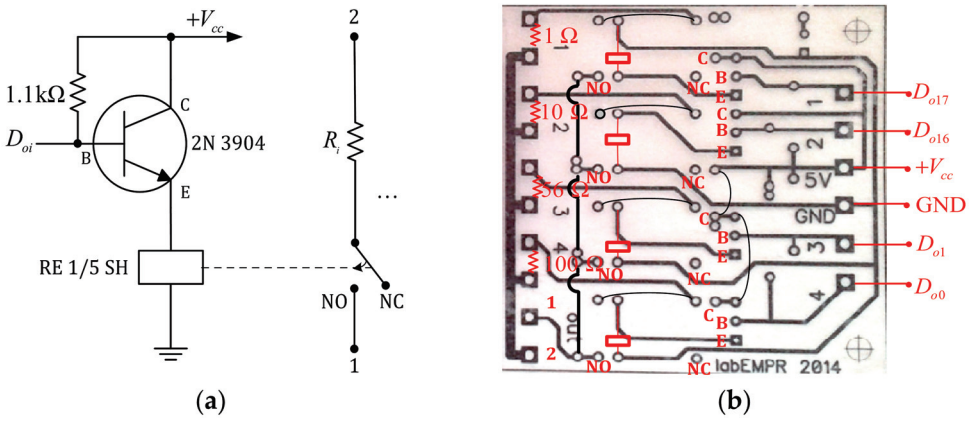


(**a**) (**b**)

**Figure 3.** Relay for switching resistance: (**a**) Electronic schematic; (**b**) Physical board.

Figure 3b represents an example of a printed circuit board used to switch on or off resistance $R_1$ in the amplifier circuit by assigning a binary value 0/1 to the corresponding digital outputs.

When the value of the *i*-th digital output ($D_{oi}$)of the NI 9403 module is 0, the 2N3904 transistor is in the conducting state, and the relay's electromagnet shifts the contact from the NC (normally closed) position to the NO (normally open) position, thereby connecting the desired resistance $R_i$ ($i$ = 1, 9, 12) (or capacitance $C_8$) into the amplifier circuit.

When the value of the digital output is 1, the bipolar transistor does not conduct, and no current flows through the relay coil. In this case, the NO contacts remain open, while the NC contacts are closed.

There are four printed circuit boards (PCBs), and each can switch between four different resistance values $R_i$ ($i$ = 1, 9, 12), or four capacitance values $C_8$ of the electronic amplifier, as specified in Table 2.

**Table 2.** Amplifier circuit parameter values that can be adjusted using relays.

| $D_{oi}$ | $R_1$ | $D_{oi}$ | $R_9$ |
|---|---|---|---|
| $D_{o17}$ | 1 Ω | $D_{o19}$ | 10 kΩ |
| $D_{o16}$ | 10 Ω | $D_{o18}$ | 33 kΩ |
| $D_{o1}$ | 56 Ω | $D_{o3}$ | 56 kΩ |
| $D_{o0}$ | 100 Ω | $D_{o2}$ | 100 kΩ |
| $D_{oi}$ | $C_8$ | $D_{oi}$ | $R_{12}$ |
| $D_{o21}$ | 47 pF | $D_{o6}$ | 10 kΩ |
| $D_{o20}$ | 1 μF | $D_{o7}$ | 5.6 kΩ |
| $D_{o5}$ | 10 μF | $D_{o22}$ | 3.3 kΩ |
| $D_{o4}$ | 47 μF | $D_{o23}$ | 2 kΩ |

*2.2. System Modeling in the Presence of Multiplicative Faults*

The electronic amplifier model, which uses an operational amplifier as its core component (Figure 2b), is influenced by the characteristics of the motor connected to its output. The total motor friction is described by a nonlinear function that combines static, dynamic, and viscous components, as defined by the Karnopp–Reynolds model (1) and illustrated in Figure 4a [46]. Moreover, since viscous friction is temperature-dependent (the value listed in Table 1 corresponds to a measurement at 23 °C), the combined motor–amplifier system exhibits nonlinear behavior [45].

$$M_f(\omega) = \begin{cases} M_s \mathrm{sgn}\omega; \ \text{ for } \ |\omega| < \Delta\omega \\ (M_c + (M_s - M_c)e^{-(\omega/\omega_k)\delta})\mathrm{sgn}\omega + B\omega; \ \text{ for } \ |\omega| > \Delta\omega \end{cases} \quad (1)$$

where $M_f$ is total friction in the motor, $M_s$ is static friction, $M_c$ is Coulomb friction, $B$ is viscous friction coefficient, $\omega$ is the angular velocity of the motor, and $\Delta\omega$ is area around $\omega = 0$. Parameter $\delta$ is estimated empirically. Some forms of this model are: Tustin's ($\delta = 1$) and Gauss's ($\delta = 2$).

After assigning constant values for $B$ and $M_c$, provided in Table 1, and after linearizing the friction curve (Figure 4b), a linearized model of the amplifier can be represented in the form:

$$\begin{aligned} U_m(s) = \ & \frac{R_{e2}(C_8R_5s+1)[(R_a+sL_a)(B+Js)+K_eK_T]}{R_{e1}[(R_{e2}+R_5)C_8s+1][(R_a+R_1+sL_a)(B+Js)+K_eK_T]}U_c(s) \\ & - \frac{R_1K_e}{[(R_a+R_1+sL_a)(B+Js)+K_eK_T]}M_c(s). \end{aligned} \quad (2)$$

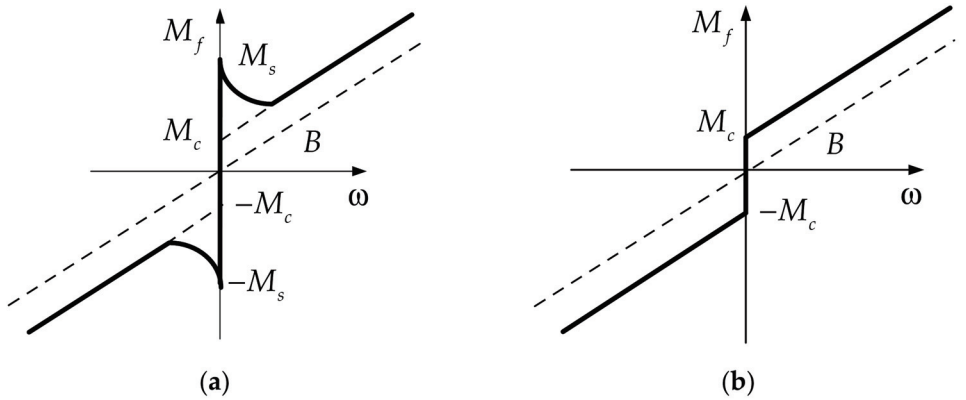


**Figure 4.** Dependence of total motor friction torque on motor rotational speed: (**a**) actual nonlinear model; (**b**) linear approximation.

By initially neglecting the inductance $L_a$ of the motor inductor circuit and subsequently reducing the resulting second-order system to a first-order one, a simplified model is obtained:

$$U_m(s) = \frac{b_{11}s + b_{01}}{a_{11}s + 1} U_c(s) - \frac{b_{02}}{a_{12}s + 1} M_c(s), \tag{3}$$

where

$$\begin{gathered} b_{01} = \frac{R_{2e}}{R_{1e}} \frac{BR_a + K_e K_T}{B(R_a + R_1) + K_e K_T}, \\ b_{11} = \frac{R_{2e}}{R_{1e}} \frac{[JR_a + C_8 R_5 (BR_a + K_e K_T)]}{B(R_a + R_1) + K_e K_T}, \\ a_{11} = \frac{J(R_a + R_1) + C_8 (R_5 + R_{2e})[B(R_a + R_1) + K_e K_T]}{B(R_a + R_1) + K_e K_T}, \end{gathered} \tag{4}$$

$$\begin{gathered} b_{02} = \frac{R_1 K_e}{B(R_a + R_1) + K_e K_T}, \\ a_{12} = \frac{J(R_a + R_1)}{B(R_a + R_1) + K_e K_T}. \end{gathered} \tag{5}$$

By omitting Coulomb friction, simplified continuous model suitable for analyzing multiplicative faults can be derived:

$$U_m(s) = \frac{b_1 s + b_0}{a_1 s + 1} U_c(s), \tag{6}$$

$$b_0 = b_{01}, b_1 = b_{11}, a_1 = a_{11}. \tag{7}$$

Discretizing the continuous amplifier model with a sampling period $T$ = 10 ms then produces:

$$U_m(z) = \frac{b_{0d} + b_{1d} z^{-1}}{1 + a_{1d} z^{-1}} U_c(z), \tag{8}$$

where the coefficients in (8) are defined by the discretization process:

$$\begin{gathered} b_{0d} = b_1 / a_1, \\ b_{1d} = b_0 (1 - e^{-T/a_1}) - b_1 / a_1, \\ a_{1d} = e^{-T/a_1}. \end{gathered} \tag{9}$$

The resulting discrete form (8) is directly applicable for implementing discrete multiplicative-fault detection algorithms.

*2.3. Sliding Window Algorithm*

The SWA is a method for estimating the parameters of a discrete model [47,48]. This algorithm is a variant of the least squares algorithm [38], where the data length $K$ is relatively small.

Consider a system model with a single input and a single output, expressed in the form:

$$y(k) = \frac{b_{0\mathrm{d}} + b_{1\mathrm{d}}z^{-1} + b_{2\mathrm{d}}z^{-2} + \ldots + b_{v\mathrm{d}}z^{-v}}{1 + a_{1\mathrm{d}}z^{-1} + a_{2\mathrm{d}}z^{-2} + \ldots + a_{v\mathrm{d}}z^{-v}}u(k), \tag{10}$$

where:

$u(k) = U_c(k)$ is the system input,
$y(k) = U_m(k)$ is the system output,
$v$ is the system order.

Defining the regression vector

$$\boldsymbol{\varphi}'(k) = [u(k)u(k-1)\ldots u(k-v); -y(k-1) - y(k-2)\ldots - y(k-v)], \tag{11}$$

and the parameter vector as

$$\boldsymbol{\pi} = [b_{0\mathrm{d}}\ b_{1\mathrm{d}}\ b_{2\mathrm{d}}\ \cdots\ b_{v\mathrm{d}};\ a_{1\mathrm{d}}\ a_{2\mathrm{d}}\ \cdots\ a_{v\mathrm{d}}]', \tag{12}$$

the output can be defined as follows:

$$y(k) = \boldsymbol{\varphi}'(k)\boldsymbol{\pi}. \tag{13}$$

The parameter estimation using the least squares algorithm is provided in the form:

$$\hat{\boldsymbol{\pi}}(k,K) = \left[\sum_{j=0}^{K-1} \boldsymbol{\varphi}(k-j)\boldsymbol{\varphi}'(k-j)\right]^{-1}\left[\sum_{j=0}^{K-1} \boldsymbol{\varphi}(k-j)y(k-j)\right], \tag{14}$$

$$\hat{\boldsymbol{\pi}}(k,K) = \left[\boldsymbol{\Phi}'(k,K)\boldsymbol{\Phi}(k,K)\right]^{-1}\boldsymbol{\Phi}'(k,K)\boldsymbol{Y}(k,K), \tag{15}$$

$$\boldsymbol{\Phi} = \begin{bmatrix} \boldsymbol{\varphi}'(k) \\ \vdots \\ \boldsymbol{\varphi}'(k-K+1) \end{bmatrix}, \boldsymbol{Y} = \begin{bmatrix} y(k) \\ \vdots \\ y(k-K+1) \end{bmatrix}, \tag{16}$$

where: $k$ denotes current time step, and $K$ represents the length of the data used in the algorithm.

When estimating parameters to detect and analyze multiplicative faults, a transient response occurs following a parameter jump, lasting for $K-1$ samples. As a result, the detection of such faults is delayed by at least $K-1$ samples. To reduce this delay, the window length $K$ in the least squares algorithm must be limited, prompting a shift to the SWA. A shorter window reduces detection delay but increases sensitivity to noise and variance in parameter estimates. Additionally, successful parameter estimation requires the input signal to be sufficiently informative, satisfying the persistent excitation condition [49].

*2.4. Sliding Integral Algorithm*

The SIA [3,44,50,51] is a control or signal processing method that computes the integral (i.e., the accumulated sum) of a signal over a moving (sliding) window of time or samples, Figure 5. It can identify the parameters of a continuous-time model directly from sampled data, which is often more complex than discrete-time identification but yields physically

meaningful parameters. To reduce sensitivity to noise from derivative approximations, an equivalent integral form of the differential equation is used, typically over a sliding window, to avoid the need for initial conditions, as proposed in [52].

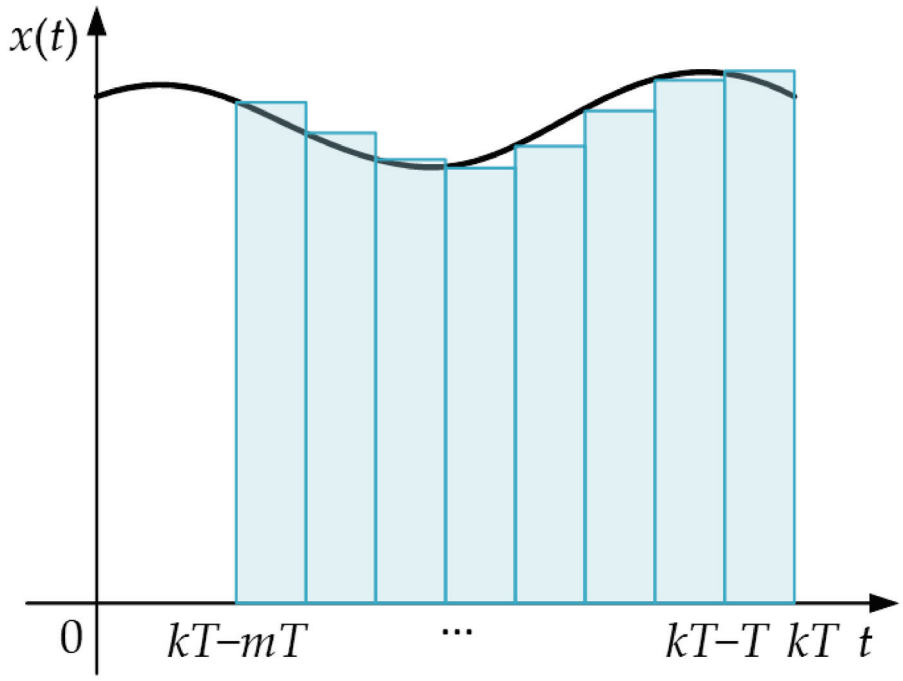


**Figure 5.** Rectangular approximation of the sliding integral.

The SIA is explained in detail in [3,51], and a more concise version is presented here. The sliding integral of a continuous-time variable $x(t)$ is:

$$I_1[x,k] = \int_{t=kT-mT}^{kT} x(t)dt, \tag{17}$$

where $T$ is sampling interval, $k$ is current time step, and $m$ is window length and sample counts representing the number of samples within the integration interval.

With rectangular approximation, this can be written as

$$I_1[x,k] = T\sum_{i=1}^{m} x(kT-iT) = TQ(z)x(k), \tag{18}$$

where

$$Q(z) = (\mathrm{z}^{-1} + \mathrm{z}^{-2} + \ldots + \mathrm{z}^{-m}).$$

In general, the $j$-th sliding integral is expressed as:

$$I_j[x,k] = T^jQ^j(z)x(k). \tag{19}$$

The following expression also holds [3,51]

$$I_j[x^{(j)},k] = (1-\mathrm{z}^{-m})^j x(k), \tag{20}$$

where $x^{(j)} = d^jx(t)/dt^j$.

By combining Equations (19)–(21), this equation can be obtained:

$$I_n[x^{(j)},k] = I_{n-j}[I_j(x^{(j)},k\prime),k] = \rho_j(z)x(k), \tag{21}$$

where

$$\rho_j(z) = T^{n-j}Q^{n-j}(1-z^{-m})^j, j = 0, 1, \ldots, n. \tag{22}$$

For a single-input single-output (SISO) linear time-invariant (LTI) system, the system dynamics can be described by the following differential equation:

$$y(t) + a_1\frac{dy(t)}{dt} + \ldots + a_n\frac{d^n y(t)}{dt^n} = b_0 u(t) + b_1\frac{du(t)}{dt} + \ldots + b_n\frac{d^n u(t)}{dt^n}, \tag{23}$$

where $u(t)$ is input, $y(t)$ is output of the system.

By applying the sliding integral to the differential Equation (23) $n$ times, it is obtained

$$I_n[y,k] + a_1 I_n[y^{(1)},k] + \ldots + a_n I_n[y^{(n)},k] = b_0 I_n[u,k] + b_1 I_n[u^{(1)},k] + \ldots + b_n I_n[u^{(n)},k]. \tag{24}$$

Using (21), (24) can be rewritten as follows:

$$\rho_0(z)y(k) + a_1\rho_1(z)y(k) + \ldots + a_n\rho_n(z)y(k) = b_0\rho_0(z)u(k) + b_1\rho_1(z)u(k) + \ldots + b_n\rho_n(z)u(k). \tag{25}$$

This is alternatively represented as

$$v(k) = \boldsymbol{\varphi}'(k)\theta, \tag{26}$$

where

$$v(k) = \rho_0(z)y(k), \tag{27}$$

$$\boldsymbol{\varphi}'(k) = [\rho_0(z)u(k) \ldots \rho_n(z)u(k); -\rho_1(z)y(k) \ldots - \rho_n(z)y(k)], \tag{28}$$

$$\theta = [b_0 \cdots b_n; a_1 \cdots a_n]'. \tag{29}$$

Accordingly, the least squares algorithm can be formulated as:

$$\theta = (\boldsymbol{\Phi}'\boldsymbol{\Phi})^{-1}\boldsymbol{\Phi}'\boldsymbol{V}, \tag{30}$$

where

$$\boldsymbol{\Phi} = \begin{bmatrix} \boldsymbol{\varphi}'(k) \\ \vdots \\ \boldsymbol{\varphi}'(k-K+1) \end{bmatrix}, \boldsymbol{V} = \begin{bmatrix} v(k) \\ \vdots \\ \mathrm{v}(k-K+1) \end{bmatrix}. \tag{31}$$

Although the identification procedure still relies on sampled data, the SIA is more complex and computationally intensive than parameter identification in the discrete-time case. Due to the inherent trade-off between computational complexity and noise attenuation, a window length $m$ of up to 20 is recommended [3]. Furthermore, the literature does not impose any specific constraints on the length of the identification dataset $K$.

### *2.5. The Main Steps of the Proposed FDII Methodology*

A flowchart representing the main steps of the proposed FDII methodology is presented in Figure 6, providing a clear visual overview of the detection, isolation, and identification process.

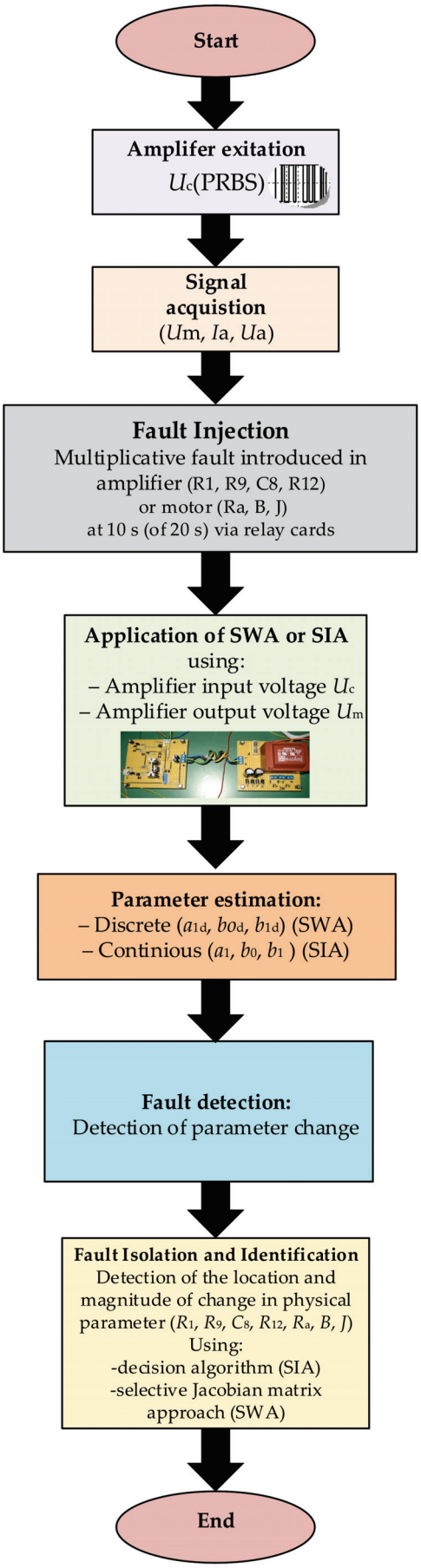


**Figure 6.** Flowchart of the main steps of the FDII.

## 3. Results

To demonstrate the effectiveness of detecting and isolating individual multiplicative amplifier faults, the amplifier parameters were deliberately and abruptly altered (one at a time) at the midpoint of the recording interval using relay cards (Figure 3). In this experimental setup, two parameter estimation approaches were developed.

The first approach can be described as offline. Signal data were collected in the LabVIEW environment and stored as text files. The estimation process was then carried out in batch mode using MATLAB 2020b, where the estimation algorithm was implemented through dedicated m-files.

Figure 7 presents a portion of the LabVIEW block diagram for generating and recording signals under multiplicative fault conditions. It illustrates the generation of the amplifier's input signal $U_c$, using a PRBS (Pseudo-Random Binary Sequence) and the measurement of the amplifier's output signal $U_m$. The system also enables monitoring of the armature voltage $U_a$, the armature current $I_a$ (by monitoring the voltage on the series resistor $R_d$, Figures 2b and 7), and the motor speed $n$.

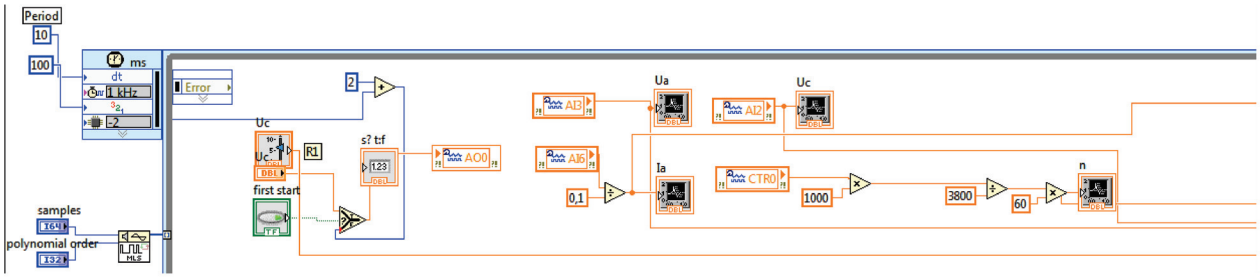


**Figure 7.** A segment of the LabVIEW Block Diagram developed for generating and recording signals under multiplicative fault conditions.

Figure 8 presents a portion of the LabVIEW Block Diagram, which activates specific amplifier parameters by switching the corresponding relays, thereby inducing individual multiplicative faults.

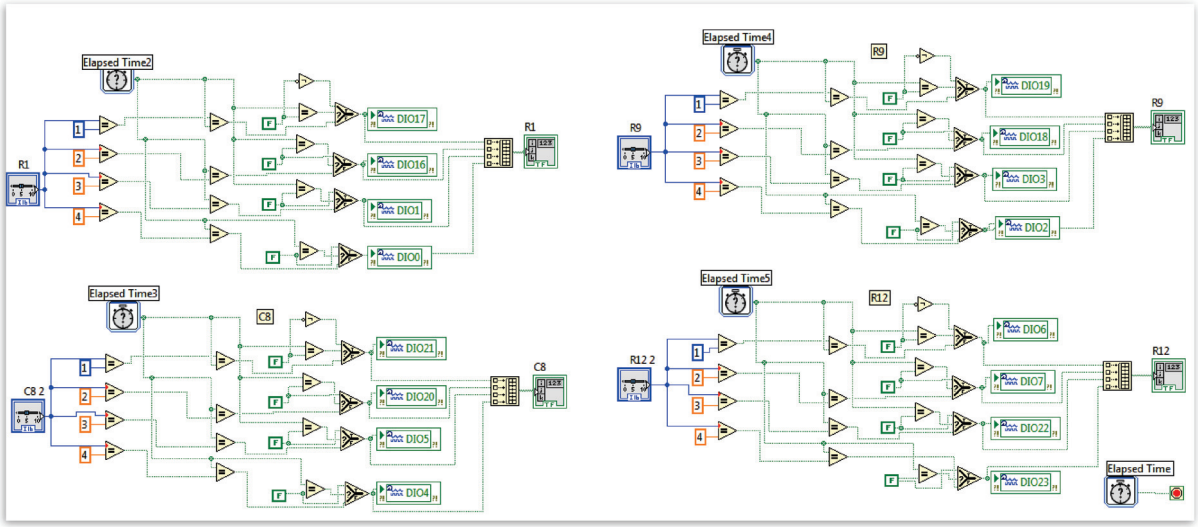


**Figure 8.** A segment of the LabVIEW Block Diagram developed to inject multiplicative faults into the system.

Figure 9 shows the Front Panel of the LabVIEW program used for monitoring input-output signals, featuring controls for the abrupt changing of one of the amplifier's parameter values in the event of a multiplicative fault. The software is configured so that all parameters are set to their nominal values (slider position 1) prior to the occurrence of a

fault. At the fault moment, one of the amplifier parameters is changed. In the example shown, the resistance $R_{12}$ is in 10 s reduced from its nominal value of 10 kΩ to a lower value of 5.6 kΩ (slider position 3) by automatically activating the corresponding relay.

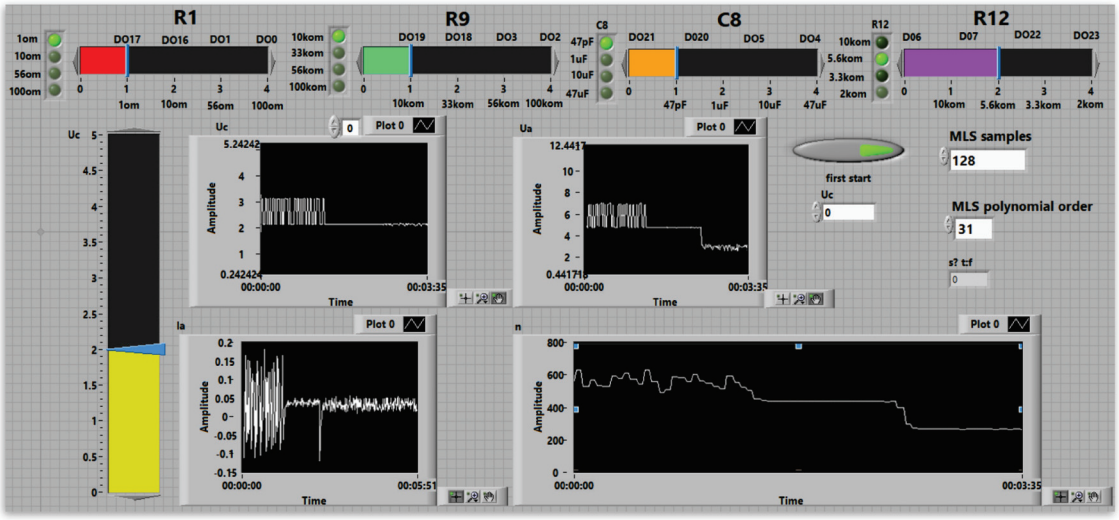


**Figure 9.** LabVIEW Front Panel for acquisition of input–output signals under multiplicative fault conditions.

The second approach to detecting multiplicative faults in the amplifier and DC motor was developed entirely within the LabVIEW environment and can be classified as a real-time method. After acquiring the input–output signals (Figures 7 and 9) during the injection of specific multiplicative faults using relays (Figures 8 and 9), the signals are passed to the next frame of the Flat Sequence structure. Within this structure, the desired estimation algorithm, either discrete (SWA), based on (14)–(16), or continuous (SIA), based on (30) and (31), is implemented using a MathScript Node within the LabVIEW software (Figure 10). The estimated parameters of the amplifier $b_{0d}$, $b_{1d}$, and $a_{1d}$ from the discrete model of the amplifier (8) (SWA), or $b_0$, $b_1$, and $a_1$ from the continuous model of the amplifier (6) (SIA), are then displayed in the Chart block of the LabVIEW program. Figure 11 displays section of the LabVIEW Front Panel displaying the estimation of continuous parameters $b_0$, $b_1$, and $a_1$ using the SIA.

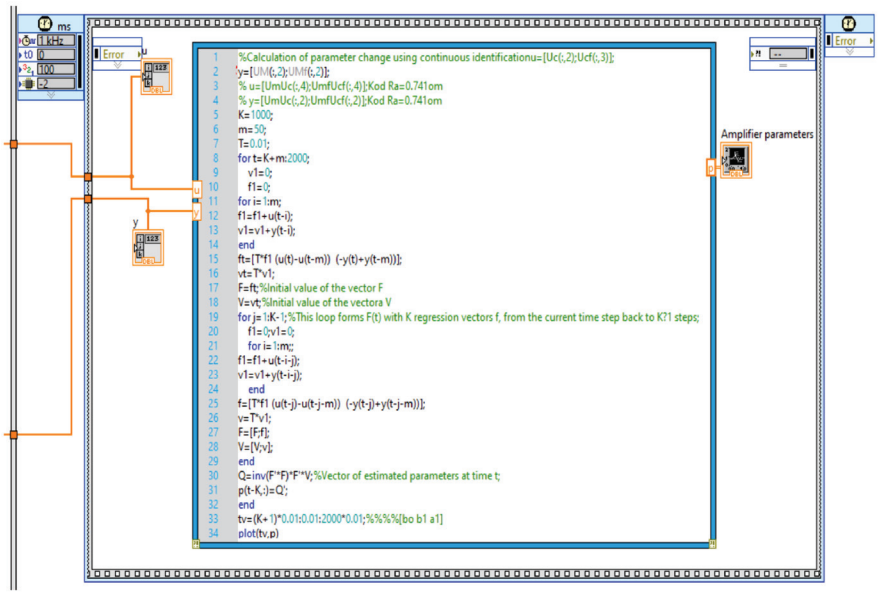


**Figure 10.** LabVIEW MathScript Node for SIA-based parameter estimation.

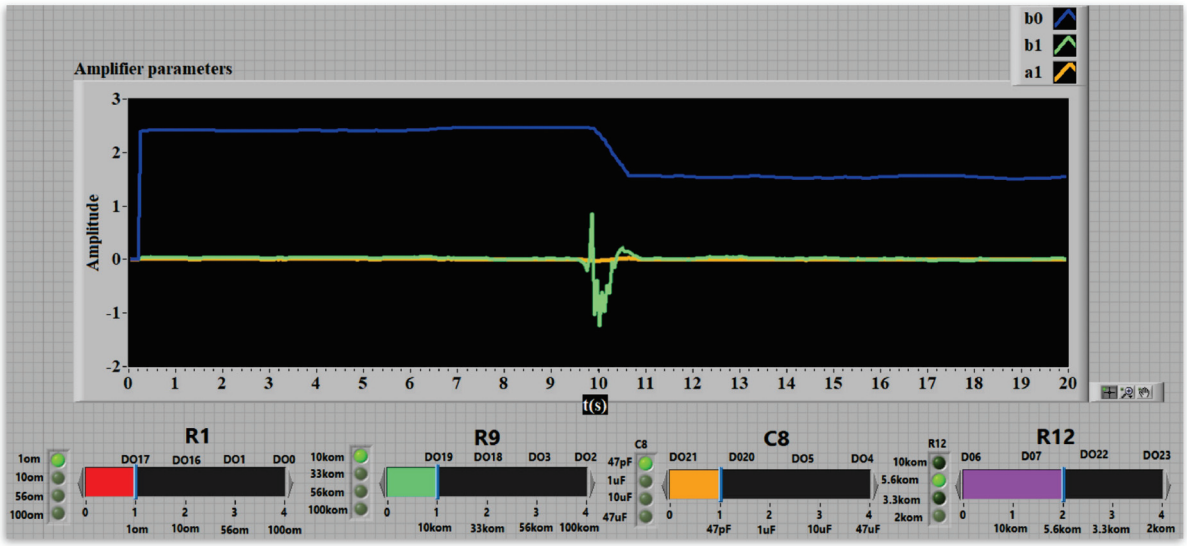


**Figure 11.** Section of the LabVIEW Front Panel displaying the estimation of parameters $b_0$, $b_1$, and $a_1$ using the SIA.

The procedure for generating multiplicative motor faults, specifically changes in inductance ($L$), armature resistance ($R_a$), moment of inertia ($J$), and viscous friction coefficient ($B$), was implemented at the simulation level using the Multisim environment. This setup utilized the amplifier model shown in Figure 12 and the motor model illustrated in Figure 13. In this configuration, the input signal for parameter estimation was a Pseudo-Random Binary Sequence (PRBS) control voltage ($U_c$), while the output voltage of the amplifier ($U_m$) was recorded using the Parameter Sweep faults. This approach leverages the mapping of motor parameters onto the electronic amplifier model.

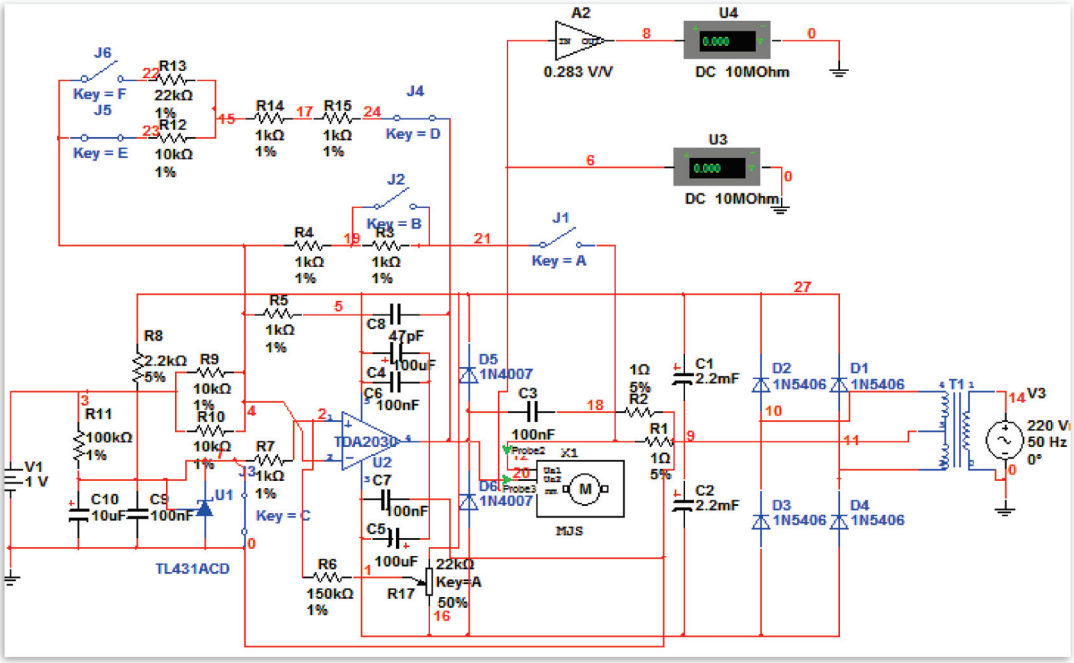


**Figure 12.** Multisim model of the electronic amplifier.

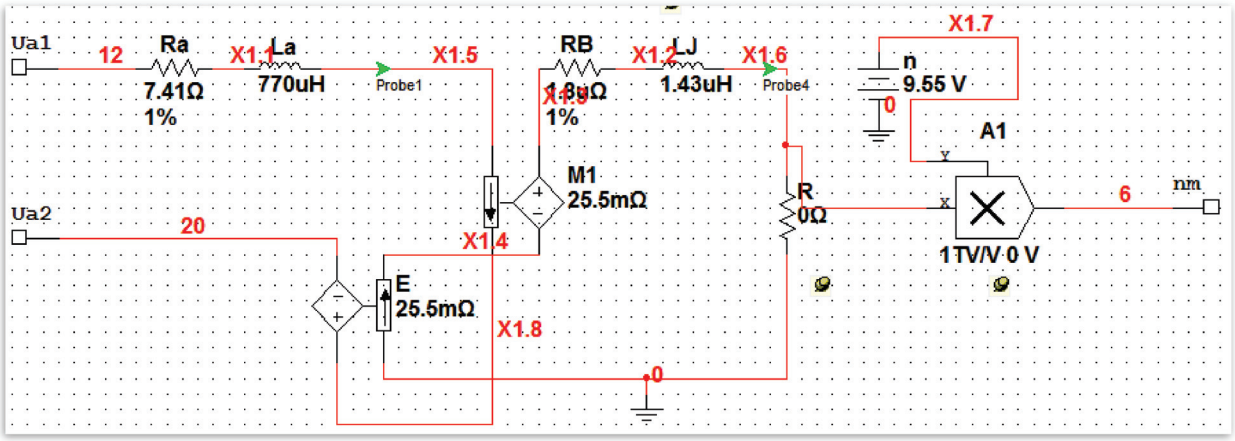


**Figure 13.** Multisim model of the DC motor.

### *3.1. Multiplicative Fault Detection*

#### 3.1.1. Input–Output Signals Under Multiplicative Faults

To ensure accurate estimation of sudden multiplicative faults, the input signal must be persistently exciting, i.e., rich enough to guarantee a unique and identifiable set of parameter estimates [49]. The Pseudo-Random Binary Sequence (PRBS), which is readily available in most software libraries, is, therefore, widely adopted for system identification.

A PRBS signal with values between 2 V and 3 V, as shown in Figure 14, was generated using LabVIEW and applied as the input to the electronic amplifier. Figures 15 and 16 illustrate the amplifier and motor output voltages over a 20 s period, during which a sudden multiplicative fault is introduced at the 10th s. This fault corresponds to an abrupt change in a selected amplifier or motor parameter from its nominal value to a predefined fault value. For the amplifier, faults were introduced in the following components: $R_1$ (from the nominal value of 1 Ω to fault values 10 Ω, 56 Ω, and 100 Ω), Figure 15a; $R_9$ (from the nominal value of 10 kΩ to the faults values 33 kΩ, 56 kΩ and 100 kΩ), Figure 15b, $C_8$ (from the nominal value of 47 pF to the fault values 1 µF, 10 µF, 47 µF), Figure 15c; $R_{12}$ (from the nominal value of 10 kΩ to the fault values 2 kΩ, 3.3 kΩ and 5.6 kΩ), Figure 15d. For the motor, faults were introduced in the parameters: armature resistance $R_a$ (from the nominal value 7.41 Ω to the fault values 0.741 Ω and 74.1 Ω), Figure 16a,b, viscous friction coefficient $B$ (from the nominal value $1.8{\cdot}10^{-6}$ Nm/rad/s to the fault values $1.8{\cdot}10^{-4}$ Nm/rad/s and $1.8{\cdot}10^{-8}$ Nm/rad/s), Figure 16c, moment of inertia J (from the nominal value $1.43{\cdot}10^{-6}$ kgm$^2$ to the fault values $1.43{\cdot}10^{-4}$ kgm$^2$ and $1.43{\cdot}10^{-8}$ kgm$^2$), Figure 16d.

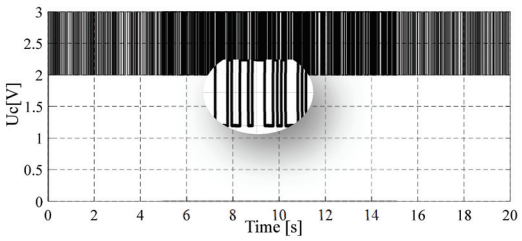


**Figure 14.** Amplifier input voltage $U_c$(t)—PRBS excitation signal with a magnified view of the waveform.

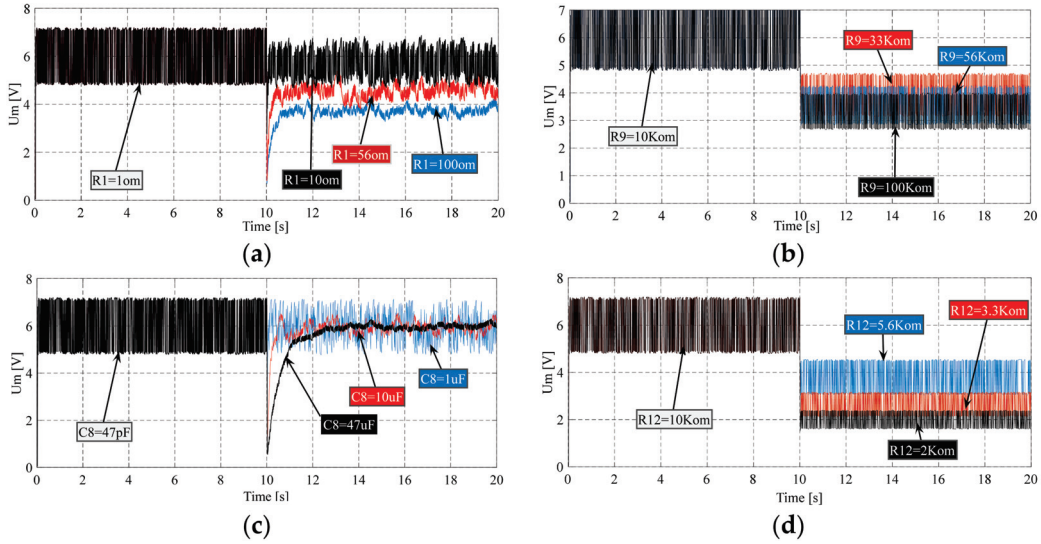


**Figure 15.** Amplifier output voltage $U_m(t)$ during multiplicative faults on: (**a**) $R_1$; (**b**) $R_9$; (**c**) $C_8$; (**d**) $R_{12}$.

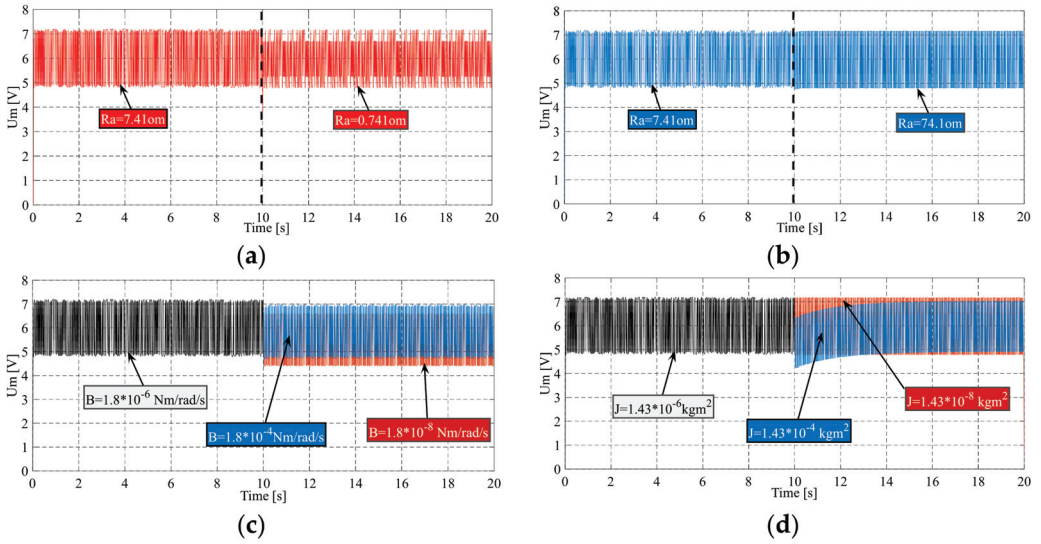


**Figure 16.** Amplifier output voltage $U_m$(t) during multiplicative faults on: (**a**) *Ra*; (**b**) *Ra*; (**c**) *B*; (**d**) *J*. The symbol "*" denotes a multiplication sign.

### 3.1.2. Multiplicative Fault Detection Using Sliding Window Algorithm

The following diagrams present selected results from the application of the SWA for estimating amplifier parameters using various window lengths ($K$). The result of applying the SWA is the set of discrete amplifier parameters, $a_{1d}$, $b_{0d}$, and $b_{1d}$, described in model (8). Figures 17 and 18 show SWA-based parameter estimation in response to a multiplicative fault in the amplifier resistance $R_1$ and the motor's viscous friction coefficient $B$, respectively.

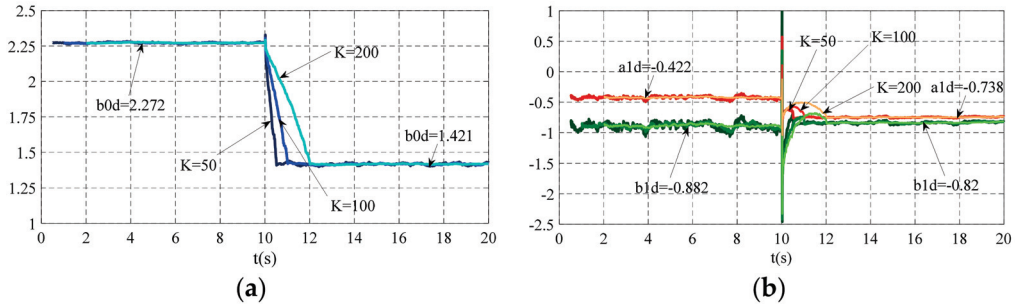


**Figure 17.** SWA amplifier parameters estimation: (**a**) $b_{0d}$ (**b**) $a_{1d}$, $b_{1d}$ during the change of $R_1$ from 1 Ω to 10 Ω.

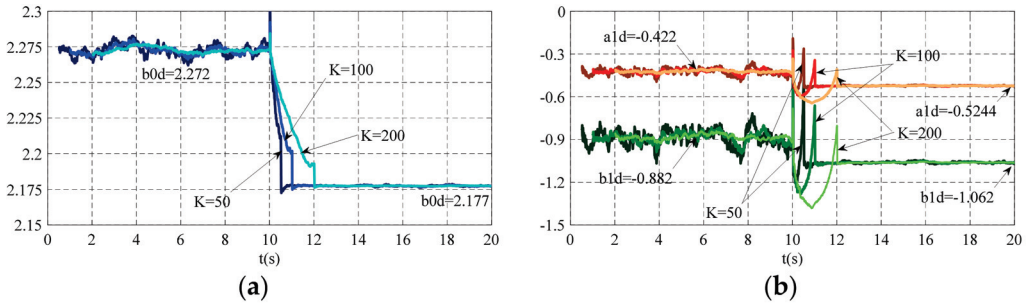


**Figure 18.** SWA amplifier parameter estimation: (**a**) $b_{0d}$, (**b**) $a_{1d}$, $b_{1d}$, during the change of $B$ from $1.8{\cdot}10^{-6}$ kgm$^2$ to $1.8{\cdot}10^{-5}$ kgm$^2$.

In Figures 17 and 18, the time interval from 0 to 10 s represents the estimated parameters before the fault occurs, while the interval from 10 to 20 s corresponds to the post-fault parameter estimation. A transient interval is noticeable within this post-fault period, lasting approximately $(K-1){\cdot}T$ s, where $T = 0.01$ s denotes the sampling period.

The graphical estimation results indicated that a sudden change in the amplifier or motor parameters triggers a transient response in the identification algorithm during the measurement period. Consequently, selecting a shorter window length is more advantageous in terms of reducing fault detection delay. However, it is also evident that as the window length decreases, the variance of the estimates increases and the sensitivity to noise becomes more pronounced. In the conducted experiments, $K = 50$; $K = 100$; and $K = 200$, different window lengths were tested. Since the total measurement period was 20 s, the chosen window lengths corresponded to transient durations of approximately 0.49 s, 0.99 s, and 1.99 s. In this particular case, the parameter choice of $K = 100$ proved to be the most effective.

Tables 3–6 summarize the complete results of applying the SWA for various multiplicative faults in the four amplifier parameters $R_1$, $R_9$, $R_{12}$, and $C_{8,}$ and the three motor parameters $R_a$, $J$, and $B$. The obtained results pertain to the discrete amplifier parameters $b_{0d}$, $b_{1d}$, and $a_{1d}$ from model (8).

**Table 3.** Amplifier parameter estimation using the SWA for multiplicative faults in $R_1$ and $R_9$.

| | $R_1$ = 1 Ω | | | | $R_9$ = 10 kΩ | | |
|---|---|---|---|---|---|---|---|
| **Fault** | $b_{0d}$ | $b_{1d}$ | $a_{1d}$ | **Fault** | $b_{0d}$ | $b_{1d}$ | $a_{1d}$ |
| 10 Ω | 1.421 | −0.82 | −0.738 | 33 kΩ | 1.488 | −0.5 | −0.373 |
| 56 Ω | 0.472 | −0.279 | −0.896 | 56 kΩ | 1.337 | −0.412 | −0.35 |
| 100 Ω | 0.29 | −0.18 | −0.925 | 100 kΩ | 1.258 | −0.359 | −0.316 |

**Table 4.** Amplifier parameter estimation using the SWA for multiplicative faults in $R_{12}$ and $C_8$.

| $R_{12}$ = 10 kΩ | | | | $C_8$ = 47 pF | | | |
|---|---|---|---|---|---|---|---|
| **Fault** | $b_{0d}$ | $b_{1d}$ | $a_{1d}$ | **Fault** | $b_{0d}$ | $b_{1d}$ | $a_{1d}$ |
| 2 kΩ | 0.757 | −0.368 | −0.514 | 1 µF | 1.148 | −0.013 | −0.526 |
| 3.3 kΩ | 1 | −0.458 | −0.492 | 10 µF | 0.312 | −0.142 | −0.929 |
| 5.6 kΩ | 1.434 | −0.784 | −0.572 | 47 µF | 0.21 | −0.168 | −0.982 |

**Table 5.** Estimation of motor parameters using the SWA for multiplicative faults in $R_a$ and $J$.

| $R_a$ = 7.41 Ω | | | | $J = 1.43 \cdot 10^{-6}$ kgm$^2$ | | | |
|---|---|---|---|---|---|---|---|
| **Fault** | $b_{0d}$ | $b_{1d}$ | $a_{1d}$ | **Fault** | $b_{0d}$ | $b_{1d}$ | $a_{1d}$ |
| 0.741 Ω | 1.9 | 0.356 | −0.06 | $1.43 \cdot 10^{-4}$ kgm$^2$ | 2.12 | −2.13 | −1 |
| 74.1 Ω | 2.369 | −2.227 | −0.94 | $1.43 \cdot 10^{-8}$ kgm$^2$ | 2.34 | −0.192 | −0.083 |

**Table 6.** Estimation of motor parameters using the SWA for multiplicative fault in $B$.

| $B = 1.8 \cdot 10^{-6}$ Nm/rad/s | | | |
|---|---|---|---|
| **Fault** | $b_{0d}$ | $b_{1d}$ | $a_{1d}$ |
| $1.8 \cdot 10^{-4}$ Nm/rad/s | 2.162 | −0.34 | −0.172 |
| $1.8 \cdot 10^{-5}$ Nm/rad/s | 2.177 | −1.062 | −0.524 |

### 3.1.3. Multiplicative Fault Detection Using Sliding Integral Algorithm

The following figures show selected results from applying the SIA to estimate amplifier parameters under different window lengths ($m$) and data lengths ($K$). In each case, multiplicative faults were introduced abruptly at 10 s. In Figures 19 and 20, the time interval from 0 to 10 s corresponds to the parameter estimates prior to the fault occurrence, while the interval from 10 to 20 s reflects the parameter estimation after the fault has been introduced. During this post-fault period, a transient response can be observed, lasting approximately $(K + m - 1) \cdot T$ seconds, where $T = 0.01$ s is the sampling period.

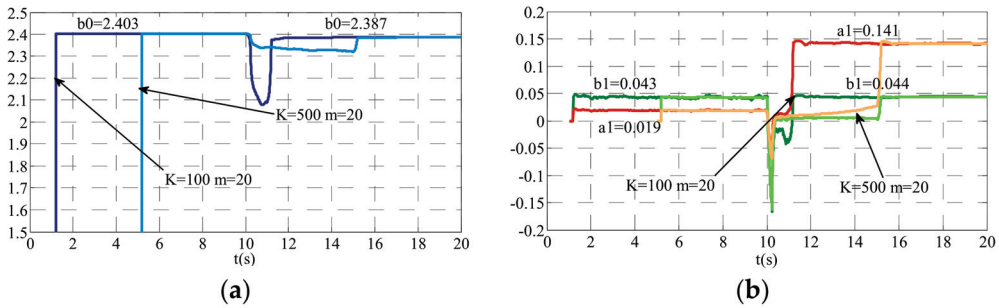


(**a**) (**b**)

**Figure 19.** SIA amplifier parameters estimation: (**a**) $b_0$, (**b**) $a_1$, $b_1$ during the change of $C_8$ from 47 pF to 10 µF.

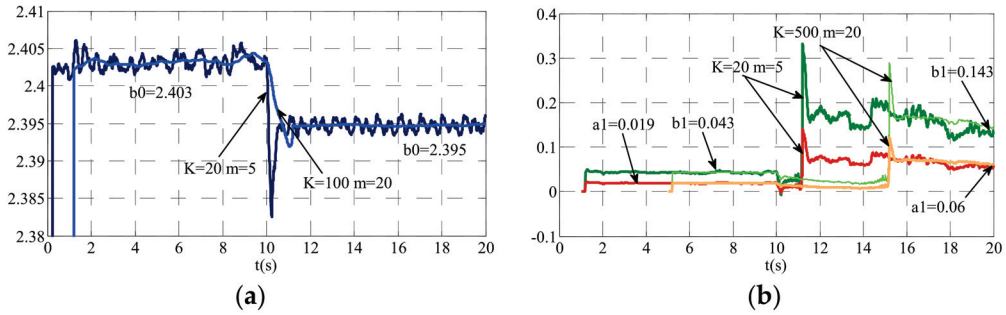


**Figure 20.** SIA amplifier parameters estimation: (**a**) $b_0$, (**b**) $a_1$, $b_1$ during the change of $R_a$ from 7.41 Ω to 74.1 Ω.

Figure 19 shows amplifier parameter estimation using the SIA in response to a multiplicative fault in the amplifier capacitor $C_8$, while Figure 20 corresponds to a multiplicative fault in the motor armature resistance $R_a$.

When applying the estimation algorithm for the detection of abrupt parameter changes, it has been observed that the length of the identification dataset $K$ should be selected to be sufficiently small (yet greater than $m$, $K > m$), as the estimation process effectively operates as a "window of length $m$" nested within a broader window of length $K$. Such changes induce a transient in the identification process lasting $K + m - 1$ samples. The used window configurations were: $K = 20$, $m = 5$; $K = 100$, $m = 20$, and $K = 500$, $m = 20$. Since the sampling period $T = 10$ ms, these configurations correspond to transient durations of approximately 0.24 s, 1.19 s, and 5.19 s, respectively.

Tables 7–10 summarize the complete results of applying the SIA for various multiplicative faults in the four amplifier parameters $R_1$, $R_9$, $R_{12}$, and $C_8$, and the three motor parameters $R_a$, $J$, and $B$. The obtained results pertain to the continuous amplifier parameters $b_0$, $b_1$, and $a_1$ from model (6).

**Table 7.** Amplifier parameter estimation using the SIA for multiplicative faults in $R_1$ and $R_9$.

| | $R_1$ = 1 Ω | | | | $R_9$ = 10 kΩ | | |
|---|---|---|---|---|---|---|---|
| **Fault** | $b_0$ | $b_1$ | $a_1$ | **Fault** | $b_0$ | $b_1$ | $a_1$ |
| 10 Ω | 2.306 | 0.0546 | 0.038 | 33 kΩ | 1.331 | 0.0245 | 0.0199 |
| 56 Ω | 1.85 | 0.047 | 0.1 | 56 kΩ | 1.425 | 0.03 | 0.0221 |
| 100 Ω | 1.495 | 0.0352 | 0.126 | 100 kΩ | 1.575 | 0.032 | 0.022 |

**Table 8.** Amplifier parameter estimation using the SIA for multiplicative faults in $R_{12}$ and $C_8$.

| | $R_{12}$ = 10 kΩ | | | | $C_8$ = 47 pF | | |
|---|---|---|---|---|---|---|---|
| **Fault** | $b_0$ | $b_1$ | $a_1$ | **Fault** | $b_0$ | $b_1$ | $a_1$ |
| 2 kΩ | 0.8 | 0.0175 | 0.023 | 1 µF | 2.39 | 0.024 | 0.0209 |
| 3.3 kΩ | 1.059 | 0.0228 | 0.0228 | 10 µF | 2.387 | 0.044 | 0.141 |
| 5.6 kΩ | 1.521 | 0.032 | 0.022 | 47 µF | 2.386 | 0.1142 | 0.56 |

**Table 9.** Estimation of motor parameters using the SIA for multiplicative faults in $R_a$ and $J$.

| | $R_a$ = 7.41 Ω | | | | $J = 1.43 \cdot 10^{-6}$ kgm$^2$ | | |
|---|---|---|---|---|---|---|---|
| **Fault** | $b_0$ | $b_1$ | $a_1$ | **Fault** | $b_0$ | $b_1$ | $a_1$ |
| 0.741 Ω | 2.393 | 0.02 | 0.011 | $1.43 \cdot 10^{-4}$ kgm$^2$ | 2.392 | 3.794 | 1.824 |
| 74.1 Ω | 2.395 | 0.143 | 0.06 | $1.43 \cdot 10^{-8}$ kgm$^2$ | 2.394 | 0.018 | 0.008 |

**Table 10.** Estimation of motor parameters using the SIA for multiplicative faults in *B*.

| $B = 1.8 \cdot 10^{-6}$ Nm/rad/s | | | |
|---|---|---|---|
| **Fault** | $b_0$ | $b_1$ | $a_1$ |
| $1.8 \cdot 10^{-4}$ Nm/rad/s | 2.2 | 0.026 | 0.012 |
| $1.8 \cdot 10^{-5}$ Nm/rad/s | 2.346 | 0.0462 | 0.0213 |

### *3.2. Multiplicative Fault Isolation and Identification*

#### 3.2.1. Decision Algorithm

The applied techniques for detecting multiplicative faults provide information about changes in the system model parameters but do not reveal the values of the specific physical parameters that caused those changes. Hence, they are capable of fault detection, i.e., they confirm that a fault has occurred in the system.

In order to isolate faults (i.e., identify the fault location), a decision algorithm based on the amplifier model, (6), with parameters provided with (4) and (7), has been developed as shown in Figure 21.

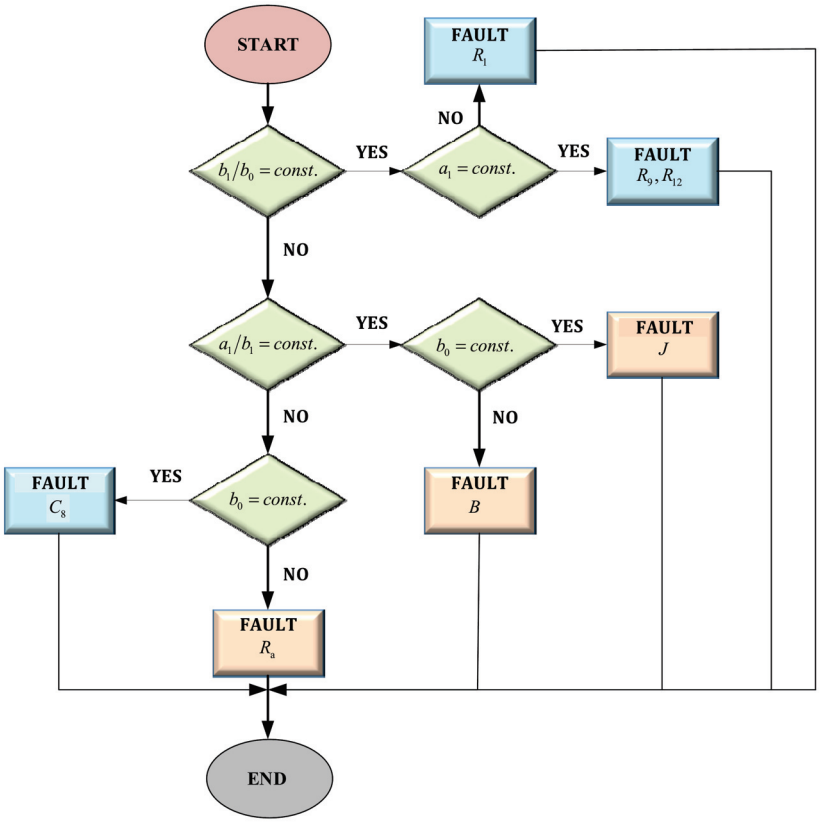


**Figure 21.** Multiplicative fault isolation using a decision algorithm with the SIA.

This algorithm can be performed in the case of application of continuous fault detection procedure, i.e., SIA. Fault identification, in terms of determining the magnitude of the change in the corresponding physical parameter, is straightforward in this case. The actual faulty physical parameter can be directly determined from the relations provided in (4) and (7), thereby completing the identification.

#### 3.2.2. Indirect Estimation Procedure

An alternative solution to the fault identification problem, which can also be applied in the case of discrete parameter estimation using the SWA, the actual physical parameters can

be determined through one of the indirect estimation procedures [3]. This approach is fully applicable when the relationship between the estimated and physical parameters is linear. However, if the relationship is nonlinear (which is more common), the procedure remains applicable only when the change (i.e., the fault) in the physical parameter is relatively small compared to its nominal value.

The starting point is the relationship between the physical parameters $\theta$, whose number is $L$, and the model parameters $\boldsymbol{\pi}$, whose number is $N$, expressed through the relation:

$$\boldsymbol{\pi} = f(\theta). \tag{32}$$

When $L = N$, the actual physical parameters can be indirectly estimated according to:

$$\Delta\hat{\theta} = \boldsymbol{R}^{-1}\Delta\hat{\boldsymbol{\pi}}, \tag{33}$$

$$\boldsymbol{R} = \left[\frac{\partial\boldsymbol{\pi}}{\partial\theta}\right]_{\Delta\theta=0} = \begin{bmatrix} \frac{\partial\boldsymbol{\pi}_1}{\partial\theta_1} & \cdots & \frac{\partial\boldsymbol{\pi}_1}{\partial\theta_L} \\ \vdots & & \vdots \\ \frac{\partial\boldsymbol{\pi}_N}{\partial\theta_1} & \cdots & \frac{\partial\boldsymbol{\pi}_N}{\partial\theta_L} \end{bmatrix}_{\Delta\theta=0}, \tag{34}$$

where:

$\Delta\hat{\boldsymbol{\pi}} = \hat{\boldsymbol{\pi}} - \boldsymbol{\pi}_{\mathrm{n}}$ is estimation in model parameters variation,
$\boldsymbol{\pi}_{\mathrm{n}}$ is the nominal model parameters,
$\hat{\boldsymbol{\pi}}$ is estimating model parameters,
$\Delta\hat{\theta}$ is estimation of actual physical parameters.

The partial derivatives in (34) are calculated using the nominal values of the parameters. If $L < N$, a slightly modified form of (33) defined in [3] can be used:

$$\Delta\hat{\theta} = (\boldsymbol{R}'\boldsymbol{R})^{-1}\boldsymbol{R}'\Delta\hat{\boldsymbol{\pi}}. \tag{35}$$

In the specific example, the vector of actual physical parameters is defined as:

$$\theta = \begin{bmatrix} R_1 & R_9 & R_{12} & C_8 & R_{\mathrm{a}} & J & B \end{bmatrix}', \tag{36}$$

so, the columns of the Jacobian matrix (matrix of partial derivatives) are:

$$\boldsymbol{R}_1 = \begin{bmatrix} \frac{db_0}{dR_1} \\ \frac{db_1}{dR_1} \\ \frac{da_1}{dR_1} \end{bmatrix} = \begin{bmatrix} -\frac{R_{\mathrm{e}2}B}{R_{\mathrm{e}1}}\frac{R_{\mathrm{a}}B+K_{\mathrm{T}}K_{\mathrm{e}}}{((R_1+R_{\mathrm{a}})B+K_{\mathrm{T}}K_{\mathrm{e}})^2} \\ \frac{R_{\mathrm{e}2}}{R_{\mathrm{e}1}}\frac{R_{\mathrm{a}}JB}{((R_1+R_{\mathrm{a}})B+K_{\mathrm{T}}K_{\mathrm{e}})^2} \\ \frac{JK_{\mathrm{T}}K_{\mathrm{e}}(R_1+R_{\mathrm{a}})}{((R_1+R_{\mathrm{a}})B+K_{\mathrm{T}}K_{\mathrm{e}})^2} \end{bmatrix}; \boldsymbol{R}_2 = \begin{bmatrix} \frac{db_0}{dR_9} \\ \frac{db_1}{dR_9} \\ \frac{da_1}{dR_9} \end{bmatrix} = \begin{bmatrix} -\frac{R_{\mathrm{e}2}}{R_9^2}\frac{R_{\mathrm{a}}B+K_{\mathrm{T}}K_{\mathrm{e}}}{(R_1+R_{\mathrm{a}})B+K_{\mathrm{T}}K_{\mathrm{e}}} \\ -\frac{R_{\mathrm{e}2}}{R_9^2}\frac{JR_{\mathrm{a}}}{(R_1+R_{\mathrm{a}})B+K_{\mathrm{T}}K_{\mathrm{e}}} \\ 0 \end{bmatrix} \tag{37}$$

$$\boldsymbol{R}_3 = \begin{bmatrix} \frac{db_0}{dR_{12}} \\ \frac{db_1}{dR_{12}} \\ \frac{da_1}{dR_{12}} \end{bmatrix} = \begin{bmatrix} \frac{1}{R_{\mathrm{e}1}}\frac{R_{\mathrm{a}}B+K_{\mathrm{T}}K_{\mathrm{e}}}{((R_1+R_{\mathrm{a}})B+K_{\mathrm{T}}K_{\mathrm{e}})^2} \\ \frac{1}{R_{\mathrm{e}1}}\frac{R_{\mathrm{a}}J}{((R_1+R_{\mathrm{a}})B+K_{\mathrm{T}}K_{\mathrm{e}})^2} \\ 0 \end{bmatrix}; \boldsymbol{R}_4 = \begin{bmatrix} \frac{db_0}{dC_8} \\ \frac{db_1}{dC_8} \\ \frac{da_1}{dC_8} \end{bmatrix} = \begin{bmatrix} \frac{R_{\mathrm{e}2}}{R_{\mathrm{e}1}}\frac{R_5(R_{\mathrm{a}}B+K_{\mathrm{T}}K_{\mathrm{e}})}{(R_1+R_{\mathrm{a}})B+K_{\mathrm{T}}K_{\mathrm{e}}} \\ 0 \\ R_5+R_{2\mathrm{e}} \end{bmatrix}; \tag{38}$$

$$\boldsymbol{R}_5 = \begin{bmatrix} \frac{db_0}{dR_{\mathrm{a}}} \\ \frac{db_1}{dR_{\mathrm{a}}} \\ \frac{da_1}{dR_{\mathrm{a}}} \end{bmatrix} = \begin{bmatrix} \frac{R_{\mathrm{e}2}}{R_{\mathrm{e}1}}\frac{B^2R_1}{((R_1+R_{\mathrm{a}})B+K_{\mathrm{T}}K_{\mathrm{e}})^2} \\ \frac{R_{\mathrm{e}2}}{R_{\mathrm{e}1}}\frac{J(R_{\mathrm{a}}B+K_{\mathrm{T}}K_{\mathrm{e}})}{((R_1+R_{\mathrm{a}})B+K_{\mathrm{T}}K_{\mathrm{e}})^2} \\ \frac{JK_{\mathrm{T}}K_{\mathrm{e}}(R_1+R_a)}{((R_1+R_{\mathrm{a}})B+K_{\mathrm{T}}K_{\mathrm{e}})^2} \end{bmatrix}; \boldsymbol{R}_6 = \begin{bmatrix} \frac{db_0}{dJ} \\ \frac{db_1}{dJ} \\ \frac{da_1}{dJ} \end{bmatrix} = \begin{bmatrix} 0 \\ \frac{R_{\mathrm{e}2}}{R_{\mathrm{e}1}}\frac{R_{\mathrm{a}}}{(R_1+R_{\mathrm{a}})B+K_{\mathrm{T}}K_{\mathrm{e}}} \\ \frac{(R_1+R_{\mathrm{a}})}{(R_1+R_{\mathrm{a}})B+K_{\mathrm{T}}K_{\mathrm{e}}} \end{bmatrix}; \tag{39}$$

$$\boldsymbol{R}_7 = \begin{bmatrix} \frac{db_0}{dB} \\ \frac{db_1}{dB} \\ \frac{da_1}{dB} \end{bmatrix} = \begin{bmatrix} -\frac{R_{e2}}{R_{e1}} \frac{K_T K_e R_1}{((R_1+R_a)B+K_T K_e)^2} \\ -\frac{R_{e2}}{R_{e1}} \frac{JR_a(R_1+R_a)}{((R_1+R_a)B+K_T K_e)^2} \\ -\frac{J(R_1+R_a)}{((R_1+R_a)B+K_T K_e)^2} \end{bmatrix}. \quad (40)$$

After substituting the nominal values of the amplifier and motor model parameters (provided in Table 1), the Jacobian matrix with respect to the actual physical parameters was obtained as:

$$\boldsymbol{R} = \begin{bmatrix} -6.5 \cdot 10^{-3} & -1.197 \cdot 10^{-4} & 1.995 \cdot 10^{-4} & 2.39 \cdot 10^{3} & 1.76 \cdot 10^{-5} & 0 & -3.52 \cdot 10^{3} \\ -1 \cdot 10^{-4} & -1.9 \cdot 10^{-6} & 3.2 \cdot 10^{-6} & 0 & 5.1 \cdot 10^{-3} & 2.67 \cdot 10^{4} & -4.83 \cdot 10^{2} \\ 2.1 \cdot 10^{-4} & 0 & 0 & 1.3 \cdot 10^{3} & 2.1 \cdot 10^{-3} & 1.26 \cdot 10^{4} & -2.28 \cdot 10^{2} \end{bmatrix}. \quad (41)$$

It has been concluded that modifying (35) into the form:

$$\Delta\hat{\theta}_i = (\boldsymbol{R}'_i \boldsymbol{R}_i)^{-1} \boldsymbol{R}'_i \Delta\hat{\boldsymbol{\pi}}_i, \quad (42)$$

leads to significantly more accurate parameter estimation, resulting in improved precision and reliability of the results compared to the original approach, where:

$\Delta\hat{\theta}_i$ is the estimate of the change in the *i*-th physical parameter,
$\mathbf{R}_i$ is the *i*-th column of the Jacobian matrix (matrix of partial derivatives)
$\Delta\hat{\boldsymbol{\pi}}_i = \hat{\boldsymbol{\pi}}_i - \boldsymbol{\pi}_n$ is the estimate of the change in model parameters due to the *i*-th fault,
$\boldsymbol{\pi}_n$ is nominal model parameters,
$\hat{\boldsymbol{\pi}}_i$ is estimated model parameters in the presence of a fault in the *i*-th physical parameter.

Tables 11 and 12 present the estimates of the actual physical parameters of the amplifier and DC motor in the presence of individual multiplicative faults, using the described indirect method provided in (42). Thereby, the parameter estimates were calculated using:

$$\hat{\theta}_i = \Delta\hat{\theta}_i + \theta_n, \quad (43)$$

where $\theta_n$ represent nominal values of the actual physical parameters of the system.

**Table 11.** Estimation of amplifier physical parameters under multiplicative faults.

| **Parameter** | $R_1$ **= 1 Ω** | | | $R_9$ **= 10 kΩ** | | | $R_{12}$ **= 10 kΩ** | | | $C_8$ **= 47 pF** | | |
|---|---|---|---|---|---|---|---|---|---|---|---|---|
| Fault | 10 Ω | 56 Ω | 100 Ω | 33 kΩ | 56 kΩ | 100 kΩ | 2 kΩ | 3.3 kΩ | 5.6 kΩ | 1 μF | 10 μF | 47 μF |
| Estimated fault | 9.8 Ω | 49 Ω | 79 Ω | 17 kΩ | 18.2 kΩ | 19 kΩ | 2 kΩ | 3.3 kΩ | 5.6 kΩ | 0.97 μF | 9.7 μF | 46 μF |

**Table 12.** Estimation of motor physical parameters under multiplicative faults.

| **Parameter** | $R_a$ **= 7.41 Ω** | | $J$ **= 1.43·10$^{-6}$ kgm$^2$** | | $B$ **= 1.8·10$^{-6}$ Nm/rad/s** | |
|---|---|---|---|---|---|---|
| Fault | 0.741 Ω | 74.1 Ω | $1.43 \cdot 10^{-4}$ kgm$^2$ | $1.43 \cdot 10^{-8}$ kgm$^2$ | $1.8 \cdot 10^{-4}$ Nm/rad/s | $1.8 \cdot 10^{-5}$ Nm/rad/s |
| Estimated fault | 0.62 Ω | 64.4 Ω | $1.43 \cdot 10^{-4}$ kgm$^2$ | $1.45 \cdot 10^{-8}$ kgm$^2$ | $0.57 \cdot 10^{-4}$ Nm/rad/s | $1.53 \cdot 10^{-5}$ Nm/rad/s |

Based on the values presented in Tables 11 and 12, it can be concluded that the indirect estimation of physical parameters $R_{12}$, $C_8$, and $J$ is most accurate in the presence of multiplicative faults. This accuracy arises from the linear relationship with parameters $b_0$, $b_1$, and $a_1$ of the continuous amplifier model. During the estimation of $R_1$, $R_9$, $R_a$, and $B$,

due to the nonlinear relationship with the amplifier parameters and the large deviation of these parameters from their nominal values, the estimation results were less accurate. Nevertheless, the deviations obtained using the proposed solution (42) are significantly smaller than the completely unacceptable results produced by applying the approach available in the literature (35).

## 4. Discussion

### *4.1. Validation of Fault Detection Measurement Results*

To evaluate the effectiveness of different methods for detecting multiplicative faults in the motor and amplifier, the outputs of the amplifier model (3), obtained by substituting system parameters into Equations (4) and (5) for three different values of Coulomb friction [45] ($M_c$ = 0, $M_c$ = 0.48 mNm and $M_c$ = 0.33 mNm), with the outputs of model (6), which incorporates parameters estimated using the SIA, and model (8), based on the SWA results, have been compared. These outputs were compared with the measured output voltage $U_m$, and the percentage agreement was calculated using MATLAB's System Identification Toolbox, as shown in Tables 13–20.

**Table 13.** Percentage match of amplifier output before fault occurrence.

| SWA | SIA | $M_c = 0$ | $M_c = 0.48$ mNm ($M_c = 0.33$ mNm) |
|---|---|---|---|
| 98.6% | 98.59% | 92.27% | 91.92% (92%) |

**Table 14.** Percentage match of system output during parametric fault in $R_1$.

| $R_1 = 1\ \Omega$ | SWA | SIA | $M_c = 0$ | $M_c = 0.48$ mNm ($M_c = 0.33$ mNm) |
|---|---|---|---|---|
| 10 Ω | 95.71% | 96.42% | 70.78% | 69% (72.11%) |
| 56 Ω | 81.65% | 86.5% | −30.61% | 35.13% (76.74%) |
| 100 Ω | 74.44% | 76.75% | −150.2% | −17.67% (79%) |

**Table 15.** Percentage match of system output during parametric fault in $R_9$.

| $R_9 = 10$ kΩ | SWA | SIA | $M_c = 0$ | $M_c = 0.48$ mNm ($M_c = 0.33$ mNm) |
|---|---|---|---|---|
| 33 kΩ | 97.7% | 97.14% | 90.54% | 89.01% (89.52%) |
| 56 kΩ | 97.28% | 96.72% | 91.07% | 89.26% (89.87%) |
| 100 kΩ | 93.09% | 97.57% | 90.25% | 88.27% (88.93%) |

**Table 16.** Percentage match of system output during parametric fault in $R_{12}$.

| $R_{12} = 10$ kΩ | SWA | SIA | $M_c = 0$ | $M_c = 0.48$ mNm ($M_c = 0.33$ mNm) |
|---|---|---|---|---|
| 2 kΩ | 98.32% | 98.57% | 92.14% | 90% (90.89%) |
| 3.3 kΩ | 95.89% | 98.59% | 92% | 91.4% (91.6%) |
| 5.6 kΩ | 98.77% | 97.96% | 92.48% | 91.52% (91.89) |

**Table 17.** Percentage match of system output during parametric fault in $C_8$.

| $C_8 = 47$ pF | SWA | SIA | $M_c = 0$ | $M_c = 0.48$ mNm ($M_c = 0.33$ mNm) |
|---|---|---|---|---|
| 1 μF | 97.85% | 90.6% | 75.41% | 75.4% (75.43%) |
| 10 μF | 95.07% | 97.57% | 88.53% | 89.04% (88.98%) |
| 47 μF | 87.96% | 96.72% | 96.3% | 96.69% (96.7%9 |

**Table 18.** Percentage match of system output during parametric fault in $R_a$.

| $R_a$ = 7.41 Ω | SWA | SIA | $M_c$ = 0 | $M_c$ = 0.48 mNm ($M_c$ = 0.33 mNm) |
|---|---|---|---|---|
| 0.741 Ω | 99.68% | 89.53% | 95.43% | 95.01% (95.25%) |
| 74.1 Ω | 95.84% | 99.31% | 99.75% | 98.53% (98.93%) |

**Table 19.** Percentage match of system output during parametric fault in $J$.

| $J = 1.43 \cdot 10^{-6}$ kgm$^2$ | SWA | SIA | $M_c$ = 0 | $M_c$ = 0.48 mNm ($M_c$ = 0.33 mNm) |
|---|---|---|---|---|
| $1.43 \cdot 10^{-4}$ kgm$^2$ | 85.84% | 96.63% | 99.59% | 98.72% (99.12%) |
| $1.43 \cdot 10^{-8}$ kgm$^2$ | 82.76% | 82.69% | 75.73% | 75.71% (75.73%) |

**Table 20.** Percentage match of system output during parametric fault in $B$.

| $B = 1.8 \cdot 10^{-6}$ Nm/rad/s | SWA | SIA | $M_c$ = 0 | $M_c$ = 0.48 mNm ($M_c$ = 0.33 mNm) |
|---|---|---|---|---|
| $1.8 \cdot 10^{-4}$ Nm/rad/s | 99.54% | 99.21% | 96.88% | 96.84% (96.86%) |
| $1.8 \cdot 10^{-5}$ Nm/rad/s | 99.45% | 99.1% | 96.5% | 96.2% (96.35%) |

An example of the Simulink models and the comparison interface for model outputs with the measured output voltage, in the case of a fault $R_1$ = 100 Ω, is shown in Figure 22. The corresponding output signals are presented in Figure 23.

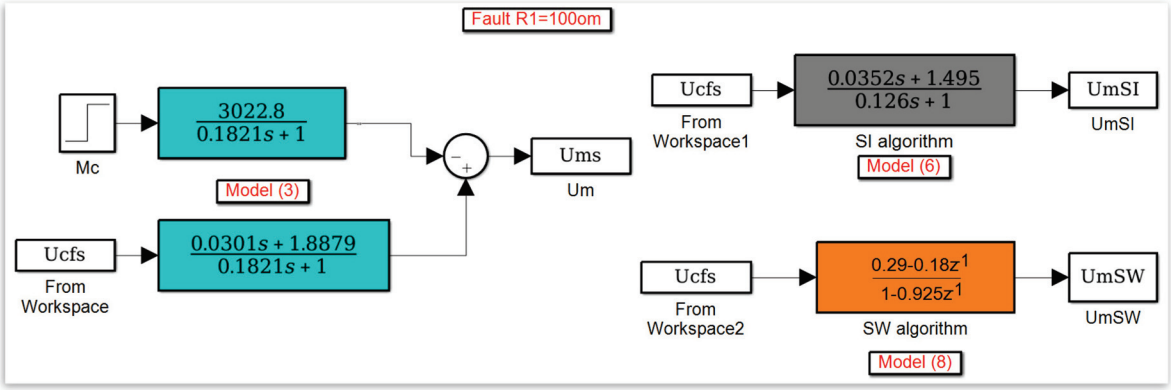


**Figure 22.** Simulation models of the amplifier under a fault $R_1$ = 100 Ω.

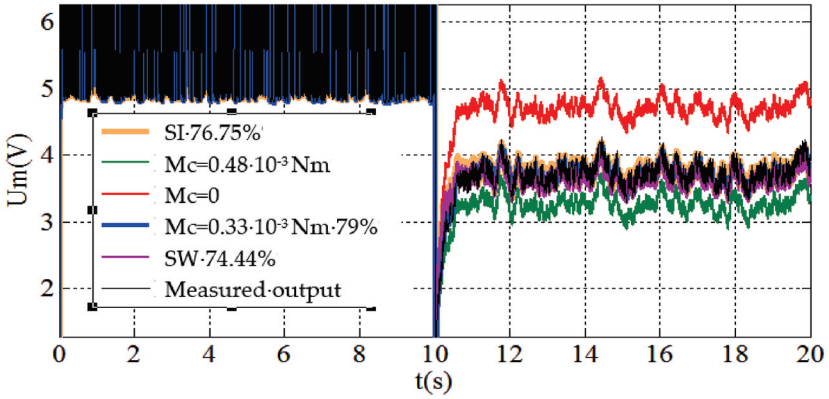


**Figure 23.** Measured and simulated outputs of the amplifier during the fault $R_1$ = 100 Ω.

Based on the results, it is clear that a multiplicative fault in resistor $R_1 = 100\ \Omega$ (Table 14) significantly amplifies the effect of Coulomb friction (Figure 23). In this scenario, the model incorporating $M_c = 0.33$ mNm achieves the closest match to the measured output (79%), compared with the SIA-based model (76.8%) and the SWA-based model (74.4%). By contrast, for faults in $C_8$, $R_{9,}$ or $R_{12}$, including Coulomb friction makes virtually no difference: the percentage match to the measured output is effectively the same whether friction is modeled or not.

A comparison of the fault-detection algorithms and the linearized models (with and without Coulomb friction) yields the following insights:

- Although the SIA is computationally more complex and more sensitive to noise than the discrete-time approach, it proved almost as effective at detecting multiplicative faults. As it has been observed, it is important to ensure that the length of the identification dataset $K$ is chosen to be sufficiently small yet greater than $m$ (i.e., $K > m$).
- The SWA is computationally simpler and more robust to measurement noise, making it better suited for real-time applications. Its parameter estimates also showed strong agreement with the actual system response.
- Obtained results confirm that, at the nominal resistance $R_1 = 1\ \Omega$, Coulomb friction is negligible. When $R_1$ increases abruptly, however, Coulomb friction can no longer be ignored (which is consistent with Equation (2)). Hence, simplified SIA and SWA models based on (6) and (8) that omit Coulomb friction lose accuracy. Also, the Coulomb friction value $M_c = 0.33$ mNm, which yields the best fit, appears to be more accurate than the value reported in [45]. However, the agreement between the measured system output and the output of the linearized model (2), with $M_c = 0.33$ mNm, does not exceed 80% for any fault magnitude in $R_1$, indicating that the system can only be linearized approximately.

### *4.2. Discussion of Multiplicative Fault Isolation and Identification*

#### 4.2.1. Discussion of the Decision Algorithm

After the fault isolation procedure is carried out using the decision algorithm, fault identification can be performed (when using one of the continuous estimation procedures, such as the SIA) based on a known, generally relatively simple relationship with the model parameters.

#### 4.2.2. Discussion of the Indirect Estimation Procedure

When fault detection is performed through parameter estimation of a discrete model, such as the SWA, faults can only be identified using indirect approaches. However, due to the higher complexity and nonlinearity of the relationship with the model parameters in this case, the accuracy of the method is directly affected by how much the fault magnitude deviates from nominal values.

Here, too, the advantage of the continuous estimation method over the discrete one becomes evident, particularly in terms of the complexity of diagnosing multiplicative faults.

Also, more accurate parameter estimation in the indirect identification procedure has been achieved by extracting only selected columns from the Jacobian matrix (matrix of partial derivatives), instead of applying the full matrix as suggested in the literature. This is supported by the analyzed case involving large multiplicative faults that significantly deviate from the nominal operating point, where the literature-proposed method proved inapplicable. In such cases of large faults, when the relationship between model parameters and actual physical parameters is linear, the proposed method provides highly accurate identification. In the case of a nonlinear relationship, the result remains approximate but

is still more acceptable than the entirely inaccurate solution obtained using the literature-based approach.

### 4.3. Comparison of the Results

A summary of key parameter estimation, knowledge-based, and optimization methods used in fault detection, isolation, and identification (FDII) is presented in Table 21, highlighting their real-time applicability, computational complexity, robustness to noise and transients, and overall FDII capability.

As shown in Table 21, each method presents a trade-off between real-time capability, complexity, and fault coverage. The proposed SWA and SIA approaches demonstrate a favorable balance, offering full diagnostic functionality with low-to-moderate complexity and strong robustness to noise.

**Table 21.** Comparison of Proposed FDII Framework with Existing Literature.

| Method | Real-Time Capability | Effectiveness | Computational Complexity | Characteristics | Fault Detection/Isolation/ Identification |
|---|---|---|---|---|---|
| Least Squares (LS) [18,32,38] | Offline | Effective for static faults | Low | Not suitable for real time; sensitive to noise; poor performance under transients | Detection only |
| Recursive Least Squares (RLS) RLS [30,31] | Real time | Effective for gradual parameter changes | Moderate | Sensitive to noise and abrupt faults; requires forgetting factor tuning | Detection + Identification |
| Extended Kalman Filter (EKF) [29,34,35] | Real time (with tuning) | Suitable for nonlinear systems | High | Requires accurate model; sensitive to noise covariance; tuning required | Full (Detection, Isolation, Identification) |
| Unscented Kalman Filter (UKF) UKF [36,37] | Real time (with tuning) | High estimation accuracy for nonlinear systems | Very High | Computationally intensive; complex tuning process | Full (Detection, Isolation, Identification) |
| Algebraic-Geometric Technique (AGT) [33] | Offline | High analytical accuracy | High | Requires symbolic derivation; not robust to noise | Full (Detection, Isolation, Identification) |
| Genetic Algorithm (GA) [42]. | Offline (training/optimisation) | Effective in feature selection, parameter tuning | High | Not suitable for real time; used primarily for offline training/optimisation | Detection, Optimisation (offline) |
| Particle Swarm Optimisation (PSO) [41]. | Offline (training/optimisation) | Effective for weight tuning in ML models | Moderate–High | Not real time; applied offline for tuning; performance depends on swarm settings | Detection, Optimisation (offline) |
| Neural Networks (NN) [6,18,41] | Possible (inference only) | High accuracy with nonlinear and complex patterns | High (training), Low–Mod (inference) | Training is offline; real time only feasible if model is simple and pretrained | Full (if combined with logic/rules) |
| Proposed method: Sliding Window Algorithm (SWA)+ selected Jacobian | Real-time | Robust to noise; suited for abrupt faults; | Low | Performance depends on window size; | Full (Detection, Isolation, Identification) |
| Proposed method: Sliding Integral Algorithm (SIA)+ Decision algorithm | Real-time | Robust to noise; suited for abrupt faults; clear model-parameter link | Moderate | Performance depends on window lengths and data lengths | Full (Detection, Isolation, Identification) |

## 5. Conclusions

The paper discusses diagnosis of multiplicative faults caused by sudden changes in one of the parameters of the converter or motor, which significantly deviate from the nominal operating point. Four amplifier faults were considered (changes in resistances $R_1$, $R_9$, $R_{12}$, and capacitance $C_8$), along with three motor faults (changes in moment of inertia $J$, viscous friction coefficient $B$, and armature resistance $R_a$). The method leverages the advantageous fact that the electromechanical parameters of the motor are reflected in the parameters of the amplifier model, which is realized as a linear electronic circuit with an operational amplifier. Therefore, the fault detection algorithms could be based solely on parameter estimation of the discrete or continuous model of the amplifier, which is a unique approach to the problem.

Diagnosing faults caused by abrupt parameter changes is particularly demanding. Classical parameter estimation techniques yield unsatisfactory results because a sudden change in one system parameter initiates a transient process during which the effect of the change spreads to other parameters as well. To address this, more advanced estimation techniques were employed for detecting multiplicative faults induced by sudden parameter changes in the amplifier or motor. These included: the SWA for estimating parameters of the discrete model and the SIA for estimating parameters of the continuous model.

An additional requirement for the application of these techniques is the necessity of a sufficiently informative input signal (i.e., persistent excitation) of adequate order to enable parameter identification. To satisfy this, a PRBS (Pseudo-Random Binary Sequence) signal was used in the experiments.

This paper implements a modified version of the SIA, which introduces a constraint on the data length in the least squares algorithm, within which the sliding integral is applied. This modification aims to reduce the impact of transients on parameter estimation.

To compare the two approaches to multiplicative fault detection and to assess estimation quality, as well as the influence of Coulomb friction disturbances on system behavior under fault conditions, the responses of the respective models were compared with the measured system response. It was concluded that although the continuous parameter estimation method is more demanding to implement (particularly in real-time applications), it proved equally effective in detecting multiplicative faults in the specific case studied. Furthermore, the influence of Coulomb friction as a disturbance was most pronounced in cases involving a fault in resistance $R_1$, where both the SWA and SIA algorithms yielded the best results.

To support fault isolation in case of SIA, a new decision algorithm was developed to enable accurate fault localization. In the case of continuous parameter estimation, fault identification—defined as the determination of both the faulty physical parameter and the magnitude of its change—is straightforward. The faulty parameter can be directly identified using the analytical relationships that define the amplifier model.

An alternative approach, applicable when fault detection is performed using the SWA method, involves indirect estimation of changes in physical parameters. This technique is based on evaluating the partial derivatives (i.e., sensitivity coefficients) of the model parameters with respect to the physical parameters at the nominal operating point. The method yields accurate results when the relationship between estimated model parameters and physical parameters is linear. However, in the more common case of nonlinear dependencies, the estimation becomes an approximation, valid primarily for small deviations around the nominal point. Consequently, its accuracy diminishes as the magnitude of the physical fault increases.

It was observed that better estimation results are obtained by selecting specific columns of the Jacobian matrix (i.e., the matrix of partial derivatives), rather than using the full

matrix, as suggested in the literature. This approach proved especially effective in cases of nonlinear dependencies, even when the multiplicative faults are large and significantly deviate from the nominal operating point—representing one of the key contributions of this paper.

For the considered multiplicative faults, LabVIEW codes with partial real-time implementation were developed, using the Flat Sequence Frame structure. After signal acquisition, they are processed within LabVIEW MathScript Nodes for implementing the required parameter estimation algorithms. This results in practical solutions suitable for remote laboratories and training in the FDII.

Based on the above, it can be concluded that FDII techniques originally intended for LTI models, with appropriate modifications, can be successfully applied to certain classes of nonlinear dynamic systems, such as the analyzed permanent magnet DC motor with the corresponding amplifier.

Supported by the experimental results, which include precise fault detection, reliable fault isolation, and identification, it can be concluded that the presented findings are fully supported by the obtained data and the observed system behavior.

Feature work will be based on development of a fault-tolerant control (FTC) system that is robust against faults by incorporating a compensation mechanism between the faulty plant and the nominal controller. This compensation mechanism should allow the fault to be accommodated by the controller, ensuring that the faulty plant, under nominal control, remains globally stable and delivers satisfactory performance in both the transient and steady-state regimes.

**Author Contributions:** Conceptualization, S.A., M.R. and A.M.; methodology, S.A., M.R. and A.M.; software, S.A., B.K. and M.L.; validation, S.A. and M.R.; formal analysis, B.K., A.M. and M.L.; investigation, S.A. and M.R.; resources, B.K. and M.L.; data curation, S.A. and M.L.; writing—original draft preparation, S.A. and A.M.; writing—review and editing, M.R., B.K. and M.L.; visualization, S.A., M.R., B.K. and M.L.; supervision, A.M. All authors have read and agreed to the published version of the manuscript.

**Funding:** This study was supported by the Ministry of Science, Technological Development, and Innovation of the Republic of Serbia, and these results are part of the Grant No. 451-03-136/2025-03/200132, with University of Kragujevac—Faculty of Technical Sciences Čačak.

**Institutional Review Board Statement:** Not applicable.

**Informed Consent Statement:** Not applicable.

**Data Availability Statement:** The original contributions presented in this study are included in the article. Further inquiries can be directed to the corresponding author.

**Conflicts of Interest:** The authors declare no conflict of interest.

## References

1. Park, Y.J.; Fan, S.K.S.; Hsu, C.Y. A review on fault detection and process diagnostics in industrial processes. *Processes* **2020**, *8*, 1123. [CrossRef]
2. Du, X. Fault detection using bispectral features and one-class classifiers. *J. Process Control* **2019**, *83*, 1–10. [CrossRef]
3. Gertler, J.J. *Fault Detection and Diagnosis in Engineering Systems*; CRC Press: Boca Raton, FL, USA, 2017. [CrossRef]
4. Mariano-Hernández, D.; Hernández-Callejo, L.; Zorita-Lamadrid, A.; Duque-Pérez, O.; Santos García, F. A review of strategies for building energy management system: Model predictive control, demand side management, optimization, and fault detect & diagnosis. *J. Build. Eng.* **2021**, *33*, 101692. [CrossRef]
5. Mercorelli, P. Recent advances in intelligent algorithms for fault detection and diagnosis. *Sensors* **2024**, *24*, 2656. [CrossRef]
6. Adouni, A.; Ben Hamed, M.; Flah, A.; Sbita, L. Sensor and actuator fault detection and isolation based on artificial neural networks and fuzzy logic applicated on induction motor. In Proceedings of the 2013 International Conference on Control, Decision and Information Technologies (CoDIT), Hammamet, Tunisia, 6–8 May 2013; pp. 917–922. [CrossRef]

7. Guzmán-Rabasa, J.A.; López-Estrada, F.R.; González-Contreras, B.M.; Valencia-Palomo, G.; Chadli, M.; Pérez-Patricio, M. Actuator fault detection and isolation on a quadrotor unmanned aerial vehicle modeled as a linear parameter-varying system. *Meas. Control* **2019**, *52*, 1228–1239. [CrossRef]
8. Debele, Y.; Shi, H.Y.; Wondosen, A.; Ku, T.W.; Kang, B.S. Deep learning-based robust actuator fault detection and isolation scheme for highly redundant multirotor UAVs. *Drones* **2023**, *7*, 437. [CrossRef]
9. Tirandaz, H.; Keliris, C.; Polycarpou, M. Actuator fault detection and isolation in a class of nonlinear interconnected systems. *Int. J. Control* **2024**, *97*, 2914–2934. [CrossRef]
10. Antic, S.; Djurovic, Z.; Kvascev, G. Application of structured and directional residuals for fault detection and isolation on permanent-magnet DC motor with amplifier. *Qual. Reliab. Eng. Int.* **2016**, *32*, 2601–2621. [CrossRef]
11. Antic, S.; Rosic, M.; Djurovic, Z.; Bozic, M. Comparison of structured residuals design techniques for actuator and sensor fault detection and isolation in a permanent magnet DC motor. *Electr. Eng.* **2024**, *106*, 2087–2105. [CrossRef]
12. Antić, S.; Luković, V.; Đurović, Ž. Expert system for FDI of DC motor faults using structured residuals design technique. *Serb. J. Electr. Eng.* **2023**, *20*, 93–105. [CrossRef]
13. Boulkroune, B.; Gálvez-Carrillo, M.; Kinnaert, M. Additive and multiplicative fault diagnosis for a doubly-fed induction generator. In Proceedings of the IEEE International Conference on Control Applications (CCA), Denver, CO, USA, 28–30 September 2011; pp. 1302–1308. [CrossRef]
14. Ding, S.X.; Frank, P.M.; Ding, E.L. An approach to the detection of multiplicative faults in uncertain dynamic systems. In Proceedings of the IEEE Conference on Decision and Control, Las Vegas, NV, USA, 10–13 December 2002; Volume 4, pp. 4371–4376. [CrossRef]
15. Huang, H.P.; Li, C.C.; Jeng, J.C. Multiple multiplicative fault diagnosis for dynamic processes via parameter similarity measures. *Ind. Eng. Chem. Res.* **2007**, *46*, 4517–4530. [CrossRef]
16. Zhu, C.C.; Li, L.; Ding, S.X. Multiplicative fault detection and isolation in dynamic systems using data-driven K-gap metric based KNN algorithm. *IFAC-Pap.* **2022**, *55*, 169–174. [CrossRef]
17. Ben Brahim, A.; Dhahri, S.; Ben Hmida, F.; Sellami, A. Multiplicative fault estimation-based adaptive sliding mode fault-tolerant control design for nonlinear systems. *Complexity* **2018**, *2018*, 1462594. [CrossRef]
18. Liu, X.Q.; Zhang, H.Y.; Liu, J.; Yang, J. Fault detection and diagnosis of permanent-magnet DC motor based on parameter estimation and neural network. *IEEE Trans. Ind. Electron.* **2000**, *47*, 1021–1030. [CrossRef]
19. Lu, L.; Wang, W. Fault diagnosis of permanent magnet DC motors based on multi-segment feature extraction. *Sensors* **2021**, *21*, 7505. [CrossRef]
20. Dobra, P.; Trușcă, M.; Sita, I.V.; Munteanu, R.A.; Munteanu, M. Model based approach in fault detection and diagnosis for DC motor. In Proceedings of the 8th IEEE Symposium on Diagnostics for Electrical Machines, Power Electronics and Drives (SDEMPED), Bologna, Italy, 5–8 September 2011; pp. 229–233. [CrossRef]
21. Liu, M.; Yang, X.; Cui, S. Online fault detection and diagnosis of permanent-magnetic DC motor. In Proceedings of the 2008 IEEE Vehicle Power and Propulsion Conference (VPPC), Harbin, China, 3–5 September 2008. [CrossRef]
22. Nandi, S.; Toliyat, H.A.; Li, X. Condition monitoring and fault diagnosis of electrical motors—A review. *IEEE Trans. Energy Convers.* **2005**, *20*, 719–729. [CrossRef]
23. Akin, B.; Choi, S.; Orguner, U.; Toliyat, H.A. A simple real-time fault signature monitoring tool for motor-drive-embedded fault diagnosis systems. *IEEE Trans. Ind. Electron.* **2011**, *58*, 1990–2001. [CrossRef]
24. Park, J.-K.; Seo, I.-M.; Hur, J. Fault type detection using frequency pattern of stator current in IPM-type BLDC motor under stator inter-turn, dynamic eccentricity, and coupled faults. In Proceedings of the 2013 IEEE Energy Conversion Congress and Exposition (ECCE), Denver, CO, USA, 15–19 September 2013; pp. 2516–2521. [CrossRef]
25. Saadaoui, W.; Jelassi, K. Induction motor bearing damage detection using stator current analysis. In Proceedings of the 2011 International Conference on Power Engineering, Energy and Electrical Drives (POWERENG), Málaga, Spain, 11–13 May 2011; pp. 1–6. [CrossRef]
26. Chan, C.W.; Hua, S.; Hong-Yue, Z. Application of fully decoupled parity equation in fault detection and identification of DC motors. *IEEE Trans. Ind. Electron.* **2006**, *53*, 1277–1284. [CrossRef]
27. Lee, J.H.L.J.; Lyou, J.L. Fault Diagnosis and Fault Tolerant Control of DC Motor Driving System. In Proceedings of the 2001 IEEE International Symposium on Industrial Electronics (ISIE 2001), Pusan, Republic of Korea, 8–11 July 2001; Volume 3, pp. 1719–1723. [CrossRef]
28. Najafabadi, T.A.; Salmasi, F.R.; Jabehdar-Maralani, P. Detection and Isolation of Speed-, DC-Link Voltage-, and Current-Sensor Faults Based on an Adaptive Observer in Induction-Motor Drives. *IEEE Trans. Ind. Electron.* **2011**, *58*, 1662–1672. [CrossRef]
29. Kargar, S.M.; Salahshoor, K.; Yazdanpanah, M.J. Integrated Nonlinear Model Predictive Fault-Tolerant Control and Multiple-Model-Based Fault Detection and Diagnosis. *Chem. Eng. Res. Des.* **2014**, *92*, 340–349. [CrossRef]
30. Jiang, Z.; Huang, X.; Cao, W. RLS-Based Algorithm for Detecting Partial Demagnetization under Both Stationary and Nonstationary Conditions. *Energies* **2022**, *15*, 3509. [CrossRef]

31. Kuric, M.; Lacevic, B.; Osmic, N.; Tahirovic, A. RLS-Based Fault-Tolerant Tracking Control of Multirotor Aerial Vehicles. In Proceedings of the IEEE/ASME International Conference on Advanced Intelligent Mechatronics (AIM), Munich, Germany, 24 August 2017; pp. 1148–1153. [CrossRef]
32. Leite, D.F.; Hell, M.B.; Diez, P.H.; Ganglio, B.S.L.; Nascimento, L.O.; Costa, P. Real-time model-based fault detection and diagnosis for alternators and induction motors. In Proceedings of the IEEE International Electric Machines and Drives Conference (IEMDC), Miami, FL, USA, 3–5 May 2007; Volume 1, pp. 202–207. [CrossRef]
33. Menini, L.; Possieri, C.; Tornambè, A. Application of algebraic geometry techniques in permanent magnet DC motor fault detection and identification. *Eur. J. Control* **2015**, *25*, 39–50. [CrossRef]
34. Fernández Gómez, A.J.; Jaramillo, V.H.; Ottewill, J.R. Fault Detection in Electric Motors by Means of the Extended Kalman Filter as Disturbance Estimator. In Proceedings of the 2014 UKACC International Conference on Control (CONTROL 2014), Loughborough, UK, 9–11 July 2014; pp. 432–437. [CrossRef]
35. Miniach, M.; Orlowska-Kowalska, T. Innovative Extended Kalman Filter in a Coherent System for Detection and Compensation of Various Current Sensor Faults in the Induction Motor Drive. *IEEE Trans. Ind. Electron.* **2025**, *72*, 7772–7784. [CrossRef]
36. Xiong, K.; Chan, C.W.; Zhang, H.Y. Unscented Kalman Filter for Fault Detection. *IFAC Proc. Vol.* **2005**, *38*, 113–118. [CrossRef]
37. Karami, F.; Poshtan, J.; Poshtan, M. Model-Based Fault Detection in Induction Motors. In Proceedings of the IEEE International Conference on Control Applications (CCA), Yokohama, Japan, 8–10 September 2010; pp. 1957–1962. [CrossRef]
38. Rao, C.R.; Toutenburg, H. *Linear Models: Least Squares and Alternatives*; Springer: New York, NY, USA, 1999. [CrossRef]
39. Isermann, R. *Fault-Diagnosis Applications: Model-Based Condition Monitoring; Actuators, Drives, Machinery, Plants, Sensors, and Fault-Tolerant Systems*; Springer: Berlin/Heidelberg, Germany, 2011. [CrossRef]
40. de Miguel, L.J.; Blázquez, L.F. Fuzzy Logic-Based Decision-Making for Fault Diagnosis in a DC Motor. *Eng. Appl. Artif. Intell.* **2005**, *18*, 423–450. [CrossRef]
41. Lee, C.Y.; Maceren, E.D.C. Induction motor bearing fault classification using deep neural network with particle swarm optimization-extreme gradient boosting. *IET Electr. Power Appl.* **2024**, *18*, 297–311. [CrossRef]
42. Toma, R.N.; Prosvirin, A.E.; Kim, J.M. Bearing fault diagnosis of induction motors using a genetic algorithm and machine learning classifiers. *Sensors* **2020**, *20*, 1884. [CrossRef]
43. Patton, R.J.; Frank, P.M.; Clark, R.N. (Eds.) *Issues of Fault Diagnosis for Dynamic Systems*; Springer: London, UK, 2000.
44. Isermann, R. *Fault-Diagnosis Systems: An Introduction from Fault Detection to Fault Tolerance*; Springer: Berlin/Heidelberg, Germany, 2006.
45. Bjekic, M.; Antic, S.; Milovanovic, A. Permanent Magnet DC Motor Friction Measurement and Analysis of Friction's Impact. *Int. Rev. Electr. Eng. (IREE)* **2011**, *6*, 2261–2269.
46. Karnopp, D. Computer Simulation of Stick-Slip Friction in Mechanical Dynamic Systems. *J. Dyn. Syst. Meas. Control* **1985**, *107*, 100–103. [CrossRef]
47. Ljung, L. *System Identification: Theory for the User*, 2nd ed.; Prentice Hall: Upper Saddle River, NJ, USA, 1999.
48. Gholami, A.; Haddadnia, J.; Ghasemi, J.B. A Sliding Window Approach for Signal Processing in Fault Detection. *Signal Process.* **2013**, *93*, 2760–2771. [CrossRef]
49. Zhao, J.; Wang, X.; Gao, G.; Na, J.; Liu, H.; Luan, F. Online Adaptive Parameter Estimation for Quadrotors. *Algorithms* **2018**, *11*, 167. [CrossRef]
50. Yang, B.; Wang, J.; Sun, Y. Fault Detection and Diagnosis Based on Sliding Mode Integral Algorithm for Nonlinear Systems. *Appl. Sci.* **2020**, *10*, 1234. [CrossRef]
51. Antić, S.; Đurović, Ž. Application of Sliding Integral Algorithm for Parametric Fault Detection of a DC Motor Amplifier. In Proceedings of the 2nd International Conference on Electrical, Electronic and Computing Engineering (IcETRAN 2015), Silver Lake, Serbia, 8–11 June 2015; pp. AUI1.5.1–AUI1.5.6, ISBN 978-86-80509-71-6.
52. Sagara, S.; Zhao, Z.Y. Numerical Integration Approach to On-Line Identification of Continuous-Time Systems. *Automatica* **1990**, *26*, 63–74. [CrossRef]


**Disclaimer/Publisher's Note:** The statements, opinions and data contained in all publications are solely those of the individual author(s) and contributor(s) and not of MDPI and/or the editor(s). MDPI and/or the editor(s) disclaim responsibility for any injury to people or property resulting from any ideas, methods, instructions or products referred to in the content.

MDPI AG
Grosspeteranlage 5
4052 Basel
Switzerland
Tel.: +41 61 683 77 34

*Applied Sciences* Editorial Office
E-mail: applsci@mdpi.com
www.mdpi.com/journal/applsci




Disclaimer/Publisher's Note: The title and front matter of this reprint are at the discretion of the Guest Editors. The publisher is not responsible for their content or any associated concerns. The statements, opinions and data contained in all individual articles are solely those of the individual Editors and contributors and not of MDPI. MDPI disclaims responsibility for any injury to people or property resulting from any ideas, methods, instructions or products referred to in the content.





Academic Open
Access Publishing

mdpi.com

ISBN 978-3-7258-8002-7